Effect of different loading conditions on the accumulation of residual strain in a creep resistant 1%CrMoV steel A neutron and X-ray diffraction study

PAR

Michael Andreas WEISSER

ÉCOLE POLYTECHNIQUE
FÉDÉRALE DE LAUSANNE

Suisse
2013

Abstract

Plastic deformation of multi-phase materials can generate significant amount of stresses between the microstructural constituents due to their different mechanical properties. In ferritic carbon steels, the main microstructural constituents are the polycrystalline ferritic matrix and the cementite particles.

Several X-ray and neutron diffraction studies report on the interplay between the cementite and the ferrite. These studies, however, have been limited to ambient temperatures, where cementite is known to be a hard and brittle phase. Under that condition, large stresses between these two phases are created due to the load-redistribution from the plastifying ferrite to the cementite.

The strengthening mechanisms at both ambient and elevated temperatures in creep resistant bainitic 1% CrMoV steels are governed by the interplay between the ductile ferrite matrix and the carbides, among which vanadium carbide and cementite are the main constituents. In this dissertation, the residual stress (actually strain) accumulated during RT tensile deformation is studied and compared to the residual strain accumulated during high temperature (565°C) tensile and creep deformation. A temperature of 565°C was chosen because it is the maximum operating temperature for this material when used as a rotor steel in steam turbines. The complementary use of Time-of-flight (ToF) neutron and synchrotron X-ray diffraction accounts for the inhomogeneous microstructure and the low volume fraction of the second phase particles (3%), respectively.

ToF neutron diffraction on pre-deformed samples shows that the accumulation of residual strains strongly depends on the deformation condition: Large interphase strains are created during RT tensile deformation whereas very little strains are created after creep deformation. On the other hand, large intergranular strains are introduced for every deformation sequence but the load-redistribution between the ferrite grain families appears to be different at ambient and elevated temperatures.

In situ neutron and X-ray diffraction elucidates that the cementite contributes to the build-up of interphase strain during during deformation at both RT and HT, but only until creep mechanisms become dominating. The intergranular load-redistribution is discussed in terms of the elastic anisotropy of the ferrite grain families, which appears to be more pronounced at elevated temperatures.

The small volume fraction of cementite in the 1%CrMoV is responsible for a significant accumulation of residual interphase strain, comparable to the amount in some high-carbon steels. It appears that the microstructure and the morphology of the cementite particles can significantly influence the amount of residual strain. In addition, the cementite characteristics during tensile deformation in the 1%CrMoV have been studied and compared to that of a pearlitic and a spheroidized microstructure with spherical cementite particles. Cementite shows an elastic

anisotropy and an extensive diffraction peak broadening during plastic deformation. This broadening is discussed in terms of the range of local stress states, the individual particles experience.

Zusammenfassung

Plastische Verformung eines Mehrphasenstahls kann zu erheblichen Spannungen zwischen den einzelnen mikrostrukturellen Bestandteilen führen, da diese unterschiedlich mechanische Eigenschaften aufweisen. In ferritischen Kohlenstoffstählen sind die Hauptbestandteile die ferritische Matrix und Zementitpartikel.

Einige Studien mittels Röntgen- und Neutronenbeugung berichten über die gegenseitige Einflussnahme zwischen dem Zementit und der ferritischen Matrix. Diese Studien wurden jedoch nur bei Raumtemperatur durchgeführt, wo der Zementit als harte und spröde Phase bekannt ist. Unter diesen Bedingungen können aufgrund der Lastumverteilung von dem plastisch verformenden Ferrit hin zum Zementit grosse Spannungen zwischen den Phase auftreten.

Die Festigkeitsmechanismen bei Raum- und erhöhter Temperatur in einem kriechresistentem 1%CrMoV Stahl sind dominiert durch das Zusammenspiel zwischen der duktilen ferritischen Matrix und den Karbiden, welche hauptsächlich aus Vanadiumkarbid und Zementit bestehen. In dieser Dissertation werden die Eigenspannungen (eigentlich Eigendehungen) untersucht, die entstehen, wenn der Stahl verformt wird. Dabei werden drei verschiedene Verformungsbedingungen untersucht: Zugversuch bei Raumtemperatur und bei 565°C und Kriechverformung bei 565°C. Die gewählte Temperatur von 565°C entspricht der maximalen Betriebstemperatur dieses Materials, welches als Rotorenstahl in Dampfturbinen verwendet wird. Ein komplementärer Ansatz von Neutronen- und Röntgenbeugung trägt der inhomogenen Mikrostruktur und dem niedrigen Volumenanteil an Zweitphasenpartikeln (3%) Rechung.

Neutronenbeugung an vorverformten Proben zeigt, dass die Anhäufung von Eigendehungen stark von der Verformungsbedingung abhängt: Grosse Dehnungen zwischen den Phasen entstehen durch Zugverformung bei Raumtemperatur, durch Kriechverformung entstehen hingegen nur kleine Dehnungen. Andererseits werden durch jede Verformungsbedingung grosse Spannungen zwischen den Ferritkörnern erzeugt. Die Lastumverteilung zwischen den verschiedenen Kornorientierungen des Ferrits scheint jedoch temperaturabhängig zu sein.

In situ Neutronen- und Röntgenbeugung zeigt, dass der Zementit zum Aufbau der Eigendehungen nur solange beiträgt, bis Kriechmechanismen die Verformung dominieren. Die Lastumverteilung zwischen den einzelnen Kornorientierungen des Ferrits wird diskutiert mit Blick auf die elastische Anisotropie des Ferrits, die bei hohen Temperatur grösser zu seinen scheint.

Der kleine Volumenanteil an Zementit in dem 1%CrMoV Stahl ist verantwortlich für einen beträchtlichen Anteil an Eigendehungen, vergleichbar mit dem, was in manchen Stählen mit hohem Kohlenstoffanteil auftritt. Es scheint, dass die Mikrostruktur und die Morphologie des Zementits die Grösse der Eigendehungen erheblich beeinflussen kann. Des Weiteren wurden einige Besonderheiten des Zementits während der Zugverformung des 1%CrMoV Stahls untersucht

und verglichen mit Zugverformungen an perlitischem Stahl und einem Stahl mit sphärischen Zementitpartikeln. Der Zementit zeigt eine elastische Anisotropie und während der plastischen Verformung eine extreme Verbreiterung des Beugungsreflexes. Diese Verbreiterung wird diskutiert mit Blick auf die lokalen Spannungszustände der einzelnen Zementitpartikel.

List of abbreviations

<u>Sample description:</u>

FCC, BCC	face centred cubic, body centred cubic,
RT, HT	Room temperature, high temperature (in chapter 3 and 4: 565°C)
Cem	Cementite

<u>Methods:</u>

EBSD, EDX	Electron backscattered diffraction, Energy Dispersive Xray spectroscopy
SEM, TEM	Scanning and Transmission electron microscopy
XRD, ToF	X-ray diffraction, Time-of-Flight
EPSC	Elasto-plastic self-consistent (modelling)
MTM, ETMT	Miniaturized Tensile Machine, Electro-Thermal Mechnical Testing device
SLS, ESRF	Swiss Light Source, European Synchrotron Radiation Facility
TTT, CCT	Time-temperature- and continuous-cooling transition diagram

<u>Units:</u>

eV	electronvolt (= 1.602 x 10^{-19} J)
µε	mirostrain (= 10^{-6})

<u>Symbols:</u>

$\sigma_I, \sigma_{II}, \sigma_{III}$	Macrostress, Type II microstress, Type III microstress
$\sigma_{ij}, \varepsilon_{ij}, C_{mn}$	Stress tensor, strain tensor, single crystal elastic constants
E, G, ν	Young's modulus, shear modulus, Poisson's ratio
A_{hkl}, S_0	Cubic elastic anisotropy factor, Degree of cubic elastic anisotropy
F, A, σ	Force, Cross section, Uniaxial tensile stress
α, T	Thermal expansion coefficient, Temperature
T_c	Curie temperature
λ, θ, ε	Wavelength, Bragg-angle, elastic lattice strain

Table of contents:

1 Introduction

When a material is plastically deformed and the applied load is then taken away, residual stresses are typically left within this material. This is, for instance, when the applied load created a stress/strain gradient throughout the component, as during bending or torsion, or when the microstructural constituents have different mechanical properties and react differently on the applied load, as in polycrystalline and multi-phase materials.

In the latter case, intergranular and interphase types of residual stresses are introduced. These are the subject of numerous studies using diffraction techniques, often coupled with simulations to test micromechanical models. Ferritic carbon steels constitute an important class of materials because of their technological applications and have therefore been investigated in the past with both X-rays and neutrons during deformation at ambient temperatures. A typical microstructure consists of a polycrystalline ferritic matrix with precipitates of iron carbide (cementite), known as a hard and brittle phase. During deformation the plastifying matrix is shedding part of its load to the cementite, which hence, at least at room temperature (RT), is functioning as a reinforcing phase in steel. After removal of the applied load, matrix and cementite are therefore left in a residual stress state with opposing sign.

The interplay between these constituents at elevated temperature has not yet been investigated in detail. Ferritic steels have been used for high temperature applications already for a long time, experiencing static and cyclic stresses at temperatures up to 500-650°C with a tempered bainitic or a tempered martensitic microstructure. Under these conditions, the formation of residual stresses might be different for various reasons comprising for instance a change in the deformation mechanisms from dislocation glide to dislocation creep or even diffusional flow. Further, the cementite might eventually plastically deform, chamfer, coarsen or transform into other types of carbide.

In the present work, X-ray and neutron diffraction is applied to study the accumulation of residual strain in a 1%CrMoV steel subjected to different loading conditions and the role of the second phase particles. The so-called creep resistant 1%CrMoV steel with a tempered bainitic microstructure is used as rotor steel in steam turbines at temperatures up to 565°C. The original motivation for the first diffraction experiments was linked to damping measurements that reflected the changes in dislocation condition arising from the accumulation of inelastic strain due to monotonic loading at RT and creep loading at 565°C [1]. Of particular interest were observations relating to the kinetics of anelastic recovery in the steel, the importance of which relates to the development of a complete understanding of deformation response under conditions of variable stress and/or temperature and the fundamental modelling of this behaviour.

This introduction is structured as follows: The first part introduces the intergranular and interphase type of stresses. The second part introduces the materials' microstructure. The third part presents the literature review on intergranular and interphase stresses in carbon steels due to deformation at RT. The introduction then concludes with the statement of the aim of this project and the research outline.

1.1   Development of residual stress

The term "residual stress" is commonly defined for stresses that are left within a material in the absence of external load and under homogeneous and static temperature conditions [2]. These stresses are self-equilibrating over the volume and "arise from the elastic response of the material to an inhomogeneous distribution of nonelastic strains, such as plastic strains, precipitation, phase transformation, mistfit, thermal expansion strains, etc." [3]. An example is shown in the schematic below (Figure 1) with a thermo-mechanical cycle. Consider an alternating array of slabs of material A and B in (a). For convenience, only two slabs are considered in the figures (b) - (d) and the inclined lines indicate the periodic boundary of the composite. Both materials A and B are initially at the same temperature T_1.
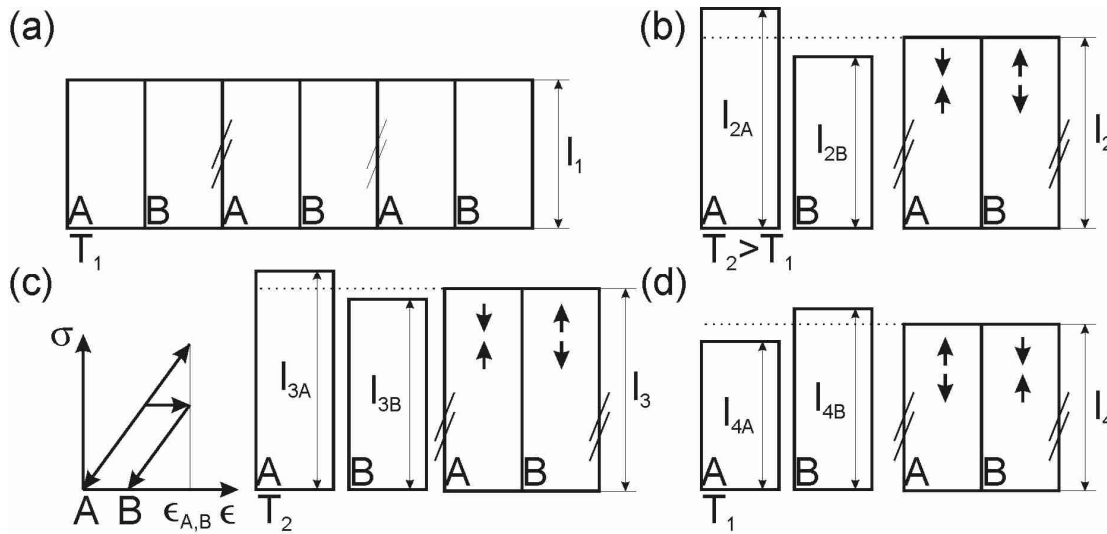
Figure 1 Slab model to illustrate the generation of residual stress in a material A and B (without relaxation at the interface A-B): (a) Periodic arrangement of A and B indicated by the inclined lines: starting condition without residual stresses at temperature T_1. (b) At T_2: compressive stresses in A and tensile stresses in B due to the different thermal expansion coefficients ($\alpha_A > \alpha_B$). (c) At T_2 after tensile loading: A and B are still in compression and tension, respectively. Since $l_{3A} = l_{2A}$ and $l_{3B} > l_{2B}$, the magnitude of the residual stresses are reduced compared to figure b. (d) At T_1: A only deformed elastically in figures (a) to (d), therefore $l_{4A} = l_1$. B deformed plastically in figure c, therefore $l_{4B} > l_1$. Material A is now in tension and B in compression.

In (b), the temperature is increased to $T_2 > T_1$. The thermal expansion coefficient α of material A is larger than that of material B, $\alpha_A > \alpha_B$, the length of slab A will be larger than that of slab B. When

these materials are bonded together, then the length l_2 of the composite will be $l_{2A}>l_2>l_{2B}$ and material A will be in compression and B in tension, indicated by the arrows. In (c), the composite is loaded to a strain $\varepsilon_{A,B}$ and then unloaded again. For convenience, A and B are assumed to have the same Young's modulus. Material A only deformed elastically ($l_{3A}=l_{2A}$), whereas B also deformed plastically ($l_{3B}>l_{2B}$). In the composite, both materials are still in an opposite stress state ($l_{3A}>l_3>l_{3B}$), although its magnitude is reduced. In (d), the temperature is decreased to its initial value T_1. For material A, $l_{4A}=l_{1A}$, and since B deformed plastically at T_2, $l_{4B}>l_{1B}$. In this example, material A is left with residual tensile stresses and material B with residual compressive stresses at the end of the thermo-mechanical cycle.

1.1.1 Classification of residual stresses

Residual stresses can be classified according to their length scale into three types, dating back to the 1920s by Heyn [4] and Masing [5] and defined later by Macherauch [6]. A corresponding schematic is shown in Figure 2. The top row shows a polycrystalline material at three different length scales. Here, the microstructural constituents, i.e. the grain size or the size of the precipitates from a second phase, define the characteristic length scale. The lower row shows the corresponding stress component in the y-direction when scanning along the x-direction.
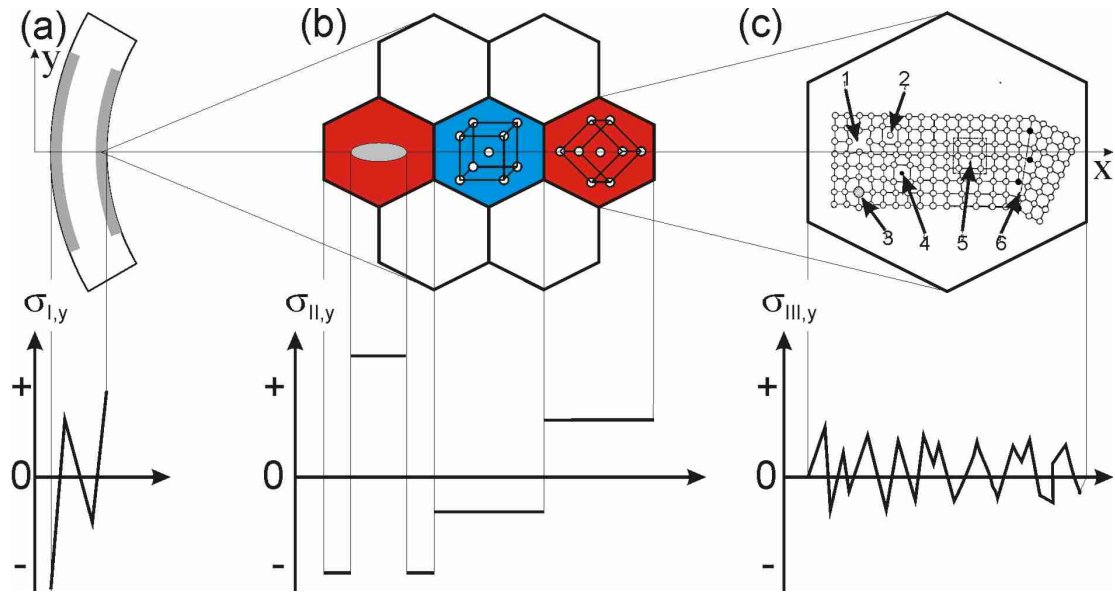
Figure 2 Schematic representation of the three types of residual stresses: (a) Type I stresses (σ_I) in a bent bar; the grey regions have been plastically deformed. (b) Type II stresses (σ_{II}): Intergranular stresses between the grains of the same material but with different orientation (e.g. red and blue grain) and interphase stresses between the constituents of different materials (e.g. red and grey grain). (c) Type III stresses (σ_{III}) due to the strain field around defects e.g. a vacancy (1), interstitial atom (2), substitution foreign atom (3), interstitial foreign atom (4), edge dislocation (5), small angle grain boundary (6): Schematic of the lattice defects from Macherauch [6].

Type I stresses (σ_I) are uniform over larger areas, i.e. several grains. One might consider the material as a continuum without a microstructure and these stresses are therefore called *macrostresses*. An example is shown in (a): The bar was bent such that the outer regions (in grey) have been plastically deformed. Due to this inhomogeneous deformation, residual stresses are left in the material, which vary along the cross-section and may be compressive or tensile.

Type II stresses (σ_{II}) are uniform on the level of the individual constituents, i.e. grains or particles of different phases and are therefore distinguished by the terms *intergranular* and *interphase stresses*, respectively. An example is shown in (b) with a microstructure taken from a plastified area. The blue and red grains are of the same material but have a different crystallographic orientation, the grey precipitate is from a second phase with different mechanical properties. This phase for instance may not have been plastically deformed. The presence of second phase particles can considerably alter the stress experienced by a grain family since interphase and intergranular stresses superimpose each other. For instance, σ_{II} for the red grain is either tensile or compressive.

Type III stresses (σ_{III}) vary within the individual constituents, i.e. grains, and originate from the characteristic strain fields around lattice defects. Some of these lattice defects are exemplified in (c).

Since Type II and III stresses both vary on the scale of the microstructure, they are summarized with the term *microstresses*. Figures of Type II stresses are often expressed with the unit $\mu\varepsilon = 10^{-6}$ (microstrain). Note that the actual residual stress is given by the superposition of macro- and microstresses.

For the practical measurement of residual stresses, there exist several methods, some destructively and other non-destructively [7]: Type I stresses may for instance be characterized by hole drilling with attached strain gauges and by diffraction, respectively. In order to observe the stress profile as shown in Figure 2, the measurements have to be spatially resolved and the characteristics of the probe have to be adapted accordingly. Consider therefore the extreme case in Figure 3(a): When the spatial resolution of the probe decreases from Δx_1 to Δx_2, then the two stress states with opposing sign will not any more be captured. With diffraction, typical illuminated gauges volumes are of the order of some cm^3 for neutrons. Since the grain size typically is smaller than the illuminated gauge volume, one averages over many grains, each of which may have a slightly different stress state (cf. Figure 3(b)). Diffraction is sensitive to grain orientation {*hkl*}, and therefore allows characterizing the stresses for different orientations, as shown in Figure 3(b) for a {111} and a {200} grain family, i.e. intergranular stresses. In a similar way, the interphase stresses can be characterized. The values of intergranular and interphase stresses measured are hence an average over the stress state of many grains and particles.
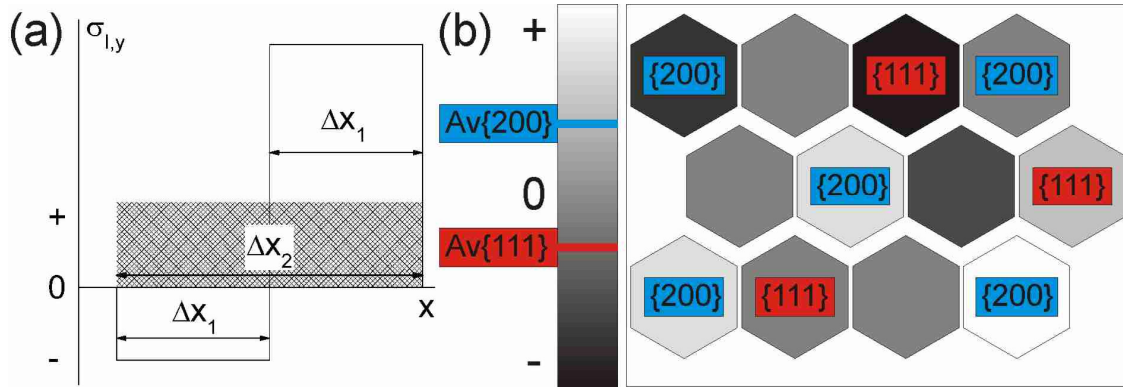
Figure 3 Potential effect of the spatial resolution in the measurements of residual stress: (a) The macrostresses, actually both compressive and tensile are measured to be tensile. (b) The grey levels represent different stress states. Though there are discrete strain states for the same grain family, e.g. {200} one only measures an average strain state.

In this dissertation, Type II stresses are the matter of interest. These intergranular and interphase stresses, as just mentioned, can be observed and distinguished by diffraction and the principles of this method are given in §2.2. At this point, two examples are presented to illustrate the evolution of both types of stresses upon uniaxial tensile deformation. Diffraction does not measure stresses. In fact, this and any other method, only provides average values for the elastic strain experienced by the constituents and the stresses then need to be calculated considering the appropriate elastic relationship between stain and stress. In the following examples as well as throughout this dissertation, elastic strains are considered only rather than stresses.

1.1.2 Example of intergranular strains

The first example is a single-phase polycrystalline austenitic steel, documented in the thesis of Clausen [8], and provides a good dataset with little scatter on the data points. Figure 4(a) shows a stress-strain curve of this material. At various positions along this curve, diffraction patterns have been acquired and these positions are marked with the squared symbols. From these diffraction patterns, the elastic lattice strain in the individual grain families can be determined. This lattice strain is then plotted as a function of the applied stress and is shown in Figure 4(b). In the steel elastic regime, some grain families are stiffer than others. For instance, the <111> is the stiffest direction whereas the <200> is the most compliant direction. This is due to the elastic anisotropy, the origin of which is described in §1.1.2.1.1. Around the yield stress of the material, the <331> direction deviates first from its hitherto linear behaviour and bends upwards. It does so because the shear stress in this grain family may have reached a critical value and grains of this family now start to deform plastically rather than being further strained only elastically. As a consequence, the grains with another orientation and which do not yet plastically deform, must carry a larger portion of the applied load. For instance, the <200> direction is initially strained further elastically. At higher

stresses, when the load-redistribution between the grains is finished, the <331> direction bends back to approximately follow its original behaviour experienced during elastic loading. The behaviour of other grain families, for instance the {220} is similar to the {331} in the steel elastic regime but different in the plastic regime. This preferred yielding of some grain families is known as plastic anisotropy and its origin is described in §1.1.2.1.2. The interplay between elastic and plastic anisotropy is rather complex and may be addressed with modelling approaches (cf. §1.1.2.2). The competition of the elastic and plastic anisotropy between the individual grain families during loading then results in the build-up of intergranular type of residual strains after unloading. The measurements in the unloaded state have been performed on a second sample and are shown in Figure 4(c) underneath the stress-strain curve. Some grain families are in residual compression (e.g. {220} and {331}) and some are in residual tension (e.g. {200} and {311}).
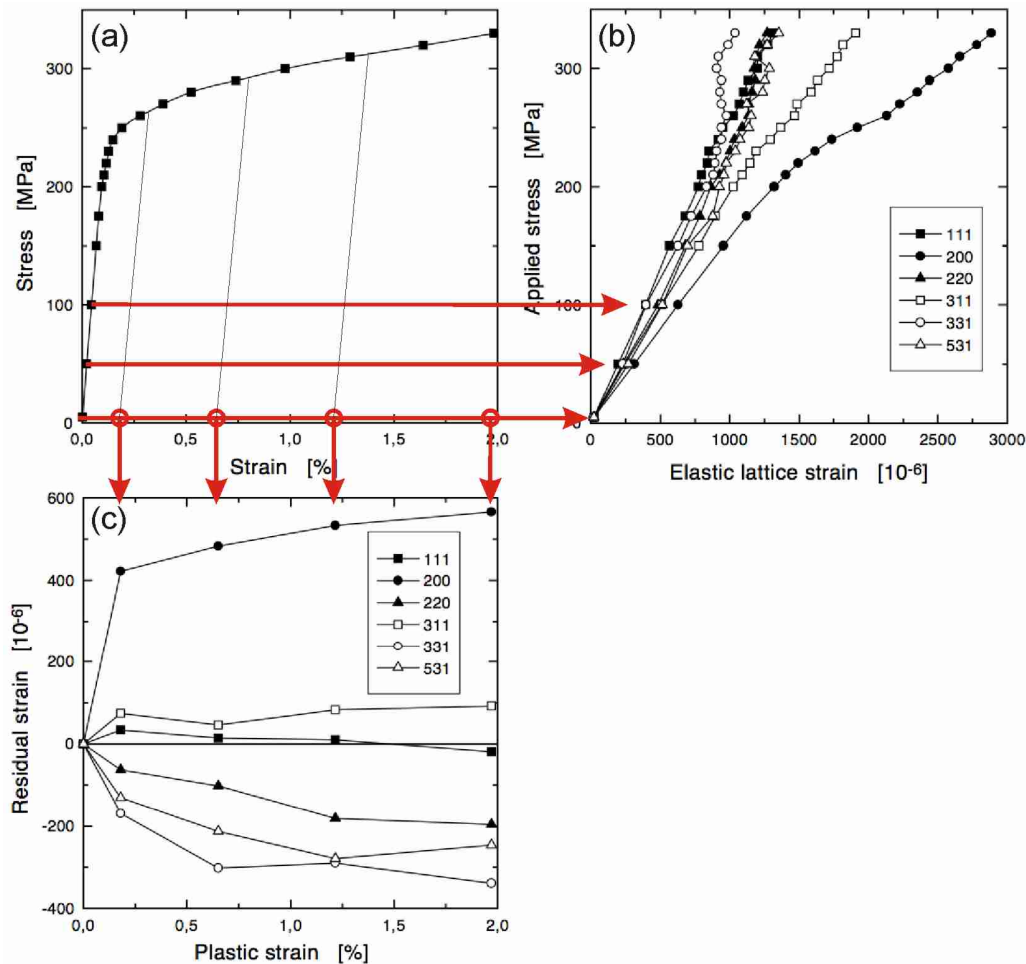
Figure 4 In situ neutron diffraction during RT tensile deformation of a single-phase polycrystalline austenitc steel (γ-iron): (a) The symbols on the stress-strain curve indicate the measurement of the lattice strain. (b) Elastic lattice strains of various grain families with the plane normal parallel to the loading axis. (c) Residual elastic lattice strains of various grain families with the plane normal parallel to the formed loading axis measured in the unloaded state on a second sample. From Clausen [8].

1.1.2.1 Single crystal response upon deformation

1.1.2.1.1 Single crystal elastic anisotropy

In what follows is a brief summary of the elastic properties of single crystals to finally address the elastic anisotropy. An excellent and more comprehensive treatment on this topic is given by Nye [9] for further reading. Consider the interaction energy ϕ between two atoms with an equilibrium spacing a_0 (Figure 5(a)). The energy ϕ can be expressed in a Taylor series and the force F necessary to displace the atom from its equilibrium position is the derivative of ϕ with respect to the displacement $u = a - a_0$. For small displacements u, one may neglect the higher order terms of the Taylor series and the force F may be written as $F = k \cdot u$, which is Hooke's law in its original form, i.e. the displacement is linear proportional to the applied force. The stiffness k, however, may depend on the equilibrium distances between the atoms. Since in crystals, this distance varies with the direction, the stiffness may also vary with direction and cause some degree of elastic anisotropy. For a solid in the limit of the linear elastic behaviour, stress and strain are related by Hooke's law in its general form:

$$\sigma_{ij} = C_{ijkl}\varepsilon_{kl} \qquad \varepsilon_{ij} = S_{ijkl}\sigma_{kl} \qquad\qquad \text{Eq. 1}$$

where σ_{ij} and ε_{ij} are the second-rank stress and strain tensors, respectively and using the Einstein summation convention. The definition of the components of σ_{ij} (same for ε_{ij}) is shown with the unit-cube in Figure 5(b). It can be shown that $\sigma_{ij} = \sigma_{ji}$ (same for ε_{ij}).
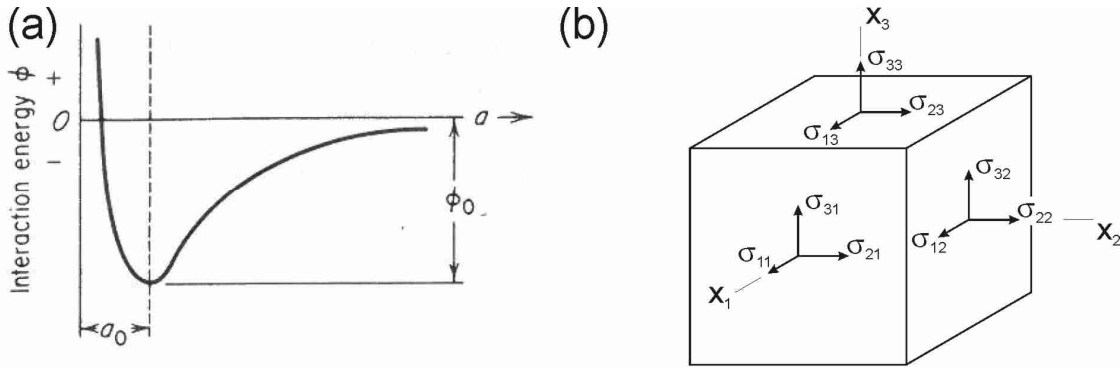
Figure 5: (a) Interaction energy vs. separation between atoms, from Dieter [10] and (b) The stresses σ_{ij} on the unit cube. To better distinguish the shear stress from the stress acting normal to the plane, the shear stress is often written with the symbol τ, e.g. $\tau_{12} = \sigma_{12}$.

C_{ijkl} and S_{ijkl} are the elastic stiffness and compliance tensors, respectively, and both are centro-symmetrical fourth-rank tensors (with 81 entries). It can be shown that $S_{ijkl} = S_{ijlk}$, $S_{ijkl} = S_{jikl}$, $S_{ijkl} = S_{klij}$ (same for C_{ijkl}) and the number of independent parameters therefore reduces to 21. One may further write Eq. 1 in the matrix notation:

$$\varepsilon_n = S_{nm}\sigma_m \tag{Eq. 2}$$

Note that:

- o Suffixes in tensor notation: 11   22   33   23,32 31,13 12,21
- o Suffixes in matrix notation: 1   2   3   4   5   6
- o $S_{ijkl} = S_{nm}$ when m and n are 1, 2 or 3
- o $2S_{ijkl} = S_{nm}$ when either m or n are 4,5 or 6
- o $4S_{ijkl} = S_{nm}$ when both m and n are 4, 5 or 6
- o but $C_{ijkl} = C_{nm}$ for all m, n
- o One must go back to the tensor notation to transform the S_{mn} and C_{mn} to another set of axis

The matrix S_{mn} takes then the following form (same for C_{mn}):

$$S_{mn} = \begin{pmatrix} S_{11} & S_{12} & S_{13} & S_{14} & S_{15} & S_{16} \\ & S_{22} & S_{23} & S_{24} & S_{25} & S_{26} \\ & & S_{33} & S_{34} & S_{35} & S_{36} \\ & & & S_{44} & S_{45} & S_{46} \\ & & & & S_{55} & S_{56} \\ & & & & & S_{66} \end{pmatrix} \tag{Eq. 3}$$

The matrix is symmetrical about the leading diagonal and the lower part is therefore omitted. In a triclinic system, all 21 entries are independent. That number, however, reduces with increasing crystal symmetry and the details for the cubic symmetry, the orthorhombic symmetry, which are relevant in this dissertation and the isotropic case, are given here:

In orthorhombic system (e.g. cementite), S_{mn} reduces to 9 independent entries, since:

$$S_{14} = S_{15} = S_{16} = S_{24} = S_{25} = S_{26} = S_{34} = S_{35} = S_{36} = S_{45} = S_{46} = S_{56} = 0 \tag{Eq. 4}$$

In cubic systems (e.g. iron), S_{mn} reduces to 3 independent entries since in addition to Eq. 4:

$$S_{11} = S_{22} = S_{33} \quad and \quad S_{44} = S_{55} = S_{66} \quad and \quad S_{12} = S_{13} = S_{23} \tag{Eq.5}$$

In the isotropic case, S_{mn} reduces to 2 independent entries, since in addition to Eq. 4 and Eq.5:

$$S_{44} = 2(S_{11} - S_{12}) \tag{Eq. 6}$$

Expanding Eq. 2 for ε_1 in the isotropic case yields:

$$\varepsilon_1 = S_{11}\sigma_1 + S_{12}\sigma_2 + S_{12}\sigma_3 \tag{Eq. 7}$$

where the elastic (or Young's) modulus E, the Poisson ration v and the shear modulus G are expressed as:

$$S_{11} = \frac{1}{E} \quad and \quad S_{12} = -\frac{\nu}{E} \quad and \quad 2(S_{11} + S_{12}) = \frac{1}{G} \qquad \text{Eq. 8}$$

If the material is not isotropic, then the stiffness E_{hkl} (expaning Eq. 2 for $m, n = 1$) may vary with the crystallographic direction. The expression for a cubic symmetry reads:

$$\frac{1}{E_{hkl}} = S_{11} - 2 \cdot (S_{11} - S_{12} - \tfrac{1}{2} S_{44}) \cdot (l_1^2 l_2^2 + l_2^2 l_3^2 + l_1^2 l_3^2)$$

$$= S_{11} - 2 \cdot (S_{11} - S_{12} - \tfrac{1}{2} S_{44}) \cdot \frac{h^2 k^2 + k^2 l^2 + h^2 l^2}{\left(h^2 + k^2 + l^2\right)^2} = S_{11} - 2 \cdot (S_{11} - S_{12} - \tfrac{1}{2} S_{44}) \cdot A_{hkl} \qquad \text{Eq. 9}$$

where l_i are the direction cosines between the direction [hkl] and the unit vector [100], [010], [001]. The direction cosines can be derived from the dot products of the vectors. The term A_{hkl}:

$$A_{hkl} = \frac{h^2 k^2 + k^2 l^2 + h^2 l^2}{\left(h^2 + k^2 + l^2\right)^2} \qquad \text{Eq. 10}$$

is the cubic elastic anisotropy factor and vanishes if the term $(S_{11} - S_{12} - 0.5 \cdot S_{44}) = 0$. The degree of elastic anisotropy of a cubic crystal can thus be defined as

$$S_0 = \frac{2(S_{11} - S_{12})}{S_{44}} \qquad \text{Eq. 11}$$

which for fcc and bcc iron (i.e. the two examples in Figure 4, Figure 11) becomes 3.8 and 2.5, respectively. An elastically rather isotropic material is tungsten with $S_0 = 1.0$.
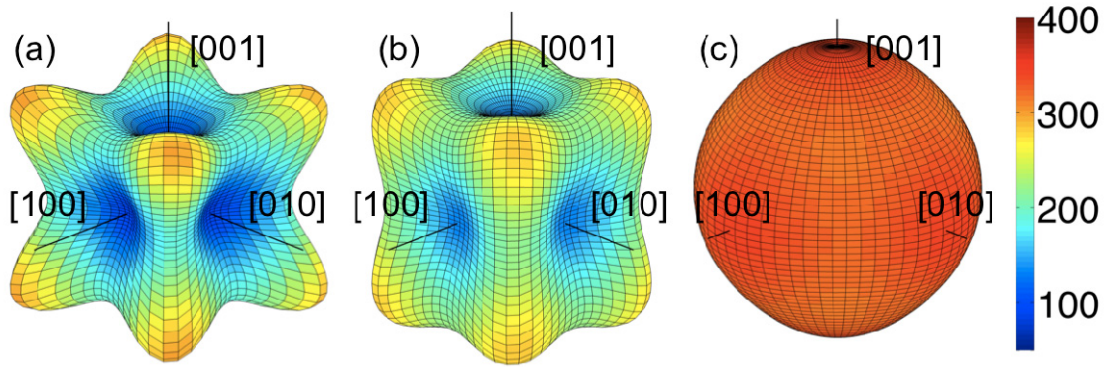
Figure 6 Representation surfaces for the stiffness E_{hkl} along the direction [hkl]. The unit of the colour code is GPa. Reconstructed from the S_{mn}: (a) fcc iron with $S_{11}=10.7$, $S_{12}=-4.3$, $S_{44}=7.9$ (Hutchings [11]), (b) bcc iron with $S_{11}=8.0$, $S_{12}=-2.8$, $S_{11}=8.6$ (Hutchings [11]) and (c) fcc tungsten with $S_{11}=2.6$, $S_{12}=-0.7$, $S_{44}=6.6$ (Dieter [10]). Compliance S_{mn} constants are in units of TPa^{-1}.

The representation surface of Young's modulus for these elements is shown in Figure 6. For the values of the S_{mn}, see the figure caption. One often can find in literature either the S_{mn} or the C_{mn} and the remaining quantity can then be obtained by matrix inversion. Note, that the stiffness in the directions <hkl> depends on the cubic anisotropy factor and since S_0 is positive for iron, the <111> are the stiffest and the <200> are the most compliant directions.

The expression for the the stiffness E_{hkl} for the orthorhombic system reads:

$$\frac{1}{E_{hkl}} = l_1^4 S_{11} + 2l_1^2 l_2^2 S_{12} + 2l_1^2 l_3^2 S_{13} + l_2^4 S_{22} + 2l_2^2 l_3^2 S_{23} + l_3^4 S_{33} + l_2^2 l_3^2 S_{44} + l_1^2 l_3^2 S_{55} + l_1^2 l_2^2 S_{66} \qquad \text{Eq.12}$$

and is required later in the discussion chapter (§4.4.1) for the cementite.

1.1.2.1.2 Single crystal plastic anisotropy

In what follows is a brief summary of plastic deformation in a single crystal by slip deformation. A more comprehensive treatment is for instance given by Dieter [10]. Consider the atomic lattice in Figure 7(a). In order to displace the upper and the lower half of the perfect lattice, a shear stress τ must act as indicated.
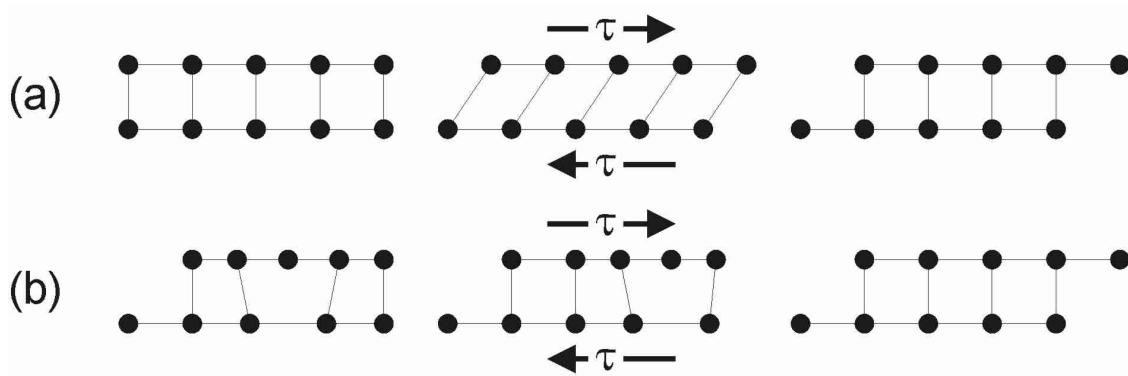
Figure 7 Plastic deformation by slip of two atomic planes under a shear stress τ: (a) Without and (b) with dislocation motion.

The shear stress τ_{max} necessary to displace the upper half of the crystal in one step is related to the shear modulus G and can be approximated to:

$$\tau_{max} = \alpha \cdot G \qquad \qquad \text{Eq. 13}$$

where α is a value close to 0.1. τ_{max} is called the theoretical shear strength and defines the upper stress limit for all possible deformation mechanism in materials (cf. the deformation mechanisms maps shown in Figure 17). Hardly any material, however, has a perfect lattice, but materials often contain various types of defects. Whether or not the material then deforms plastically or simply fails depends on the type of bonding between the atoms. Ceramics for instance would break before reaching τ_{max}, most metals however may deform plastically by incremental displacements of atoms, as shown in Figure 7(b). One atom initially is dislocated by the amount b and this dislocation crosses the lattice with the help of the shear stress $\tau < \tau_{max}$. The required shear stress depends on the arrangement of the atoms and takes the smallest value for slip within the most dense packed planes along the most dense packed directions. Figure 8 shows the unit cell of a bcc (e.g. ferrite), fcc (e.g. austenite) and an orthorhombic cementite crystal structure.
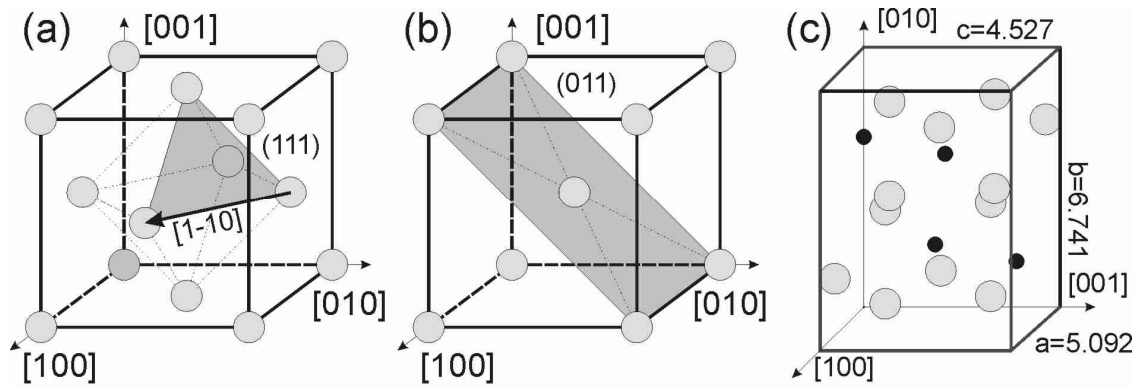
Figure 8 Unit cell of (a) fcc with the (111) plane: space group Fm-3m, Fe atoms on (0,0,0), (0.5,0.5,0), (0.5,0,0.5), (0,0.5,0.5), (b) bcc with the (011) plane: space group Im-3m, Fe atoms on (0,0,0), (0.5,0.5,0.5) and (c) Orthorhombic cementite: space group Pnma, Fe atoms (grey) on (0.1834,0.0689,0.3344), (0.0388,0.2500,0.8422); C atoms (black) on (0.8764,0.2500,0.4426), with lattice parameter a=5.092Å, b=6.741Å and c=4.527Å, cementite data from [12] (at RT).

In fcc, slip occurs in the <110> direction on {111} planes since these are the close packed directions and planes. There are in total twelve different slip systems (listed in Table 1) and the (111)[1-10] slip system is exemplarily shown in Figure 8(a). In bcc, slip occurs in the <111> directions but there are no closed packed planes. Taylor and Elam [13] suggested that slip can occur on any plane associated with any of the <111> type slip directions. The most common planes observed [14] are the {110}, {112} and {123}, which are also used for modelling intergranular strains [15].

Consider now a single crystal with cross section A and with a uniaxial load F applied parallel to the plane normal (Figure 9). A slip system may be defined by the slip plane A' and the slip direction, the corresponding angles with the load direction are ϕ and λ, respectively.
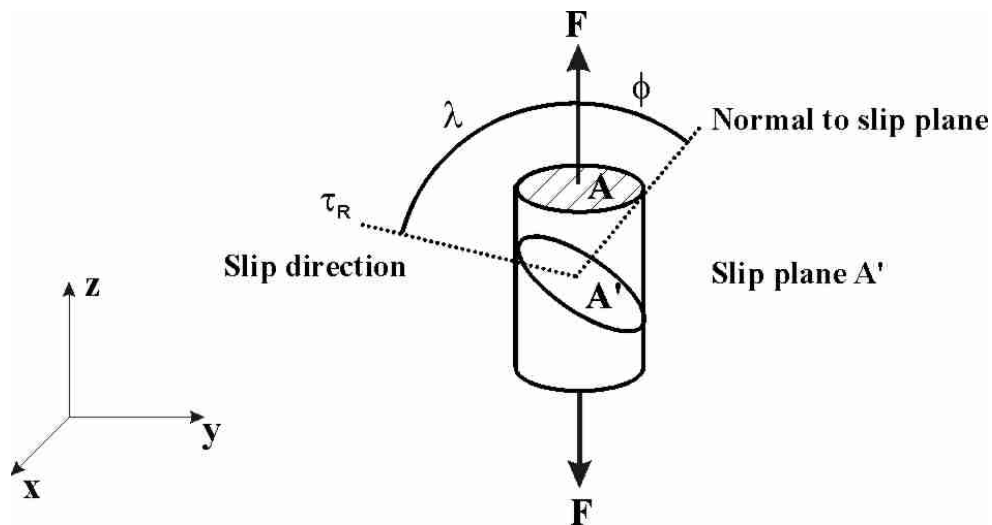
Figure 9 Schematic of the stress axis F, slip plane A' and slip direction.

One may then easily derive the expression for the resolved shear stress τ_R on that slip system:

$$\tau_R = \frac{F}{A}\cos\phi\cos\lambda = \frac{F}{A}m \qquad\qquad \text{Eq. 14}$$

The term m is known as the Schmid factor and may be regarded as a conversion of the applied uniaxial tensile stress $\sigma = F/A$ to the shear stress τ_R. For slip deformation to happen, a minimum shear stress (or: critical resolved shear stress CRSS) τ_{CRSS} is necessary. The required uniaxial tensile force to reach τ_{CRSS} depends on the orientation of the slip systems with respect to the loading direction. An example with the uniaxial load applied along two different crystal orientations for an fcc structure is calculated in Table 1: Assuming $\tau_{CRSS} = 100$ MPa, then the required uniaxial tensile stress is $\sigma = 245$ MPa for a (001) orientation and $\sigma = 367$ MPa for a (111) orientation. This means that the (111) oriented single crystal yields at higher stresses and before the (001) oriented crystal and in general that some grain orientations are preferentially oriented for slip, yielding a plastic anisotropic behaviour.

Table 1 The twelve slip systems in fcc metal, the corresponding Schmid factor m for an uniaxial load applied along the [001] and the [111] axis and the corresponding required uniaxial tensile stress σ to reach τ_{CRSS}=100MPa. Units in MPa.

Slip plane	Slip direction	m along loading axis: [001]	[111]	σ along loading axis: [001]	[111]
(111)	$[0\bar{1}1]$	$1/\sqrt{6}$	0	245	undef
	$[\bar{1}01]$	$1/\sqrt{6}$	0	245	undef
	$[\bar{1}10]$	0	0	undef	undef
$(\bar{1}11)$	$[0\bar{1}1]$	$1/\sqrt{6}$	0	245	undef
	$[101]$	$1/\sqrt{6}$	$\sqrt{2/27}$	245	367
	$[110]$	0	$\sqrt{2/27}$	undef	367
$(1\bar{1}1)$	$[011]$	$1/\sqrt{6}$	$\sqrt{2/27}$	245	367
	$[\bar{1}01]$	$1/\sqrt{6}$	0	245	undef
	$[110]$	0	$\sqrt{2/27}$	undef	367
$(11\bar{1})$	$[011]$	$-1/\sqrt{6}$	$\sqrt{2/27}$	-245	367
	$[101]$	$-1/\sqrt{6}$	$\sqrt{2/27}$	-245	367
	$[\bar{1}10]$	0	0	undef	undef

1.1.2.2 Modelling of intergranular strains

In polycrystalline materials, each grain is surrounded by the others and must deform in such a way that its change is compatible with that of its neighbours.

Because of the heterogeneity of the elastic and plastic response of different grain orientations, neither the stress nor the strain will be homogeneous throughout the mechanically loaded sample. The polycrystalline elastic stiffness of a grain family therefore will differ from its single crystal elastic stiffness and two extreme cases can be considered: (i) All grains in a polycrystalline sample experience a uniform strain, that is known as the Voigt limit [16], and (ii) all grains in a polycrystalline sample experience a uniform stress, that is known as the Reuss limit [17]. The corresponding models for plastic deformation are the Taylor [18] and Sachs [19] model. An overview on the various polycrystalline elasticity and plasticity models is, for instance, given in the thesis of Oliver [20].

Clausen [8] implemented an **E**lasto-**P**lastic **S**elf-**C**onsistent model (EPSC) model to describe his experimental neutron diffraction results on polycrystalline single-phase aluminum, copper and γ-iron (austenite). The EPSC model is based on the Eshelby-Hill formulation with an elliptical inclusion in an infinite medium (Figure 10(a)). The infinite medium represents the average properties of the matrix, therefore the term self-consistent. The inclusion has uniform stress and anisotropic properties, i.e. different orientations have different elastic moduli and plastic deformation is only allowed by slip on specific slip systems. With the hardening of the stress-strain curve, the evolution of the individual grain families throughout the elasto-plastic regime can be modelled and the results on the polycrystalline single-phase polycrystalline austenite phase is shown in (Figure 10(b)).
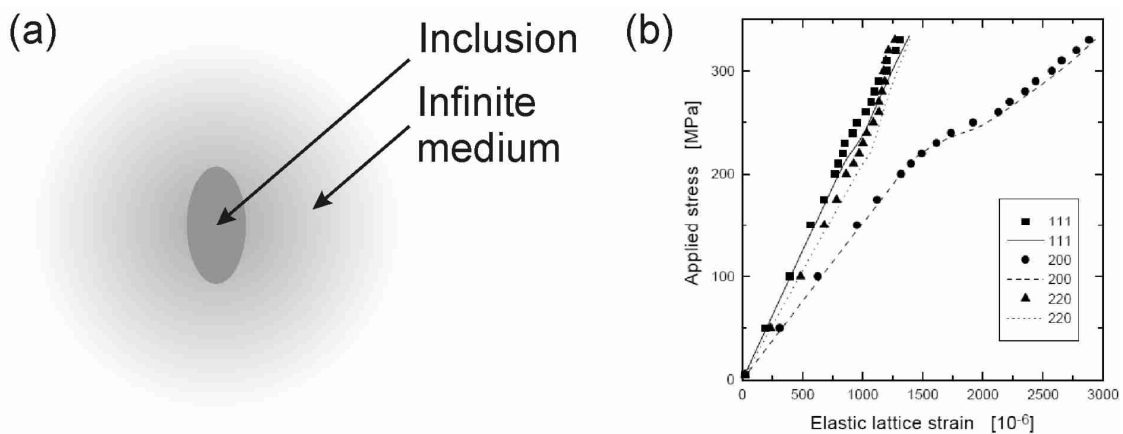
Figure 10: (a) Schematic of an elliptic inclusion in an infinite medium representing the average properties of the matrix. (b) EPSC results (lines) compared to the experimentally measured data points of three grain families during RT tensile deformation of the single-phase polycrystalline austenitic steel from Figure 4(b). From Clausen [8].

1.1.3 Example of interphase strains

The second example is on a polycrystalline ferritic steel which contains second phase particles with a volume fraction of about 20% and is documented in the thesis of Oliver [20]. This second phase is the iron carbide cementite, which is known as a hard phase at ambient temperatures. Figure 11(a) shows the stress-strain curve with a Lüders straining until about 2% plastic strain. Figure 11(b) shows the behaviour of different ferrite grain families with applied stress. Despite the scatter in the datapoints, it is obvious that, like in the previous example with austenitic steel, the individual grain families behave differently during the elasto-plastic regime. However, and that is different, the grain families all experience a shift towards lower lattice strains around the yield point but then continue approximately with their previous trend experience during elastic loading. After unloading, all of these grain families are now in residual compression. Keeping that in mind, the phase average behaviour of the ferrite and the cementite during loading is now considered and shown in Figure 12(a). The interphase strain can be determined from diffraction patterns taken along the stress-strain curve in the same fashion as the intergranular strains. In the steel elastic regime, the ferrite and cementite behaviour is rather similar. Around the yield point, there occurs the sudden shift in lattice strain: The ferrite experiences a compressive and the cementite a tensile shift. The plastifying ferritic matrix is shedding part of its load to the cementite: The matrix relaxes and the cementite is further strained elastically. These interphase strains are superimposed on the intergranular strains. This explains why there is a compressive shift for all ferrite grain families in Figure 11(b). Unloading then results in interphase type of residual strains. These residual interphase strains are then shown with the plastic strain in Figure 12(b). Both phases are left in a residual strain state but with opposing sign: The ferrite is left in residual compression and the cementite in residual tension.
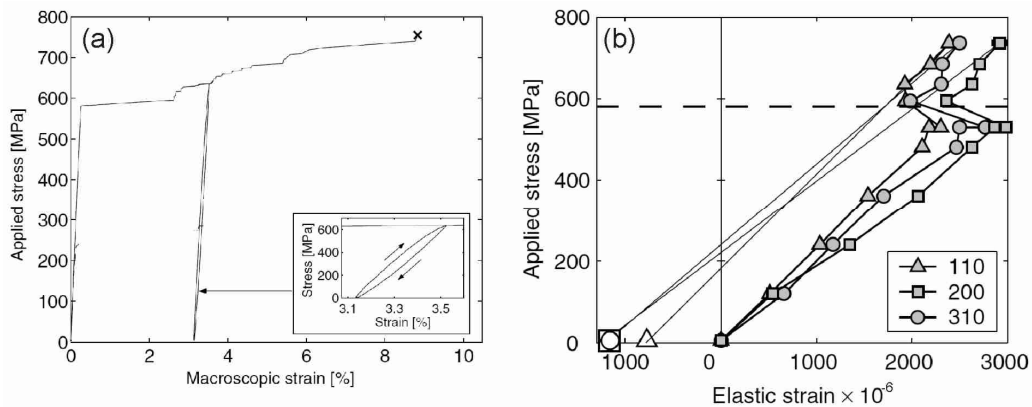
Figure 11 (a) Stress-strain curve of a high-carbon steel: The microstructure consists of a polycrystalline ferritic matrix with spherical cementite inclusions. Yield point and Lüders straining until about 2% plastic strain. (b) Elastic lattice strain of three ferrite grain families in the direction parallel to the applied load. From Oliver [15], some information in the original plot in (a) is here skipped for clarity.
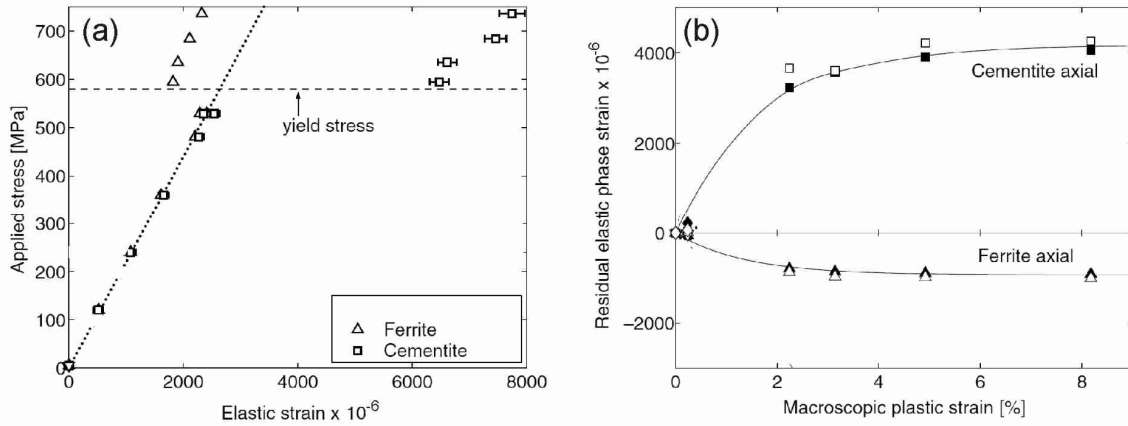
Figure 12 Elastic phase strain of the sample Figure 11(a). (a) Elastic lattice strain of the ferrite and the cementite in the high-carbon steel in the direction parallel to the applied load. (b) Residual elastic lattice strain of the ferrite and the cementite phase in the high-carbon steel. The direction parallel to the applied load is termed "axial". From Oliver [15], some information in the original plots is skipped for clarity.

1.1.4 Residual strains from thermal expansion

A further potential source of Type II microstresses is temperature variations of a material, where the microstructural constituents have different thermal expansion coefficients α. Upon a temperature variation ΔT, the thermal strain induced may generally be expressed as:

$$\varepsilon_{ij} = \alpha_{ij}\Delta T \qquad\qquad\qquad\qquad \text{Eq. 15}$$

Since ε_{ij} is a symmetrical second-rank tensor, so is α_{ij} and Eq. 15 can therefore be reduced to:

$$\varepsilon_{i} = \alpha_{i}\Delta T \qquad\qquad\qquad\qquad\quad \text{Eq. 16}$$

where $i = 1, 2, 3$ represent the principal axes. The number of independent α_i's dependents on the crystal symmetry. For cubic crystals, $\alpha_1 = \alpha_2 = \alpha_3$, but for orthorhombic crystals, all α_i may be different. Furthermore, the thermal expansion coefficient itself might be temperature dependent. The thermal expansion coefficient of bcc iron and cementite in the range of RT to 450°C is shown in Figure 13. At high temperatures, the thermal expansion coefficient of bcc iron and cementite are similar. At ambient temperatures, the thermal expansion coefficient of bcc iron is larger than those of the cementite. The coefficient of bcc iron falls slightly and continuous with temperature, the coefficients of cementite suddenly strongly fall at around the Curie temperature (T_c), which marks the paramagnetic (at high T) to ferromagnetic (at low T) transition. The Curie temperature is around 230°C for pure Fe_3C but may be in a range of 180 to 230°C when additional elements are dissolved and partially replace the Fe atoms [21, 22]. The individual α_i's for cementite are quite different in particular at temperatures below T_c, with the one in the [010]-direction being even negative.
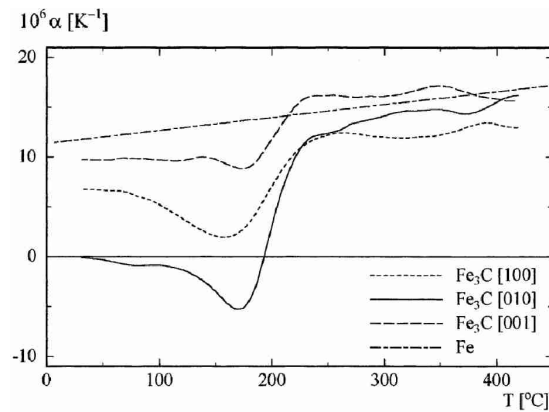
Figure 13 Thermal expansions coefficients of the two main constituents of common ferritic steels in the temperature range RT to 450°C: matrix bcc Fe and orthorhombic cementite with a ferromagnetic (at low T) to paramagnetic (at high T) transition around 230°C. Here, the cementite axis notation is a=4.5246 Å : [100], b=5.0884Å : [010], c=6.7423Å : [001]. From Hartman *et al.* [21].

Internal stresses can thus be induced during fabrication when the phases are consolidated at HT and the material is then subsequently cooled down to RT. Those stresses will also superimpose the stresses created during deformation at HT, thus modifying the footprints of the load-redistribution when the samples are measured at RT.

1.2   Microstructure of the tempered bainitic 1%CrMoV steel

The microstructure of the tempered bainitic 1%CrMoV steel comprises a polycrystalline ferritic matrix with second phase particles and is introduced in this following section.

1.2.1 Ferritic microstructures

Figure 14(a) shows an iron-carbon phase diagram in the regime that is considered as steel (< 2.1 wt% C). The region $T \geq 1200$ °C (and > 2.1 wt% C) is not relevant in this work and therefore omitted. There are two single-phase regimes, austenite (γ-Fe) and ferrite (α-Fe). The carbon solubility in ferrite is orders of magnitude lower than in austenite and only about 0.008 wt% at RT and 0.025 wt% at 723°C. As a consequence, the carbon might precipitate during phase transformation from austenite into ferrite as an iron-carbide. This iron-carbide is known as cementite (Fe_3C). Austenite with an eutectoid carbon content of 0.8 wt% starts to transform at 723°C, upon slow cooling, into pearlite. A pearlitic microstructure can be regarded as a lamellar arrangement of ferrite and cementite in 2-dimensions (2D) and as a bicrystal of intersecting ferrite and cementite single crystals in three-dimensions (3D). Austenite with an hypoeutectoid carbon content (< 0.8 wt%) will produce a microstructure of pearlite with pre-eutectoid ferrite. Austenite with an hypereutectoid carbon content (> 0.8 wt%) will produce a microstructure of pearlite with pre-eutectoid cementite.

The resulting microstructure of a ferritic steel, however, depends not only on the carbon content but also on the kinetics of the phase transformation. This dependency can be visualized by a time-temperature-transformation (TTT) diagram, schematically shown in Figure 14(b) for a steel with an eutectoid (0.8 wt% C) composition. The C-shaped curves for pearlite and bainite, which intersect, indicate when transformation starts (1%) and transformation finishes (100%). At lower temperatures, martensite ($T = M_s$) starts to form. A larger volume fraction of martensite is only formed when cooling to a lower temperature and the transformation is finished at $T = M_f$. TTT-diagrams exist in the databases for transformation upon continuous cooling (CCT) and for isothermal transformation. Slow cooling will produce a pearlitic microstructure that is close to the equilibrium microstructure predicted by the phase diagram. Faster cooling or quenching might change the transformation mechanism from diffusive to displacive and microstructures like bainite and martensite form. TTT-diagrams are, however, very sensitive to the steel's chemical composition: A decrease in the carbon content shifts the C-shaped curves to the left and increases the martensitic start temperature. Alloying elements other than carbon also alter the transformation: Increasing for instance the molybdenum content shifts the C-shaped curves to the right and also separates the pearlitic from the bainitic region. Note that alloying elements also give rise to additional types of precipitates other than cementite.

The commercial transformation product of the 1%CrMoV material (0.25 wt% C), which is investigated in this dissertation, is a bainite and this microstructure is therefore described in more detail in the following section. For a comprehensive course of the transformation mechanisms and the resulting microstructures in steel, the reader is referred to standard textbooks, such as Ref [23].
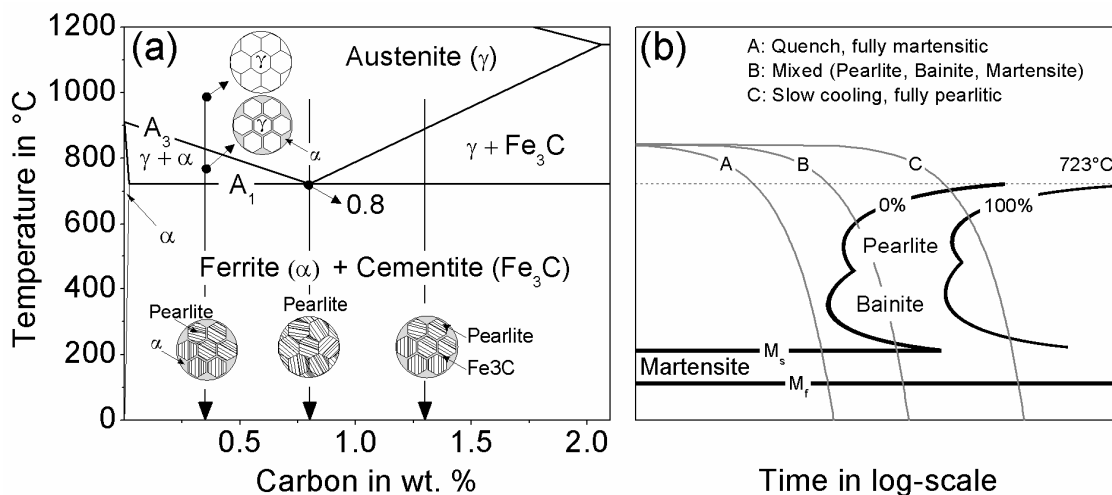
Figure 14: (a) Iron-carbon phase diagram of a plain carbon steel. (b) Schematic of a CCT-diagram of an eutectoid (0.8 wt% C) steel. Cooling from the austenitic phase to RT is shown with three different cooling rates A, B and C, each of them resulting in a different microstructure at RT.

1.2.2 Some microstructural characteristics of bainite

The CCT-diagram (Figure 14(b)) indicates the formation of bainite at intermediate cooling rates. A detailed description of this rather complex microstructure is given by Bhadeshia [24]. In brief, bainite can be regarded as aggregates of ferrite platelets and these aggregates themselves form heterogeneously at the prior austenite grain boundary (Figure 15(a)). The individual ferrite platelets (sometimes called sub-units) have a size of the order of 20 to 200 nm and 1 to 10 µm in thickness and length, respectively, and are separated by cementite or retained and carbon enriched austenite. The classification of bainite is primarily based on the morphology of the ferrite and the morphology and position of the precipitated carbides. Two extreme microstructures can be identified classically, which are related to the position of the precipitated cementite, i.e. upper and lower bainite (Figure 15(b)). Since the carbon solubility in ferrite is two orders of magnitude lower than in austenite, the excess carbon tends to diffuse from the supersaturated ferrite into the hitherto untransformed austenite. In upper bainite, the cooling rate is slow enough, so that the bainitic ferrite is finally free of carbides. In lower bainite, the increased cooling rate decreases the diffusion path for the carbon and some of the excess carbon then precipitates already within the bainitic ferrite as fine platelets. As a consequence, the carbon quantity partitioned into the austenite is reduced and this leads to a smaller fraction of inter-plate cementite, when the austenite eventually decomposes. Some elements (e.g. Si and Al) may retard the decomposition of the carbon-enriched austenite and therefore suppress the cementite formation upon fast cooling. In this case, a lower bainitic microstructure comprises only bainitic ferrite and carbon-enriched austenite. Both types of cementite, the one that forms in between and the one that forms within the ferrite platelets do have a crystallographic relationship with the prior austenite and ferrite matrix.
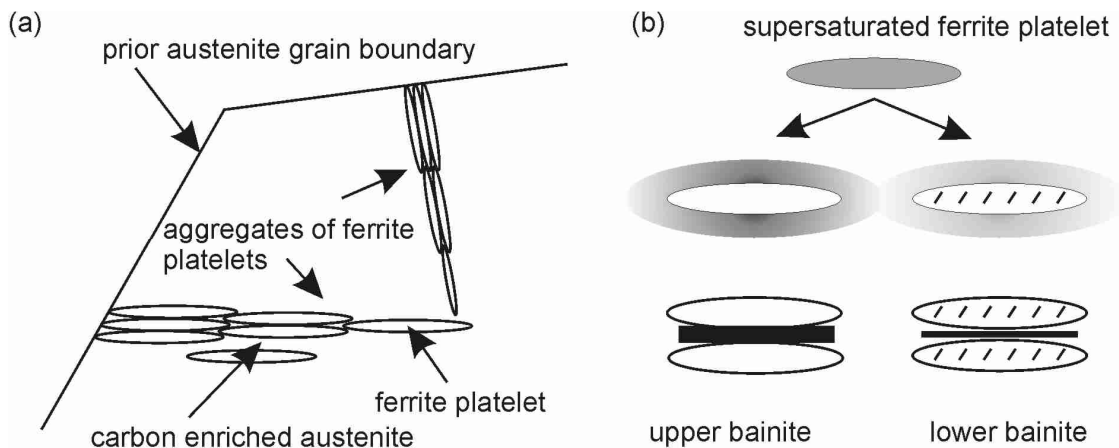
Figure 15: (a) Formation of bainite as aggregates of ferrite platelets in the prior austenite grain. (b) Schematic showing the difference between lower and upper bainite. Adapted from Bhadeshia [24].

Apart from the carbide precipitation, there are further microstructural characteristic that alter together with the cooling rate, such as ferrite platelet size, dislocation density and carbon in solid solution. A consequence of all these strengthening effects is that lower bainite often has a higher toughness than upper bainite in addition to a higher strength at ambient temperatures.

1.2.3 Some microstructural characteristics of a 1%CrMoV steel

The details on the actual batch of material are given in §2.1.1.1. The various manufacturers of 1%CrMoV steel do not have common specifications for this material in terms of chemical composition and preliminary heat treatment procedures.

There is, however, a consensus that the ideal transformation product for the 1%CrMoV steel is upper bainite. This structure, after tempering, results in the most satisfactory dispersion of fine vanadium carbides [25]. Those carbides dominate the good creep properties of the material, since they inhibit a recovery of the dislocation network [26, 27]. Therefore, a tempered bainitic microstructure is envisaged with the final heat treatment, schematically shown in Figure 16(a), and that is a common feature for the various manufactures.
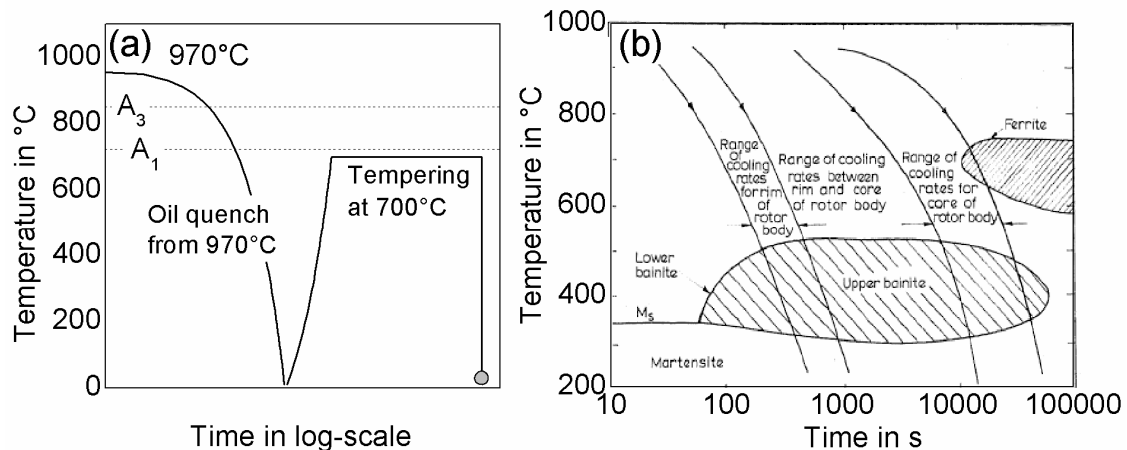
Figure 16: (a) Typical final heat treatment of a 1%CrMoV with oil quenching and subsequent tempering to obtain a tempered bainitic microstructure. The temperatures $A_1 \approx 723°C$ and $A_3 \approx 850°C$, cf. Figure 14(a). (b) CCT-diagram of a 1%CrMoV steel, from Norton and Strang [28].

The bainitic transformation product is commonly obtained by oil quenching from 970°C. Temperature gradients are obviously inherent in large component sizes so that differences in the microstructure over the component size are very likely and small amount of ferrite and pearlite can be found in thick sections (Figure 16(b)).

The quenched material is then tempered at 700°C, which implies the formation of various types of carbide in addition to the potentially pre-existing bainitic cementite, being well described in the review of Senior [25]. The major carbides observed in the tempered microstructure are cementite (i.e. M_3C) and M_4C_3 (or MC), but $M_{23}C_6$, M_6C and M_2C may also be present in small quantities. M

is here referred to as the metal atom. Cementite is thermodynamically unstable and may transform into other type of carbides during creep at 565°C. All these carbides may easily be identified by diffraction and therefore an overview of the different types of precipitates with their crystal structure is given in Table 2.

Table 2 Main type of carbides in a tempered bainitic 1%CrMoV steel, reviewed in Ref. [25]

Carbide	Crystal system	Metal atom M	Size
M_3C	Orthorhombic $a = 4.524$ Å, $b = 5.088$ Å, $c = 6.741$ Å	Fe but can contain Cr, Mn, Mo, V	Rods or ribbons. 1 to 2 μm long and up to 200 nm thick
$M_{23}C_6$	Cubic $a = 10.59$ to 10.66 Å	$(Fe,Cr,M)_{23}C_6$	Irregular and typically below 1 μm
M_4C_3	Cubic $a = 4.160$ Å	V but can contain Mo, Fe, Cr	Most generally plate like with a frequently wide particles grains size (10 nm up to 500 nm), often bimodal distribution
M_2C	Hexagonal close-packed (hcp) $a = b = 3.002$ Å, $c = 4.724$ Å	Mo but can contain Cr, Fe, V	General acicular, 200 nm long and 20 nm wide. Often found as "H" carbide with M_4C_3 in between two M_2C
M_6C	fcc (diamond type) $a = 11.00$ to 11.20 Å	Mo but can contain Fe, Cr, V	Similar as $M_{23}C_6$
M_7C_3	Pseudohexagonal $a = b = 13.982$ Å, $c = 4.506$ Å	Cr but can contain Fe, Mo, V	Similar as $M_{23}C_6$

1.2.4 HT deformation mechanisms

1.2.4.1 Deformation mechanisms

At RT, plastic deformation in this material is characterized by a glide movement of dislocations. With increasing temperature, a variety of additional deformation mechanisms can be active. This dependency can be visualized by the so-called *deformation mechanisms maps*, developed by Ashby *et al.* [29]. A simple schematic is shown in Figure 17(a). The axes show the normalized shear stress (= τ / G) and the normalized temperature (homologous temperature T / T_m, where T_m is the melting temperature of the materials). The shear modulus G is temperature dependent and decreases with increasing temperature. The whole area is divided into several subareas, which are characterized by a certain combination of stress and temperature. Within these subareas, the indicated deformation mechanism is predominant over the others. The upper limit in normalized shear stress is given by

the theoretical shear strength, which has already been introduced by Eq. 13. The subareas define the condition where the plastic deformation is dominated by dislocation motion (*dislocation glide* and *dislocation creep*) or by *diffusional flow* (without dislocations).
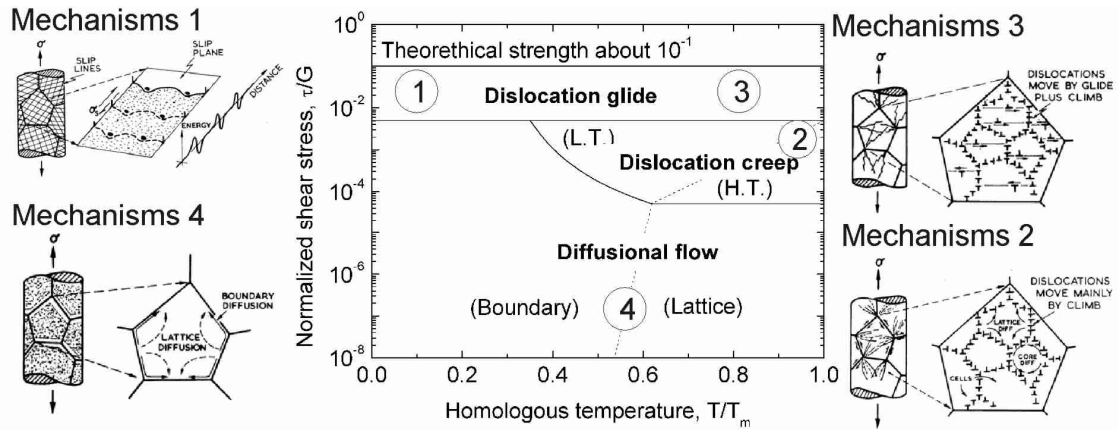
Figure 17 Simplified deformation mechanisms map indicating the dominant deformation mechanisms at a certain stress-temperature combination. The deformation mechanisms are schematically shown left and right of the diagram. T_m is the melting temperature.

Dislocation mediated deformation usually takes the dominant role at higher stresses. At position *1*, the mobile dislocations glide on their slip systems (*dislocation glide*). Once they meet some obstacles, it may be difficult for these dislocations to overcome this obstacle-barrier. The material then work-hardens and a higher stress is required to continue the dislocation motion. Obstacles in this sense are for instance other dislocations, solute atoms and second phase particles. At elevated temperatures, thermally activated processes, such as climb, may now help the dislocations to overcome the obstacles (e.g. at position *2*). This deformation mechanism is known as *dislocation creep*. Dislocation creep can be divided into low temperature (core diffusion) and high temperature (lattice diffusion). At higher stresses (at position *3*) glide-controlled flow might still dominant over climb-controlled flow.

Diffusion mediated deformation without dislocations, usually takes the dominant role at lower stresses (position *4*). Among these mechanisms, one distinguishes between diffusion around grain boundaries (Coble creep) and bulk diffusion (Nabarro-Herring creep) at higher temperatures.

A deformation mechanisms map for a 1%CrMoV steel is shown in Figure 18(b), taken from Ashby [30]. This map has been constructed for a particular batch of material in terms of grain size, precipitation, and so on. One must therefore be careful to compare such maps with other microstructures. This figure hence only provides a rough indication of the possible mechanisms for the operating conditions (up to 565°C, uniaxial tensile stress of 270 to 330 MPa) studied in this dissertation; this area is marked with a red ellipse in the figure. The relevant mechanisms hence are

mainly dislocation mediated. Diffusional flow without dislocations might partly contribute at temperatures close to 565°C and lower stresses [30].
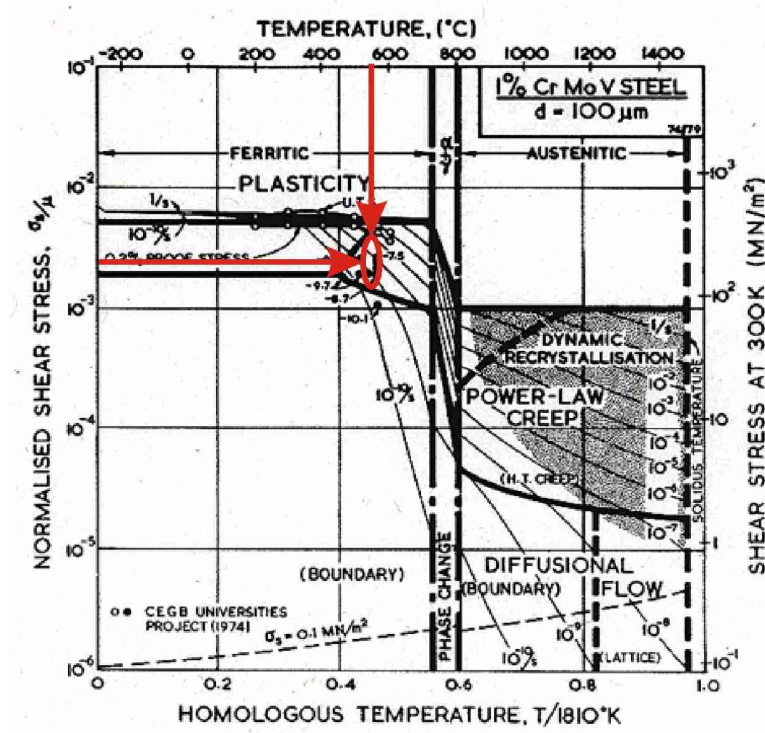
Figure 18 Deformation mechanisms map of a 1%CrMoV steel, from Ashby [30]. The red arrows pointing towards the condition, indicated by the red circle, of HT creep deformation investigated in this work, i.e. at 565°C and 270 to 330 MPa uniaxial tensile stress.

1.2.4.2 Loading schemes

The two mechanical loading schemes applied in this study are uniaxial tensile and uniaxial creep loading. The typical mechanical responses are shown schematically in Figure 19.

Tensile testing is usually done by applying a constant strain rate and recording the stress-strain data (Figure 19(a)). The material is hence loaded beyond the yield stress σ_y (see RT curve). The yield stress may be defined by the interception of a linear line parallel to the early elastic regime with a certain strain offset, e.g. $\sigma_{0.02\%}$ as the 0.02% yield stress. Two curves (RT and HT) are shown here, adapted from Frost and Ashby [30], which may represent the tensile behaviour of the same material but at different temperatures. By increasing the temperature (RT→HT), the mechanical behaviour is typically accompanied by both a reduction in yield stress and a change in the work hardening behaviour. Work hardening means that the stress to generate further deformation (flow stress) changes with strain, as indicated by $\sigma_{y,A}$.

A typical creep test (Figure 19(b)) implies first loading the sample elastically to a certain stress state (*elastically* implies that this stress state is lower than a corresponding yield stress at that

temperature). The temperature is usually above a threshold where creep mechanisms become active – about 350°C for the quality heat-treated condition of the 1%CrMoV steel [31]. Then the stress – for practical reasons usually the load – is kept constant and the strain is recorded as a function of time. The creep curve is divided in three regimes: The primary creep regime is defined as the time between the applications of the load until the onset of the minimum creep rate and comprises microstructural arrangements. The secondary or steady-state creep regime is the time during which the creep rate is constantly at its minimum creep rate. The tertiary creep is defined as the increase in strain rate through microstructural degradation, such as for instance the formation of creep cavitations, leading finally to rupture [32]. The balance between the three creep regimes, the steady-state strain rate and the time to creep rupture for a given microstructure strongly depends on the creep stress and temperature.
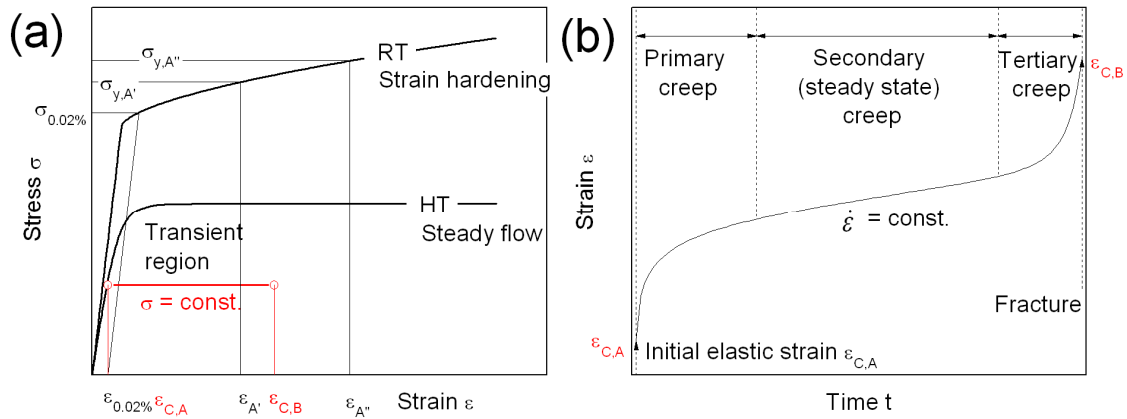
Figure 19: (a) Typical stress-strain curves at RT and high temperatures (HT): The strain rate (or more practically: displacement rate) is constant. The red part illustrates the stress-strain response of a creep test. (b) Typical creep curve: The stress (or more practically the load) is kept constant and the strain is recorded with time.

1.3   Literature review on Type II microstresses

1.3.1   In carbon steels during deformation at RT

A variety of RT deformation studies on ferritic steels in conjunction with X-ray and neutron diffraction have been reported. First, laboratory X-ray sources have been used being the only available technique at that time. In 1964, the work of Wilson and Konnan [33] reported the build-up of internal stresses in a high-carbon steel (1.1 wt% C) after tensile deformation. The average stresses in the matrix are approximately balanced by stresses of opposing sign within the coarse dispersed spheroidal cementite particles with a volume fraction of about 17%. The stresses have been calculated from the diffraction elastic constants and peak shifts after deformation of selected ferrite and cementite peaks. The largest error in the stress determination has been recognized by the uncertainty for the appropriate choice of the diffraction elastic constants. Note, that cementite is an

essential component in many ferritic steels and in spite of the vital importance of ferritic steels in industry and nowadays life, cementite's elastic constants remain uncertain up to date (cf. review in Refs [34, 35]). For strain to stress conversion, the elastic constants most often are assumed to equal those of the ferrite. That also implies that no strengthening influence has been attributed to the cementite in the steel elastic regime. This, however, has to be considered if the stiffness of the reinforcement is larger than that of the matrix [36]. Recent investigation suggest the cementite to be stiffer than bcc iron by about 10% in the Young's modulus [34] and its anisotropic elastic behaviour has only recently been studied by first-principle calculations [37-40] and experimentally on bulk cementite [35, 40]. Wilson and Konnan further reported that the initially high rate of work hardening coincides with the rapid build-up of interphase stress. It was concluded that the stresses within the matrix, acting as so-called back-stresses to impede dislocation motion, are responsible for a major part of the observed work hardening, "but that in materials with a much smaller volume fraction or particle size of the precipitate, other mechanisms of hardening may assume the principal role". Further, cementite diffraction peaks broaden with deformation and finally become too broad for reliable measurements, a phenomenon, which has been realized in all subsequent experiments, without, however, being elucidated. Significant stress relaxation in the freestanding carbide particles has then been observed when the constraining surface ferrite was etched away. This, although not explicitly mentioned by Wilson and Konnan, provides a first evidence of the nature of the cementite peak broadening, i.e. the cementite particles experience a range of local stress levels. In the following decades, further authors reported on the generation of interphase stresses during tensile [41-43] and fatigue loading [44-47], while in that latter case, these stresses apparently fade out with cycling.

As the penetration depth of the laboratory X-rays is only a few tens of micrometers, tedious sample manipulation and preparation (e.g. [33, 45]) are required but the measurement certainly still suffers from near surface effects, such as decarburization [45], residual stresses stemming form the preparation [33] and contribution of macrostresses (biaxial stress state near surface). Neutron and, later, synchrotron facilities with highly penetrating radiation probes overcome this problem and bulk properties can be investigated. The subject of interphase [48-50] and, in addition, intergranular strains in the ferrite matrix [51, 52] developing during tensile loading remained of considerable interest, with the experimental results starting to be compared with predictions from modelling approaches, such as finite element modelling and the EPSC scheme [53]. For more industrial relevant applications, residual stress profiling in cold-drawn steel wires [54-56], rods [57-60] and sheets [61] was performed. Some few studies deal with the influence of different microstructures on the internal stress state due to tensile deformation: Morooka *et al.* [62] in ferritic, martensitic, tempered martensitic and pearlitic steels and Tomota *et al.* [63] in pearlitic steels with different cementite volume fractions. The study of Morooka *et al.* would be of interest in what sense the

build-up of interphase stress depends on the shape of the cementite particles, e.g. lamellar in pearlite and presumably spheroidized in tempered martensite. However, the nominal carbon content and hence the cementite volume fraction in the tempered martensitic and pearlitic steel are very different. A comparative investigation on the quantitative accumulation of internal stresses in steel with a given cementite volume fraction but different morphology, e.g. lamellar and spheroidal, is yet missing. Varying the ferritic grains size appears not to affect the intergranular stresses, as studied in an interstitial-free steel [64]. The work of Oliver *et al.* (thesis [20] and corresponding paper [15]) is of particular interest since it compares the evolution of internal stress during tensile deformation in a high-carbon (1 wt % C) steel with spherical cementite particles with that in a low carbon (0.07 wt. %) steel without cementite particles. The experimental results on the intergranular (in ferrite) and interphase stresses are further described by a coupled model of the finite element and elasto-plastic self-consistent method. Significant load transfer takes place from the plastifying ferrite matrix to the cementite phase yielding these residual interphase stresses after unloading, whereas there is no redistribution of load possible in the low carbon steel. The interphase stresses saturate after a few percent of plastic strain, as pointed out by Wilson and Konnan [33] earlier, but the origin of this relaxation (e.g. local plastic flow, interface damage, cementite particle fracture or deformation) remains unclear, being, however, frequently hypothesized as local plastic flow at the ferrite-cementite interphase [15, 33, 65]. The description of the transverse intergranular stresses is difficult since it strongly depends on the sample texture. This is because the grains possess a range of axial *hkl*-orientations, with the elastic and plastic anisotropy altering the Poisson response, which is measured with the transverse direction (cf. §2.2.3.1).

The carbon content and the corresponding cementite volume fraction of the material in the studies cited in this review vary in between 0.35 to 1.8 wt% C and 8 to 34 vol% cementite, respectively. The signal from the second phase cementite has throughout been reported to be very low compared to that of the ferrite matrix and the background yielding large uncertainties in the lattice strain. It therefore, remains a challenge to investigate the characteristics of the second phase particles with a volume fraction certainly below 4% within the current project. Especially for in situ studies, when the scattering from the cementite peaks has found to be too weak for reasonably single peak fitting due to the limited counting time, full pattern fitting procedures, e.g. Rietveld refinement, were applied to study the phase average behaviour of cementite [15]. Hence, inherent cementite characteristics such as peak shape evolution or possible elastic and plastic anisotropic effects of the cementite were not observed. Recently, Young *et al.* [65] studied the load-partitioning between ferrite and cementite in an ultrahigh-carbon steel (1.8 wt% C) with a large cementite volume fraction of 34% using X-ray diffraction (XRD) from highly penetrating, high flux synchrotron radiation and single peak fitting. The results were consistent with those of Oliver *et al.*

[15]. While it was reported that the cementite phase behaves relatively isotropic in the elastic regime, in the macroscopic plastic regime, a greater proportion is of the load is carried by certain cementite crystallographic orientations compared to others.

The increasing evidence of elastic anisotropy [35, 37-40] and anisotropic effects in the steel's plastic regime [65] in cementite may be of particular importance during deformation of a bainitic steel, where the cementite particles are typically oriented along certain crystallographic directions with the ferritic matrix [24]. This crystallographic relationship is a direct consequence of the bainitic phase transformation and might still be retained after tempering [25]. In general, the mechanical properties of cementite are far from being entirely understood [66] at both RT and HT. During RT deformation, the cementite from pearlitic structures may eventually plastically deform, dissolve or break [67-70]. Plastic deformation may become more likely at elevated teperatures [71]. The actual behaviour of cementite in a ferritic matrix deformed at elevated temperature has not been reported so far. Therefore, a brief summary on the most relevant conclusions from HT deformation studies of metal matrix composites (MMC) studied by diffraction is given in §1.3.2

1.3.2 Selected studies during deformation at HT in metal matrix composites

The fundamental behaviour of MMCs during deformation in general and creep in particular is described by Clyne and Withers [36]. A composite is considered as effective, when a significant proportion of the load is carried by the reinforcement. The load bearing capacity strongly depends on the volume fraction, shape and mechanical properties of the latter. There seems, however, to be a consensus that the phase strains between the matrix and the reinforcement, remains essentially constant throughout the transient and steady-state creep regime, as for instance been studied by Winand *et al.* [72] on discontinuously SiC reinforced aluminium composites with neutron diffraction. Since matrix creep would continuously increase the misfit, they concluded that stress relaxation mechanisms must be operating. Mori et al. suggested diffusional and sliding processes [73, 74] as relaxation mechanism of the stress concentration due to load transfer between matrix and particle at high temperatures. Stress relaxation by void formation around the second phase particles is also a possible scenario [75]. The above-described studies relate to *plastically strong* [76] inclusions. Note, that cementite may for instance deform plastically or transform to other type of carbides at elevated temperatures. A more or less constant phase stress during creep has recently also been found in a ferritic superalloy with B2-type (Ni,Fe)Al precipitates [77]. Here, the magnitude of load-redistribution during isothermal creep increases with applied stress. However, neither the yield strength at that temperature has been mentioned nor the intergranular and interphase load-redistribution possibly happening during loading to the dedicated stress level has been considered. Combining both tensile and creep loading at the same temperature certainly allows more detailed conclusions on the mechanisms responsible for the lattice strain evolution [78].

1.3.3 Potential impact of Type II microstresses

A review on the origins and measurements techniques of and the impact on failure processes on residual stresses is given by Withers [7]. Residual type II microstresses may (i) have an influence on the component properties, e.g. to initiate cracks and (ii) affect the characterization of macrostresses determined by diffraction.

Ad (i): In conjunction with an adequate microstructure, microstresses may for instance act as a precursor for cracks in fiber reinforcements [36] or contribute to void formation in the matrix [79]. A potential deleterious effect of microstresses in ferritic steels has not been proofed so far. Some authors report cementite particle fraction upon deformation with a corresponding load-reduction in cementite [80-82]. Residual stresses in the cementite can be considerably high and of the order of a few GPa, as observed by elastic lattice strain measurements using diffraction in pearlitic (e.g. [56]) and spheroidized (e.g. [65]) microstructures. Various authors refer to a possible influence on crack initiation and propagation, stress corrosion, fatigue processes in the motivation of their work on ferritic steels (e.g. [45, 46, 54, 55]). A further influence of residual microstresses might be to act as a driving force for dislocation motion in the absence of applied stress. Recent investigations [83, 84] on austenitic steels hypothesise intergranular type of microstresses as origin of anelastic recovery, a mechanism that is most often neglected in constitutive creep relations [85, 86]. Closely related is the discussion [44, 87, 88] on the role of internal stresses to the Bauschinger effect [89], which can be quite pronounced in multi-phase materials, with both elastically [90] and plastically [91] deforming second phase particles. If the composite stresses are large enough, then a deviation from the linear stress-strain behaviour can already be observed upon unloading [92]. Finally, constitutive models, for instance to describe the behaviour of polycrystalline and composite materials under load, must be able to capture all these macroscopic features and therefore, the underlying mechanisms must first be understood.

Ad (ii): The second and well-known implication of intergranular and interphase type of microstresses is on the practical measurement of macrostresses, since diffraction measures a superposition of both. In case of a single-phase polycrystalline material, the behaviour of the intergranular type of microstrains is reasonably well understood and recommendations of the least affected crystallographic planes have been released in an ISO code of practice [93] and a National Physical Laboratory (NPL) measurement guide [94]. The knowledge is continuously extended towards further materials, non-ambient temperatures regimes (e.g. HT in fcc iron [95]) and different deformation modes (e.g. torsion in bcc iron [96]). The behaviour of the individual planes during HT deformation in bcc iron have not yet been documented. Often, a diffraction pattern can be acquired over a large range of lattice spacing range, for instance by time-of-flight (ToF) neutron diffraction, allowing the use of full pattern refinements. Here, Rietveld refinement has been

established for some cases to determine the elastic macrostrain [97]. However, if a second or even further phases contribute to the deformation, interphase stresses will superpose the intergranular stresses (e.g. [98]). If the volume fraction of the additional phases is considerably large to observe the corresponding diffraction peaks, measurements can be corrected for. Often, and in particular in alloyed steels with its various types of precipitates in small size and quantities [23], this is not the case and the error therefore can be large. Any assessment of the potential influence of second phase particles on the accumulation of interphase strains, depending on the loading condition, is therefore of interest.

1.4   Aim and research outline

The aim is to further the understanding in the build-up of intergranular and interphase strains in carbon steels, by investigating a conventional creep resistant 1%CrMoV steel. While extensive research has been devoted to this topic during deformation at ambient temperatures, no detailed study exists at elevated temperatures. That is the extension to the existing knowledge the dissertation aims to provide.

Neutron diffraction patterns of pre-deformed samples of a creep resistant tempered bainitic 1%CrMoV steel have been acquired. These measurements showed that both the magnitude and evolution of residual strain in the ferrite matrix with plastic strain depends on the prior loading condition (tensile RT and creep), the origin of which is addressed with in situ mechanical testing, i.e. mechanical testing during acquisition of diffraction patterns.

Neutrons and synchrotron X-rays are used complementary to account for the inhomogeneous microstructure and the low volume fraction of second phase particles, respectively. The mechanical tests comprise tensile loading at RT and elevated temperatures (565°C) and creep loading at 565°C.

Two particular observations of the cementite diffraction peaks during RT tensile loading motivated additional experiments: (i) In order to address the extensive peak broadening, the ferritic matrix has been dissolved electrolytically and the remaining carbide powder was characterized by XRD. (ii) In order to address an elastic anisotropic behaviour of cementite, samples with different microstructures of a high-carbon steel were prepared and tensile deformed in situ with XRD.

2   Material and experimental description

This chapter introduces the *materials*, the *experimental method* to characterize the intergranular and interphase strains, i.e. diffraction with X-rays and neutrons, and the *experimental tools*, i.e. devices, experimental set-up and data treatment.

2.1   Material

The mid-carbon low-alloy 1%CrMoV steel has been provided by S.R Holdsworth from EMPA in the quality heat-treated condition, hereafter denoted as *as-received*. Some of the as-received material has also been heat-treated within this dissertation. Furthermore, carbides of the as-received – both undeformed and after mechanical testing – and of the heat-treated material have been extracted from the 1%CrMoV steel. The second material used in this dissertation is a high-carbon steel taken from the stock of raw materials at PSI. This high-carbon steel was heat-treated to obtain various microstructures in order to verify observations obtained from the 1%CrMoV steel. This section §2.1 provides details on the material, the heat treatment and the carbide extraction procedure.

2.1.1   1%CrMoV steel

2.1.1.1   As-received microstructure

The chemical composition of the mid-carbon low-alloy 1%CrMoV steel is given in Table 3. The material was taken from the core part of a steam turbine rotor forging. A typical manufacturing process includes hot forging of the cast to the final shape followed by a heat treatment to produce the final microstructure. This commercial heat treatment comprises oil quenching from 970°C followed by tempering at 700°C. The prior austenite grain size before quenching is about 50µm [99]. The material's microstructure is rather inhomogeneous on a length scale of a few mm in terms of carbide segregation, ferrite grain size and morphology (Figure 20):

Figure 20(a) shows an optical dark-field image of the surface that was etched with picral, which provides a contrast between the carbides and the ferrite matrix (cf. §2.3.1). The micrograph reveals brighter and darker areas. In literature this is known as a mottled microstructure [28]: Its origin is attributed to segregation of carbides and its spatial extend appears to be typical for this ready-for-service microstructure of the 1%CrMoV steel. The bright areas are always found to be elongated along the same direction in the as-received microstructure. For that reason all samples in this dissertation were manufactured with the loading axis being parallel to that direction, as indicated by the arrow in Figure 20(a). A series of ten micro-hardness measurements (cf. §2.3.3) have been performed within the two indicated areas. The brighter (carbide-rich) area is found to be

significantly harder (HV0.5=330±15) than the neighbouring area (HV0.5=280±20). Furthermore, black spots are observed in the micrograph and mostly within the darker (less carbide) areas. In literature these spots have been attributed to proeutectoid ferrite grains [28]. Since these grains are free of carbides, they indeed will appear as black spots in this micrograph.

Figure 20(b) shows an EBSD map of the region highlighted with a white square in Figure 20(a). This region has been marked with indentions for relocation in the electron microscope. The EBSD map reveals an inhomogeneous ferrite grain size and morphology.

Table 3 Mean chemical composition (in wt%) of the 1%CrMoV steel for elements > 0.1 wt%, Ref. [100]

Fe	C	Cr	Mo	Mn	Ni	V	Si
Balance	0.25	0.88	0.80	0.73	0.60	0.33	0.15
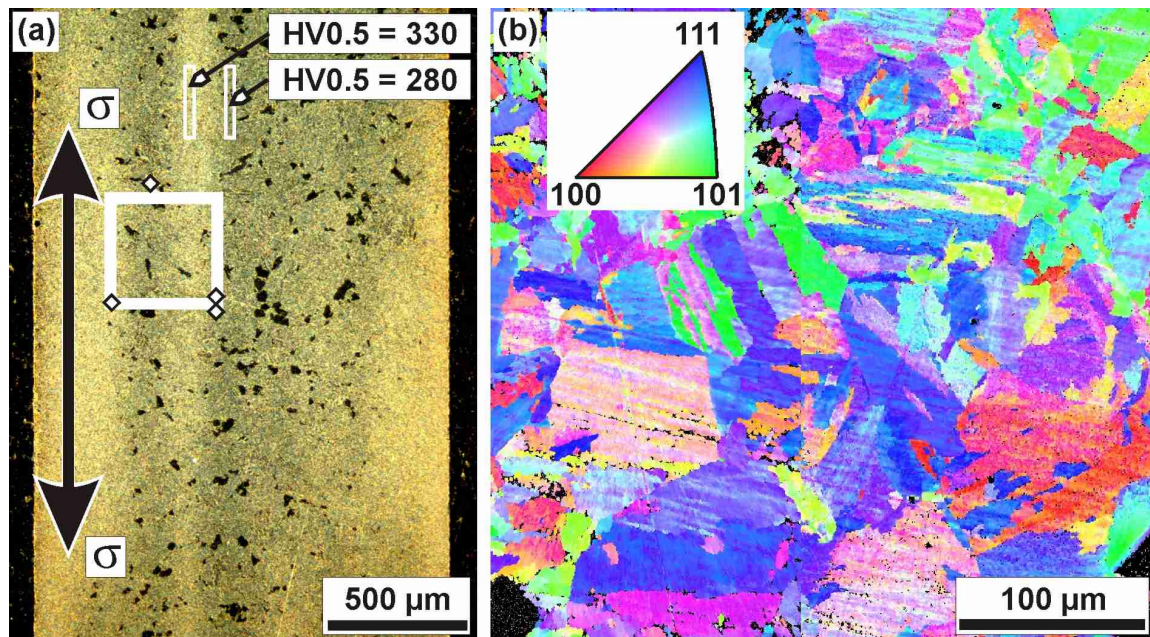
Figure 20: (a) Optical dark-field micrograph of the as-received 1%CrMoV microstructure, etched with picral for about 2 minutes. Micro-hardness measurement variations: HV0.5=330±15 in the bright areas and HV0.5=280±20 else. The arrow indicates the later tensile axis (σ), which is parallel to the elongated bright areas. The white square indicates the area for EBSD mapping. (b) EBSD ferrite grain orientation map. The colour code is indicated by the standard orientation triangle in the inset.

2.1.1.2 Heat treatment of the 1%CrMoV steel

Heat treatments have been performed on the as-received 1%CrMoV steel in order to investigate the potential influence of the *individual* types of carbide (cementite, vanadium carbide) on the accumulation of residual strain. The idea is that quenching first produces bainitic cementite and subsequent tempering then gives rise to the additional formation of vanadium carbide.

The as-received material was brought to 1150°C for 1.5h (in the following: 1150°C/1.5h) to dissolve all carbides – the dissolution temperature of vanadium carbide is about 1050°C [101] – and

to wash out the mottled regions (cf. Figure 20(a)). The material is oil-quenched from 1150°C to prohibit carbide formation and large ferritic grain sizes. The heat treatment condition to obtain a bainitic microstructure is not reported in literature for such small sample sizes and can only be approximated. Therefore, various test samples have been quenched from 970°C/1.5h. The quenching medium was either an oil bath for quenching to RT or a salt bath for quenching to various temperatures in between 300-550°C (50°C step size) and soaking times in between 5min to 3h, followed by air-cooling. For details on the used equipment, cf. §2.3.2. Each of the samples of the test matrix was prepared for optical microscopy by grinding, polishing and etching with picral (cf. §2.3.1). Initially, formation of bainitic cementite was expected. However, none of the microstructures quenched to temperatures below 450°C revealed carbides (i.e. no contrast in dark-field mode) and only a very slight contrast was found for those microstructures quenched to temperatures of 450° and above. A more detailed investigation using TEM has not been performed. The temperature was finally set to 450°C (salt bath), since according to literature [28], quenching to this temperature should certainly provide an upper bainitic microstructure. These quenched samples were then tempered at 700°C for various times (1h, 3.5h, 7h), followed by air-cooling. The corresponding heat treatment of the samples, hereafter referred to as *Heat1*, *Heat2*, *Heat3* and *Heat4*, is summarized in Figure 21(a).
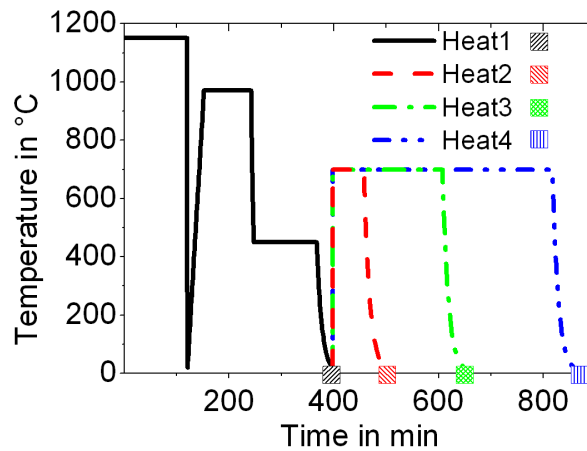
Figure 21 Heat treatment histories of the 1%CrMoV steel. The squared symbols represent the final sample conditions. All samples have been solution treated at 1150°C, quenched, austenized at 970°C, quenched to 450°C in salt batch and air-cooled (*Heat1*). *Heat2*, *Heat3* and *Heat4* are additionally temperered at 700°C.

2.1.1.3   Extraction of carbides

The particle size and the volume fraction of the carbides embedded in the ferritic matrix in the 1%CrMoV steel are considerably small. These carbides have therefore been gathered as powder, after dissolving the ferritic matrix, for a characterization by XRD. This selective electrochemical dissolution of the ferritic matrix has been achieved using a set-up schematically shown in Figure

22(a). The steel sample is wrapped with a platinum (Pt) wire and serves as an anode, a Pt-net placed aside and not being in contact with the former serves as a cathode. Pt is inert during electrolysis due to its high electrochemical potential relative to that of the steel matrix. An electrolyte of 5vol% HCl (37% conc.) and 95vol% H_2O (deionised) was used, according to Ref. [102]. The authors investigated a similar CrMoV steel and it appears that all main carbides expected in the 1%CrMoV (cf. Table 2) are inert to this procedure. The dissolution reaction reads:

$$Fe + 2HCl \rightarrow FeCl_2(aq) + H_2 \uparrow$$
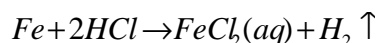
It is necessary to loosen the carbides from the steel surface using an ultrasonic bath from time to time. After the steel is dissolved, the solution has been centrifuged (5000rpm/30min) to settle out the carbides. Alternatively, the solution could be left unshaken for a few days, which showed the same results in terms of carbide weight fraction and XRD pattern. The clear but greenish liquid was poured away and the carbides were loosend from the bottle bottom using ethanol and ultrasonic bath. The greenish colour stems from the ferrous chloride $FeCl_2$ in solution. The settle out procedure, now with ethanol, was repeated once in order to avoid any residuals of ferrous chloride that might otherwise contribute to the XRD pattern and complicate the analysis. The solution was then air-dried in a watch glass and the weight difference between the glass and the glass with the dried carbides was determined. The carbides were scratched from the watch glass and the agglomerates were gently broken in a mortar. The powder for XRD investigation on the Materials Science beamline, a dedicated powder diffraction beamline at the SLS (cf. §2.3.5.1), was then put in glass capillaries of 0.3mm diameter (0.01mm glass thickness). Only a few micrograms of powder are necessary, as illustrated in Figure 22(b). Two sample capillaries were prepared for each powder, one with the powder only and one with the powder mixed with *Si NIST640c*, which is a standard powder for the accurate determination of diffraction line position in order to account for potential variations in the lattice parameter caused, for instance, by changes in the chemical composition and systematic errors of the beam line (offset detector and sample misalignment).
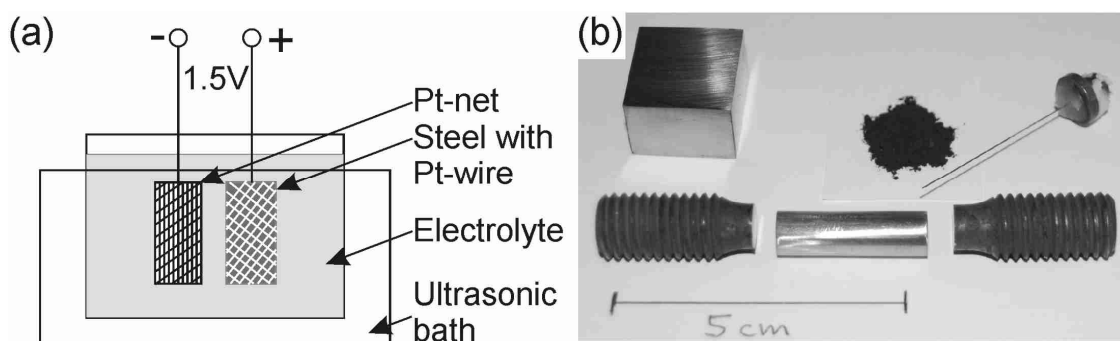

Figure 22 Selective electrochemically dissolution of the ferrite matrix: (a) Schematic of the set-up and (b) remaining carbide powder (*about 0.6g*) dissolved from a certain quantity of steel (*about 20g*). For XRD analysis, only a few micrograms of the powder are required and inserted in a 0.3mm-diameter capillary. Also the gauge section of deformed samples has been dissolved.

2.1.2 Heat treatment of the high-carbon steel

To test the hypothesis of an elastic anisotropy of cementite, observed during in situ tensile loading in the as-received 1%CrMoV steel (cf. §3.3.2.3), three different microstructures, hereafter referred to as *HC1*, *HC2* and *HC3*, from a high-carbon steel (1.15 wt% C) were prepared. The chemical composition of this so-called "silversteel" (Material code: *DIN 1.2210*, *ASTM L2*, *JIS SKS43*) is given in Table 4. Such a high-carbon steel possesses a large volume fraction of cementite and therefore eases the experimental and analysis procedure with diffraction. The heat treatment history is indicated in Figure 23.
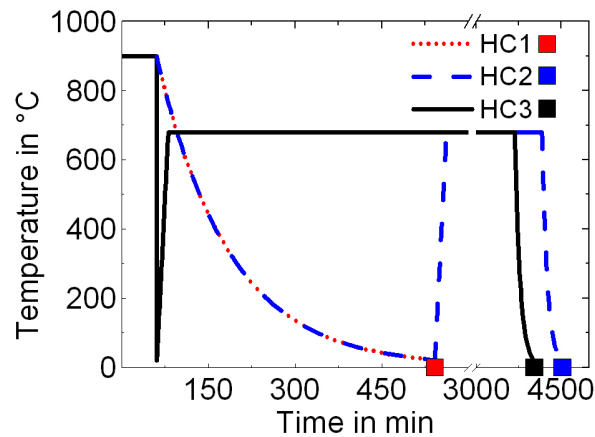
Figure 23 Heat treatment histories of the high-carbon steel. The squared symbols represent the final sample conditions. Note the interruption of the x-axis from 600 to 3000min.

Because of the potential problem with the sampling statistics during the in situ deformation studies by X-ray powder diffraction (cf. §2.2.4), the prior austenite grain size needs to be kept small. That requires a low austenitization temperature (cf. Figure 14) and short soaking times. Austenitization has finally been performed at 900°C for 1h, followed either by oil quenching (Sample *HC3*) or furnace cooling (Samples *HC1*, *HC2*). The furnace-cooled material shows a mixture of proeutectoid cementite and pearlite (Sample *HC1*, Figure 24(a)). Oil quenching on the other hand, forms a martensitic structure and therefore prevents carbide network formation. Another furnace cooled and the quenched sample is then tempered at 680°C for 60h yielding a mixed microstructure of pearlite and spheroidized cementite (Sample *HC2*, Figure 24(b)) and a microstructure with entirely spheroidized cementite (Sample *HC3*, Figure 24(c)), respectively. All samples were furnace-cooled from 680°C to RT in order to minimize the temperature gradient from the surface to the interior and therefore the residual (Type I) stresses.

Table 4 Mean chemical composition (in wt%) of the high-carbon steel (silversteel) for elements > 0.1 wt%

Fe	C	Cr	V	Mn	Si
Balance	1.15	0.65	0.1	0.3	0.25
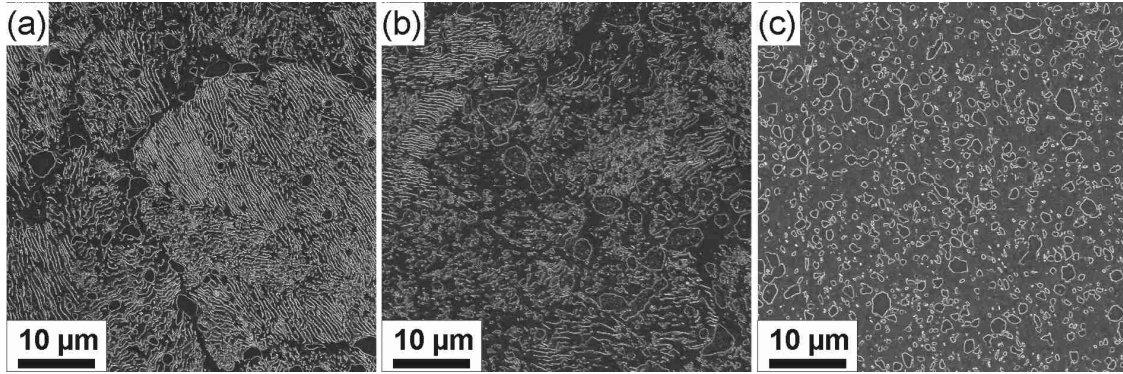
Figure 24 SEM micrographs of the surfaces etched with picral: The different microstructures of the high-carbon steel after heat treatment (cf. Figure 23) are: (a) Pearlitic with proeutectoid cementite (Sample *HC1*), (b) Tempered pearlitic (Sample *HC2*) and (c) Spheroidized cementite particles (Sample *HC3*).

2.2 Experimental method

This section describes first some basics about strain measurement by diffraction, followed by an overview on the characteristics of the neutrons and X-rays probes, which are both used complementarily in this dissertation.

2.2.1 Crystal lattice as a strain gauge

Consider an incident radiation with wavelength λ that falls on a regular array of scattering centres, as represented in Figure 25(a) by the atoms within the crystal lattice with a lattice spacing d_{hkl}, where h, k and l are the Miller indices.
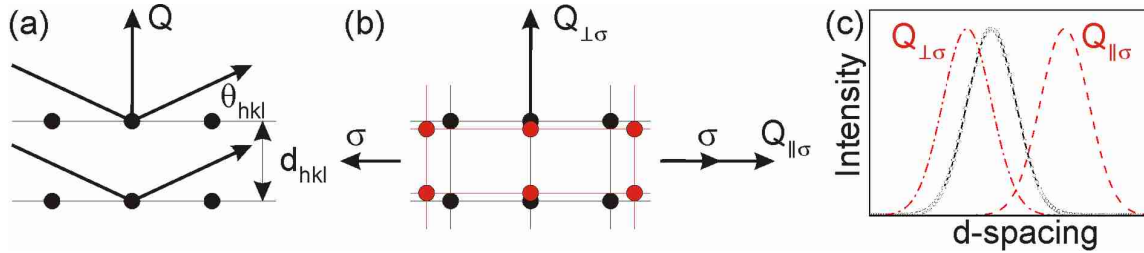
Figure 25 Schematic of elastic lattice strain measurements by diffraction.

Constructive interference of the scattered waves occurs under certain diffraction angles θ_{hkl}, when the path length of the waves is an integer multiple of λ, described by the Bragg condition:

$$\lambda = 2 \cdot d_{hkl} \cdot \sin(\theta_{hkl})$$

Eq. 17

These diffracted waves give rise to a diffraction peak (Figure 25(c)) on a detector. Fitting this diffraction peak with a mathematical function provides, for instance, the mode of the d-spacing. As can be seen from Bragg's law, the d-spacing can be determined when either the wavelength or the diffraction angle is fixed and the remaining quantity is measured. Both angle dispersive (diffraction angle is measured) and energy dispersive (energy is measured) can be performed with neutrons and

X-rays. In this dissertation, angle dispersive X-ray diffraction and energy dispersive neutron diffraction are used. The corresponding set-ups set-ups are described in section §2.2.3. The scattering vector Q is the difference between the outgoing and the incoming wave vector. In case Bragg's law (Eq. 17) is fulfilled, then:

$$Q = 4 \cdot \pi \cdot \sin(\theta_{hkl})/\lambda = 2 \cdot \pi/d_{hkl}$$
<div align="right">Eq. 18</div>

The direction vector of Q is parallel to the normal of the diffracting (*hkl*)-plane. When the sample is loaded in a uniaxial way, the distance d between the lattice planes is increases along the loading direction and decreases along the direction perpendicular to the loading direction due to the Poisson response (Figure 25(b)). These directions are frequently used throughout this dissertation and are denoted as "axial" (parallel) and "transverse" (perpendicular) in the following. The diffraction peaks with the scattering vectors $Q_{//\sigma}$ and $Q_{\perp\sigma}$ shift accordingly (Figure 25(c)). Since diffraction allows to determined d_{hkl} very accurately – the peak position can typically be obtained within a statistical error of the order of 10^{-5} – the crystal lattice can hence be considered as a strain gauge and the elastic lattice strain for one *hkl*-orientation, ε_{hkl}, is calculated accordingly:

$$\varepsilon_{hkl} = \frac{d_{hkl} - d_{hkl}^0}{d_{hkl}^0}$$
<div align="right">Eq. 19</div>

where the index 0 indicates the strain-free reference value. The d-spacing for an *hkl*-direction is related to the unit cell parameters a, b, c of the crystal lattice and the expression for a cubic ($a = b = c$) and an orthorhombic ($a \neq b \neq c$) system reads:

$$d_{hkl} = \frac{a}{\sqrt{h^2 + k^2 + l^2}} \qquad\qquad d_{hkl} = \frac{abc}{\sqrt{b^2 c^2 h^2 + a^2 c^2 k^2 + a^2 b^2 l^2}}$$
<div align="right">Eq. 20</div>

Within a certain range of d-spacings, a number of diffraction peaks from one phase will hence appear. These peaks can be fitted separately to determine the mean d_{hkl} value and the strain for that (*hkl*)-grain family can be determined according to Eq. 19. This allows investigating the strains between the individual (*hkl*)-grain families, i.e. the intergranular type of strains, as has for instance been reported in §1.1.2. On the other hand, one can use several different (*hkl*) diffraction peaks in order to refine the unit cell parameters whereat the individual d_{hkl} are constrained by the unit cell parameters. For a cubic crystal system, the average strain of a phase can be determined according to

$$\varepsilon_{Phase} = \frac{a - a^0}{a^0}$$
<div align="right">Eq. 21</div>

This allows investigating the strains in each phase of the material, i.e. the interphase type of strains, as has for instance been reported in §1.1.3. Full pattern refinements such as Pawley [103] and Rietveld [104] are frequently used to estimate the unit cell parameters in order to calulate the phase strain [97, 105]. The essential difference with the Rietveld method is that the integrated peak

intensities are considered as refinable parameters, which makes a Pawley refinement sometimes more convenient for treating textured samples. Whereas calculating the phase strain for cubic systems seems to be straight forward, the situation is different for orthorhombic systems (e.g. cementite) with three unit cell parameters a, b, c. A possibility [58] to estimate the phase strain is to calculate an average parameter $Av = (a + b + c) / 3$ and to define the phase strain as:

$$\varepsilon_{Phase} = \frac{Av - Av^0}{Av^0}$$
<div align="right">Eq. 22</div>

The stress-free parameters a^0 and d^0_{hkl} in any residual stress measurement have to be determined with great care, because it determines the absolute value of the residual stresses. Examples of how to obtain these parameters are, for instance, described in [7, 11]. Since we are interested in the change of lattice parameter upon defomation and as the illuminated gauge volume is not changing, a^0 and d^0_{hkl} are obtained from the sample before deformation, ideally with a relaxed microstructure, i.e. without significant intergranular and interphase stresses.

2.2.2 Neutron vs. X-ray

Both, neutrons and X-rays may be used for elastic lattice strain determination and this section provides a brief overview on the most relevant characteristics. For more details on neutron (e.g. Bacon [106]) and X-ray (e.g. Cullity [107]) scattering, the reader is referred to standard textbooks.

2.2.2.1 Interaction with matter

The interaction with matter is different for neutrons and X-rays. X-rays interact primarily with the "electron cloud" surrounding each atom. The "power" of the scatter from an atom may be expressed by the atomic scattering factor

$$f = \frac{\text{amplitude of the wave scattered by an atom}}{\text{amplitude of the wave scattered by one electron}}$$

and since Fe has 26 electrons, that yields in forward direction (($\theta=0$)) to f($\theta=0$)=26. The contribution to the diffracted X-ray intensity increases therefore with the atomic number, as illustrated in Figure **26**(a). The size of the circles is proportional to the scattering amplitude. In fact, the term "cloud" mentioned above does not precisely describe the situation, since the electrons are somehow localized within that cloud. The wave scattered from each of those electrons with the wave from another one then may interfere with the consequence that the atomic scattering factor falls off with increasing scattering vector $Q \propto \sin(\theta) / \lambda$ (Figure 26(b)). The atomic scattering factor as a function of Q for all elements is tabulated for instance in Ref [106]. Neutrons, on the other hand, interact primarily with the nucleus of the atom and the contribution to the diffracted intensity can therefore be different for each isotope (Figure 26(a)). For instance, C_{12} scatters about as equally well as U_{283}, and Fe_{56} scatters better than Fe_{54} and Fe_{57}. Care must be taken when considering

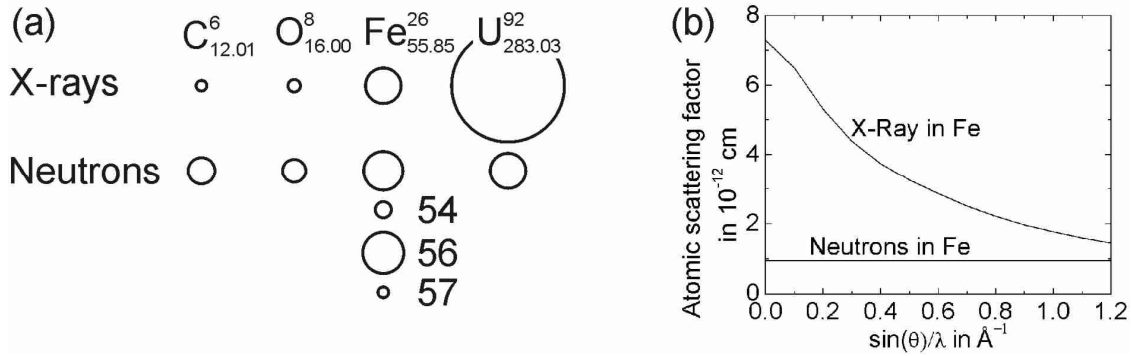mixtures of isotopes and elements. The atomic scattering factor for neutrons basically does not fall off with Q.

Figure 26: (a) Scattering "power" (in fact: scattering cross section) of X-rays and neutrons with different elements. The radii of the circles are proportional to the scattering amplitudes within each probe (not directly comparable for X-rays with neutrons), adapted from Bacon [106]. (b) The atomic scattering factor with $\sin(\theta)/\lambda$ for one Fe atom, adapted from Bacon [106] and Cullity [107].

2.2.2.2 Wavelength

Considering Bragg's law (Eq. 17), the upper limit for an acceptable wavelength to obtain d_{hkl} and to perform lattice strain measurements is given by

$$\lambda \leq 2 \cdot d_{hkl} \qquad \text{Eq. 23}$$

which, for instance, becomes 4.1 Å for the bcc Fe reflection with the largest measurable d-spacing, i.e. {110}. Both radiation probes, X-rays and neutrons, possess wavelengths that are in the order of the lattice spacing and below 4.1 Å. The relationship between energy E and wavelength λ is for X-rays given by:

$$\lambda(\text{Å}) = \frac{c}{\nu} = \frac{c \cdot h}{E} = 12.398 / E(keV) \qquad \text{Eq. 24}$$

and for neutrons using the De Broglie relation (in a non-relativistic approach) by:

$$\lambda(\text{Å}) = \frac{h}{p} = \frac{h}{m_n \cdot v_n} = \frac{h}{\sqrt{2 \cdot m_n \cdot E}} = \frac{9.045}{\sqrt{E(meV)}} \qquad \text{Eq. 25}$$

with the velocity of light $c = 2.998 \times 10^8$ m/s, Planck's constant $h = 6.626 \cdot 10^{-34}$ Js, rest mass of a neutron $m_n = 1.675 \cdot 10^{-27}$ kg, energy conversion $1eV = 1.602 \cdot 10^{-19}$ J and $1J = 1$ kg·m^2·s^{-2}; further v_n and p are the frequency and the momentum, respectively. To fulfil Eq. 23, the X-ray and neutron energy must be larger than 3.024 keV and 4.857 meV, respectively. Neutrons are classified according to their energy: For instance, cold neutrons hold an energy range of 0.12 to 12 meV (26.1 to 2.6Å), thermal neutrons of 12 to 100 meV (2.6 to 0.9Å) [108]. Thermal neutrons are therefore well suited for diffraction. The typical energies of the radiation probes produced in the large scale facilities are given below in §2.2.2.4.

2.2.2.3   Attenuation

Any beam (neutron and X-ray) is attenuated when it passes through matter. For a given material with thickness z, the ratio of the intensities of the transmitted beam I_z and incident I_0 beam can be written as

$$\frac{I_z}{I_0} = e^{-\mu \cdot z}$$

Eq. 26

where μ is the linear attenuation coefficient. Various processes (absorption, coherent and incoherent scattering) can contribute to the attenuation, as illustrated in the inset of Figure 27(a). The attenuation length l_μ, is defined as the thickness of the material when the transmitted beam loses about 63% of the incident intensity ($I_z/I_0 = 1/e$, Figure 27(a)).
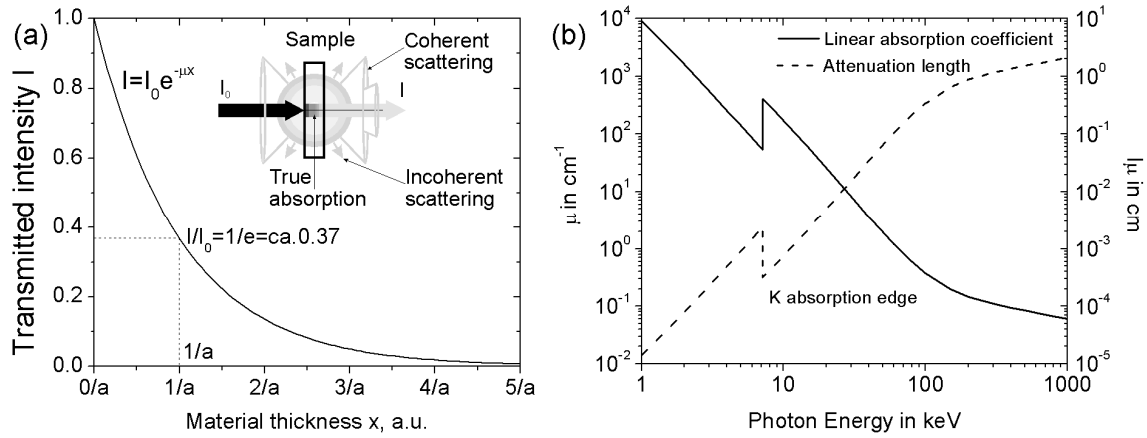
Figure 27: (a) Intensity of a transmitted beam passing through a material of thickness x. The schematic inset illustrates the various contributions to the attenuation and is adapted from Hutchings [11] (b) Linear attenuation coefficient and attenuation length for an X-ray beam at different energies transmitting Fe, with the K absorption edge at 7.112keV. The data is taken from the mass absorption coefficient, tabulated in the National Institute of Standards and Technology (NIST) database [109] for 1keV to 20MeV, multiplied by the density ρ(Fe)=7.874g/cm^3.

The linear absorption coefficient and the attenuation length for X-rays in the energy range of 1 to 1000 keV in steel are shown in Figure 27(b). The attenuation length exponentially increases with the photon energy: It is only of the order of μm at low energies, but of the order of mm at higher energies. At 7.112 keV the attenuation length drops by about one order of magnitude. This drop is due to the so-called absorption edge, which is related to the generation of photoelectrons. In the photoelectric effect, a photon knocks an electron from an electron shell around the nucleus out of the atom. For this to happen, a minimum energy W is necessary. In Fe, the W_K for an electron of the inner K-shell is 7.112 keV. For higher electron shells (L, M, *etc.*), $W_{L,M}$ is smaller than 1 keV and does therefore not occur in the spectrum of Figure 27(b). The photoelectric effect hence lowers the attenuation length but contributes to the background radiation by the emission of fluorescence light,

as the "hole" in the shell is filled by another electron from a higher shell, thereby emitting photons with a characteristic energy that equals the energy difference between these shells.

The attenuation of neutrons depends, as for X-rays, on the energy and the material that is penetrated. For thermal neutrons (12 to 100 meV) in Fe, the attenuation is predominated by coherent scattering. That causes some fluctuations of the attenuation length within that energy spectrum (so-called Bragg-edges) with a drop in the transmitted intensity at $\lambda = 2 \cdot d_{hkl}$. It is accepted to take the characteristics of a 25 meV neutron beam as reference value for thermal neutrons. The attenuation length for thermal neutrons in steel is therefore considered to be about 8 mm.

The attenuation length of thermal neutrons is therefore larger as for X-rays of a similar wavelength. High energy X-rays, however, can penetrate as deep in Fe as thermal neutrons do.

2.2.2.4   Radiation sources

2.2.2.4.1   X-ray

X-rays for diffraction experiments are essentially produced in two ways, either with an X-ray tube or in a synchrotron. Some characteristic properties of these X-rays are summarized in Figure 28(a). In an X-ray tube, electrons are accelerated towards a metal target and then produce both bremsstrahlung and the characteristic line spectrum. The bremsstrahlung has a continuous distribution with the upper energy threshold given by the kinetic energy of the electrons hitting the target. Hence, the photon energy is tunable and can be shifted towards higher energies by increasing the accelerating voltage for the electrons. Typical values for X-ray tubes are in between 20 and 150 kV. The characteristic line spectrum is then superimposed on the bremsstrahlung and stems from the emission of photons with a discrete energy. That energy equals the difference of energy levels when an electron from an outer shell level jumps to a vacant place, giving the series of K, L, *etc.* emission lines (Figure 28(b)). The energy at which the emission occurs is therefore fixed and given by the target material. Generally, the $K\alpha l$ line is used for diffraction experiments since it provides a relatively high intensity and also can easily be monochromatized, e.g. with absorption filters. The $K\alpha l$ lines of the most common target materials, e.g. copper and molybdenum, lie at 8.0 and 17.5 keV and hence only penetrate a few tens of µm in material, e.g. steel (cf. Figure 27(b)). That is why X-rays from laboratory diffractometers are often considered to have a limited penetration depth and only probe the surface region. There is, however, always the possibility to increase the acceleration voltage of the electrons. In that case, the $K\alpha l$ line of, for instance, tungsten at 59.3 keV or even the continuous high energy bremsstahlung can be exploited for diffraction experiments. An example for the latter technique is the development of an instrument for bulk

residual stress analysis at Oxford University, UK [110]. However, most of the electron energy (about 99%) is dissipated (heat) rather than being converted in X-rays.
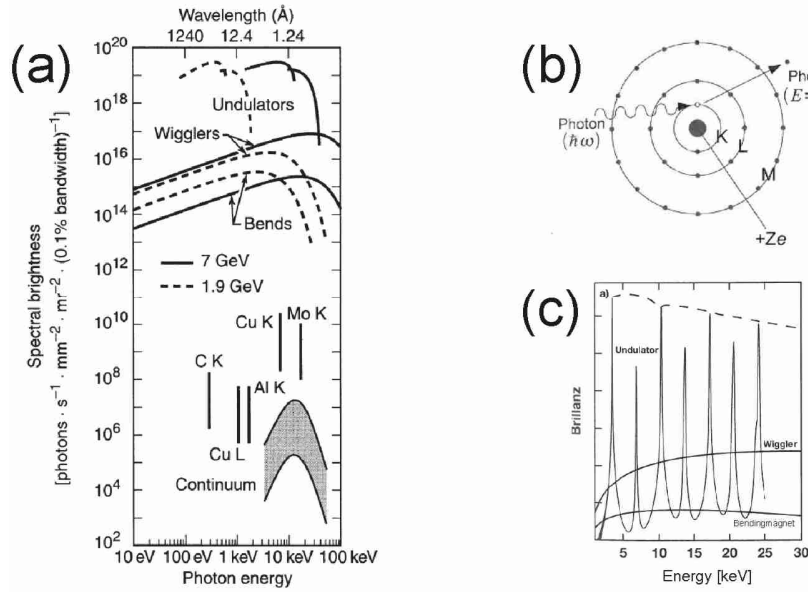

Figure 28: (a) Spectral brightness at the sample position as a function of the photon energy for several synchrotron devices (bending magnet, wiggler and undulator) and for conventional X-ray tubes with the continuous bremsstrahlung and the characteristic line spectrum (here K and L). The data is a rough estimate but indicates the trend for the different electron storage energies in synchrotrons (i.e. 1.9 and 7GeV). Taken from the X-ray data booklet [111]. (b) Schematic of absorption/photo ionisation [112]. (c) Spectral characteristics of several insertion devices [112].

One major advantage of synchrotron radiatione over X-ray tubes, apart form its high collimation, in this regard is the gain in photon flux at the sample position by orders of magnitude. In synchrotrons, schematically shown in Figure 29, electrons are generated, accelerated and finally circulate in bunches within the storage ring with energies of a few GeV. In order to keep the electrons on the orbit, they are bent with magnets. This change in momentum causes an emission of radiation perpendicular to the momentum vector. The same principal actually holds for the generation of the bremsstrahlung where the electron is deflected in the electric field of the atomic nucleus. In synchrotrons, to optimize the gain in radiation, the electron bunches enter so-called insertion devices with a periodic arrangement of magnets. There, the electrons are forced to move in a slalom course and produce a narrow and high intense beam with a certain wavelength spectrum, called white or pink beam. There are two types of insertion devices, a wiggler and an undulator. Their essential difference lies in the characteristics of the magnets, causing an interference of the radiation in the undulators. The emitted spectrum of a wiggler is continuous but moderated for an undulator (Figure 28(c)). Since in this dissertation only a monochromatic X-ray beam is used, it is not further relevant whether the beamline receives its light from a wiggler or an undulator. The energy

spectrum accessible at a beamline then depends on both, the characteristics of the insertion device (e.g. strength of magnetic field) and the energy of the electrons circulating in the storage ring. There are beamlines located at a synchrotron, which, for instance, operate with ultraviolet light (e.g. 10 to 100 eV), whereas others operate with harder X-rays (e.g. > 2 keV). On the other hand, increasing the energy of the electrons that circle in the storage ring and enter the insertion device provides access to a brighter X-ray beam in particular at higher energies. For instance, the high energy beamlines at the Swiss Light Source (SLS) with a 2.4 GeV electron beam and at the European Synchrotron Radiation Facility (ESRF) with a 6 GeV electron beam provide X-rays with a maximum of 40 keV (MS beamline) and 500 keV (ID15A), respectively. The corresponding achievable penetration depth is hence quite different (cf. Figure 27(b)).
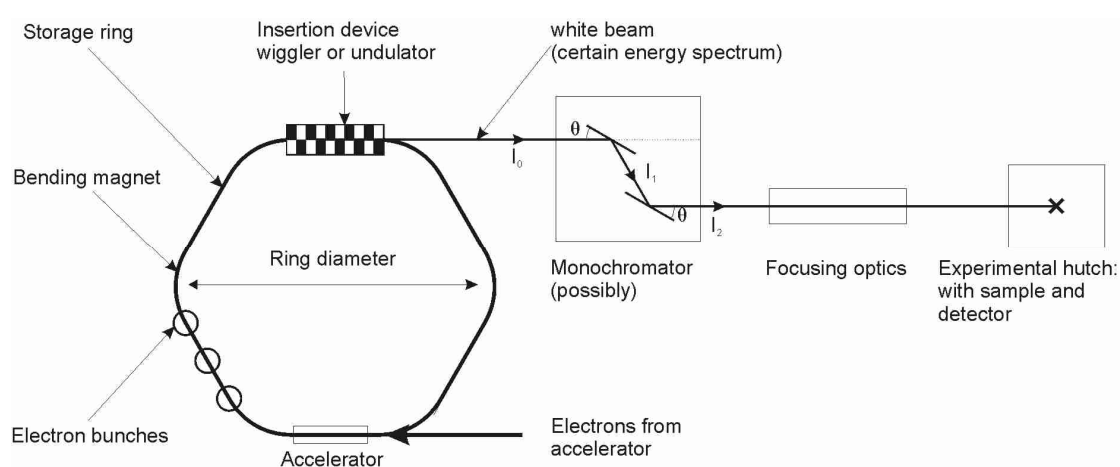
Figure 29 Schematic of a synchrotron providing X-rays towards the experimental hutch for experiments. The ring diameter of the 2.4 GeV SLS is ~92 m, that of the 6 GeV ERSF is ~269 m. Normally, the larger the storage ring, the higher the electron energy that can be stored.

The electron bunches circulate for hours in the storage ring, which is under a high vacuum to minimize collisions with air particles. The loss of electrons may be compensated by continuous injection of "new" electrons (top-up) to keep the electron current essentially constant (top-up, e.g. at SLS). Otherwise, the beam intensity will decrease over time, until new bunches of electrons are inserted (e.g. at ESRF). Further, since the electrons loose energy by, for instance, passing the insertion devices, they are accelerated again at some location within the storage ring.

Depending on the user requirements, the white beam from the insertion device can be used directly in the experimental hutch, or, first needs to be monochromatized. This may for instance be achieved by a double crystal monochromator, which can be oriented to diffract the desired wavelength out of the white beam and towards the experimental hutch. A set of focusing optics then collimates and dimensions the X-ray beam.

2.2.2.4.2 Neutrons

Neutrons for diffraction experiments are essentially produced in two ways, either by a fission or by a spallation process. An example of the former is the research reactor at the Institut Laue-Langevin (ILL) in Grenoble, France [113]. There, Uranium-235 (U^{235}) undergoes fission with the help of a thermal neutron $n_{thermal}$

$$n_{thermal} + U^{235} \rightarrow 2 \text{ fission fragments} + 2.5 n_{fast} + 180 \text{MeV}$$
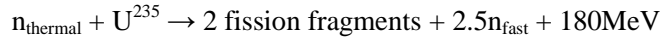
producing a continuous stream of neutrons. In a spallation source a high energetic proton beam (10 to 1000 MeV) is directed onto a heavy metal target (e.g. lead). This is schematically shown in Figure 30(a). The following sequential process comprises excitation of the atom, the emission of hard X-rays (γ-radiation, MeV) and neutrons with a broad energy spectrum (fast and thermal neutrons). Typically, 20 to 30 neutrons are produced per incident proton. Depending on the type of the proton acceleration the neutrons will be produced in bursts or continuously: If the proton beam is pulsed and arrives in bunches at the target, then also bunches of neutrons are generated at a certain frequency. The fact that the neutrons are separated in bunches can then be exploited in ToF diffractometers, described in §2.2.3.3. The energy of the neutrons produced by the spallation process (same as for the neutrons produced by fission processes) is too high for being a useful probe for the scientific purposes. Therefore, the neutrons are "cooled down" in a moderator tank, making a large number of collisions with the atoms of the moderator, which for instance can be heavy water.
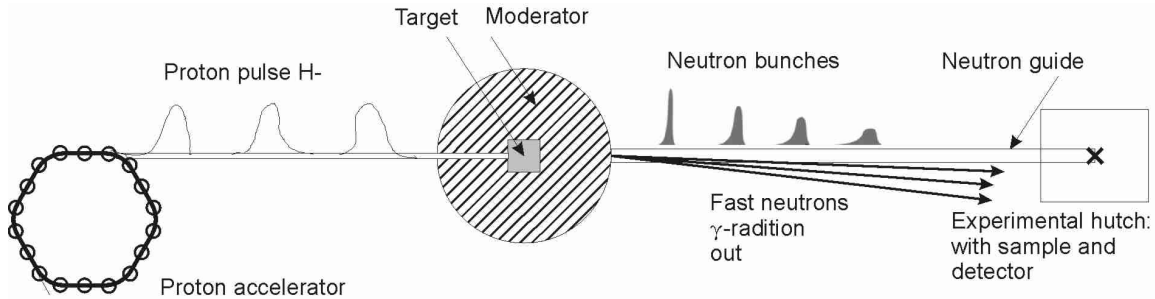
Figure 30 Schematic of a spallation source providing thermal neutrons towards the experimental hutch for experiments.

The neutrons will then have a root-mean-square velocity v appropriate to the temperature T of the moderator

$$\tfrac{1}{2}mv^2 = \tfrac{1}{2}k_B T \qquad\qquad\qquad \text{Eq. 27}$$

before they are allowed to escape towards the experimental hutch. $k_B = 8.61733 \cdot 10^{-5}$ eV/K is the Boltzmann constant. The peak of the energy distribution (for thermal neutrons) is typically around 25 meV in order to provide a high flux of thermal neutron for experiments.
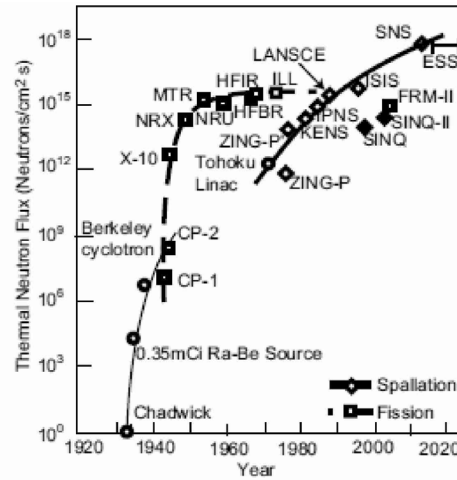
Figure 31 Thermal neutron flux of various neutron sources from both spallation sources and reactors from the discovery of the neutron in 1932 until nowadays, from [114].

The typical flux of thermal neutrons produced in various neutron sources is shown in Figure 31. The thermal neutrons are guided to the experimental hutch. The neutron flux at the sample position (with running chopper) is for instance about $6 \cdot 10^6$ neutrons s^{-1} cm^{-2} at POLDI/SINQ [115] (cf. §2.3.5.3). A long flight path within the neutron guide is then also beneficial to remove fast neutrons and γ-radiation that otherwise might contribute to the background noise of the detector.

2.2.3 Typical beamline and measurement set-up

2.2.3.1 Axial and transverse lattice strain

As introduced in §2.2.1, the response of the lattice strain parallel (*axial*) and perpendicular (*transverse*) to the loading direction can be measured. Figure 32(a) illustrates the diffracted beam paths from lattice planes the normal of whose are parallel and perpendicular to the loading axis. When the sample is loaded, these lattice planes are elongated and compressed, respectively. The axial and transverse lattice strain then evolves with the applied stress as shown in Figure 32(b).
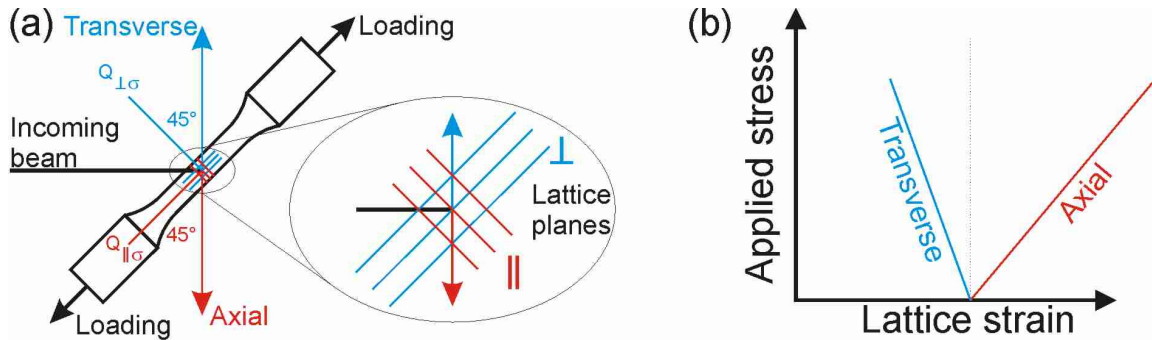
Figure 32: (a) Schematic of the beam diffracted by the lattice planes parallel and perpendicular to the loading axis in order to measure (b) lattice strain in the axial and the transverse direction during tensile testing.

The data from the transverse direction may be difficulat to interpret. This is because members of a transverse grain family may have a range of orientations with respect to the tensile axis. Oliver *et al.* [15] used an EPSC model to evaluate the response of individual grains. In Figure 33 (a) and (b) all grains have a common <110> and <200> transverse direction, respectively, along which the lattice strain is resolved by the model. The individual curves are the response to an axially applied load for different rotation angles θ. For instance, θ_1 varies from 0° when a <200> direction lies axially to 90° when a <110> direction lies axially. The response might vary considerably for different axial orientations. Diffraction only gives an averaged resolve lattice strain. However, when a non-representative quantity of material is investigated, one may observe large variations in the transverse response for different samples.
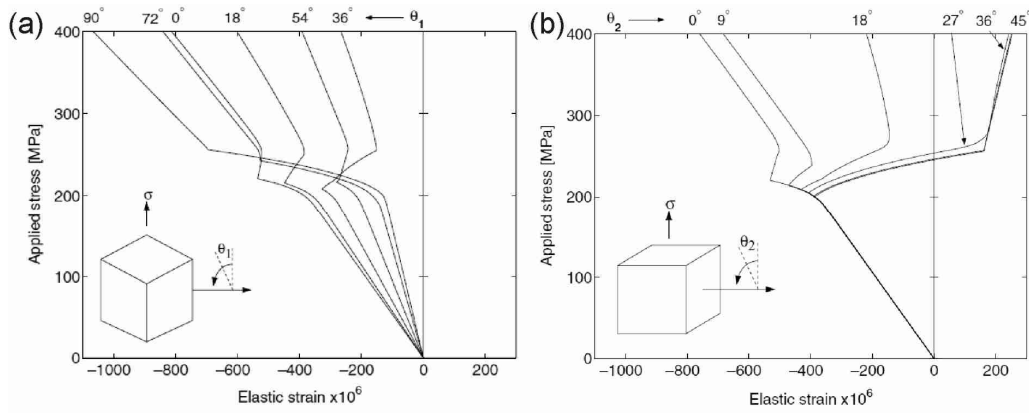
Figure 33 EPSC simulations of transverse lattice strain development with applied stress in ferrite grains of specific orientations: Strain resolved along (a) <110> and (b) <200> transverse directions, for various rotations θ_1 and θ_2, respectively, about these directions. The insets illustrate these rotations. Form Oliver *et al.* [15].

2.2.3.2 X-ray powder diffraction

In §2.2.2.4.1, it was described how a monochromatized and focused beam arrives in the experimental station. Figure 34(a) describes the further procedure. The beam size can be customized by slits. The beam then probes the polycrystalline sample and the diffracted signal gives rise to the diffraction rings (the *Debye-Scherrer* rings) that can be recorded with a 2D detector. The transmitted beam is cut with a beam stop. A shutter can be triggered so that the incident beam is cut between image frames. Knowing the distance a_1 between the diffracted signal and the beam centre and the distance a_2 between sample and detector, the diffraction angle 2θ is determined to:

$$2\theta_{hkl} = \arctan\left(\frac{a_1}{a_2}\right)$$ Eq. 28

The elastic lattice strain is then obtained from the Bragg equation (Eq. 17) by shifts in diffraction angle and the expression reads:

$$\varepsilon_{hkl} = \frac{\sin(\theta^0_{hkl})}{\sin(\theta_{hkl})} - 1$$

Eq. 29

The diffraction rings comprise the scattering vectors $Q_{\perp\sigma}$ and $Q_{//\sigma}$. Note that Q is not exactly parallel or perpendicular to the loading axis, but inclined by the Bragg angle θ (cf. Figure 34(b)). Using a wavelength of 0.138 Å (90 keV), the first five bcc iron reflections are within 4.5°, but this spread increases with larger wavelengths. It therefore must at least be remembered that using radiation with large wavelengths, the scattering vector of the higher angle peaks can be quite off from the loading axis and one may not any more measure the same quantity as if the scattering vector was parallel to the loading axis. The width of the diffraction peak may be expressed as the full width at half **M**aximum (FWHM). The peak width depends on two contributions, the intrinsic peak width (microstructure related: Size and strain broadening) and the instrumental resolution. The latter comprises the beam divergence, wavelength spread $\Delta\lambda$, but also, and which often is predominant, the beam size, sample thickness and pixel size of the detector. If one needs for instance to increase the illuminated gauge volume (represented by the grey rectangle in Figure 34(b) by increasing the sample thickness or the beam size, the FWHM may become larger. The problem that comes along with is illustrated later in §2.2.4.1.
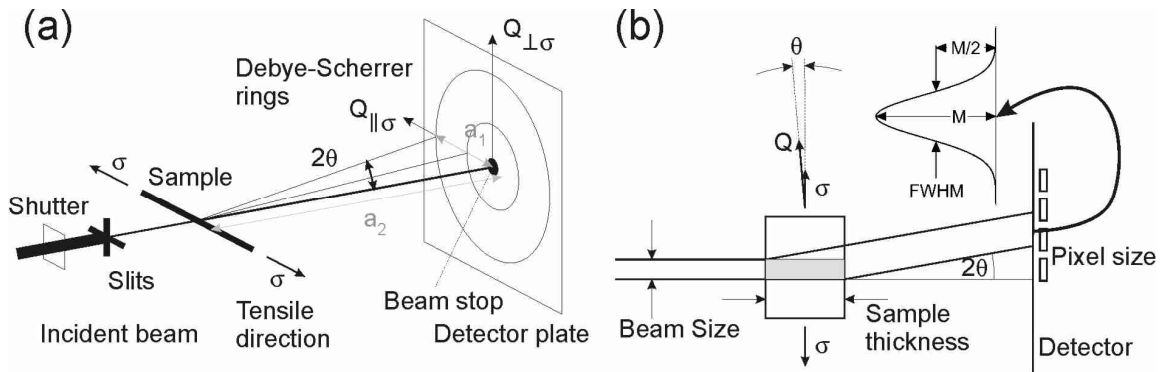
Figure 34 Schematic of a powder diffraction experiment in transmission (Debye-Scherrer) geometry: (a) Overview (b) Detail of the incoming and the diffracted beam path.

2.2.3.3   ToF neutron diffraction

In §2.2.2.4.2, it was described how neutrons are produced and "cooled down" before being allowed to emerge towards the experimental station. Figure 35 describes the further procedure for a traditional ToF strain scanning instrument. The neutrons arrive in separated pulses, i.e. there is no pulse overlap and the fastest neutrons of the successive pulse do not catch up the slowest neutrons of the current pulse before being counted by the detector. These neutrons are then scattered by the sample and arrive at the detector. Using a reference point in the beginning of the flight path (e.g. a neutron sensitive monitor), the travelling time t_{hkl} for the total travelling length $L = L_1 + L_2$ is

known. The wavelength of the neutrons with velocity $v_{hkl} = L \, / \, t_{hkl}$ can then be determined with relation Eq. 25 to:

$$\lambda_{hkl} = h \cdot t_{hkl} \, / (m_n \cdot L)$$ Eq. 30

The interplanar spacing d is then given by

$$d_{hkl} = \lambda_{hkl} \, / (2 \cdot \sin \theta_{hkl}) = h \cdot t_{hkl} \, / (2 \cdot m_n \cdot L \cdot \sin \theta_{hkl})$$ Eq. 31

and the elastic lattice strain can then be obtained from the Bragg equation (Eq. 17) by shifts in the arrival time and the expression reads:

$$\varepsilon_{hkl} = \frac{t_{hkl} - t_{hkl}^0}{t_{hkl}^0}$$ Eq. 32

Deriving Eq. 31, the resolution $\Delta d \, / \, d$ of the diffraction peak can be approximated [11] to:

$$(\Delta d / d)^2 = (\Delta t / t)^2 + [\Delta(L \cdot \sin \theta) / (L \cdot \sin \theta)]^2$$ Eq. 33

The term in the squared brackets will disappear by time focusing. This means that the set-up can be adjusted so that the contributions in the brackets are cancelled out. In other words, a good resolution $\Delta d \, / \, d$ (in FWHM) can be obtained, while large gauge volumes can be investigated simultaneously.
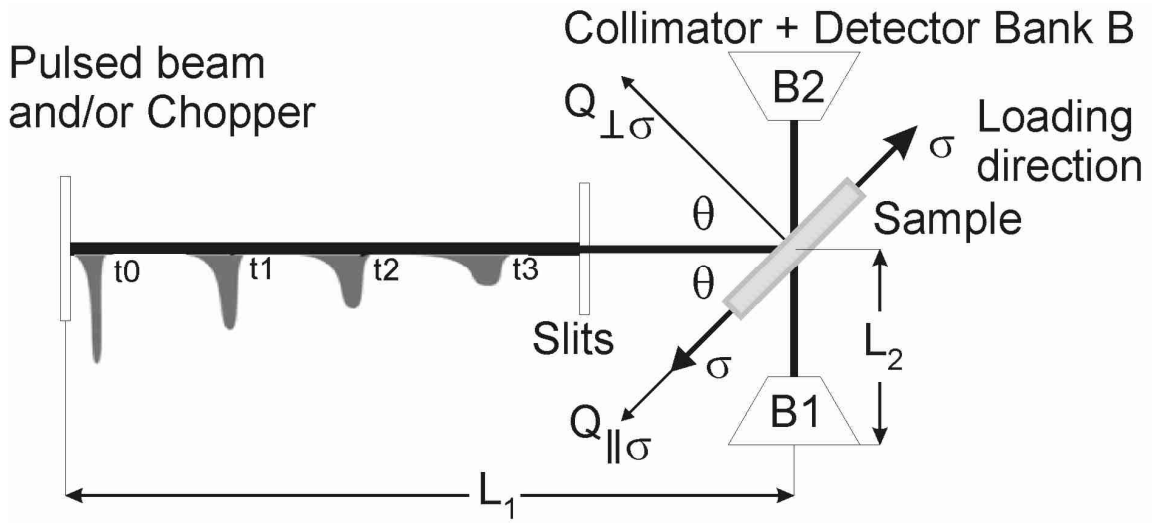
Figure 35 Schematic of a ToF strain scanner, adapted from Bacon [106]. The chopper is open at time t_0 and the shaded area indicates the spatial distribution of the neutrons at successive later times. Neutrons of successively smaller velocities, shown in the heavy shading, will be detected at succeeding moments t1, t2, etc. The acceptance angle of the diffracted neutrons can be quite large and radial collimators are therefore used. The slit size and the size of the collimators define the gauge volume.

The wavelength for thermal neutrons is such that the diffraction of the common lattice planes of typical engineering materials occurs under angles near $\theta = 45°$. The detector bank typically has a larger acceptance angle. Radial collimators made of thin and neutron absorbing blades are used to collimate the diffracted beam and ensure that all detector elements look exactly at the same volume

of the sample [116]. Many instruments are equipped with two detector banks at angles of ±90° to the incident beam. It is therefore possible to capture the axial ($Q_{//\sigma}$) and the transverse ($Q_{\perp\sigma}$) direction simultaneously.

Typically, the pulsed neutron beam arrives directly from the moderator through the neutron guide and there is no pulse overlap. The particular situation for the two instruments that have been used in this study is now briefly mentioned:

At ENGIN-X (§2.3.5.4), the flight path has now been extended (machine upgrade of ENGIN [117]) to 50 m to increase the resolution. Because of the extended flight path, one now would have a pulse-overlap when using the full flux of the spallation process with a frequency of 50 Hz. Therefore, two choppers at the beginning of the flight path have been installed to modify the pulses: Three different frequencies can be selected: (i) 50 Hz with a reduced d range of 1.1 Å (ii) 25 Hz (one pulse out of two) with a d-range of 2.2 Å and (iii) 16.67 Hz (one pulse out of three). These ranges can be shifted in time to cover various intervals, such as 2.3 to 1.2 Å at 50 Hz, which correspond to the (111) to (311) reflections for aluminium.

At POLDI (§2.3.5.3): Since the spallation source SINQ provides an almost continuous beam, the conventional concept of ToF diffractometer (no-pulse overlap) would drastically limit the neutron flux at the sample position by "cutting out" pulses. Therefore, POLDI operates with the concept of a pulse-overlap, which is, however, not further important for the strain measurements for the experiments reported in this dissertation. This concept is described by Stuhr [118].

2.2.4 Concluding remarks

2.2.4.1 Sampling statistics

Good sampling statistics, i.e. probing a representative volume to obtain the material's bulk average behaviour, is essential. Otherwise, the information of the measured data will vary from sample to sample. For an inhomogeneous microstructure this may require a large illuminated volume. Figure 36(a) shows two {110} diffraction peaks acquired at the MS beamline (cf. §2.3.5.1). The peak with the dot-dashed line shows a typical peak profile. When the beam size was increased to obtain a larger illuminated volume, the instrumental contribution (here: beam size, sample geometry) affects severely the peak shape. There lies one difference between the methods: With powder X-ray diffraction, the resolution decreases with increasing the illuminated gauge volume by increasing the beam size and the sample thickness (cf. Figure 34(b)). On the other hand, ToF neutron diffraction allows using large illuminated gauge volumes and provides a good resolution simultaneously. Second, the broad wavelength distribution in ToF neutron diffraction is a second advantage over powder X-ray diffraction to increase the sampling statistics. Figure 36(b) shows three grains that

have a similar orientation with respect to the incoming beam direction. Using a monochromatic radiation λ, only one grain may be oriented such that the Bragg equation is satisfied. Using a beam with a range of wavelengths $\lambda_{1,2,3}$, a larger number of grains will diffract within a given volume.

To improve the sampling statistics for the inhomogeneous microstructure (cf. Figure 20(a)) with a large ferrite grain size (cf. Figure 20(b)), ToF neutron diffraction is envisaged in this dissertation.
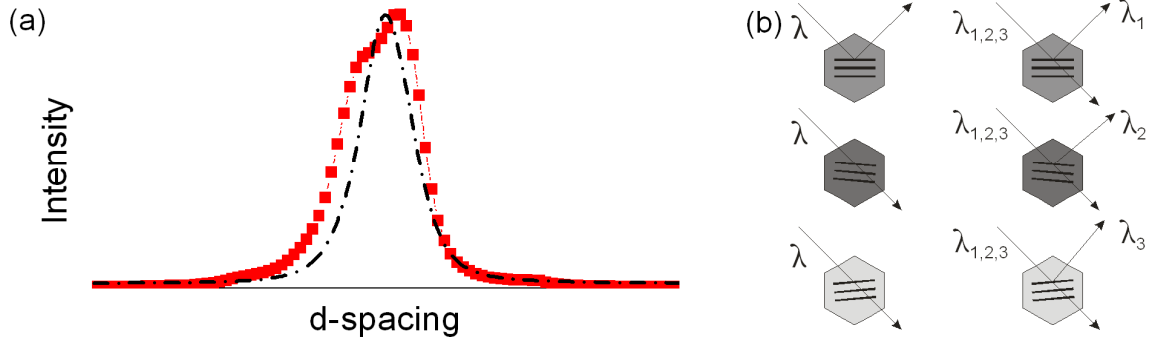
Figure 36: (a) {110} diffraction peak acquired at the MS Beamline. When the beam size is increased to obtain a large illuminated gauge volume, the peak shape gets severely affected by the instrumental contribution (red curve with datapoints). (b) More subsets of grains in a given volume will diffract when the incident beam has a certain wavelength distribution $\lambda_{1,2,3}$.

2.2.4.2 Counting statistics

Good counting statistics are essential to describe the diffraction peak shape and minimize the error in elastic lattice strain determination. An example is shown in Figure 37. Diffraction patterns have been acquired with synchrotron radiation at the MS beamline on the 1%CrMoV steel with acquisition times of 10s and 600s.

Figure 37 Part of the diffraction pattern of a 1%CrMoV steel, acquired at the MS beamline with (a) 10 seconds acquisition time and (b) 600 seconds acquisition time. The inset shows peaks from a low volume fraction second phase.

Assuming a Poisson distribution for the number of photons diffracted and counted by the detector, the standard deviation is then given by the square root of the number of counts [119]. Note that this is only approximately valid when applying a flat field correction. For the diffraction peaks in the inset of Figure 37, the standard deviation amounts to about $\sqrt{80} \cong 9$ and $\sqrt{4000} \cong 63$ and the relative uncertainty to $9/80 \cong 11\%$ and $63/4000 \cong 2\%$. Therefore, with higher counting statistics, the background smoothens and low intense peaks can be distinguished from the background.

Synchrotrons provide much more flux at the sample position than neutrons sources. On some neutron scattering instruments, a combination of high flux and large detection areas allows following the behaviour of the matrix phase with a reasonable uncertainty during short acquistion times (ca. 3min), for instance at ENGIN-X during high temperature tensile loading of stainless steel [95]. The need for synchrotron X-rays is given by the low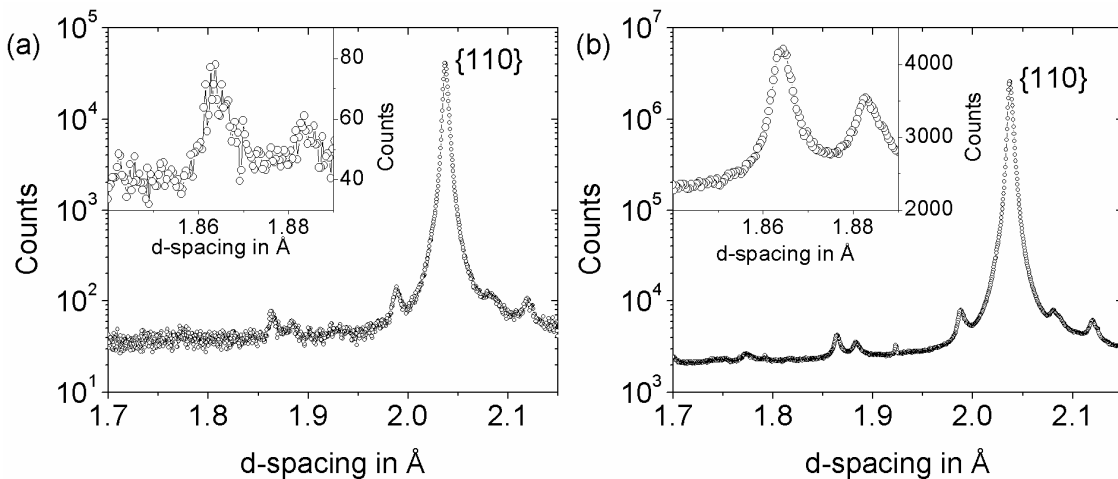 volume fraction second phases with a typical ratio in intensities of 10^2 to 10^3 between the average matrix and second phase diffraction peaks for the 1%CrMoV steel (Figure 37). That is why X-ray diffraction at synchrotron sources is envisaged in this dissertation. The diffraction pattern of a 1%CrMoV steel from the various instruments used in this thesis and for typical acquisition times are compared in §2.3.5.5.

2.3   Experimental tools

2.3.1   Microscopy

Light microscopy:

The samples prepared for light microscopy have been ground with silicon carbide (SiC) paper (Buehler P1200 and P4000), followed by polishing with a vibrating polisher (Buehler Virbromet2®) using an alumina 0.05 µm solution (MasterPrep®) and immediate cleaning with water and acetone in an ultrasonic bath. Etching was performed with 2% nital (98 ml ethanol and 2 ml nitric (68% conc.)) and picral (100 ml ethanol, 4 g picric acid). Picral is used to bring up the carbides only, whereas nital also etches the ferrite grain boundaries. There is, however, a diversity of options for phase selective etching [120, 121]. Microscopy of the etched surface was conducted on optical microscopes using bright and dark field mode with magnification factors up to 100.

Electron microscopy:

SEM:

A Zeiss Supra 55VP **f**ield **e**mission **s**canning **e**lectron **m**icroscope (FE-SEM) was used for high-resolution microscopy using the conventional (*Everhart-Thornley* and *InLense*) and the EsB (energy and angle selective backscattered) detectors, the latter for a better material contrast (ferrite-carbides).

EBSD and EDX:

Electron **b**ack**s**cattered **d**iffraction (EBSD) and **e**nergy **d**ispersive **X-ray** spectroscopy (EDX) were conducted on a Zeiss Ultra 55 by the principal machine operators M. Ramesh and H. Leber. For EBSD, the sample surface has been prepared in the final step with the vibrating polisher (cf. *§2.3.1 Light microscopy*). This gives a uniformly flat surface, which means that there is no contrast in the dark field mode with field light microscopy. Electrolytical polishing on the other hand often created a carbide topography due to a preferred dissolution of the ferrite matrix and was therefore not used as a final preparation step for EBSD. The parameters for EBSD were: Acceleration voltage of 20 kV, working distance of 12 mm, tilt angle of 70° and step size of 0.25 µm.

TEM:

A JEOL2010 was used for **t**ransmission **e**lectron **m**icroscopy (TEM). To reduce the electron beam deflection, a 1 mm disc of the ferromagnetic 1%CrMoV samples were punched out and inserted in a 1mm hole within a 3 mm disc of a 301 stainless steel (paramagnetic) A 3 mm disc diameter is required for the sample holder. The assembly was then glued with epoxy, ground (Buehler P4000 SiC paper) and finally electrolytically polished in a Struers Tenupol-5 twin-jet machine in a solution of 10% perchloric acid (70% conc.) and 90% ethanol at -20°C.

2.3.2 Heat treatments

Furnace:

Heat treatments were performed in a Nabertherm N-210/H (T_{max} = 1340°C), a Borel CUBE400/2-1050 (T_{max} = 1050°C) with an argon inert gas atmosphere and a Borel chamber furnace (T_{max} = 1050°C). The first two furnaces are located at PSI, the latter is located at the Laboratory of Mechanical Metallurgy at EPFL and was used to heat up the samples prior to the salt bath quench. The temperature was monitored with a NiCr-Ni (type K) thermocouple that was inserted in a tight hole within a steel dummy sample. This dummy sample was then placed next to the actual samples.

Quenching:

Quenching was performed in oil at ambient temperatures or in a salt bath, being a mixture of sodium and potassium nitrate ($NaNO_3/KNO_3$), at temperatures in between 300 and 550°C. The salt bath quenching has been performed in the Laboratory of Mechanical Metallurgy at EPFL with instruction from E. Klay. The salt bath temperature was monitored with a NiCr-Ni (type K) thermocouple.

2.3.3 Mechanical testing

Tensile and creep testing:

The samples for the ex situ measurements (cf. Table 5) were deformed in a standardized test machine at EMPA by Th. Mayer (RT tensile and creep samples in 2007 as part of his bachelor thesis) and an EMPA technician (HT tensile samples in 2010).

Further mechanical (offline) testing was conducted on the machines that are also used for in situ measurements (loading rigs at MS §2.3.5.1, ID15B §2.3.5.2, POLDI §2.3.5.3).

Hardness measurements:

A Leitz microhardness device (loads from 0.0981 to 4.9 N using a Vickers indenter) was used for both, local hardness measurements and marking of areas for microscopy.

2.3.4 Laboratory X-ray diffraction

A Bruker D8 Advance machine with a Cu anode was used for a pre-characterization of some materials. The measurements were made by the principal operator E. Pomjakushina.

2.3.5 Experimental set-up at beamlines and data treatment

The diffraction experiments presented in this dissertation were performed at four different beamlines: Neutron diffraction at POLDI and ENGIN-X and synchrotron X-ray diffraction at MS and ID15B. In this section, first the experimental set-ups with the sample geometry and data treatment are briefly described, followed by a qualitative comparison of the diffraction patterns from these four instruments, a chronology of the various beamtimes and a sample nomenclature for the various tests performed.

2.3.5.1   Materials Science (MS) beamline: synchrotron X-ray diffraction

The MS beamline [122] at the Swiss Light Source (SLS) is located at the Paul Scherrer Institute (PSI), Switzerland. It is a dedicated powder diffraction beamline using monochromatic energies in between 5 and 40 keV. The photon flux, however, exhibits a maximum around 12 keV and then falls significantly with increasing energy and around two orders of magnitude until 40 keV. Figure **38**(a) shows the beamline at the sample position and with the **m**iniaturized **t**ensile **m**achine (MTM) mounted on the goniometer. The MTM has been constructed within the group **M**aterials **S**cience and **S**imulation (MSS, [123]) and frequently used at the beamline for more than 10 years [124]. When the MTM is removed, the standard powder diffraction apparatus can be mounted on the goniometer [125]. Two detectors can be used to record the diffracted signal. The first detector is a one-dimensional (1D) solid-state silicon microstrip detector (called MYTHEN, [126]), which

covers an angular range of 120°. The entire spectrum can be read out in a few milliseconds and the detector exhibits a high dynamic range of 24 bit (2^{24}). The detector is therefore well suited for time-resolved measurements and for acquisition of diffraction patterns, where the difference in intensities between individual peaks is large. Hence, good counting statistics can be obtained for low intensity peaks while there is no saturation (until about 16 million counts) for high intensity peaks. The intrinsic angular resolution of the detector is 0.0037°, the actual resolution then depends on the sample size [124]. The second detector is a fivefold Si(111) crystal-analyzer detector for high-resolution measurements. Obtaining a full diffraction pattern, however, requires scanning along 2θ, and hence poses a drawback for in situ deformation studies because of the large acquisition time. All data reported in this dissertation has been acquired with the MYTHEN detector. In 2011, the beamline was upgraded. The main user relevant modifications are a replacement of the wiggler device by an undulator and a modification of the MYTHEN detector. The latter now provides two stacked microstrip layers, avoiding gaps in the diffraction pattern between the individual detector modules, as described in [127]. This upgrade has no implication on the diffraction data presented in this dissertation, but is mentioned for readers who follow the continuing MSS group activities on this beamline.
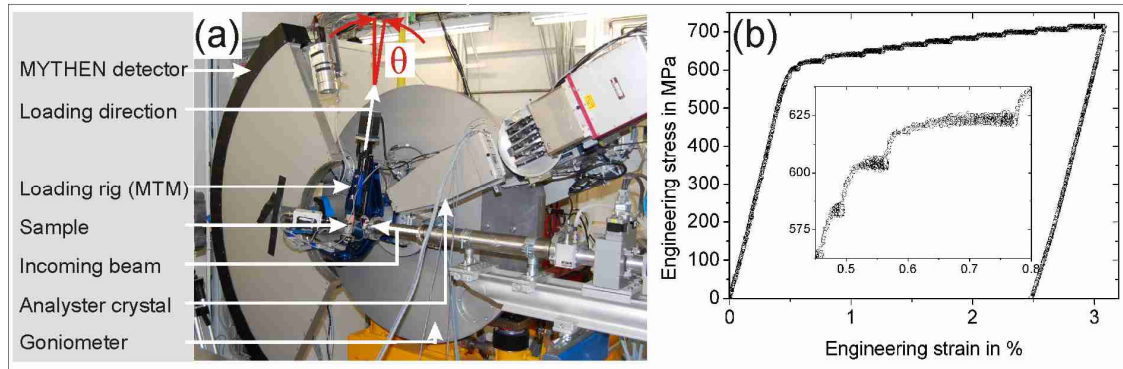
Figure 38: (a) Set-up at Materials Science beamline with the miniaturized tensile machine mounted on the goniometer for in situ loading experiments (only at RT). (b) Loading curve recorded during in situ tensile deformation. During the measurement, the load was kept constant in both the elastic and plastic regime. X-ray data acquisition for about 5min was started after the load level (±2MPa) has been reached. The inset shows the stress-strain curve in more detail around the elasto-plastic transition.

Two kinds of measurements have been performed at the MS beamline:

(i) In situ tensile testing at RT with an energy of 25 keV, being a trade-off between penetration depth and photon flux. The beam size matched the uniform gauge section of the tensile sample. For details on the execution of the in situ tensile experiments on this beamline using the MTM, the reader is referred to the theses of Brandstetter [127] and Budrovic [128]. In brief, the MTM can be mounted both vertically (cf. Figure 38(a)) and horizontally (not shown) on the goniometer. This allows measuring the scattering vector parallel (in transmission) and perpendicular (usually in

reflection) to the loading axis, respectively. The MTM, however, is not strictly vertical but inclined on purpose (ascribed in §2.2.3.2) by an angle θ through a rotation of the goniometer. For the 25 keV beam energy, θ is about 8° and the loading direction then lies in between the scattering vectors of the {110} and {200} ferrite reflections. The typical loading scheme during in situ tensile deformation is shown in Figure 38(b). In order to obtain sufficient counting statistics for the diffraction peaks of the second phase particles, the sample is not loaded continuously during X-ray acquisition. Rather, the samples are stepwise loaded to defined stress levels. At each stress level, the stress is then kept constant for 5 min while the diffraction pattern is acquired. In the plastic regime, this causes a so-called *cold creep*, as highlighted in the figure inset. The sample geometry is shown in Figure 39. The samples were cut by EDM and then mechanically ground with silicon carbide paper (Buehler P1200 and P4000) followed by electrolytic polishing in a solution of 30% perchloric acid (70% conc.) and 70% ethanol at -20° to remove any damaged layer caused by the spark erosion process. Due to the limited penetration depth (attenuation length of a few tens of μm, cf. Figure 27), the samples for transmission were thinned down to about 150 μm by grinding with SiC paper, followed by electrolytic polishing.

(ii) Diffraction on the extracted carbide powder at RT with a beam energy of 17 keV. The carbide powder is loaded in a capillary available from the beamline sample environment. A glass capillary (Hilgenberg 0140) with 0.3 mm diameter is used and aligned in a Huber goniometer head and mounted on the powder diffraction set-up on the goniometer, so that the capillary is spinning around its axis normal to the diffracting planes with 10 Hz (for particle randomization) during the acquisition of the diffraction pattern.
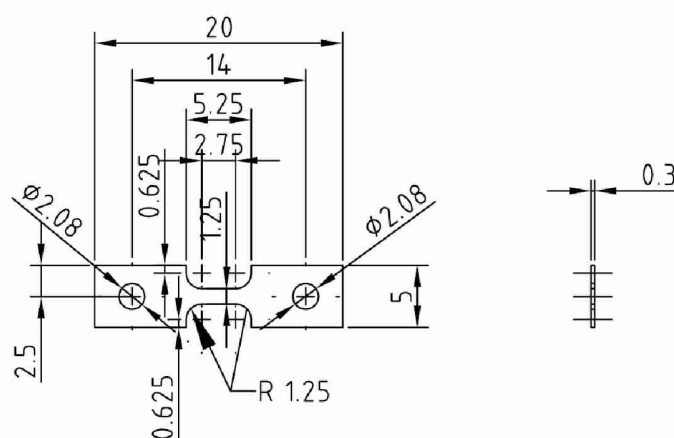

Figure 39 Sample geometry of the tensile specimen used with the miniaturized tensile machine at the Materials Science beamline. Units are given in mm.

Data treatment: Single peak fitting was done using an asymmetric Pearson VII function:

$$P(\theta \leq \theta_0) = h\left[1 + \left(\frac{(1 + 10^{\alpha})(\theta - \theta_0)\sqrt{2^{1/M_L} - 1}}{w}\right)\right]^{-M_L}$$

$$P(\theta \geq \theta_0) = h\left[1 + \left(\frac{(1 + 10^{\alpha})(\theta - \theta_0)\sqrt{2^{1/M_R} - 1}}{w}\right)\right]^{-M_R}$$

Eq. 34

where θ is the diffraction angle, θ_0 is the angle at maximum intensity, h is the peak height, w the full width at half maximum (FWHM), α the asymmetric parameter and the Pearson M give the left (M_L) and the right (M_R) decay exponents. As the M approaches 1, it resembles a Lorentzian in character and as it approaches infinity, it becomes Gaussian. The fitting routine was written by P. Derlet as a Fortran routine and is described in more detail in [124].

Full pattern Rietveld refinement was done using the GSAS software package [129] to identify the various phases in the carbide powder. The wavelength and the instrumental resolution were obtained by refining diffraction patterns of a certified silicon powder (Si NIST 640C, [130]) and a fluoride $Na_2Ca_3Al_2F_{14}$ (NAC, [131]).

2.3.5.2   ID15B beamline: synchrotron X-ray diffraction

The ID15 beamlines [132] at the **E**uropean **S**ynchrotron **R**adiation **F**acility (ESRF) are located in Grenoble, France. ID15 hosts two experimental stations, ID15A and ID15B, which operate simultaneously. The main station, ID15A, can receive a monochromatic or a white beam within a useful energy range in between 30 to 500 keV. Both, angular and energy dispersive measurements of the elastic lattice strains are hence possible. The latter method has not been exploited in this dissertation. The side-station, ID15B, can only receive monochromatic radiation of about 30, 60 or 90 keV. The experiments presented in this dissertation were made at ID15B at 90 keV (actual 87.7 keV). The set-up with the loading rig is shown in Figure 40(a).
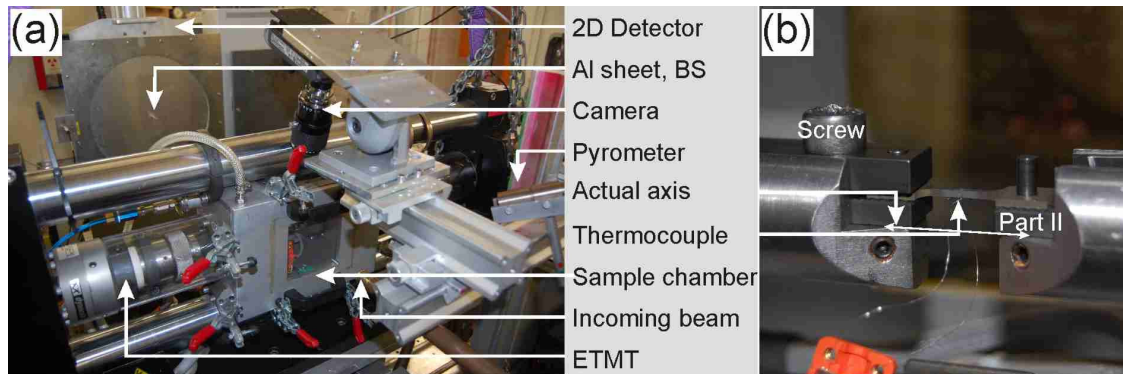

Figure 40 In situ mechanical testing set-up with the ETMT load rig at ID15B: (a) Overview picture. The direct beam path is indicated as black arrow towards the beamstop (BS). (b) Sample chamber with grips, tensile sample and thermocouple.

The loading rig is mounted in between the tube with the incoming X-ray beam and the two dimensional (2D) detector. The detector is located behind an aluminium sheet, which serves as a filter for low-energy fluorescence X-rays and as support for the beamstop. The detector translation along the beam axis is motorized; the sample to detector distance is limited to about 1.1 m by the table on which both the detector and the loading rig are mounted. A *National Instruments 1764 Smart Camera* and a pyrometer are installed around the loading rig. The camera focuses on the sample gauge length through a window in the sample chamber and the pyrometer is looking at the sample position where the thermocouple is attached.

Loading rig: An Instron **e**lectro-**t**hermo **m**echanical **t**esting (ETMT) device is used for the experiment, available from the beamline sample environment. The machine can apply forces up to 3 kN in tension and compression and uses high electric currents to induce heating rates in electrically conductive samples with a power limitation of the heater output of 400A/8V. Grips are water-cooled.

Sample mounting: A Pt/PtRh (type R) thermocouple is first spot welded on the sample bottom (where it is not sampled by the X-ray beam) and in the centre of the gauge section. The thermocouple provides the feedback for the ETMT electric current steering. The quality of the spot welding may affect measured temperature value and the temperature is therefore checked with the pyrometer. The sample is loaded in the sample chamber as shown in Figure 40(b). Sample and grips have been designed for this experiment: The geometry is shown in Figure 41. The pin-hole system, adapted from the MTM used at the MS beamline (§2.3.5.1, [124]), avoids sample slipping in the grips during loading. With the counter part for the pin (Part II, Figure 40(b)), the sample is now slightly off-axis in height. The machine, however, is considered as stiff and bending forces on the sample have not been observed. The sample is then first loaded to 100 N (about 40 MPa) at RT, the screws are then tightened while the machine is in load control and the sample is then unloaded again. Next, the sample is positioned in the beam just above the position of the thermocouple. This can easily be achieved by scanning the sample with respect to the beam while recording the transmitted intensity with a photo diode located in the beamstop. The sample positioning is crucial since there is a temperature gradient along the sample gauge length as indicated in Figure 42 and measured by the pyrometer. The hottest region is indeed in the centre of the gauge length, where also the thermocouple is mounted, and that is why the deformation is localized there. The beam (size of 300 μm x 300 μm) hence probes well this hottest region.

If no current is applied, the sample chamber can be left open during the experiment. Otherwise, the sample chamber has to be closed and can then also be flooded with inert gas to minimize oxidation of the sample surface.
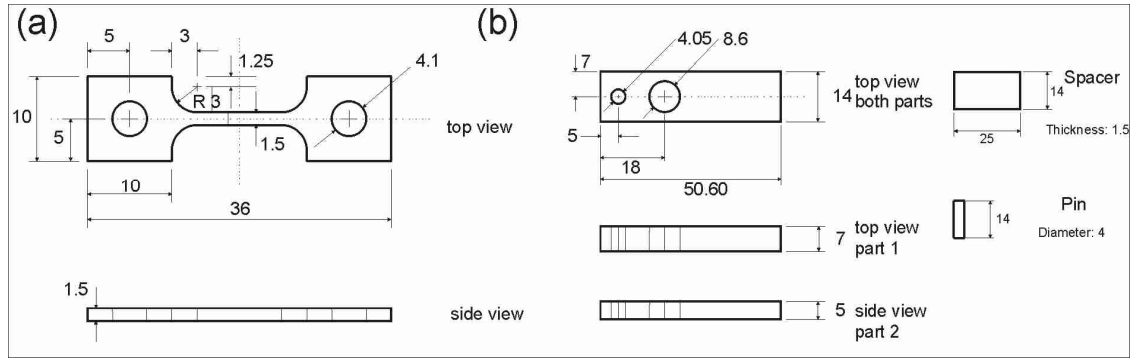
Figure 41 Sample geometry of the tensile specimen used with the ETMT loading rig at the ID15B beamline. The grips are made of hardened steel. Units are given in mm.

Strain measurement (correction): Strain measurement with this set-up is not straightforward: At RT, a clip-on extensometer could in principal be used if there would be enough space within the sample chamber. This has not been tested since it also would not help at high temperature where the deformation is localized due to the temperature gradient in the sample (Figure 42). The idea was therefore to take images of the gauge length during loading and determine the strain by image correlation with a Matlab routine [133]. The accuracy, however, was very poor and limited by the marker/contrast morphology. The strain was therefore finally determined from the changes in the loading rig motor encoder position, in the following called *displacement*. This displacement comprises the sample elongation but also the machine compliance and a certain contribution from a sample alignment during loading. The latter causes sample-to-sample variation in the displacement value for a given applied stress and a general correction of the machine compliance, as for instance suggested by [134], was therefore not successful. An approximate conversion of the displacement data to strain is listed in the following:

At RT: A sample gauge length of 10 mm is considered, i.e. the parallel part of the sample gauge section (cf. Figure 41). A linear compliance correction was then applied. The correction *constant* (in: *displacement – (constant x force)*) is obtained by fitting the stress-strain curve in the early elastic regime (0 to 200 MPa) and this slope was forced to a value of 210 GPa, which is the Young's modulus of this steel at RT.

At HT: The displacement correction is done by a slightly modified approach: *displacement – (c_1 x force^c_2)*. This corrected displacement is then divided by a modified gauge length of 2 mm, since the plastic deformation seems to be restricted within this range (cf. Figure 42). Using this modified gauge length provides a good correlation of residual lattice strain vs. plastic strain with the data obtained from ENGIN-X (cf. Figure 82). To account for the elastic contribution of the remaining 8 mm gauge length, the values of c_1 and c_2 have been adapted such that the stress-strain curve matches the standard one. In fact, c_1 was considered to be the machine compliance obtained at RT. Moreover, the applied stress (when expressed in true stress) was corrected: Measuring the

smallest cross-section after the test indicates that the true stress, i.e. the load divided by the actual sample cross-section, is rather constant.
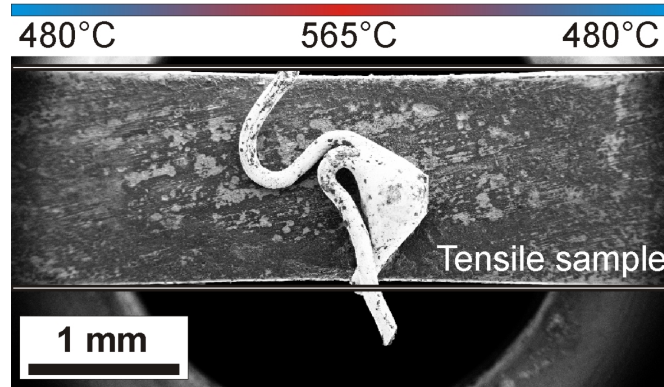
Figure 42 Part of the gauge length of a sample tensile deformed at 565°C (SEM image). Due to the temperature gradients along the sample gauge length, the deformation is localized around the hottest region (centre of gauge length) where also the thermocouple was spot-welded.

Detector: A Pixium area detector [135] was used in the experiment. The detector has a pixel array of 1910 × 2480 pixels with a pixel size of 154 μm × 154 μm, a dynamic range of 14 bit (2^{14}=16384) and negligible small read-out time.

Data treatment: To calibrate the wavelength, the sample-to-detector distance and the detector parameters (beam centre, detector tilt), a capillary of ceria powder was placed on top of the tensile sample. Diffraction patterns of the ceria were acquired at several detector distances relative to the sample position. This data was then processed by the FIT2D program [136, 137]. With those calibrated parameters, the 2D diffraction pattern (**Figure 43**(a)) of the steel sample can be reduced to a 1D pattern (**Figure 43**(b)). Finally, two 1D patterns have been obtained, one for the axial ($Q_{||\sigma}$) and one for the transverse ($Q_{\perp\sigma}$) direction. For each 1D pattern, the data has been integrated over an azimuthal range of twice·Δη = 30° (=±15°) using a FIT2D python script for batch processing [138].

Figure 43 Data reduction from (a) a 2D to (b) a 1D diffraction pattern. The line in (b) is just connecting the data points. Angles up to 3° are not relevant.

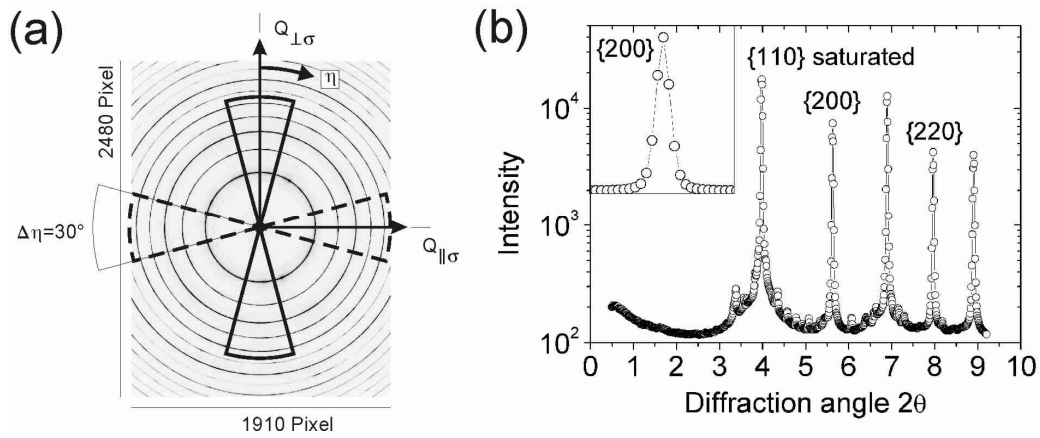The azimuthal integration range of $\Delta\eta = 30°$ is equivalent to the range sampled with the ToF neutron diffractometers POLDI (§2.3.5.3) and ENGIN-X (§2.3.5.4). At the MS-Beamline (§3.3) with the 1D detector, one averages over about ±1°. With the 2D detector one can test the influence of different azimuthal integration ranges on the evolution of the lattice strain. This was done for ±1°, ±7.5° and ±15°. Figure 44 shows the results for the axial direction of the as-received 1%CrMoV steel with the {220}, {200} and {310} ferrite grain families: (a) shows the results from ±1° and (b) shows the results from ±7.5°. The data for ±15° is shown as black lines in both figures for a direct comparison. The major difference is seen in the plastic regime, i.e. above the 0.02%: The {310} compares relatively well for ±1°, ±7.5° and ±15°; the {220} compares relatively well for ±7.5° and ±15°; the {200} is quite different for all three intergration ranges. This can also be seen in the elastic regime: The slope of the {200} is the stiffest for ±1° and most compliant for ±7.5°; the slope for ±15° lies in between. The {200}, which shows no agreement for the three different integration ranges, is also known to be the grain family that is most affected by intergranular strains. This points towards the conclusion that the origin for this different behaviour is that a non-representative number of grains are sampled. This has to be taken into account for the interpretation of the results (cf. also §3.3.1).
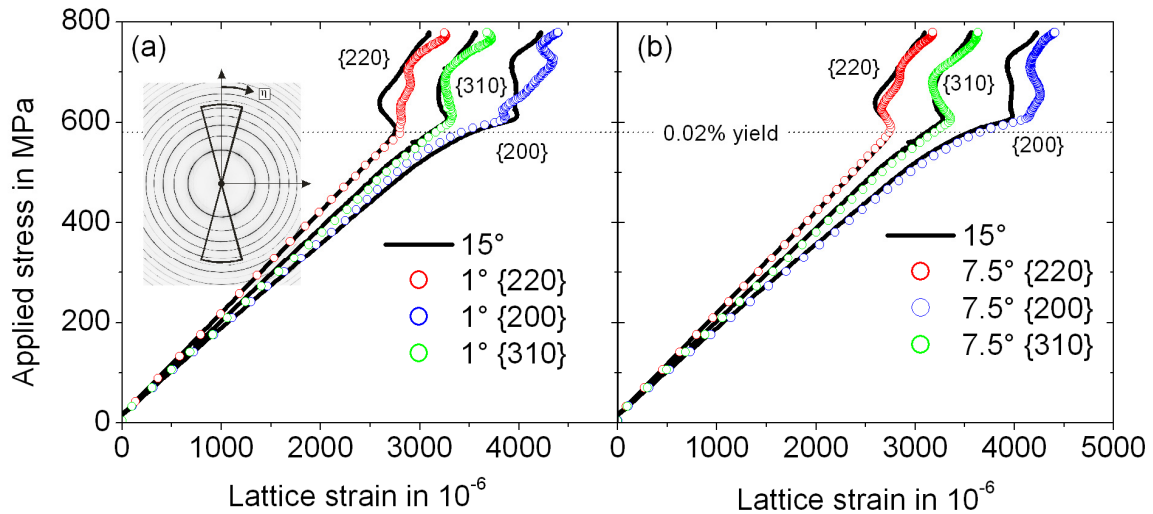
Figure 44 Influence of the azimuthally integration range by the data reduction of the 2D pattern, see inset in (a), on the evolution of ferrite lattice strain in the axial direction. The black lines in both plots correspond to a range of ±15° and are taken as reference; (a) With an integration range of ±1° and (b) with and integration range of ±7.5°. The disagreement between the datasets is even worse in the transverse direction. Sample *ID0* was tensile deformed at RT.

The minimum acquisition time of the detector is 0.4s and several patterns have been summed to obtain good counting statistics for the cementite and saved in one file (size of one file about 20 MB, one tensile test requires several GB) in order to save disk space. Typically, four patterns for an on-load state and 40 patterns in the unloaded state have been summed. With the low dynamic range of

14 bit, care must be taken that the high intense peaks do not saturated, i.e. exceed 2^{14} counts. In fact, this happened for the {110} ferrite peak, which is therefore omitted in the analysis. The {220} is used instead. However, the {110} and the {200} will diffraction under different Bragg angles. Here, the wavelength is considerably low so that the peaks are all at very low angle and within 2° in θ. Therefore, the {110} and the {220} are indeed assumed to show the same behaviour.

Only single peak fitting was performed. For the single peak fitting, the asymmetric Pearson VII function (Eq. 34) has been implemented in a Matlab fitting routine with the help of S. Van Petegem since the standard MSS group peak fitting routine (cf. §2.3.5.1) could not handle peaks described with that few data points.

Uncertainty on peak position: The pixel size is rather large for this small sample-to-detector distance, which cannot be significantly extended. The peak shape is therefore described by only a few data points (cf. Figure 43(b) inset). The error obtained from the fitting routine, where several parameters are free to vary, is much larger than the scatter on the data points of several successive measurements. Important is rather the excellent counting statistics (uncertainty on a measurement point is $1/\sqrt{Intensity}$, cf. §2.2.4.2), obtained by the integration over a large azimuthal range.

2.3.5.3   POLDI beamline: neutron diffraction

Pulse-**O**ver**L**ap **DI**ffractometer (POLDI) [139] is a ToF diffractometer at the Swiss Spallation Neutron Source (SINQ) located at PSI. Figure 45(a) shows the set-up of the beamline at the sample position and with the loading rig mounted on the sample table. POLDI is equipped with one detector bank that is positioned at 90° with respect to the incident neutron beam. Two different samples therefore have to be deformed in order to obtain data from the axial and transverse direction. The angular acceptance angle is horizontally ±15° and vertically about ±3°. A 25 kN loading rig for RT deformation studies in tension and compression is available. For measurements along the axial direction the machine is mounted in horizontal position (see also Figure 45(a)). For the transverse direction the machine is usually positioned vertically, in order to optimize the illuminated gauge volume (as the beam is elongated along the vertical direction).

At the time when the experiments were performed, only a flat sample geometry ("dogbone", Figure 46) could be tested with a 10 kN load cell. The strain measured was performed using two pairs of resistance strain gauges and attached to the sample as shown in the inset of Figure 45(a). Strain gauging was done at EMPA by F. Bürki. In the meantime, the loading rig equipment has been upgraded, comprising grips for threaded specimens, clip-on axial extensometers, video extensometer and a 25 kN load cell. A loading rig with furnace for measurements at elevated temperatures and a second detector bank are in commission. Performing the experiment and data analysis is now straightforward.
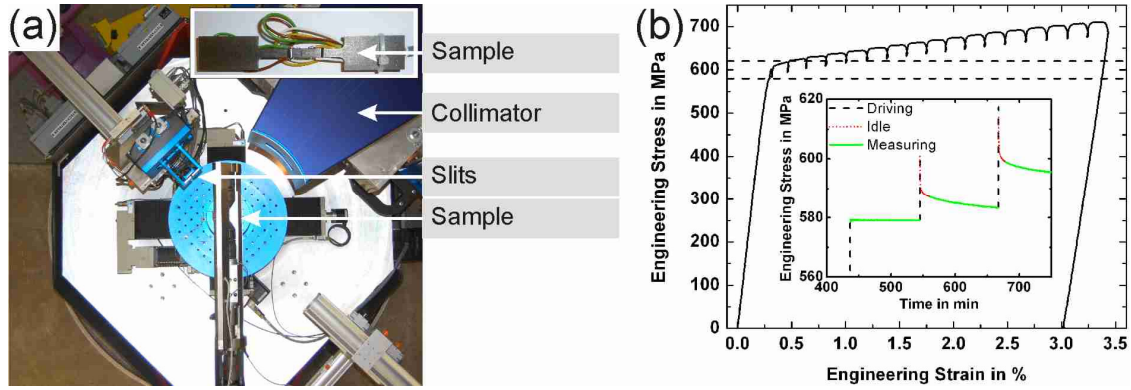
Figure 45: (a) Set-up at POLDI and (b) loading curve recorded during in situ tensile deformation. During the measurement, the load was kept constant in the elastic regime and the displacement was kept constant in the plastic regime. Superimposed are lines drawn with the 0.02% (580MPa) and 0.2% (620MPa) yield stresses. The inset shows the stress-time relationship at the elastic-plastic transition. Neutron acquisition started instantaneous in the case where the load was kept constant and after 10 min relaxation time (indicated as idle in the legend) when the displacement was kept constant.

Two types of measurements have been performed on this instrument: Ex situ measurements on pre-deformed samples and in situ tensile loading at RT. One measurement point takes about 120 min in the axial and 60 min in the transverse direction since the gauge volume is vertically higher. For in situ tensile loading, the load was kept constant in the elastic regime and the displacement was kept constant in the plastic regime in order to avoid too severe cold creep. This results in stress relaxation for the latter case: Neutron diffraction has been started after 10 min relaxation time when the stress variations are relatively small. The loading scheme is shown in Figure 45(b).
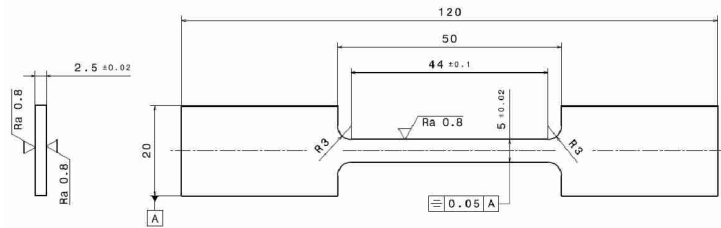
Figure 46 Sample geometry of the tensile specimen used at the POLDI beamline. The dog-bone shaped samples were cut by electro-discharge machining (EDM). Units are given in mm.

Data treatment: The lattice parameter a of the ferrite and the interplanar spacing d_{hkl} of the individual hkl ferrite grain families are determined by the standard fitting routines available at POLDI, which are the full pattern Pawley refinement and single peak fitting.

2.3.5.4   ENGIN-X beamline: neutron diffraction

ENGIN-X is a ToF diffractometer [140] at the spallation neutron source ISIS located at the Rutherford Appleton Laboratory (RAL), UK. For this experiment the choppers were set to 25 Hz

and 50 Hz (cf. §2.2.3.3). Figure 47 shows the corresponding diffraction patterns at 565°C. At 25 Hz, the first seven ferrite peaks with the highest lattice spacing are recorded. At 50 Hz, only the range between the {200} and the {110} ferrite reflection is recorded, exploiting now the full neutron flux and allowing to observe the diffraction peaks from the second phase. Automatically switching between the two chopper settings was not yet implemented in the steering software and could only have be performed manually. During the mechanical test, only the information on the d-spacing range in between the {200} and {110} ferrite reflections is therefore available.
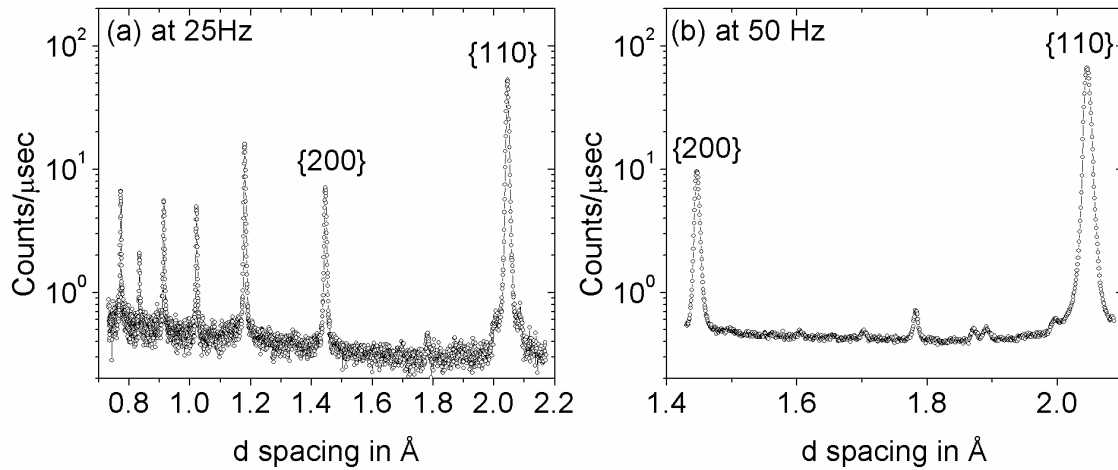
Figure 47 Diffraction pattern of the 1%CrMoV steel with about 2h acquisition time: Chopper running at (a) 25Hz and (b) 50Hz.

Figure 47 shows the set-up with the loading rig mounted on the sample position. ENGIN-X is equipped with two detector banks located at ±90° degree with respect to the incident neutron beam.
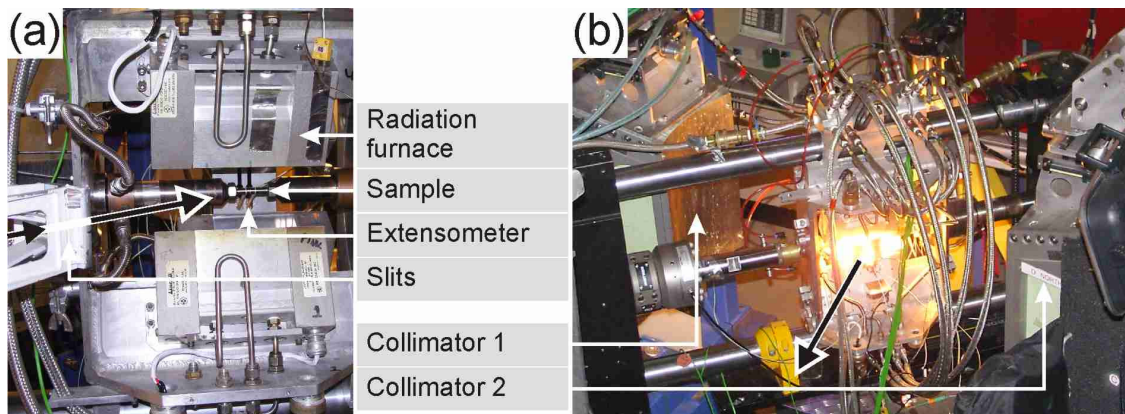
Figure 48 Set-up at ENGIN-X with the 100kN loading rig and the four radiation furnaces at two different views: (a) Beam towards the sample and (b) primary beam that has passed the sample. The beam axis is indicated by a black arrow.

Therefore only one sample has to be deformed in order to obtain data from the axial and transverse direction. The angular acceptance angle is horizontally ±16° and vertically ±21°, hence providing a

much larger detection area compared with POLDI. A 100 kN loading rig for RT deformation studies in tension and compression is available from the beamline sample environment. The rig can be equipped with a radiant air furnace for testing up to 1100°C. Thermocouples mounted at several positions along the sample gauge length ensured that there is no temperature gradient. The strain was measured with a high temperature extensometer. The set-up is described in more detail in [141]. Performing the experiment and data analysis is rather straightforward.

Three types of measurement have been conducted: Ex situ measurements on pre-deformed samples, in situ creep and HT tensile deformation. For the latter, diffraction patterns have only been acquired in the unloaded state since the acquisition time for cementite is about 2 h and for the ferrite only a few minutes, causing nevertheless significant creep (load control) or stress relaxation (displacement control). The sample geometry is shown in Figure 49.
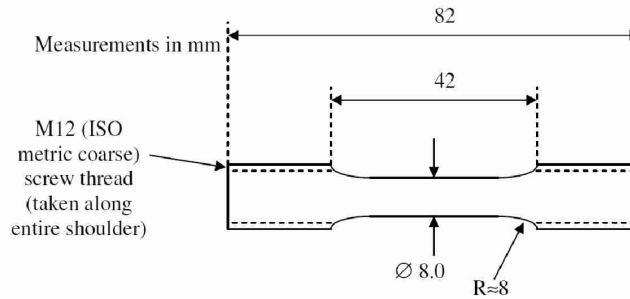
Figure 49 Sample geometry of the tensile specimen used at the ENGIN-X beamline. Units are given in mm.

Data treatment: The lattice parameter a of the ferrite and the interplanar spacing d_{hkl} of the individual {hkl} ferrite grain families and their peak widths are determined by the standard fitting routines available at ENGIN-X, which are the single peak fitting and the full pattern Pawley fitting and Rietveld refinement. The full pattern methods are based on the GSAS software package [129].

2.3.5.5   Comparison of the diffraction patterns from all beamlines

Figure 50 shows diffraction patterns from the same 1%CrMoV sample (*HT134*) at all four different beamlines, plotted in the range between the {110} and {200} ferrite peaks and in log-scale for the intensity in order to visualize peaks from the low volume fraction second phase particles. These diffraction patterns are recorded with similar statistics as those shown further in chapter 3.

The spectra in Figure 50(a) from MS and ID15B are recorded with counting times of 5 min and four seconds (i.e. five frames at 0.8 s), respectively, which are the typical acquisition times for the on-load pattern (i.e. in situ loading). The acquisition time for the ID15B spectrum is significantly shorter since the azimuthal integration is performed over an angular range of 2·30° (cf. §2.3.5.2) and the counting statistics are therefore large, whereas the MS-spectrum is acquired with a 1D

detector (angular range about 1°, cf. §2.3.5.1). The large background around the {110} ferrite peak for ID15B is because the peak is saturated and is therefore also not used in the analysis.
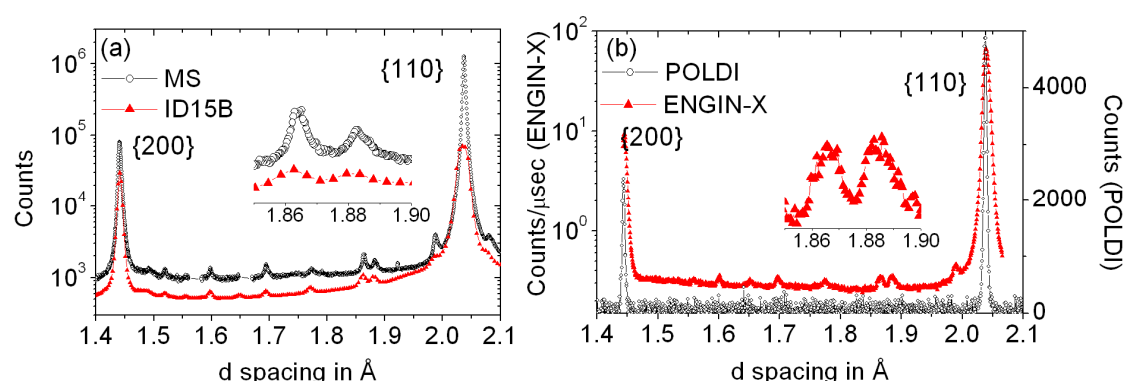
Figure 50 Diffraction pattern of the sample *HT134* in between the {110} and the {200} ferrite reflections at (a) both powder X-ray beamlines and (b) both ToF neutron beamlines. At ID15B (a), the {110} peak is saturated and the nearby background relatively high and at ENGIN-X (b) , the {200} is partly cut, but the range is extended at 565°C.

The spectra in Figure 50(b) from POLDI and ENGIN-X (50 Hz) are with typical counting times of 45 min and 2 h acquisition time, respectively. The neutron flux on the sample position at POLDI and ENGIN-X are similar. The detector area at ENGIN-X, however, is about 8 times larger.

2.3.5.6   Chronology of the various beamtimes

A number of beamtimes have been performed to achieve to goal of the project. The chronology of these beamtimes is listed in the following. The results obtained from the first beamtimes (a)-(c) were necessary to actually tackle and define the project. Also, based on this data, beamtime could be accumulated at ESRF and ENGIN-X, where also high temperature loading rigs are available for in situ mechanical testing.

(a) 2009/05 POLDI: Ex situ measurements on RT tensile and creep deformed samples => Evolution and magnitude of residual strain in the ferrite.

(b) 2009/06 POLDI: In situ tensile loading at RT (axial and transverse direction) => Behaviour of the ferrite during deformation. Second phase particles not visible in the diffraction pattern (low counting statistics).

(c) 2009/2010 MS: In situ tensile loading at RT => Load-transfer from the plastifying ferrite to cementite. Sample-to-sample variations for the ferrite matrix response (low sampling statistics).

(d) 2010 POLDI: In situ tensile loading at RT (Two times axial) => Good agreement of the lattice strain evolution throughout the elasto-plastic regime (method appears to provide representative information for this inhomogeneous microstructure).

(e) 2010/04 ID11 at ESRF: In situ HT tensile and creep loading => Experiment was not successful due to detector related problems. Report to experiment number MA-994 [142].

(f) 2010/12 POLDI: Ex situ measurements on HT tensile deformed samples => To partly compensate for the experiment (e). Evolution and magnitude of residual strain in the ferrite.

(g) 2011/10 ID15B: In situ HT tensile and creep => Cementite and ferrite behaviour during deformation.

(h) 2011/12 ENGIN-X: In situ HT tensile and creep => Representative information for the ferrite during HT deformation.

(i) 2012/05 MS: Powder diffraction on the extracted carbide powder (Beamline back in normal user operation after upgrade 2010/10-2012/02) => Cementite characteristics

2.3.5.7 Sample nomenclature

Table 5 provides the sample nomenclature that will be used throughout this dissertation. The mechanical properties and the chemical composition may vary considerably throughout a 1%CrMoV steel component (Norton and Strang [28]). The samples marked with an *A* and *B* in brackets have been provided by EMPA as tensile samples and some of them have already been prepared before the start of this project. Later in this project, a block of material (20 x 14 x 2.5 cm^3) was provided by EMPA and the samples marked with a *C* in brackets have been manufactured from very neighbouring locations within this block. *A*, *B* and *C* are from slightly different locations within the original component.

Table 5 Sample nomenclature. The *Mod. 1%CrMoV* is the heat-treated material (§2.1.1.2), the different microstructures of the high-carbon steel are pearlite, tempered pearlite and spheroidized cementite (§2.1.2), the symbols in the column *beamtime* relate to §2.3.5.6. Creep and HT deformation always at 565°C. *ps* means plastic strain.

Sample name	Material	Deformation History	Beamtime
HT134	1%CrMoV (A)	As-received	a, f, h
HT102	1%CrMoV (A)	Ex situ: 1% ps. at RT	a, f, h
HT108	1%CrMoV (A)	Ex situ: 5% ps. at RT	a, f, h
HT765	1%CrMoV (B)	Ex situ: 1% ps. at HT	f, h
HT766	1%CrMoV (B)	Ex situ: 4% ps. at HT	f, h
HT133	1%CrMoV (A)	Ex situ: 0.6% ps. Creep/270MPa	a, f, h
HT135	1%CrMoV (A)	Ex situ: 1.0% ps. Creep/270MPa	a, f, h
HT92	1%CrMoV (A)	Ex situ: 3.2% ps. Creep/270MPa	a, f, h
HT101	1%CrMoV (A)	Ex situ: 0.0% ps. Thermally aged	a, f, h
POL1	1%CrMoV (A)	In situ: 3% ps. Axial direction	b
POL2	1%CrMoV (A)	In situ: 3% ps. Transverse direction	b
POL3	1%CrMoV (A)	In situ: 1% ps. Axial direction	d
POL4	1%CrMoV (A)	In situ: 1% ps. Axial direction	d
MS1	1%CrMoV (A)	In situ: Axial direction	c
MS2	1%CrMoV (A)	In situ: Axial direction	c
MS3	1%CrMoV (A)	In situ: Axial direction	c
MS4	1%CrMoV (A)	In situ: Transverse direction	c
ID0	1%CrMoV (C)	In situ: Continuous tensile at RT	g
ID1	1%CrMoV (C)	In situ: Continuous tensile at RT	g
ID2	1%CrMoV (C)	In situ: Continuous tensile at HT	g
ID3	1%CrMoV (C)	In situ: Load-Unload tensile at RT	g
ID4	1%CrMoV (C)	In situ: Load-Unload tensile at HT	g
ID5	1%CrMoV (C)	In situ: Creep at 565°C/130MPa	g
Heat1	Mod. 1%CrMoV (C)	In situ: Tensile at RT	g
Heat2	Mod. 1%CrMoV (C)	In situ: Tensile at RT	g
Heat3	Mod. 1%CrMoV (C)	In situ: Tensile at RT	g
Heat4	Mod. 1%CrMoV (C)	In situ: Tensile at RT	g
HC1	1.15wt%C, pearlite	In situ: Tensile at RT	g
HC2	1.15wt%C, temp. pearlite	In situ: Tensile at RT	g
HC3_S1	1.15wt%C, spheroidized	In situ: Tensile at RT	g
HC3_S2	1.15wt%C, spheroidized	In situ: Tensile at HT	g
EngX1	1%CrMoV (C)	In situ: Tensile at HT $\dot{\varepsilon} = 1 \cdot 10^{-5}\, s^{-1}$	f
EngX2	1%CrMoV (C)	In situ: Tensile at HT $\dot{\varepsilon} = 5 \cdot 10^{-4}\, s^{-1}$	f
EngX3	1%CrMoV (C)	In situ: Creep/290MPa	f
EngX4	1%CrMoV (C)	In situ: Creep/330MPa	f

3   Results

The first section deals with the identification of the carbides in the as-received 1%CrMoV steel. The subsequent sections present the results of the beamtime at the various instruments in their chronological order (cf. §2.3.5.6): Starting with the ex situ measurements in §3.2.1 to study the evolution of the intergranular and interphase strains with plastic deformation for different loading conditions, followed by in situ measurements to elucidate these findings. At the end of each section, a brief summary of the main findings is given.

3.1   Identification of carbides in the as-received 1%CrMoV

The tempered bainitic microstructure of the as-received 1%CrMoV steel possesses an inhomogeneous ferrite grain morphology and size distribution, as shown earlier in Figure 20(b). The grain sizes are in between a few μm up to more than 100μm. Figure 51 shows the etched surface of the as-received material in a region with small ferrite grain sizes, investigated by SEM at two different magnifications. The etchant nital (cf. §2.3.1) reveals both the interphase and the ferrite grain boundaries. An example of the latter is indicated at the position of arrow *A*. Consider now the carbide precipitates, which presumably cause the interphase strains (cf. Figure 57(a)) in the material upon deformation. Precipitates are present within the grains, for instance at the position of arrow *B*, and also at the grain boundaries, for instance at the position of arrow *C*. The precipitates possess various morphologies ranging from spherical to ribbon type. This is more clearly shown in Figure **52**(a) at the positions of the arrows *D* and *E*, respectively.
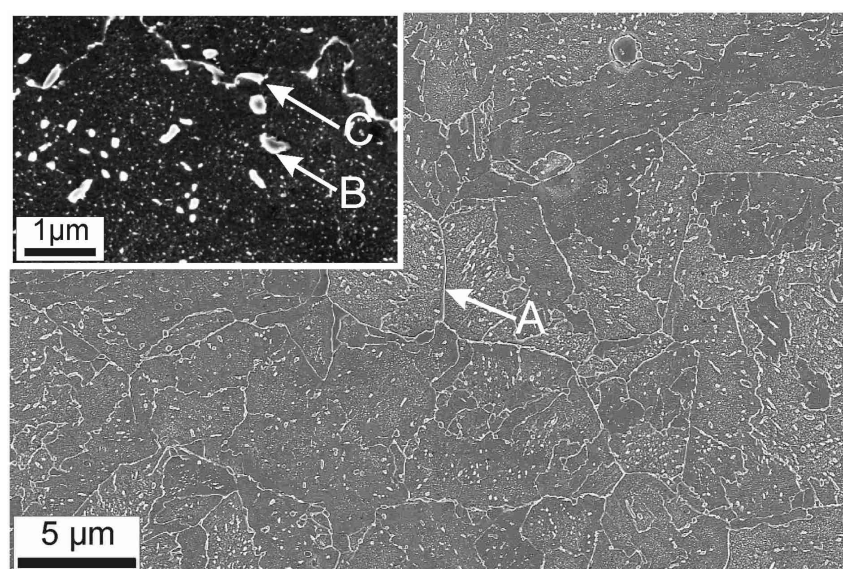

Figure 51 SEM micrograph of the etched (nital) surface of the as-received 1%CrMoV steel at two different magnifications revealing ferrite grain boundaries (*A*) and second phase particles within the ferrite grains (*B*) and along the ferrite grains boundaries (*C*).
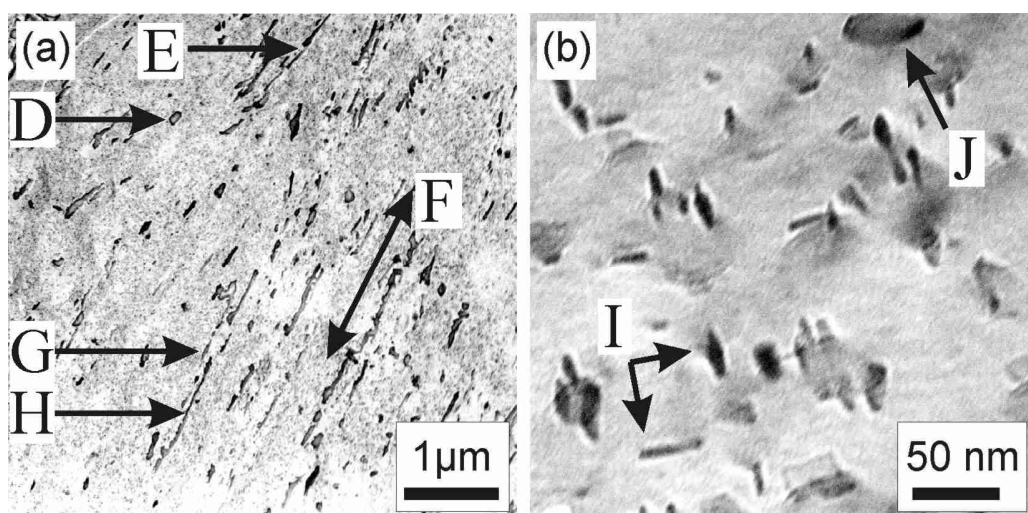
Figure 52 Carbides in the as-received microstructure: (a) SEM micrograph of the etched (picral) surface showing the different morphologies *D* and *E*, ribbon type precipitates with different sizes *G* and *H* oriented along the direction *F*. (b) TEM with absorption contrast (bright field) revealing small precipitates.

In most grains where ribbon type precipitates are present, these precipitates are oriented all along the same direction within that grain. This direction is indicated in Figure 52(a) with the arrow labelled *F*. The length of these particles is ranging from below 100 nm, for instance at the position of arrow *G*, up to 1 μm, for instance at the position of arrow *H*. An enhanced concentration of Cr, Mo and Mn and a depletion of Fe in these particles with respect to their surrounding ferrite matrix have been observed by EDX (not shown here). The TEM image in Figure 52(b) shows another type of precipitates: These are significantly smaller and below 50 nm. The image shows partially ribbon like particles, oriented rectangular with respect to each other, for instance at the position of arrow *I*, and particles with a more elliptic shape, for instance at the position of arrow *J*. This suggests that these particles belong to the same type and are actually plate-like in 3D.

For identification, the carbides have been extracted from the ferrite matrix with the procedure described in §2.1.1.3. The carbide weight fraction is 3% (for more details see §3.6.1). Figure 53 shows a XRD pattern (MS beamline) on the extracted carbide powder. The red data points are the experimental data, the blue line represents the Rietveld refinement with the marked reflections underneath and the difference between fit and experimental data is shown below. Mainly two types of carbide are present: Cementite with an orthorhombic structure, giving rise to the majority of the peaks, and vanadium carbide with an fcc structure. The broad diffraction peaks of the vanadium carbide suggest a small grain size relative to the cementite. Some few additional peaks are present with little intensity (10^{-1} to 10^{-2} relative to the average cementite peaks), which could not be indexed unambiguously. The presence of carbides of the type $M_{23}C_6$, M_6C and M_7C_3 is unlikely: Due to their large lattice parameter with respect to the vanadium and cementite (cf. Table 2), they would generate diffraction peaks almost exclusively at very high d-spacings (>2.4Å) which is not the case.
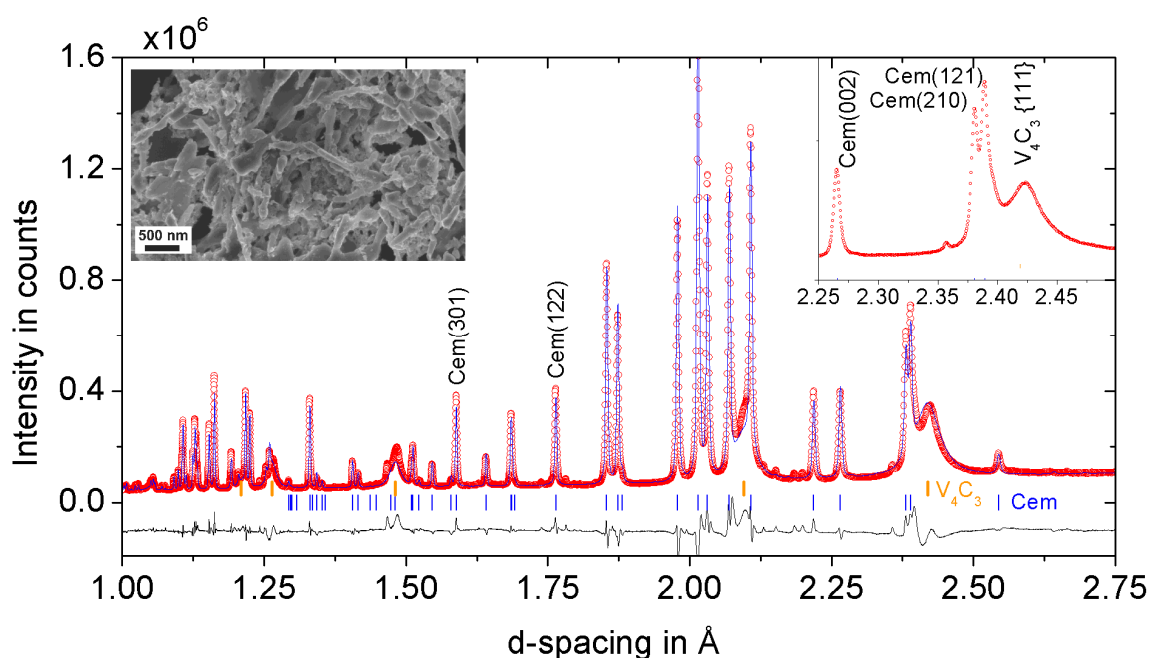
Figure 53 XRD pattern (red) from the extracted carbide powder of the as-received 1%CrMoV steel. Rietveld refinement (blue), orthorhombic cementite (Cem) and fcc vanadium carbide (V_4C_3) is considered, the corresponding position are marked underneath the patter. The inset shows a SEM image of the carbide powder.

Therefore, only cementite and vanadium carbide are considered in the following as second phase particles within the as-received material. From literature (cf. Table 2) is known that the cementite in this material is typically ribbon-like with a length up to 2 µm. That would correspond to the particles seen in Figure 51 and Figure 52(a). The fact that the cementite particles are often oriented along the same direction (cf. Figure 52(a)) is presumably a direct consequence of being a bainitic transformation product (cf. §1.2.2). The rounding of small particles may then happen during tempering. It is further reported that the vanadium carbide exhibits a plate-like structure with plate diameters of a few tens of nm (cf. Table 2). That would correspond to the particles seen in Figure 52(a).

As one can see from the various micrographs (Figure 51, Figure 52(a), Figure 53 inset), the cementite particles are rather inhomogeneous in size and morphology and are located at the grain boundaries and within the grains. No detailed characterization has been performed to statistically describe these parameters. Rather, the focus is now on the residual strain accumulation through deformation of the *same microstructure* but comparing different loading conditions.

Main findings from §3.1:

- *Carbides in the as-received 1%CrMoV material are essentially cementite (orthorhombic) and vanadium carbide (fcc): Large particles are cementite, small particles are vanadium carbide*
- *Complex arrangement of cementite particles: Different morphologies, sizes and locations (within the ferrite grains and at the grain boundaries)*

3.2   POLDI beamline: ToF Neutron diffraction

The results of residual strain measurements on pre-deformed samples are given in §3.2.1. The results from the RT in situ tensile tests are given in §3.2.2. The nomenclature of the samples tested and reported in this section is given in Table 6.

Table 6 Nomenclature of the samples reported in this section. For more details see §2.3.5.7

Sample name	Material	Deformation History
HT134	1%CrMoV (Batch A)	As-received
HT102	1%CrMoV (Batch A)	Ex situ: 1% ps. at RT
HT108	1%CrMoV (Batch A)	Ex situ: 5% ps. at RT
HT765	1%CrMoV (Batch B)	Ex situ: 1% ps. at HT
HT766	1%CrMoV (Batch B)	Ex situ: 4% ps. at HT
HT133	1%CrMoV (Batch A)	Ex situ: 0.6% ps. Creep/270MPa
HT135	1%CrMoV (Batch A)	Ex situ: 1.0% ps. Creep/270MPa
HT92	1%CrMoV (Batch A)	Ex situ: 3.2% ps. Creep/270MPa
HT101	1%CrMoV (Batch A)	Ex situ: 0.0% ps. Thermally aged
POL1	1%CrMoV (Batch A)	In situ: 3% ps. Axial direction
POL2	1%CrMoV (Batch A)	In situ: 3% ps. Transverse direction
POL3	1%CrMoV (Batch A)	In situ: 1% ps. Axial direction
POL4	1%CrMoV (Batch A)	In situ: 1% ps. Axial direction

3.2.1   Residual lattice strain measurements on pre-deformed samples

Test samples have been deformed by the collaborators at EMPA prior to the diffraction experiment under three different loading conditions. The corresponding mechanical data is shown in Figure 54: Uniaxial tensile deformation at RT and at 565°C (designated as HT in the following) both with a strain rate of 10^{-5} s^{-1} (Figure 54(a)) and uniaxial creep deformation at 565°C/270MPa (Figure 54(b)).
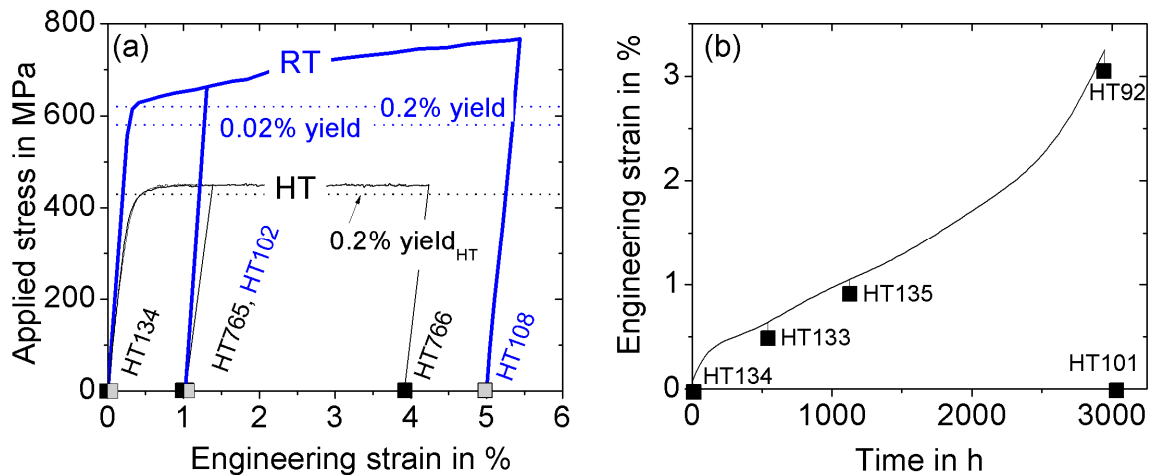

Figure 54 (a) Stress-strain curve of the samples tensile deformed at RT and HT (565°C). (b) Creep curve (at 270MPa, 565°C). The available samples are indicated by the squared symbols and the sample nomenclature is given in Table 6.

The available samples are indicated by the square symbols: (i) The undeformed reference sample *HT134*, (ii) the samples tensile deformed at RT to 1% (*HT102*) and 5% (*HT108*) plastic strain, (iii) the samples tensile deformed at HT to 1% (*HT765*) and 4% (*HT766*) plastic strain and (iv) the samples creep deformed to the end of the primary (0.6% plastic strain, *HT133*), to the secondary (1% plastic strain, *HT135*) and to the tertiary (3.2% plastic strain, *HT92*) creep regime. One sample has been thermally aged (at 565°C, *HT101*) without load for about 3000 h. The samples deformed at 565°C have been unloaded first before being air-cooled to RT. The samples were deformed in a standardized test machine. The stress-strain behaviour is therefore assumed to be highly reliable. In particular, the HT stress-strain curve is described in the following besides some comments on the RT tensile and creep curve:

RT tensile curve: The yield stress for the RT tensile curves is identified with 580 MPa (0.02% yield) and 620 MPa (0.2% yield), and the curve enters a work hardening regime.

HT tensile curves: The yield stress in bcc materials often depends on the strain rate, in particular at elevated temperatures, and typically increases with the strain rate. For strain rates in between $5 \cdot 10^{-4}$ to $5 \cdot 10^{-5}$ s^{-1} at a temperature of 565°C, the influence of the strain rate on the yield stress can be neglected [143]. Such a strain-rate range range may need to be considered because the in situ tensile tests with the loading-rig at the synchrotron X-ray beamline ID15B can only be performed with a constant displacement rate and the actual strain rate, also due to the localized deformation (cf. §2.3.5.2), may be larger than 10^{-5} s^{-1}. The range of $5 \cdot 10^{-4}$ to $5 \cdot 10^{-5}$ s^{-1} certainly provides the upper and lower limit, respectively. The 0.2% yield stress for the HT tensile curve (samples *HT765* and *HT766*, Figure 54(a)) amounts to 435 MPa. The curve, however, deviates early from the linear elastic behaviour. This is elucidated in Figure 55, where a parameter *Δε* for both samples *HT765* and *HT766* is plotted as a function of the applied stress.
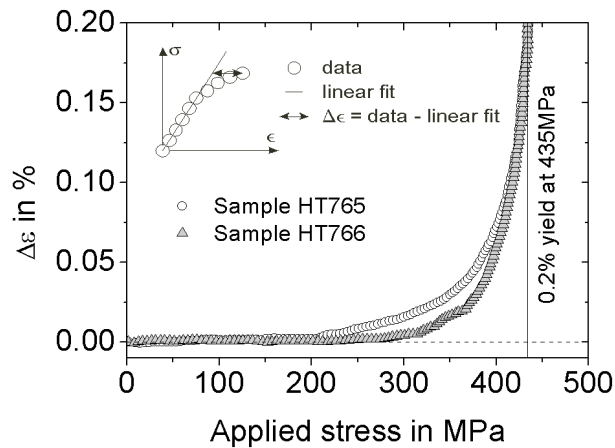

Figure 55 This curve highlights the early deviation from the linear stress-strain curve during HT tensile deformation. The parameter Δε is the difference between the linear fit and the data points, as shown in the inset and indicates the deviation from linearity. The 0.2% yield stress is indicated.

The parameter $\Delta\varepsilon$, as schematically defined in the inset, is the difference between a linear fit in the range 0 to 150 MPa, where the stress-strain curves are rather linear, and the stress-strain curve. Therefore, $\Delta\varepsilon$ is close to zero for both samples for stresses up to 150 MPa. The curves of the two samples behave differently between 200 and 400 MPa: Sample *HT765* deforms rather linearly until about 200 MPa, sample *HT766* deforms rather linearly until about 250 MPa. Beyond these stresses, $\Delta\varepsilon$ increases. This means that the stress-strain curve deviates from its linear elastic behaviour. Sample *HT766* shows some wobbling between 300 and 375 MPa. At around the 0.2% yield stress, the stress-strain response for both curves coincides again. It is not clear whether the difference in stress-strain behaviour between 200 and 400 MPa is due to sample alignment issues, which would be more likely to show up during elastic deformation, or due to variations in the sample microstructure. In fact, a higher fraction of carbides (ca. 25% higher) has been observed in the gauge section of sample *HT766* (cf. §3.6.1), which may contribute to the strength. Regardless of these details, the early deviation from linear behaviour indicates the presence of a transient regime, which based on these two curves, may start between 200 and 250 MPa. These results are discussed in §4.3 in terms of the corresponding lattice strain evolution during in-tensile loading (cf. §3.4.1.1). Beyond the 0.2% yield, the stress-strain curve enters a regime where the (true) stress is constant. This is called *steady-state like regime* in the following. The unloading branches have not been recorded and are indicated as straight lines with the slope obtained from the early elastic loading.

Creep curve: Note that the samples are loaded into the transient regime at this creep stress of 270 MPa (cf. Figure 55). *In situ* creep test at higher stresses of 290 and 330 MPa (cf. §3.5.4) and a lower stress of 130 MPa (cf. §3.4.1.2) have been performed for comparison.

Figure 56 shows the POLDI diffraction pattern obtained for the reference sample *HT134* with the first seven bcc iron reflections with the largest lattice spacing ({110} to {321}). Diffraction peaks
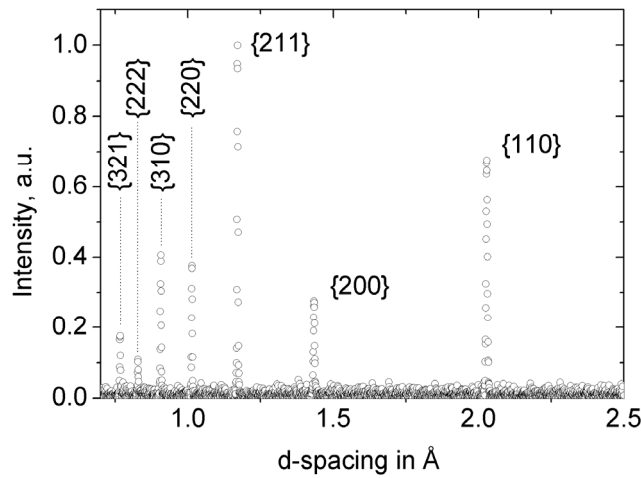

Figure 56 POLDI diffraction pattern with ferrite (bcc iron) reflections. Additional diffraction peaks cannot be distinguished from the background.

from additional phases other than ferrite cannot be distinguished from the background. This is also valid for the deformed samples.

Diffraction patterns have been acquired with the scattering vector parallel and perpendicular to the former loading direction and for all samples. Given that the microstructure is rather inhomogeneous (cf. Figure 20 and Figure 51), several diffraction patterns have been acquired at different positions along the sample gauge length. Each of these patterns – for one sample and one scattering vector – gives the same values for the lattice strain, within the resolution of the instrument. This suggests that the experiment provides representative information for the whole material. In order to increase the counting statistics, all spectra for one sample and one scattering vector are summed together before the final analysis.

Figure 57 shows the evolution of the lattice strain as a function of the accumulated plastic strain for all three deformation sequences: (a) shows the ferrite phase strain for all deformation sequences, (b) shows the {hkl} lattice strain for the RT tensile sequence, (c) shows the {hkl} lattice strains for the HT tensile sequence and (d) shows the {hkl} lattice strains for the crept sequence and the thermally aged sample. For the RT tensile sequence, an additional data point at 3% plastic strain is added and highlighted for clarity, available from the in situ tensile experiment in Figure 58. The thermally aged sample does not show a variation in peak position for any {hkl}-grain family (cf. (d)) and is therefore omitted in (a). The arrows with the corresponding values in the figures (b)-(d) describe the difference in lattice strain between the axial {110} and the axial {200}. The {hkl} lattice strains are shown for the {110}, {200}, {211}, {310} ferrite reflections. The {220} is just the higher order refection of the {110} and the intensities of the {222} and {321} are too low for single peak fitting, providing large uncertainties in the peak position. The contribution of these three reflections is therefore omitted in the figure. For the undeformed sample *HT134*, the lattice parameter a^0 calculated for the different {hkl}-grain families (Eq. 20) are, within the resolution of the instrument, all the same, suggesting a relaxed microstructure without significant intergranular strains. All figures are now described:

Phase strain (Figure 57(a)):

Axial direction: All data points lie in the compressive region and the largest phase strain occurs when tensile deformed at RT, where it appears to saturate towards a value of 650 µε at large plastic strain (>5%). When tensile deformed at HT and at large plastic strains, the phase strain is smaller by more than a factor of two (250 µε). While the HT tensile curve already entered a steady-state like regime at 1% plastic strain (cf. Figure 57(a)), the phase strain is still slightly increasing by 70 µε until the next measuring point at 4% plastic strain. Very little phase strain is observed during creep deformation in the primary (50 µε) and secondary (45 µε) regime, whilst it is higher in the tertiary (130 µε) regime.
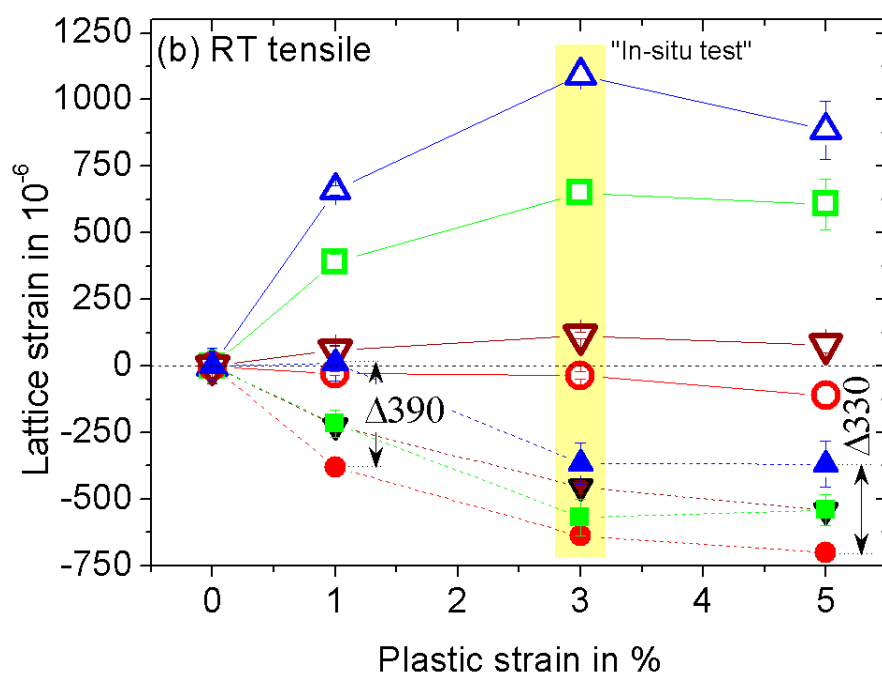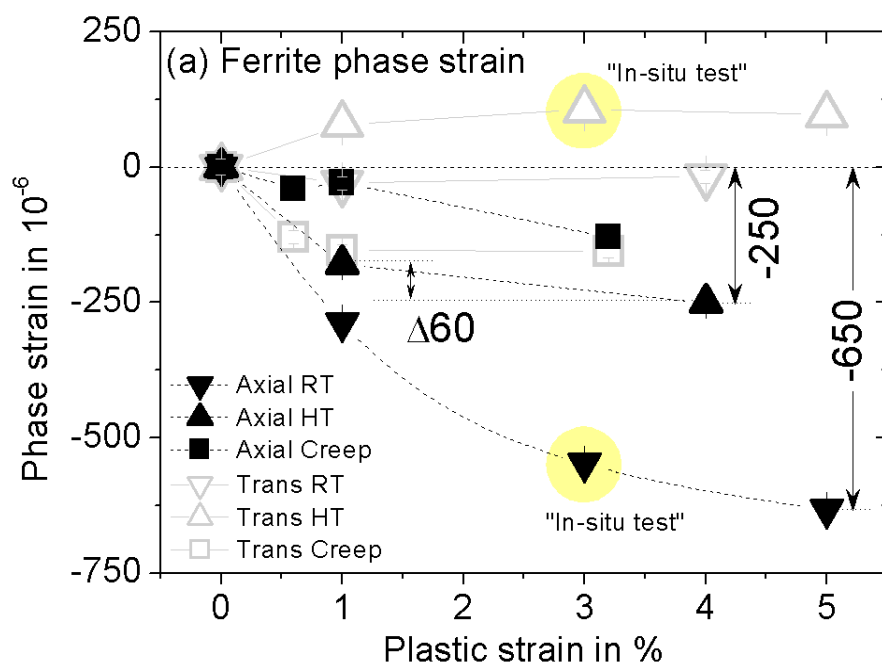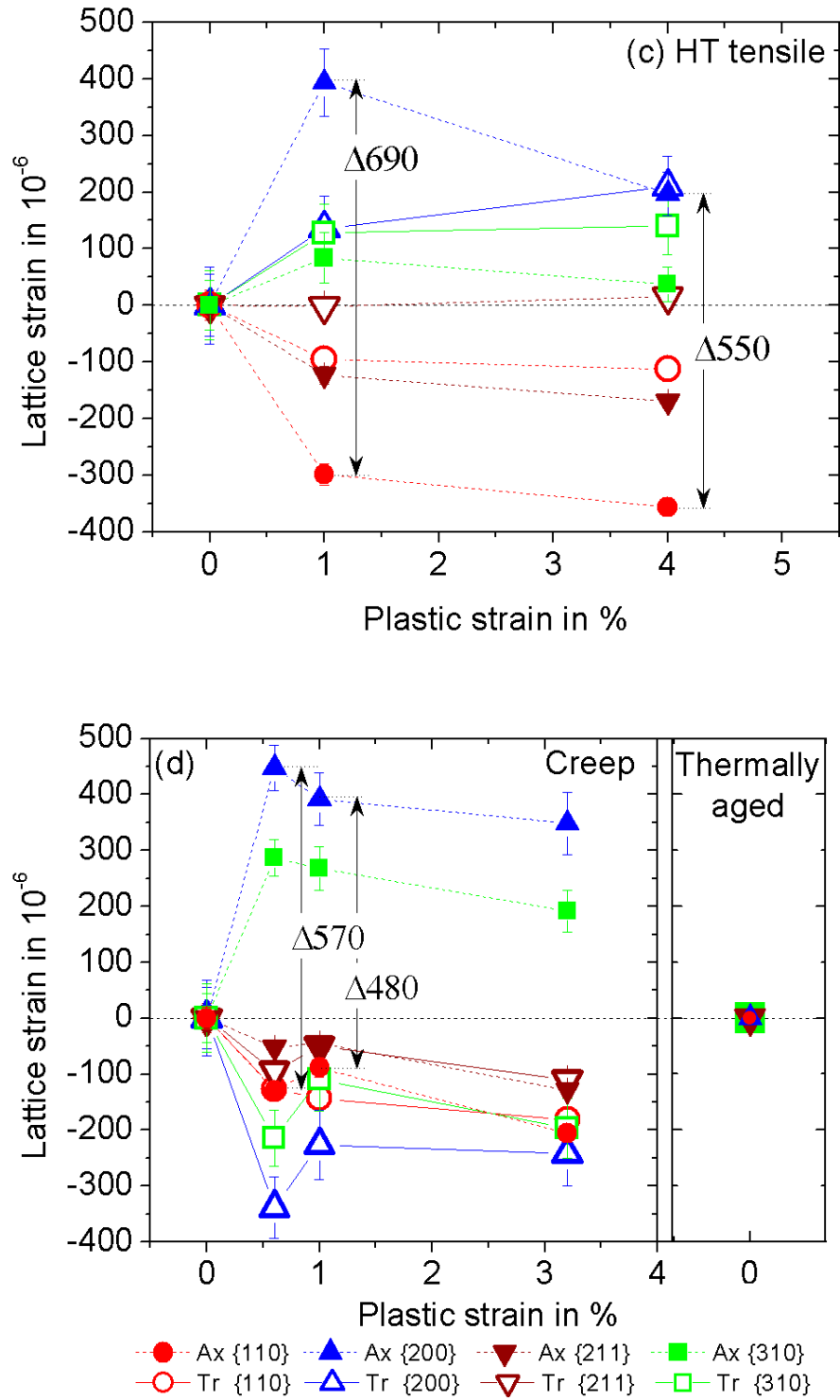
Figure 57 Evolution of residual lattice strain in the ferritic matrix as a function of the deformation history. Phase strain in (a). Lattice strain of the individual ferrite grain families when: Tensile deformed at RT in (b); Tensile deformed at HT (565°C) in (c); Creep deformed at 270MPa/565°C together with thermally aged sample in (d). Measurements have been performed in the axial (full symbols) and transverse direction (empty symbols).

Transverse direction: Only the RT tensile data points are tensile. They seem to saturate early and at value of 100με. The HT tensile data points are slightly in compression (25με). The creep data points are all compressive and to a larger magnitude as for the corresponding axial direction.

{*hkl*} lattice strain (Figure 57(b)-(d)):

As already mentioned, thermal aging (d) does not cause variations in the peak position for any grain family, neither in the axial nor the transverse direction. All three deformation sequences, however, introduce intergranular type of residual strains.

Axial direction: The {110} and {200} mark the outer bounds in each sequence and the {110} is always the one that is most compressive. The difference in lattice strain between these two grain families strongly depends on the loading sequence: At 1% plastic strain, this difference amounts to about 390, 690, 480 με for the RT tensile, the HT tensile and the creep, respectively. There are further differences in the intergranular behaviour between the sequences: While the {211} and the {310} are very close at RT, with the exception at 3% plastic strain, they are more separated for HT tensile and creep, even experiencing strain with opposing sign, i.e. compression and tension, respectively.

Transverse direction: For both tensile deformed sequences, the {110} and {200} mark the outer bounds, like in the axial direction, and the {110} grain family is most compressive. This is different for the crept sequences, where the {200} is now the most compressive grain family. The transverse strains created by RT tensile deformation than the axial strain. This is different for the HT tensile and creep sequence.

3.2.2 In situ tensile loading at RT

Figure 58 shows the lattice strain during RT tensile deformation for the axial (samples *POL1* and *POL3*) and the transverse (sample *POL2*) direction. The phase strain and the contribution from the {211} grain family are omitted for clarity but behave similar to the {110} grain family during loading. Note that two different samples are tested to obtain the axial and the transverse response since POLDI is equipped with only one detector bank (cf. §2.3.5.3). Superimposed in this figure are lines drawn at the 0.02% and 0.2% yield stresses. The samples *POL1* and *POL2* are deformed until 3% plastic strain.

Axial direction (Sample *POL1*): Only four data points are available in the elastic regime. The straight lines represent the linear regression for these four data points and are extrapolated as dashed lines until the 0.02% yield at 580 MPa. The {110} grain family appears as the stiffest and the {200} as the most compliant direction: The lattice strain for all grain families progress linearly with the applied stress. The value of the slopes are $E(110) = 220\pm2$ GPa, $E(200) = 164\pm2$ GPa,

E(310) = 175±1 GPa. At the 0.02% yield stress the {110} and the {310} start to diverge from the hitherto linear behaviour. The {200} diverges already earlier and initially shifts slightly more in the tensile direction, but converges then the same trend as observed for the {310}, indicating that the elastic lattice strain no longer increases (within the scatter of the data points beyond 580 MPa). The lattice strain of the {110} slightly decreases in between the 0.02% and 0.2% yield and increases again with further applied stress. After unloading, all grain families exhibit compressive residual lattice strains.
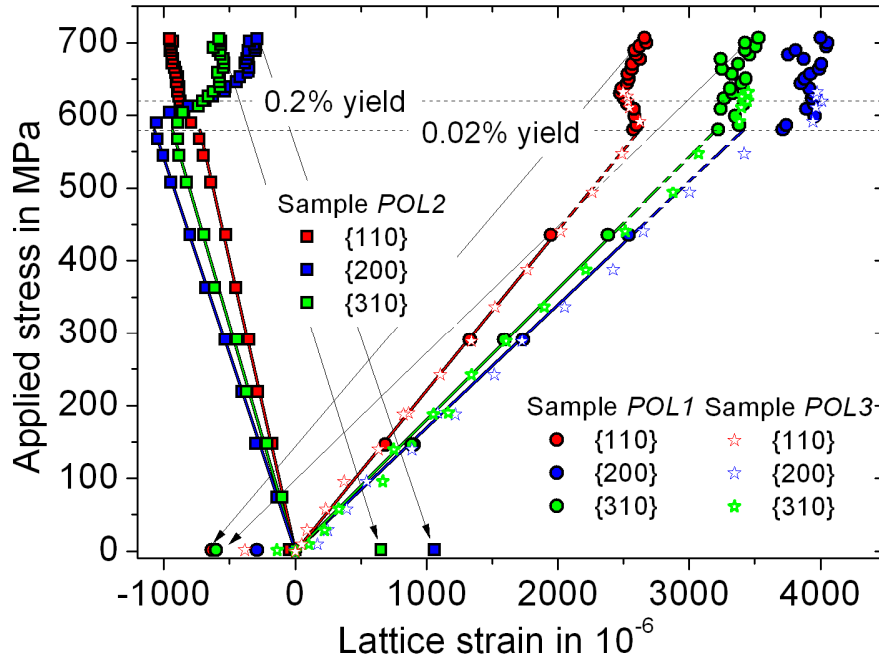
Figure 58 Lattice strain with applied stress for two samples in the axial and one sample in the transverse direction. The straight line indicates the linear regression of sample *POL1* until 450MPa and extrapolated until the 0.02% yield and of sample *POL2* until 565MPa. The arrow represents the unloading trajectory pointing towards the data points measured in the unloaded state (residual strain) and is shown, for clarity, only for some grain families. Samples deformed until 3% plastic strain, *POL1* and *POL2*, and until 1% plastic strain, *POL3*.

Transverse direction (Sample *POL2*): Here one benefits from more measurement points in the elastic regime. The corresponding slopes for the linear regression that covers the first ten measurement points in the elastic regime are $-E(110)/\nu(110) = -800\pm7$ GPa, $-E(200)/\nu(200) = -540\pm3$ GPa, $-E(310)/\nu(310) = -622\pm6$ GPa. Deviation from linearity starts at the 0.02% yield for the {200} and the {310} grain family with an initial tensile evolution somewhere beyond the 0.2% yield and then a stagnating lattice strain. The {110} shows a slight transition in between the 0.02% and 0.2% yield, exhibiting a steeper slope. After unloading, the residual lattice strain for the {200} and the {310} are strongly tensile and but almost zero for the {110}.

Data reproducibility: Two further samples (*POL3* and *POL4*) were measured in situ to 1% plastic strain and in the axial direction. The data points of sample *POL3* are shown in Figure 58 as crosses and with more measurement points in the elastic regime. The values of the slopes (not shown here) of the linear regression are E(110) = 220±2 GPa, E(200) = 169±2 GPa, E(310) = 181±3 GPa. All three samples, *POL1*, *POL3* and *POL4* (the latter is not shown for clarity) are in good coincidence in both, the elastic and plastic regime. This provides confidence that this method probes a representative quantity of material to describe the bulk average behaviour. Two detectors would be required to check both the axial and the transverse direction simultaneously for one sample. Since beamtime is limited (one tensile experiment took about 2 days), the data reproducibility in the transverse direction has not been checked. The magnitude of the residual strain, however, follows nicely the trend of the pre-deformed samples (cf. Figure 57 (a) and (b)).

Main findings from §3.2:

Mechanical data:

- *RT yield stress: 580 MPa (0.02% yield) and 620 MPa (0.2% yield). HT yield stress 435 MPa (0.2% yield). The HT stress-strain curve shows an onset of a transient regime in between 200 to 250 MPa.*

Diffraction data:

- *Only ferrite phase visible in the diffraction pattern.*

- *In situ RT tensile deformation: Multiple in situ measurements have shown that ToF neutron diffraction is a reliable measure of the lattice strain for the ferritic matrix. This technique therefore allows a comparison of the evolution and magnitude of the residual strain for samples subjected to different loading conditions.*

- *Residual lattice strain in pre-deformed samples: The magnitude and evolution with plastic strain of both the {hkl} lattice strain and the phase strain strongly depend on the loading condition. In the axial direction, the largest phase strains are accumulated during RT tensile deformation. During HT tensile deformation significant phase strains develop only in the early plastic regime. Creep only accumulates a little amount of phase strain. On the other hand, both HT tensile and creep deformation results into larger axial intergranular strains than RT tensile deformation.*

3.3 Materials Science (MS) beamline: Synchrotron XRD

In situ tensile tests at RT have been performed using a 1D detector. The nomenclature of the samples tested and reported in this section is given in Table 7.

Table 7 Nomenclature of the samples reported in this section. For more details see §2.3.5.7.

Sample name	Material	Deformation History
MS1	1%CrMoV (Batch A)	In situ: Axial direction
MS2	1%CrMoV (Batch A)	In situ: Axial direction
MS3	1%CrMoV (Batch A)	In situ: Axial direction
MS4	1%CrMoV (Batch A)	In situ: Transverse direction

3.3.1 Diffraction pattern the as-received 1%CrMoV

Figure 59 shows a XRD pattern of the as-received 1%CrMoV steel acquired at the MS beamline with long acquisition time. Basically all of the low intensity peaks can be identified as either cementite or vanadium carbide and the various *hkl*-reflections are indexed. For clarity, the cementite peaks are indexed only up to the (311) and the vanadium carbide peaks only up to the {222}.
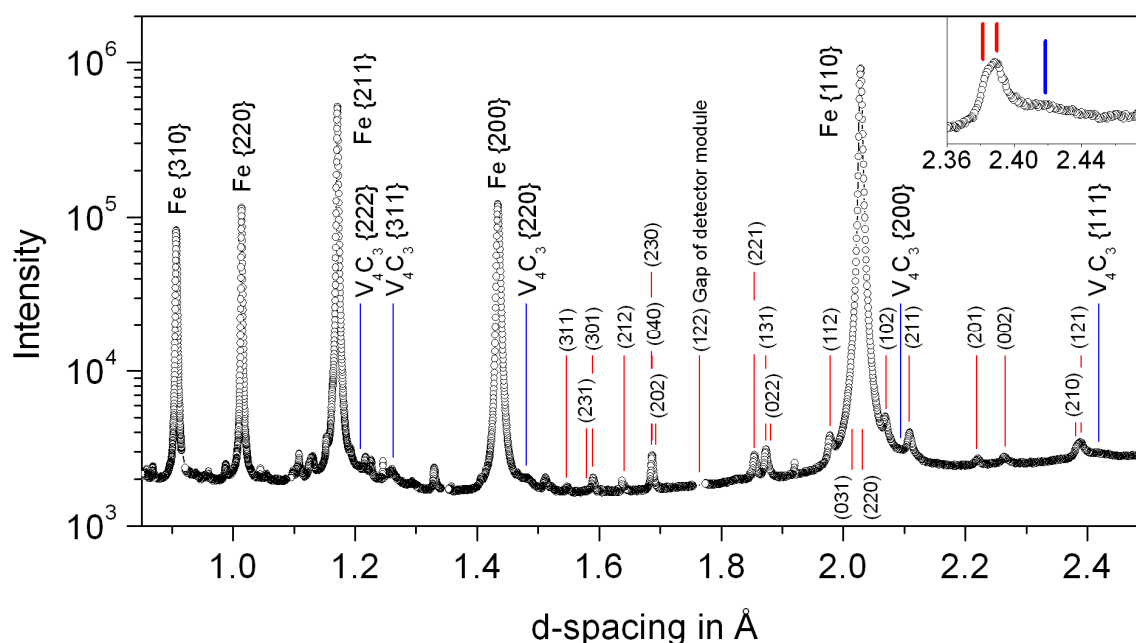
Figure 59 X-ray diffraction pattern for the as-received 1%CrMoV steel. The intensity axis is shown in log-scale to account for the low intensity peaks from the second phases cementite (orthorhombic with space group Pnma and lattice parameters a=5.0920Å, b=6.741Å, c=4.5170Å along the [100], [010], [001] direction, respectively) and vanadium carbide (fcc with a=4.160Å). The peaks of the corresponding phases are indexed until the {222} V_4C_3 (blue lines) and the (311) cementite (red lines). Detector gaps (cf. §2.3.5.1) are every 2θ=5° (beam energy 25keV). Here, the (122) cementite peak is within the gap, but for in situ measurements the detector is rotated because the (122) has a rather high intensity and can therefore be well analyzed. Then, however, the (212) cementite peak is within the gap and can not be analyzed.

Most of the cementite peaks do overlap with the peaks of ferrite, vanadium carbide and other cementite peaks and/or are too low in intensity to be resolved. For single peak fitting only the following cementite reflections are therefore suited: (002), (201), (211), (102), (112), (221), (122), (212) and (301). The (301) is not affected by its neighbouring (231) peak, which has a very low intensity (cf. also Figure 53). The relative difference between the {110} ferrite and the average cementite reflections is of the order of 10^2 to 10^3. The peaks from the vanadium carbide are very broad and overlap with those of cementite (e.g. {111} V_4C_3) and/or ferrite (e.g. {200} V_4C_3) as highlighted in the inset of Figure 59. An analysis of the behaviour of the vanadium carbide during deformation is therefore not possible by only following their diffraction peaks. Another approach considering heat-treated samples with a subsequent precipitation structure (first cementite and then additionally vanadium carbide) was therefore envisaged (cf. §3.4.2), which finally was not successful.

About sampling statistics: During the first test, large variations in the diffraction peak intensities have been observed when the sample is rotated. Figure 60 shows in (a) the ferrite peaks and in (b) a zoom to see some low intensity peaks. Three diffraction patterns are shown; in (a) they have been shifted along the x-axis for clarity. Each pattern has been acquired by rotating the sample within one degree (e.g. from 7.5°-8.5°) with respect to the incoming beam axis and during data acquisition, schematically illustrated in the inset of (a). For the three datasets acquired at 8°, 9° and 10°, there are some variations in intensities for the contribution of both the ferrite (a) and the cementite (b).
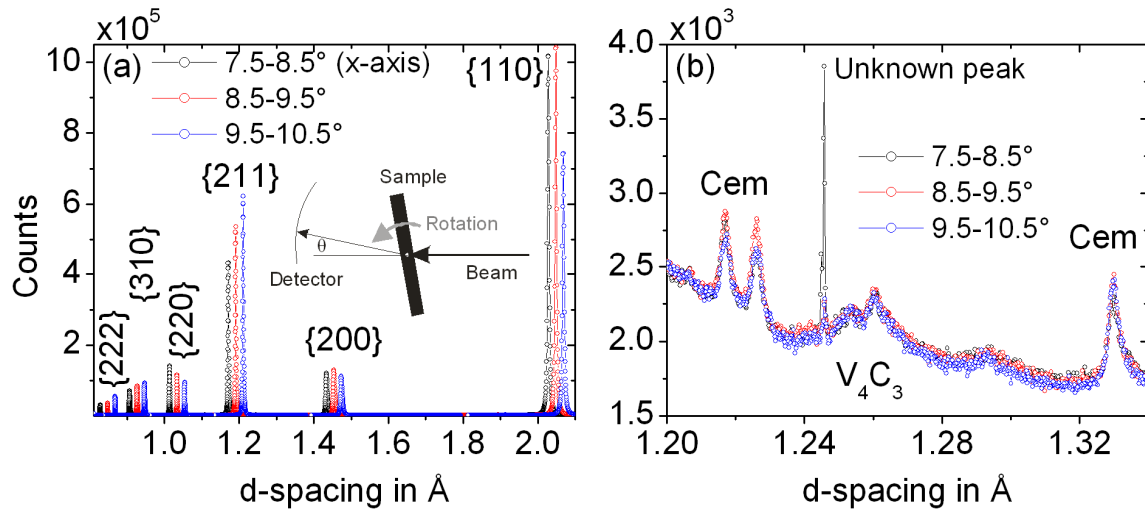
Figure 60 Diffraction pattern acquired with X-rays at the MS beamline for the as-received 1%CrMoV steel by rotating the sample within one degree during acquisition (at 8°, 9° and 10°). (a) The full pattern showing the first six ferrite reflections (curves are artificially shifted in the x-axis for clarity). (b) Reduced range showing some cementite, broad vanadium carbide with some cementite peak superimposed and a very narrow peak, that only shows up for in the range 7.5-8.5°.

Since the radiation is monochromatic, sample rotation brings different subsets of grains into diffraction condition at the Bragg angle θ. The intensity variations therefore indicate that the sampling statistics are too low. For the ferrite this is certainly because of its large grains size. Note, that one dataset in Figure 60 already represents the integration over 1°, whereas for the in situ test, the results of which are reported in §3.3.2, the angle is fixed. Note further that a few and very narrow peaks are pronounced during one rotation range (e.g. 7.5 to 8.5°) but cannot be observed for the two others. Figure 59 is a weighted sum of the three patterns in Figure 60.

3.3.2 In situ tensile loading at RT

3.3.2.1 Ferrite and cementite lattice strain behaviour

Figure 61(a) shows the evolution of the {110}, {200} and {310} ferrite grain families during RT tensile loading and in the axial direction. The datasets of two measurements (samples *MS1* and *MS2*) are shown. There are variation in both the elastic and the plastic regime for the different samples due to the low sampling statistics (cf. Figure 60 with explanation). The behaviour in the elastic regime of the {110} and {200} from the corresponding representative neutron data (sample *POL1*, Figure 58) is indicated as reference by the solid lines. In spite of the sample-to-sample variations, the order of the stiffness according to the cubic anisotropy factor (Eq. 11) is preserved for both samples *MS1* and *MS2*: The stiffness decreases from {110} to {310} to {200}. This point is important in order to report on a potential elastic anisotropy in the cementite phase in §3.3.2.3.
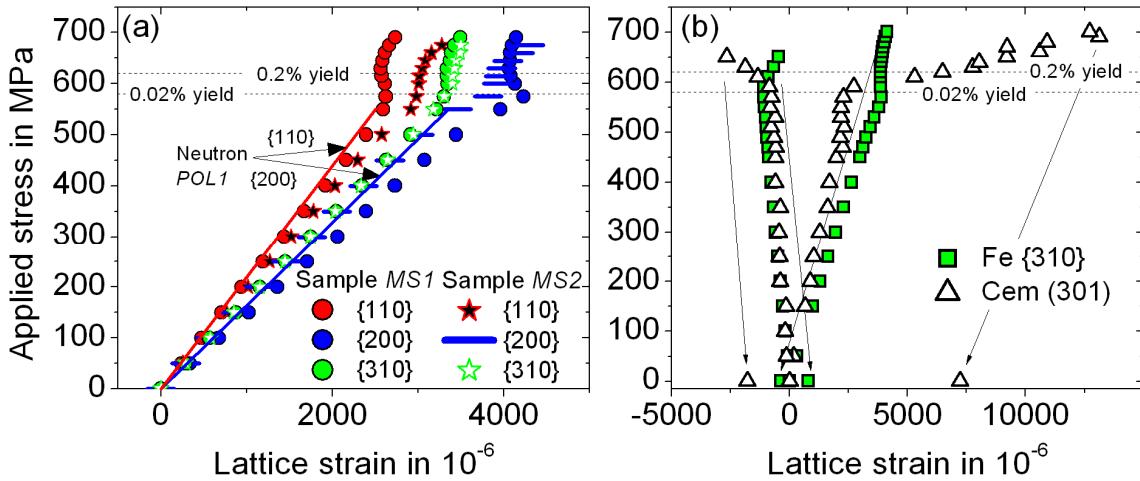
Figure 61 Lattice strain evolution during RT tensile loading: (a) Three ferrite grain families of samples *MS1* and *MS2*. The straight lines represent the elastic behaviour of the {110} and {200} ferrite grain family of measured by ToF neutron diffraction, sample *POL1*. (b) The ferrite {310} and the cementite (301) grain family in the axial (sample *MS3*) and transverse (sample *MS4*) direction, including measurement in the unloaded state. The arrows indicate the unloading trajectory.

Note that two samples have to be tested to obtain the axial and the transverse response and since already the axial direction shows sample-to-sample variations, the transverse data is omitted here. The difficulties interpreting the lattice strain from the transverse direction is described in §2.2.3.1.

A further sample (*MS3*) has been tensile deformed. A common trend for the lattice strain behaviour of the ferrite and the cementite phase during RT tensile deformation is observed for the three samples *MS1*, *MS2*, *MS3*. Figure 61(b) compares the behaviour of the {310} ferrite and the (301) cementite reflection in the elasto-plastic regime (sample *MS3* axial and sample *MS4* transverse). The {310} behaves qualitatively similar to the neutron diffraction data (cf. Figure 58). The {310} evolves linearly with the applied stress until the 0.02% yield. The slope in the axial direction is determined to E(310) = 150±1 GPa. This value is lower than that for the corresponding neutron data, i.e. 175±1 GPa for sample *POL1* and 181±3 GPa sample *POL3*. Beyond the 0.02% yield, the lattice strain deviates from its hitherto linear behaviour and is identified to be similar to the neutron diffraction data (cf. Figure 58). The lattice strain of the (301) cementite reflection increases first linearly with the applied stress until the 0.02% yield. Beyond the 0.02% yield, the cementite lattice strain increases considerably in both the axial and the transverse direction. Unloading then results into residual lattice strains, which are tensile in the axial and compressive in the transverse direction. These residual lattice strains are larger than those of the {310} ferrite grain family and of opposing sign: For instance, the ferrite is in axial compression and the cementite in axial tension. This is the typical behaviour during RT tensile deformation of a microstructure with a ferritic matrix and cementite particles (cf. §1.3.1).

3.3.2.2   Extreme cementite peak broadening

Figure 62(a) shows the stress-strain curve of the in situ test of sample *MS3*. Indicated on the stress-strain curve are markers at five different locations: Before straining, at the end of the elastic regime, in the early and late plastic regime and finally in the unloaded state. Figure 62 (b)-(d) show the diffraction peaks of the {310} ferrite and the (301) and (122) cementite in the axial direction at the corresponding locations on the stress-strain curve. The intensity of the peaks is normalized to the intensity of the most intense peak, i.e. the ferrite {110} before deformation. The {310} peak is shown as reference for the ferrite. At the onset of macroscopic yield (0.02%) and until the maximum load, the cementite peaks start broadening significantly and the peak shape becomes very asymmetric with the flatter tails towards larger d-spacings (higher lattice strains). After unloading, the peaks slightly shift back but remain very broad and asymmetric. The broadening is much more pronounced for the cementite than for the ferrite, which certainly has been plastically deformed. Increased dislocation density due to plastic deformation is known to increase the peak width. The origin of the extreme broadening and asymmetry of the cementite diffraction peaks is discussed in §4.4.2.
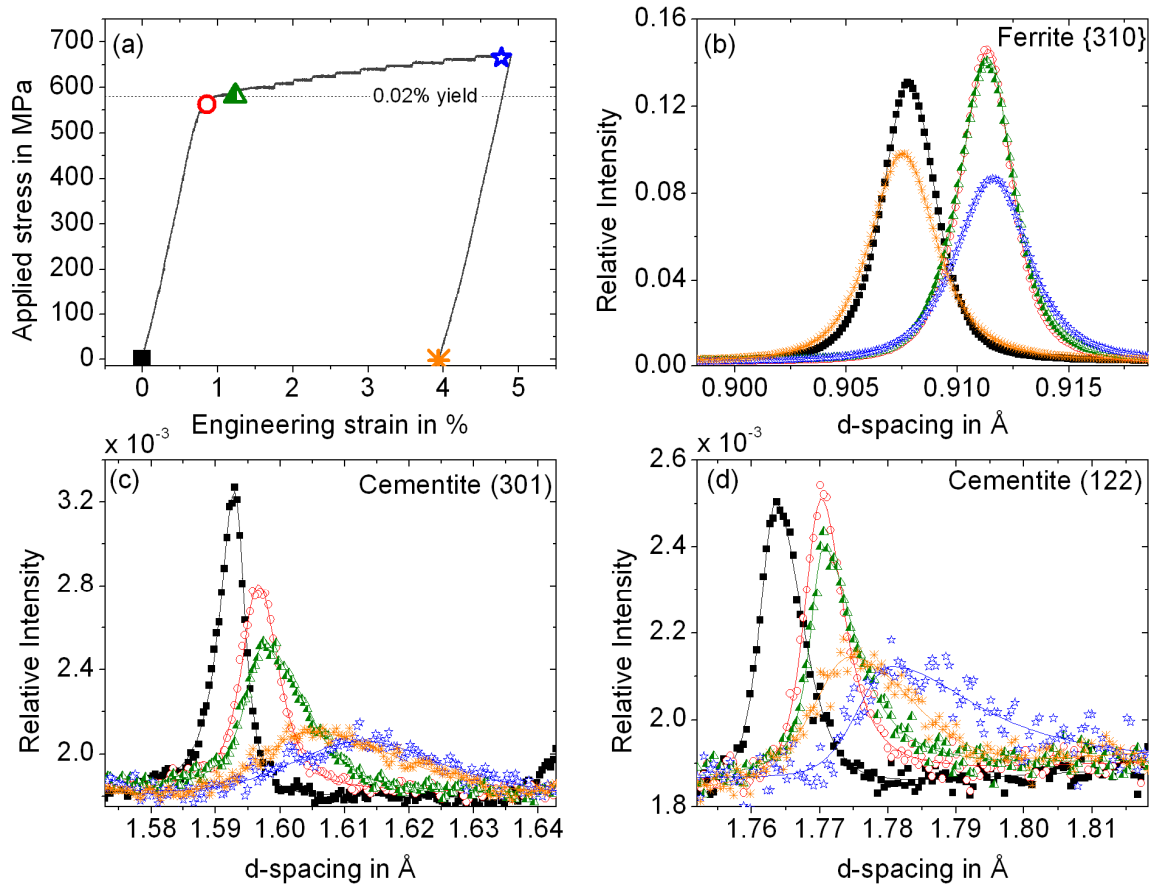
Figure 62 (a) Stress-strain curve of sample *MS3* deformed in situ. (b) Ferrite {310} and (c)-(d) cementite diffraction peaks (301) and (122) with the scattering vector parallel to the loading direction: Before loading, at the end of the elastic regime, in between the 0.02 and 0.2% yield, before unloading and in the unloaded state. The intensity of the diffraction peaks is scaled to the most intense peak, i.e. the ferrite {110} before deformation. The colour code and symbol type of the data points correspond to the symbol identifying the position on the stress-strain curve given in (a). The lines in (b) to (d) are the peak fit.

3.3.2.3 Stiffness of cementite grain orientations

Figure 63(a) shows the applied stress vs. lattice strain of the (301) and the (122) cementite grain orientations. Both diffraction peaks can be resolved well throughout the elastic regime (cf. Figure **62** (c) and (d)). The lines represent the linear regression of the first 14 data points (until 560 MPa) in the elastic regime. It follows that the slope of the (301) is steeper compared to that of the (122). This is valid in both the axial (230±4 and 160±2 GPa, respectively) and the transverse (-711±2 and -536±2 GPa, respectively) direction. Figure 63(b) shows the evolution of the applied stress vs. lattice strain of other non-overlapping cementite peaks (cf. Figure 59) focusing on the elastic regime in the axial direction. The scatter in the corresponding data points is larger than for the (122) and (301) due to the lower peak intensity. In spite of the scatter, some grain orientations appear to be stiffer than others. These results point towards an elastic anisotropic behaviour of cementite, which has not

yet been reported during in situ deformation of carbon steel. On the other hand, it has been reported that some cementite grain orientations carry more load than others in the plastic regime. This was investigated during RT tensile deformation of a high-carbon steel with a large volume fraction of cementite (34%) [65]. Considering the pronounced peak broadening during the macroscopic plastic regime, including the manifesting peak shape asymmetry (cf. Figure 62) with a correspondingly large scatter of the data points (cf. Figure 63(a) highlighted area), an anisotropic behaviour of cementite in the macroscopic plastic regime and in the amount of residual strain after unloading remains unclear for the current dataset.
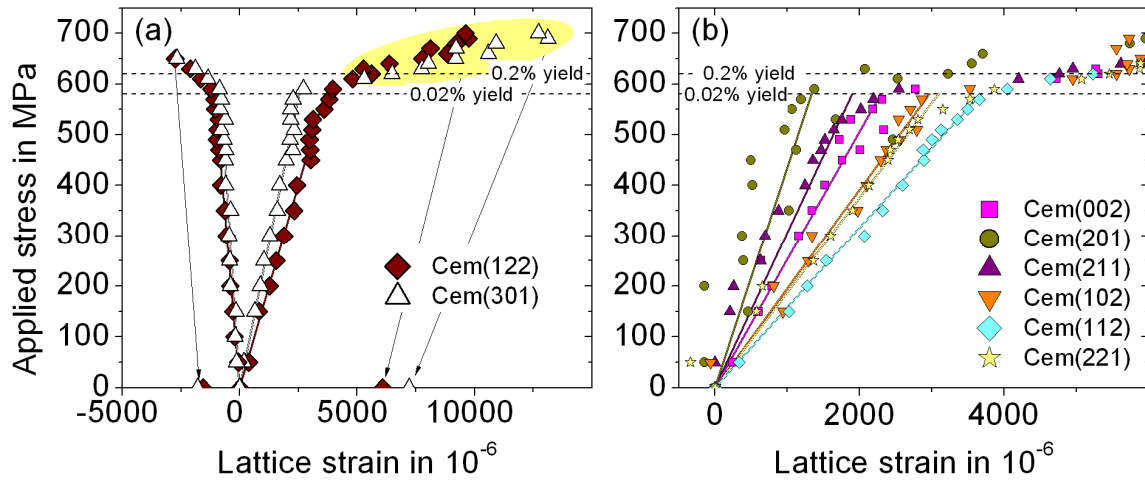
Figure 63 Lattice strain with applied true stress for various cementite grain orientations: (a) (122) and (301) in the axial and transverse direction (Sample *MS3* and *MS4*, respectively) and (b) other non-overlapping reflections; due to the large scatter only shown for the axial direction (Sample *MS3*) and to 0.6% lattice strain. The order in the legend (b) corresponds to the decreasing d-spacing, from (002) to (221).

Note that the particular arrangement of the cementite in this tempered bainitic microstructure (cf. §1.2.2 and Figure 52(a)) may have an effect on the lattice strain evolution with applied stress and hence may affect the stiffness for some orientations. Therefore, samples of a high-carbon steel with different microstructure were tensile deformed in situ, reported in §3.4.3. An anisotropic behaviour of cementite in the elastic and plastic regime is discussed in §4.4.1 and §4.4.3, respectively.

Main findings from §3.3:

Diffraction spectra:

• *Ferrite, cementite and vanadium carbide are observed in the spectra. The ratio of the intensity of the average ferrite and cementite peaks is of the order of 10^2 to 10^3. Only the ferrite and selected cementite peaks can be studied during deformation as the broad and low intensity peaks from the vanadium carbide overlap with peaks from cementite and ferrite.*

Lattice strain evolution during RT tensile:

• *Sample-to-sample variation in the ferrite response show that the sampling statistics are too low. However, the order of elastic anisotropy for the three ferrite grain families is preserved.*

• *Qualitatively: At the onset of macroscopic plasticity, ferrite is shedding load on to the cementite. As a consequence, residual strains of opposing sign in both phases are left in the sample after unloading.*

Cementite characteristics:

• *Cementite peak broadens extremely in the plastic regime and vanish almost within the background. The peaks also become asymmetric with the flatter tail towards higher lattice strains.*

• *Some cementite grain orientations are stiffer than others during elastic tensile loading.*

3.4 ID15B beamline: Synchrotron XRD

ID15B provides a high beam-energy (used: 90keV) with a correspondigly large penetration depth of the X-rays in the investigated steel samples and a 2D detector, which allows increasing the sampling statistics compared to §3.3. A HT loading rig is available, which allows investigating the findings of the ex situ measurements (§3.2) with in situ studies and considering both, the matrix and the cementite contribution.

Table 8 Nomenclature of the samples reported in this section. For more details see. §2.3.5.7

Sample name	Material	Deformation History
ID0	1%CrMoV (Batch C)	In situ: Continuous tensile at RT
ID1	1%CrMoV (Batch C)	In situ: Continuous tensile at RT
ID2	1%CrMoV (Batch C)	In situ: Continuous tensile at HT
ID3	1%CrMoV (Batch C)	In situ: Load-Unload tensile at RT
ID4	1%CrMoV (Batch C)	In situ: Load-Unload tensile at HT
ID5	1%CrMoV (Batch C)	In situ: Creep at 565°C/130MPa
Heat1	Mod. 1%CrMoV (Batch C)	In situ: Tensile at RT
Heat2	Mod. 1%CrMoV (Batch C)	In situ: Tensile at RT
Heat3	Mod. 1%CrMoV (Batch C)	In situ: Tensile at RT
Heat4	Mod. 1%CrMoV (Batch C)	In situ: Tensile at RT
HC1	1.15wt%C, pearlite	In situ: Tensile at RT
HC2	1.15wt%C, temp. pearlite	In situ: Tensile at RT
HC3_S1	1.15wt%C, spheroidized	In situ: Tensile at RT
HC3_S2	1.15wt%C, spheroidized	In situ: Tensile at HT

3.4.1 As-received 1%CrMoV

3.4.1.1 In situ tensile deformation: RT vs. HT (565°C)

The results from continuous tensile tests at RT (sample *ID1*) and HT (sample *ID2*) are shown next to each other in Figure 64 for a direct comparison. The first row shows the recorded stress-strain curve, the second and the third row show the lattice strain evolution in the axial and the transverse direction, respectively. The three ferrite ({220}, {200}, {310}) and the two cementite ((122), (301)) grain orientations are shown. Only a reduced number (every 20th data point) for the ferrite grain families is shown for clarity. The {220} is taken instead of the {110}, since the latter peak is saturated and cannot be used (cf. §2.3.5.2). Superimposed are lines at the corresponding yield stresses (cf. §3.2.1). Note that the (engineering) strain is not reliably measured (cf. §2.3.5.2). The inset in (b) and (e) focuses on the {220} and {200} grain families in the elastic regime.

The lattice strain evolution during RT tensile loading has already been described in detail for the ferrite {110}, {200}, {310} in §3.2.2 and for the ferrite {310} and the cementite (301) in §3.3.2. The behaviour of these orientations is qualitatively similar to those in sample *ID1*.

Consider the axial direction: At HT, the lattice strain of the ferrite and cementite evolves linearly with applied stress until about 200 MPa. Then it deviates from the linear behaviour. This is more clearly shown for the {220} and the {200} in the inset in (e). This deviation can only be seen by eye at higher stresses. A more detailed plot is shown in the discussion (Figure 99(b)). The {220} deviates towards smaller and the {200} towards larger lattice strains, as indicated by the arrows. The cementite behaves qualitatively similar as the {200} until around the 0.2% yield. At RT (b), a deviation of the {220} and the cementite orientations is observed at the 0.02% yield stress (580 MPa), the {200} already deviates earlier at around 500 MPa and towards higher lattice strains, as it does during HT tensile deformation. The stiffness of the {220} and the {200} are rather different at RT (215 GPa / {220} and 175 GPa / {200}) and at HT (185 GPa / {220} and 130 GPa / {200}). These values have been obtained by a linear fit in the range of 0 to 200 MPa and are summarized in Table 9. The ratio of the stiffness {220}/{200} amounts to 1.23 at RT and 1.42 at HT.

Table 9 Axial stiffness of the {220} and {200} ferrite grain families of the 1%CrMoV steel during tensile loading at RT (sample *ID1*) and 565°C (sample *ID2*) obtained a linear fit in the range 0 to 200MPa.

Temperature	Axial {220}	Axial {200}	Ration
RT	215±8GPa	175±7GPa	≈1.23
HT (565°C)	185±6GPa	130±9GPa	≈1.42
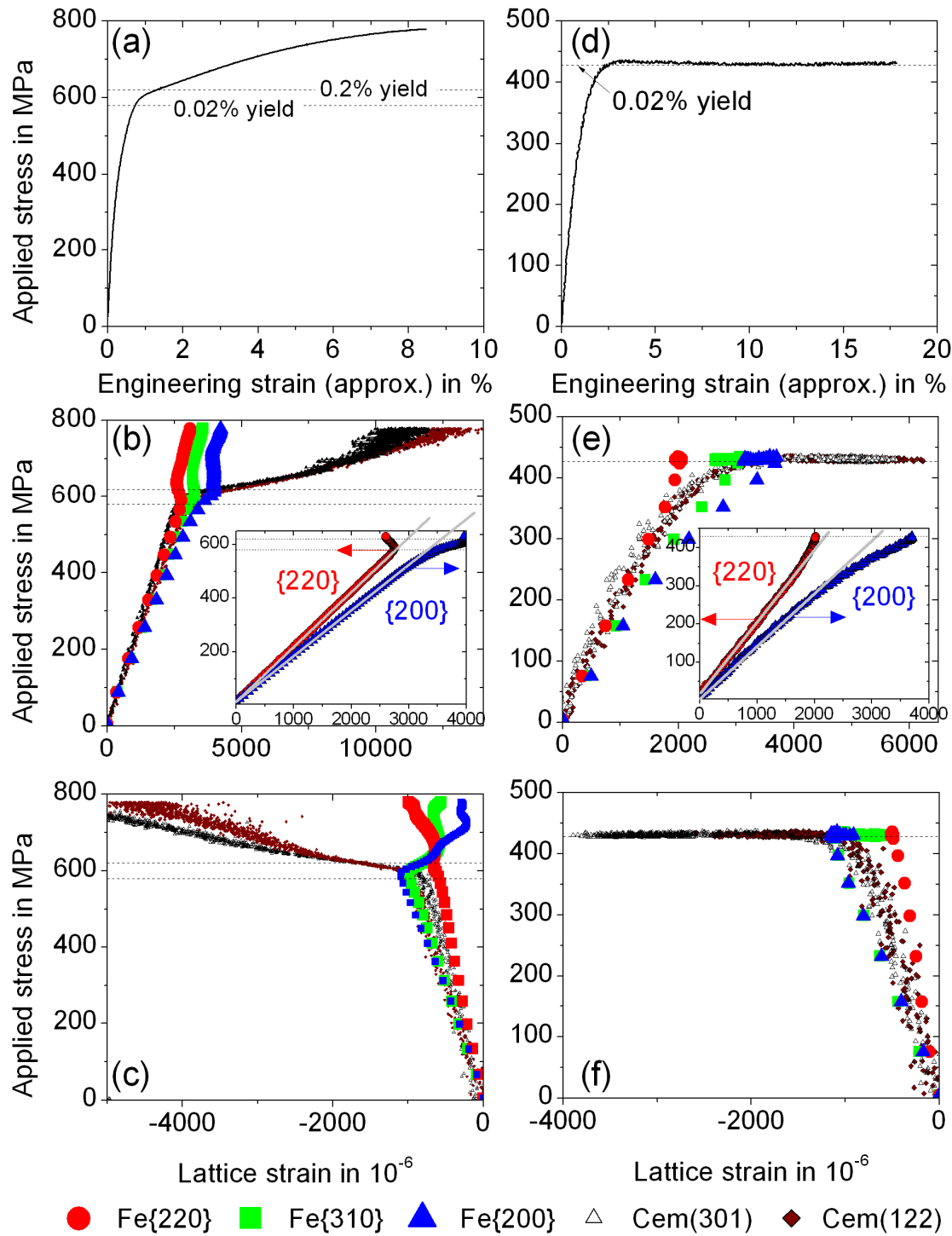
Figure 64 Stress-strain curve and applied stress vs. lattice strain (axial and transverse direction) for three ferrite grain families and the two cementite grain orientations during tensile deformation at RT in the left column (a)-(c) and 565°C (HT) in the right column (d)-(f). The dashed line indicates the corresponding yield stress. Only every 20th data point (not in the inset) is plotted for the ferrite for clarity. The indicated yield stress is the one obtained from the ex situ recorded stress-strain curve (Figure 54(a)).

Beyond the yield stress, the load transfer to the cementite becomes even more dominant, now also from the {200}. The applied stress is constant during HT tensile deformation in the plastic regime. The evolution of the lattice strain can therefore not be so well resolved from Figure 64(e). The lattice strain is now plotted as a function of engineering strain in Figure 65. The stress-strain curve is added for a direct comparison with the lattice strain evolution. Two yellow areas are shown: The first area highlights the regime where all three ferrite lattice strains reach their maximum value. This is also when the stress-strain curve reaches its steady-state like regime. The second area highlights the regime where the cementite lattice strain reaches its maximum value. This is only at later stages compared to the ferrite, indicative that the cementite phase strain is still slightly increasing within the steady-state like regime. This would agree with the results of the residual ferrite phase strain from the pre-deformed samples (cf. Figure 57(a)): The ferrite phase strain decreases slightly in between the two measuring points at 1% (-180 µε) and 4% (-250 µε) plastic strain.

The two grey areas highlight the {220} and the {200} in the plastic regime: The lattice strain of the {220} remains constant towards larger plastic strains; the {200} is decreasing. Assuming a linear unloading trajectory of the lattice stain with applies stress, the evolution of residual lattice strain with plastic strain would stagnate for the {220} and decrease for the {200}. This is indeed observed for the pre-deformed samples investigated by ToF neutron diffraction (cf. Figure 57(b), §3.2.1) and provides confidence that the lattice strain evolution in Figure 65 is bulk representative.
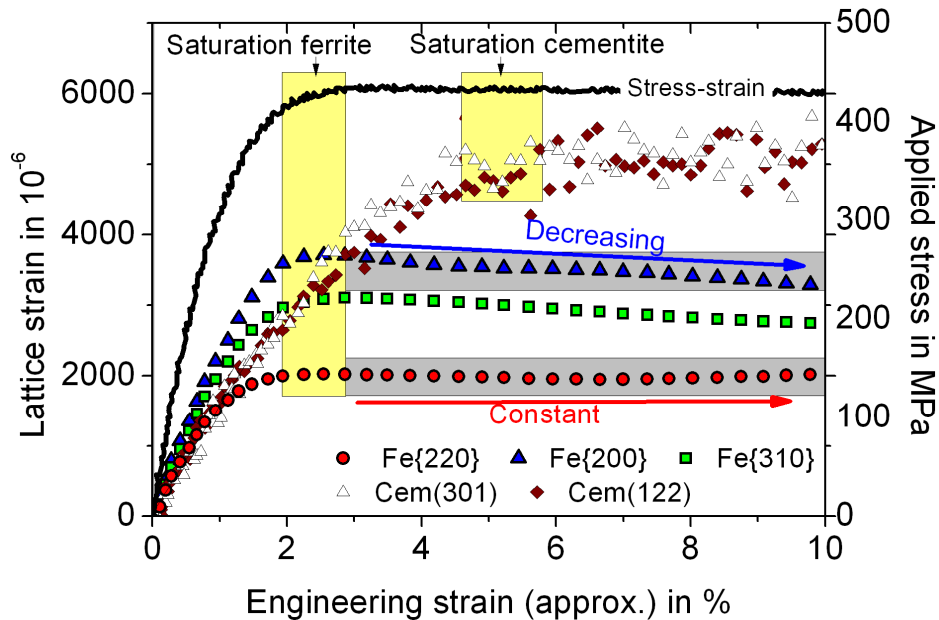

Figure 65 Axial lattice strain during HT tensile deformation plotted as a function of engineering strain (sample *ID2*, cf. Figure 64(e)): The yellow area highlights the regime where the ferrite lattice strain and the cementite lattice strain reach their maximum value. The grey area highlights the behaviour of the {220} and {200} during the plastic regime. The stress-strain curve is added.

A series of load/unload cycles have been performed at RT (sample *ID3*) and HT (sample *ID4*). Since the (engineering) strain cannot be reliably measured, the stress-strain curve does not give additional information and is not shown. Time-dependent recovery effects at HT in the unloaded state may distort the value of residual lattice strain when not directly measured after unloading. This is an important aspect for a comparison with the ex situ measured samples. Two diffraction patterns have been acquired after unloading. The acquisition of each pattern was long (32 s) to obtain good statistics for the cementite. The waiting time between the acquisition of these two patterns was 5 min.

Ferrite: Figure 66 compares the residual lattice strain for the {200} and the {211} ferrite grain families from sample *ID3* with the data points from the ToF neutron diffraction measurements (cf. 3.2.1) for a direct comparison. While the trend for the {211} agrees reasonably well, a rather poor agreement is found for the {200}. The {211} and the {200} are known to be the least and the most affected by intergranular strains in bcc iron, indicative that the sampling statistics is too low to obtain representative information for the evolution of residual strain. The evolution of residual strain during HT tensile deformation is therefore investigated with ToF neutron diffraction (cf. §3.5.2). Recovery effects on the residual ferrite lattice strain and the engineering strain are also investigated in section §3.5.2.
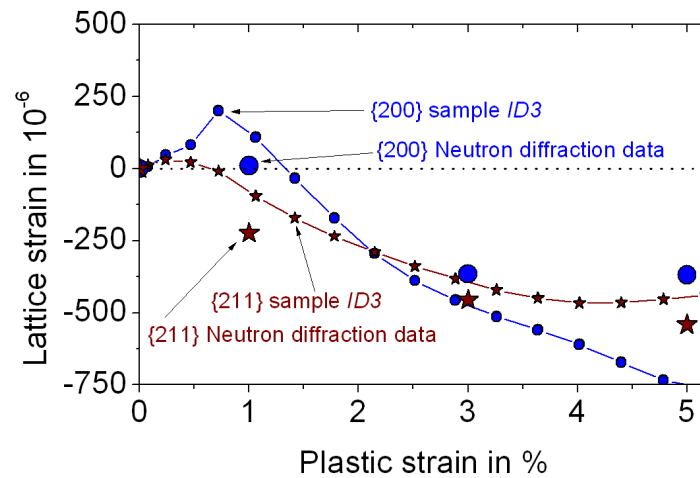
Figure 66 Residual lattice strain evolution with plastic strain for the {200} and the {211} ferrite grain families. Compared are the results from sample ID3 with data points of the bulk representative ToF neutron diffraction.

Cementite: The evolution of the residual lattice strains of the (122) and (301) orientations in the axial and transverse direction are shown in Figure 67, after (a) RT and (b) HT tensile deformation. In both cases, the axial residual lattice strain is tensile and the transverse residual lattice strain is compressive. At RT, the magnitude is constantly increasing, although its rate decreases slightly towards large plastic strain but does not reach saturation. At HT, the lattice strain increases strongly until around the third data point at 1% plastic strain and then saturates at values around 3000 $\mu\varepsilon$ in

the axial and 2000 με in the transverse direction. At low plastic strains (< 1%), the residual strain at RT and HT are of about the same magnitude. Due to the scatter of the cementite data points, it is not clear whether there is a decrease in the magnitude of the residual strain (relaxation) for the subsequent two patterns.
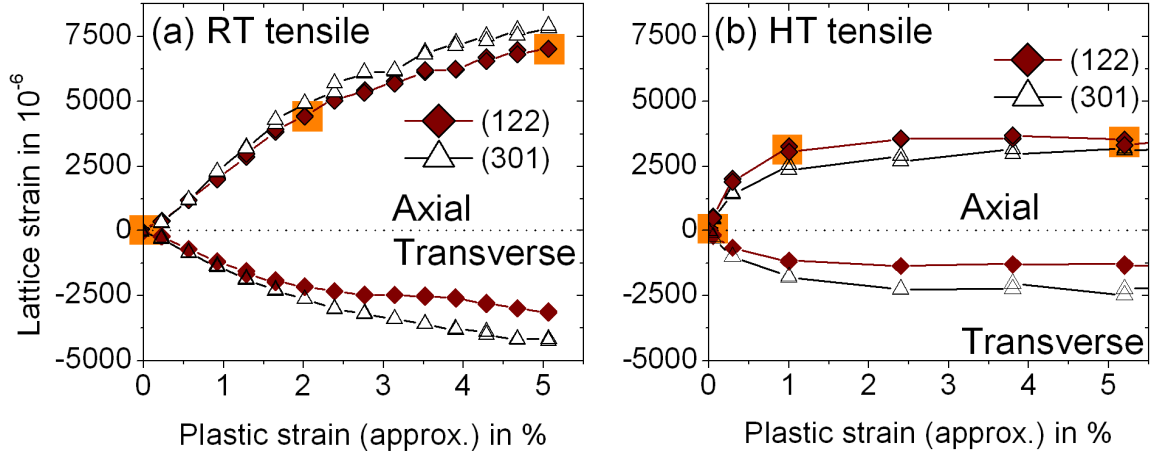
Figure 67 Residual lattice strain for the (122) and (301) cementite grain family as a function of the plastic strain after tensile deformation at (a) RT and (b) HT (565°C). The orange squares refer to the diffraction peaks, which are shown in Figure 68.

Three positions of the axial (122) cementite data points are highlighted in Figure 67 at RT and HT: Before deformation, at around 2% (RT) and 1% (HT) and at 5% plastic strain. The corresponding diffraction peaks are shown in Figure 68 (a) and (b) for the RT and the HT case, respectively. During RT tensile deformation, the peak broadens significantly and becomes asymmetric towards larger d-spacings (higher lattice strains), being in agreement with the observation in from the MS Beamline, Figure 62. During HT tensile deformation, the peak only shows a slight broadening, no significant asymmetry and hardly changes in between 1% and 5% plastic strain, where the lattice strain is saturated.

Figure 68 Axial cementite (122) peak shape before the start of the tensile test (black line) and after tensile deformation (unloaded state) at (a) RT (2, 5% plastic strain) and (b) HT (565°C) (1, 5% plastic strain).

3.4.1.2   In situ creep at 565°C / 130 MPa

One sample (*ID5*) was creep deformed at 565°C / 130 MPa, which is below the stress (200 MPa) where a deviation from the linear elastic behaviour in the HT tensile 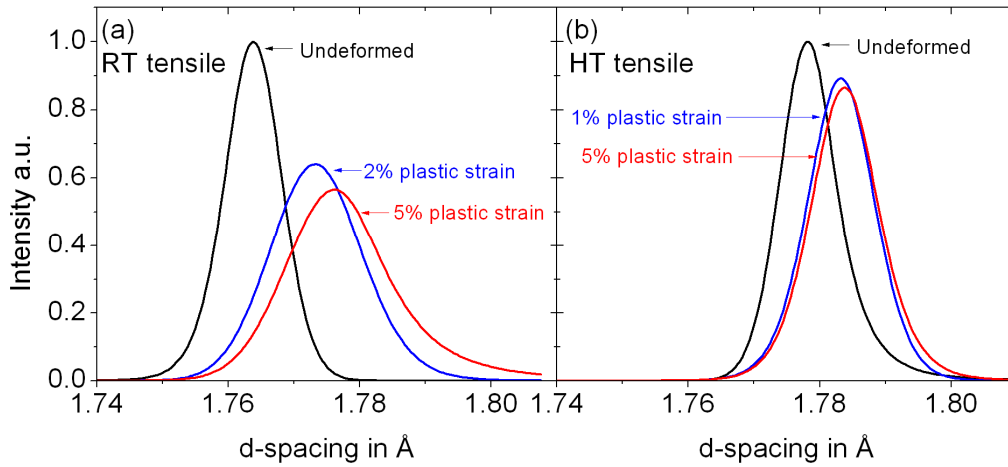stress-strain curve has been observed (cf. Figure 55). Changes in the peak position at these small creep stresses are assumed to be small. This test has therefore been performed with X-rays due to their correspondingly high counting statistics in order to minimize the scatter of the data points and make a potential trend for the ferrite grain families visible. The high counting statistics also allows to capture well the cementite behaviour. In situ creep tests at higher stresses of 290 and 330 MPa are performed with neutron diffraction, which provides representative information of the ferrite matrix and is presented in §3.5.4.

In Figure 69 (a) and (b), the lattice strain of the ferrite {220}, {200}, {310} and the cementite (122), (301) is shown in the axial and transverse direction, respectively. The lattice strain is plotted as a function of time rather than (engineering) strain since the latter is not reliably measured. The magnitude of the lattice strain for all ferrite grain families and both directions is increasing with time. The cementite behaves differently: The lattice strain for the (122) and the (301) in the axial direction remains constant with time. In the transverse direction, the magnitude of the lattice strain of both cementite orientations is soon decreasing significantly in magnitude. The (301) starts to decrease immediately and by about 40% from the beginning (-250 µε) to the end (-150 µε) of the experiment. The (122) starts to decrease only after about four hours.
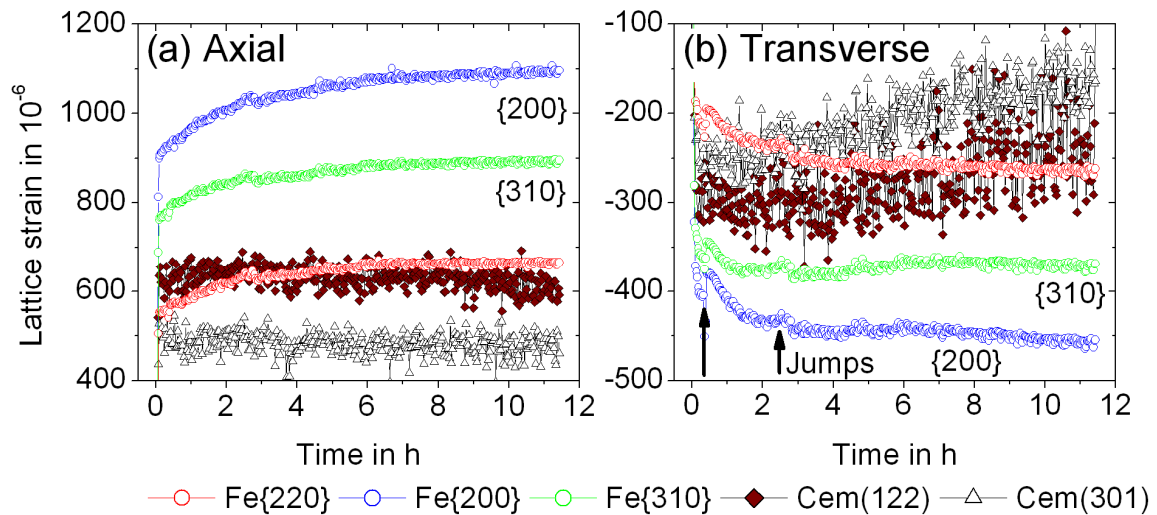
Figure 69 Evolution of lattice strain of the three ferrite and two cementite orientations as a function of time during creep at 565°C/130MPa (sample *ID5*): (a) the axial direction and (b) transverse direction. The two arrows in (b) indicate the positions where some discontinuity in the lattice strain behaviour is observed.

It has to be mentioned that there are some sudden jumps in the transverse ferrite lattice strain at 0.5 and 2.5 h, indicated be the two arrows in figure (b). To minor extend this is also visible in the axial

direction but hardly for the cementite, maybe due to its large scatter. These jumps cannot solely originate from the microstructural evolution. The stress and the temperature were constant over the whole period with 130 ± 0.5 MPa and 565 ± 1 °C, respectively. The displacement recorded by the motor encoder, however, also shows some features at the same time stamps and small sample movements can therefore not be excluded and may be responsible for these jumps. These artefacts, however, do not affect the as-described trend of the grain orientations during creep.

3.4.2 Information from the heat-treated 1%CrMoV material

In §3.1, two types of precipitates have been identified in the as-received 1%CrMoV steel: While the cementite behaviour can be studied by following some of its diffraction peaks during deformation, this is not possible for the vanadium carbide since its diffraction peaks (broad and peak overlap) cannot be resolved well (cf. Figure 59). The approach was therefore to deform samples in situ, which have different precipitation contents due to appropriate heat treatments: Quenching should produce bainitic cementite (§1.2.2) and subsequent tempering additional vanadium carbide (§1.2.3). The influence of the vanadium carbide on the accumulation of residual strain was then supposed to be elucidated by comparing the ferrite and cementite behaviour in each sample. That, of course, is only possible, if the difference in the lattice strain behaviour is significant. Samples for tensile deformation have been prepared (cf. §2.1.1.2): *Heat1* is the quenched microstructure, *Heat2* to *4* are subsequently tempered at 700°C for 1, 3.5 and 7 hours, respectively.

The diffraction patterns of the four heat-treated samples (*Heat1* to *4*) are shown in Figure 70.
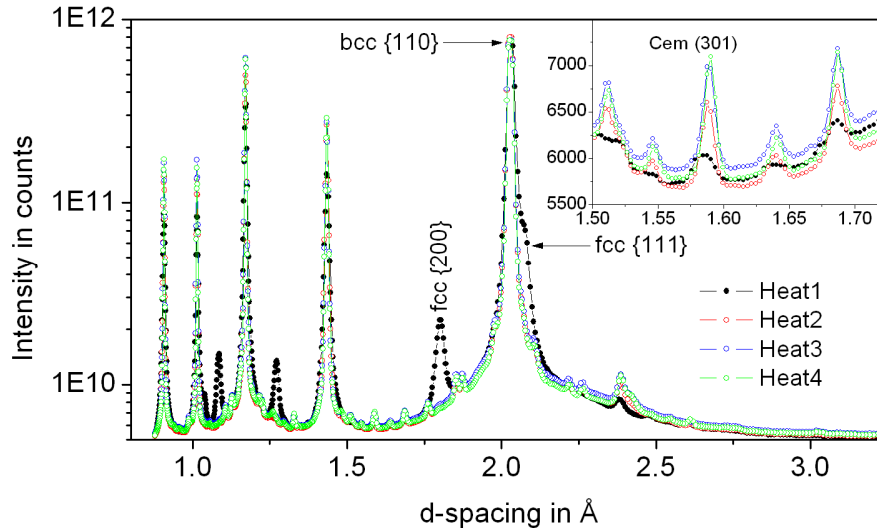

Figure 70 XRD pattern of the four heat-treated 1%CrMoV samples (*Heat1* to *4*). The intensity is scaled logarithmic in the main figure and linear in the inset. An austenitic (fcc iron) phase is present in the as-quenched sample. This phase decomposes during tempering in ferrite and carbides and the intensity of, for instance, the (301) cementite increases.

The as-quenched sample (*Heat1*) shows a dominating ferrite (bcc) phase but in addition also an austenitic (fcc) phase. To a small quantity, also cementite is present as shown in the inset. After one hour tempering (*Heat2*), the intensity of the cementite peaks increased and the austenite phase disappeared, presumably by decomposing into ferrite and carbides (cf. §1.2.2). Extracting the carbides from the matrix with the procedure described in §2.1.1.3 reveals that cementite and vanadium carbide are the main type of carbides, like in the as-received 1%CrMoV material (cf. Figure 53). Further tempering (*Heat3* and *Heat4*) does not significantly change the diffraction pattern, indicative that the ratio of cementite and vanadium carbide remains constant. Therefore, the approach to elucidate the behaviour of the vanadium carbide was not successful.

3.4.3 In situ tensile deformation of the high-carbon steel

This section reports on in situ tensile tests in a high-carbon steel (1.15 wt% C). The motivation for these experiments is the following: In §3.3.2.3 was reported that some cementite grain orientations in the 1%CrMoV steel are stiffer than others during elastic loading. Due to the low volume fraction of cementite ($< 3\%$) only the (310) and the (122) orientation could have been investigated with little scatter on the data points. In addition, some proportion of the cementite eventually has a crystallographic relationship with the ferritic matrix in the tempered bainitic microstructure, which may influence the stiffness of some orientations. To confirm the previous findings on the elastic anisotropy of cementite, samples with different microstructures of the high-carbon steel (cf. §2.1.2), i.e. pearlitic, tempered pearlitic and spheroidized, were tensile deformed in situ. Due to the high volume fraction of cementite (20%), the ratio between the intensity of the average cementite and the ferrite peaks is one order of magnitude higher than in the 1%CrMoV steel. The peak position of the cementite (122) and (301) orientations can therefore be obtained with little uncertainty, even in the highly plastic regime where peak broadening occurs (cf. §3.3.2.2). That also allows addressing a possible anisotropic behaviour of cementite in the plastic regime [65]. Other cementite grain orientations, however, cannot be resolved well due to the high background coming from the saturated {110} ferrite peak, as for the 1%CrMoV samples (cf. §2.3.5.2).

3.4.3.1 In situ RT tensile deformation of the various microstructures

The stress-strain curves and the lattice strain for the three microstructures during in situ RT tensile deformation are shown in Figure 71. The contribution of the pearlitic, the tempered pearlitic and the spheroidized microstructure are shown in the first row ((a) and (b)), the second ((c) and (d)) and the third row ((e) and (f)), respectively. The corresponding microstructures are recalled underneath the stress-strain curves. Note that the (engineering) strain is not reliably measured. The non-linear un-loading branch of the stress-strain curves does therefore not necessarily indicate large back-stresses.
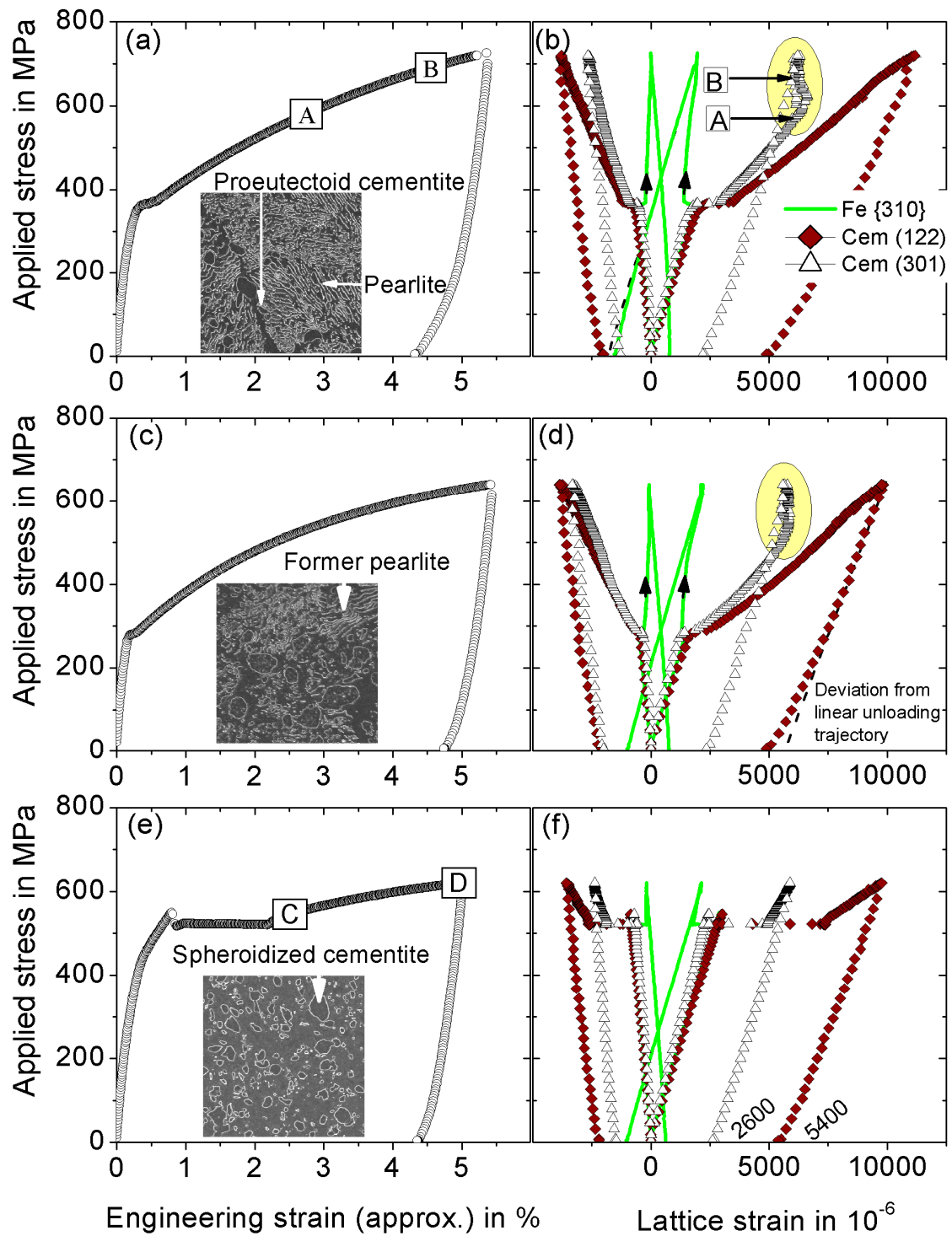
Figure 71 Stress-strain curves and corresponding lattice strain evolution during RT tensile loading of the pearlitic (sample *HC1*), the tempered pearlitic (sample *HC2*) and the spheroidized (sample *HC3_1*) microstructures. The ferrite {301} is shown as reference for the matrix and together with the (122) and (301) cementite orientations. Only every fourth data point for the cementite is shown for clarity. The inset underneath the stress-strain curve recalls the microstructure.

The stress-strain curves in (a) and (b) show a yield point at around 360 MPa and 280 MPa, respectively, followed by an extensive strain hardening. The stress-strain curve in (c) shows an upper yield point at 550 MPa followed by Lüders band deformation and a subsequent strain hardening, which is moderate compared to (a) and (b). The lattice strain is shown for the (122) and (301) cementite orientation and for the {310} ferrite grain family as reference for the matrix behaviour. We are focusing on three aspects: The stiffness of the two cementite orientations in the elastic regime, their behaviour in the plastic regime and the feature of the (301) axial lattice strain in the pearlitic and the tempered pearlitic microstructure at large plastic strains, highlighted in yellow.

Consider first the stiffness of the two cementite orientations. Figure 72 shows their lattice strain during loading for the spheroidized microstructure focusing on the elastic regime. The straight white lines superimposed on the data points represent a linear fit in between 0 to 250 MPa. Beyond 250 MPa, the lattice strain in the transverse direction already deviates from the linear elastic behaviour.
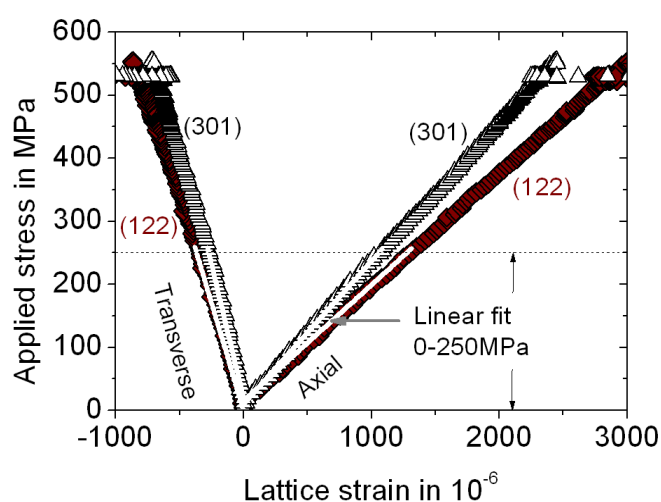
Figure 72 This graph is a zoom of Figure 71(f) (spheroidized microstructure), focusing on the elastic regime and shows the (301) and (122) cementite grain orientations. The white lines represent the linear fit of the corresponding data in the range 0 to 250MPa.

The stiffness obtained for the axial and the transverse direction is summarized in Table 10 together with the values for the pearlitic and the tempered pearlitic microstructure and the value for the spheroidized microstructure during tensile deformation at 500°C, reported in §3.4.3.2. In each case, the linear fit has been performed in between 0 to 250 MPa, where the evolution of lattice strain with applied stress is linear. The (301) is indeed stiffer than the (122) and hence agrees with the data from the 1%CrMoV steel (cf. §3.3.2.3). The values in the axial direction are all very similar with 180 GPa for the (122) and 230 MPa for the (301). The variations in the transverse direction are larger. Maybe surprising is that the values for the stiffness for the (122) and the (301) are the same at RT and at HT.

Table 10 Stiffness of the (122) and the (301) cementite orientations during elastic tensile loading at RT of the pearlitic (*HC1*), tempered pearlitic (*HC2*) and spheroidized (*HC3_1*) microstructures and elastic tensile loading at 500°C of the spheroidized (*HC3_2*) microstructure.

Microstructure	E(122) axial	E(301) axial	-E(122)/ν(122)	-E(301)/ν(301)
Pearlitic steel	180 GPa	220 GPa	-570 GPa	-830 GPa
Tempered pearlitic steel	170 GPa	220 GPa	-630 GPa	-920 GPa
Spheroidized steel	180 GPa	230 GPa	-680 GPa	-850 GPa
Spheroidized steel (500°C)	180 GPa	230 GPa	-690 GPa	-900 GPa

Consider now the cementite behaviour in the plastic regime and focus on the axial direction, for instance, in the spheroidized microstructure (Figure 71(f)). The shift in lattice strain from the onset to the end of Lüders band deformation is larger for the (122) than for the (301). At the end of Lüders band deformation, both lattice strains are increasing linear with the applied stress. The slope of the (122) is shallower than that of the (301), like in the elastic regime. This observation is true as well for the other two microstructures and for both the axial and transverse direction. The residual strain after unloading amounts to 2600 με for the (301) and to 5400 με for the (122). The residual strain of the (122) is therefore larger than that of the (301) and this is true in all three microstructures and for both the axial and the transverse direction. For the pearlitic and the tempered pearlitic steel, large deviations from the initial linear unloading trajectory are observed, as indicated for the axial (122) in Figure 72(c).

Consider now the feature of the axial (301) lattice strain highlighted in Figure 71 (b) and (d) and focus on the pearlitic microstructure (b). Figure 73 shows a zoom in the relevant region. The lattice strain evolution with applied stress is almost linear in the plastic regime until the point *A*.
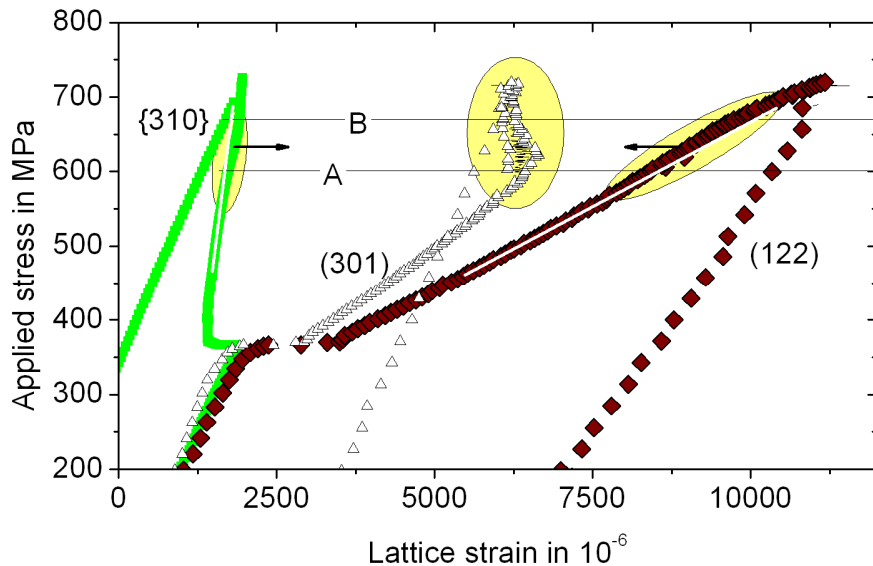

Figure 73 This graph is a zoom of Figure 71(b) (pearlitic microstructure), focusing on the plastic regime. The white lines superimposed on the ferrite {310} and the cementite (122) are a guide to the eye to observe the deviation of the lattice strain from the linear behaviour from at around the point *A*. Sample *HC1*.

The corresponding lattice strain amounts to 6000 µε. Beyond the point *A*, the lattice strain does not further increase or might even decrease. At the same time, also the (122) cementite and the {310} ferrite starts deviating slightly from the hitherto rather linear behaviour. The (122) and the {310} deviate towards opposite directions, as indicated by the arrows.

Figure 74 shows the diffraction peaks of the (301) and the (122) at the position *A* and *B*. The peaks from the axial direction are shown in (a), the peaks from the transverse direction are shown in (b). The peaks of the (122) in both directions and the (301) in the transverse direction become asymmetric with the flatter tail towards higher lattice strains, i.e. higher d-spacings in the axial and to lower d-spacings in the transverse direction in between the *A* and *B*. This behaviour has already been reported in §3.3.2.2 for the cementite in the 1%CrMoV steel. For the axial (301) peak, an additional contribution appears at stresses beyond point *A* and towards the peak tail at higher d-spacings (higher lattice strain), as shown in the highlighted region (1). The peak fit (not shown) covers well the upper region (highlighted region (2)) of the peak.

Figure 74 Diffraction pattern of the pearlitic microstructure with the (301) and the (122) cementite reflection at the stress levels *A* and *B*, as indicated in Figure 73. The axial and the transverse direction are shown in (a) and (b), respectively. Sample *HC1*.

Compare now with the spheroidized microstructure, where the lattice strain of the (301) remains linear in the plastic regime until the sample is unloaded (point *D* on the stress-strain curve Figure **71**(f)). Note that at point *D*, the (301) lattice strain amounts to 5900 µε which is smaller than the lattice strain at position *A* in the pearlitic microstructure (6000 µε). Figure 75 shows the diffraction peaks of the (301) and the (122) in the spheroidized microstructure at the positions *C* (just after Lüders band deformation) and *D* and in the axial and the transverse direction. The peaks from the axial direction are shown in (a), the peaks from the transverse direction are shown in (b). A pronounced peak asymmetry for both cementite peaks (in both directions) is not observed. The peak shape evolution is discussed in terms of the cementite morphology in §4.4.2.
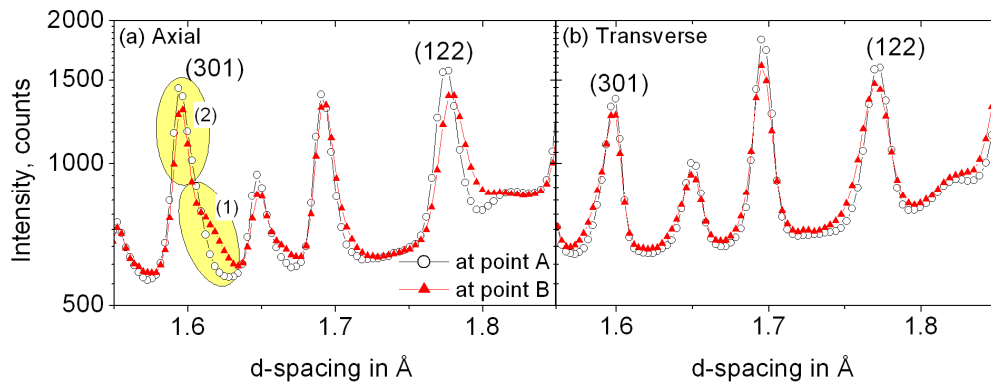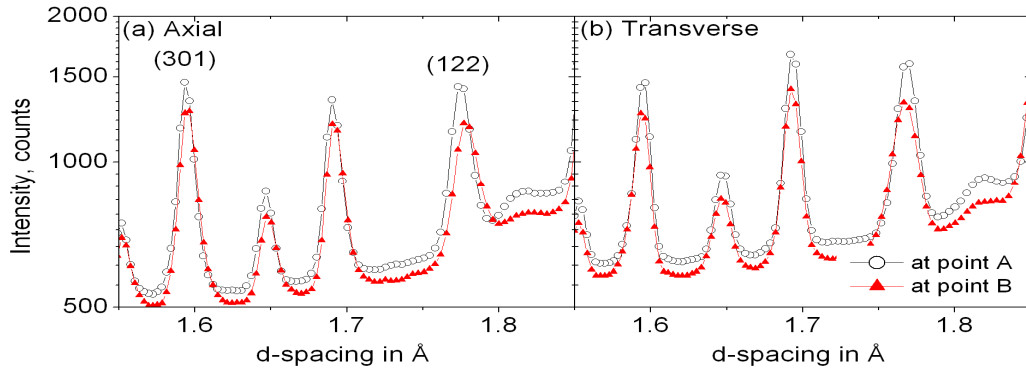
Figure 75 Diffraction pattern of the spheroidized microstructure with the (301) and the (122) cementite reflection at the stress levels *C* and *D*, as indicated in Figure 71(e). The axial and the transverse direction are shown in (a) and (b), respectively. Sample *HC3_1*.

3.4.3.2   In situ tensile loading at 500°C of the spheroidized microstructure

One sample with a spheroidized microstructure (*HC3_S2*) has been tensile deformed at 500°C to see what can be learnt from this more idealized microstructure compared to the tempered bainitic 1%CrMoV steel. Figure 76 shows the stress-strain curve and the axial lattice strain data for the ferrite {220}, {200}, {310} grain families and the cementite (122), (301) orientations. The stress-strain curve does not show a strain hardening in the plastic regime. The lattice strain is therefore shown as a function of the engineering strain and can directly be compared with the data of the 1%CrMoV steel at 565°C in Figure 65. The residual lattice strain after unloading is shown within the yellow highlighted area. The temperature control was unfortunately not working perfectly with frequent fluctuations in the range of 500 ± 20 °C. Therefore, the data is rather scattered.

Figure 76 Axial lattice strain during tensile deformation at 500°C of the spheroidized microstructure (sample *HC3_2*) plotted as a function of engineering strain. The grey areas highlight the behaviour of the {220} and {200} in the plastic regime. The stress-strain curve is added.

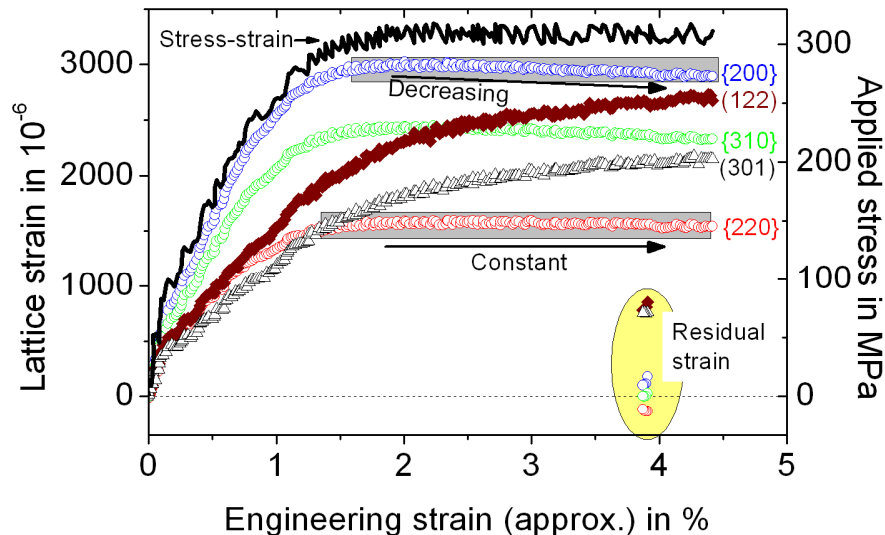The ferrite lattice strains increase during tensile loading and reach their maximum value when the stress-strain curves enter the steady-state like regime. This agrees with the 1%CrMoV data. Within the plastic regime, the {220} remains constant and the {200} is slightly decreasing. This agrees with the 1%CrMoV data. The cementite lattice strain increases throughout the elasto-plastic regime, its rate however is decreases at around the onset of the steady-state like regime. This trend also agrees with the 1%CrMoV data although the cementite experiences much higher lattice strains and already saturates at around 6% plastic strain. After unloading, the {220} and the {200} ferrite grain families are compressive and tensile, respectively and the cementite is strongly in tension.

Consider now the axial stiffness of the {220} and the {200} ferrite grain families during HT loading and compared to RT loading. Figure 77 shows the corresponding data points in the elastic regime. The data points are fitted in between 0 and 250 MPa and the values for the stiffness are summarized in Table 11. The ratio of the stiffness {110}/{200} is larger at HT (≈1.87) than at RT (≈1.29). This agrees with the 1%CrMoV data (cf. Table 9). Note that while the stiffness for the ferrite decreases from RT to HT, e.g. for the {220}: ferrite 220 GPa->180 GPa, the stiffness of the cementite is about the same at RT and HT, e.g. for the cementite (301): 230 GPa → 230 GPa, (cf. Table 10).
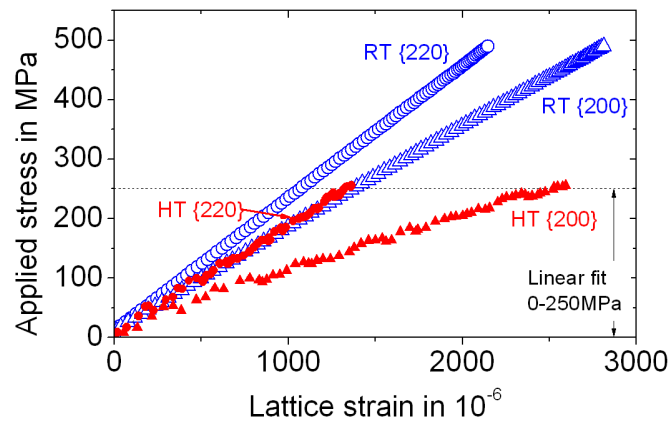
Figure 77 Evolution of the {220} and {200} lattice strain during RT (sample *HC3_1*) and HT (sample *HC3_2*) tensile loading of the spheroidized microstructure, focusing on the elastic regime.

Table 11 Axial stiffness of the {220} and {200} ferrite grain families of the spheroidized steel during tensile loading at RT (sample *HC3_1*) and 500°C (sample *HC3_2*) obtained a linear fit in the range 0 to 250MPa.

Microstructure	Axial {220}	Axial {200}	Ratio
Spheroidized steel RT	224GPa±11GPa	174±13GPa	≈1.29
Spheroidized steel (500°C)	183GPa±9GPa	98±17GPa	≈1.87

Main findings from §3.4:

As-received 1%CrMoV

- *During HT tensile deformation: There is an early redistribution of load in between the ferrite grain families and, to some extent, to the cementite already at around 200 MPa. That is about the onset of the transient regime (cf. Figure 55). The ferrite lattice strain reaches its maximum value when the stress-strain curve enters the steady-state like regime. The cementite takes further load and then saturates within the steady-state regime. Large peak broadening and evolving peak asymmetry of the cementite occurs during tensile deformation at RT but not at HT.*

- *During creep deformation, the magnitude of all three investigated ferrite grain increases with time in both the axial and the transverse direction. The lattice strain of the cementite (122) and (301) orientation stagnates in the axial and its magnitude decreases in the transverse direction.*

Heat-treated 1%CrMoV material:

- *The approach to elucidate the effect of vanadium carbide on the accumulation of residual microstrain by producing samples with a subsequent precipitation sequence by heat treatments was not successful.*

High-carbon steel:

- *The (301) and the (122) cementite grain orientation could be followed well during elastic and plastic deformation due to the high volume fraction of the cementite compared to the 1%CrMoV steel. In the elastic regime, the (301) is stiffer than the (122) for all three different microstructures and in both the axial and the transverse direction. In the plastic regime, the (122) accumulates more lattice strain than the (301) and also accumulates larger residual strains after unloading.*

- *Cementite peak broadening and evolving asymmetry with plastic deformation is most pronounced for the pearlitic and the tempered pearlitic microstructure and not for the spheroidized microstructure.*

- *During HT tensile deformation, the (301) cementite orientation is stiffer than the (122). The values of the stiffness are about the same as at RT. On the other hand, the stiffness of the ferrite grain families decreases at HT. The ratio between the stiffness of the {110} and {200} is larger at HT than at RT.*

3.5   ENGIN-X beamline: ToF Neutron diffraction

This section reports the results of the measurements made at the ToF neutron diffractometer ENGIN-X. The ToF technique can provide representative information on the ferrite bulk behaviour (see results with POLDI in §3.2). In situ HT tensile and creep test are performed. The larger detector area (compared to POLDI, cf. §2.3.5.5) provides higher counting statistics and allows observing the second phase cementite: A test diffraction pattern accumulated on the as-received 1%CrMoV steel at RT prior to the submission of the proposal for this beamtime could reveal the cementite with reasonable uncertainties (200 με) using the full flux of the spallation source (reduced d range at 50 Hz, cf. §2.3.5.4). The nomenclature of the samples tested and reported in this section is given in Table 12.

Table 12 The table reminds the nomenclature of the samples reported in this section. For more details see §2.3.5.7

Sample name	Material	Deformation History
HT134	1%CrMoV (Batch A)	As-received
HT102	1%CrMoV (Batch A)	Ex situ: 1% ps. at RT
HT108	1%CrMoV (Batch A)	Ex situ: 5% ps. at RT
HT765	1%CrMoV (Batch B)	Ex situ: 1% ps. at HT
HT766	1%CrMoV (Batch B)	Ex situ: 4% ps. at HT
HT133	1%CrMoV (Batch A)	Ex situ: 0.6% ps. Creep/270MPa
HT135	1%CrMoV (Batch A)	Ex situ: 1.0% ps. Creep/270MPa
HT92	1%CrMoV (Batch A)	Ex situ: 3.2% ps. Creep/270MPa
HT101	1%CrMoV (Batch A)	Ex situ: 0.0% ps. Thermally aged
EngX1	1%CrMoV (Batch C)	In situ: Tensile at HT $\dot{\varepsilon} = 1 \cdot 10^{-5} \, s^{-1}$
EngX2	1%CrMoV (Batch C)	In situ: Tensile at HT $\dot{\varepsilon} = 5 \cdot 10^{-4} \, s^{-1}$
EngX3	1%CrMoV (Batch C)	In situ: Creep/290MPa
EngX4	1%CrMoV (Batch C)	In situ: Creep/330MPa

3.5.1   Measurements on pre-deformed 1%CrMoV

Since the cementite peaks are also visible in the diffraction pattern acquired at ENGIN-X, the predeformed samples have been re-investigated, with both chopper settings of 25Hz (full pattern) for the ferrite phase strain and of 50Hz (reduced pattern, i.e. in between and including the {110} and the {200} ferrite peaks) for the cementite phase strain.

3.5.1.1   Diffraction pattern

The cementite behaviour has been obtained from the few peaks in the limited range shown in Figure **78**(a) of sample *HT134* (as-received). Figure 78(b) shows the same range, now of the sample *HT92*, which was creep deformed. Surprisingly, additional peaks are present, which are highlighted in grey. These additional peaks are present in all crept samples and in the thermally aged sample. These peaks are not present in the samples from the other deformation sequences (tensile at RT and

HT). The intensity of these additional peaks increases in the order *HT133* (550h) to *HT135* (1100h) to *HT92* (3000h) and hence coincides with the time that the samples have been exposed at 565°C. The peaks in the thermally aged sample *HT101* (3000h/565°C) have the same intensity as in sample *HT92*. The position of these peaks do not coincide with those of the carbides $M_{23}C_6$, M_2C, M_6C, M_7C_3 (cf. Table 2), which sometimes form during tempering and creep [25, 28]. Since these peaks cannot be indexed unambiguously (limited range with only four peaks and are not observed in the X-ray diffraction pattern, cf. §3.6.2) and disturb the refinement for the cementite lattice parameters, they have been excluded from the refinement.

A contribution of this phase to the residual strain accumulation of the ferrite, for instance through a load-transfer during deformation, can neither be confirmed nor denied. Following that peak labelled *P* at 1.47 Å by single peak fitting shows that its peak position varies for the different samples. Taking the peak position in sample *HT133* as reference and expressing the peak shift in lattice strain (axial direction) gives: -60 με (*HT135*), 320 με (*HT92*) and 800 με (*HT101*), where the latter is the thermally aged sample, which was *not* subjected to load. Since the peak intensities are increasing with the time the sample have been exposed at 565°C, the corresponding phase may have grown with time. The variations in peak position can therefore very well happen by changes in the chemical composition.
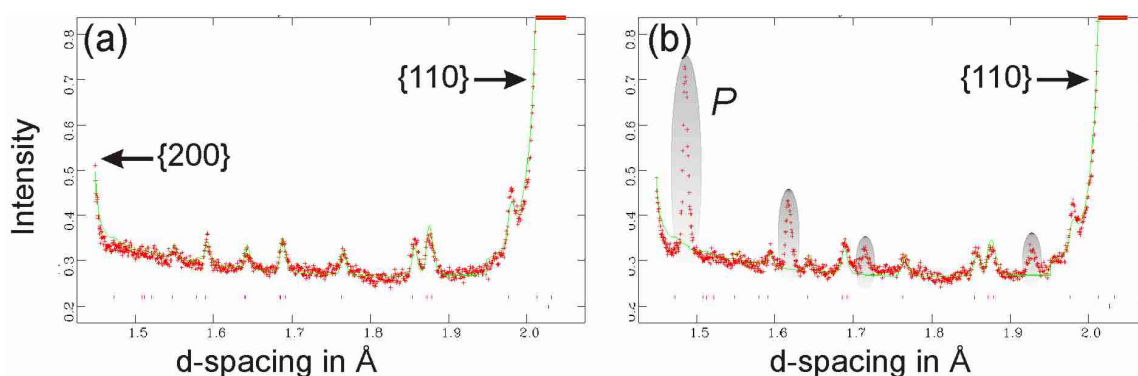
Figure 78 Diffraction pattern acquired during 2h with a chopper setting of 50Hz: (a) Reference sample (*HT134*) and (b) crept sample (*HT92:3000h at 565°C/270MPa*). Additional diffraction peaks in the latter, shown in the grey areas The other peaks in between the edges of the Fe{200} and Fe{110} correspond to the cementite and are reasonable well captured with the Rietveld refinement (green line).

3.5.1.2   Residual lattice strain

Figure 79 shows the residual lattice strain of (a) the ferrite phase and (b) the cementite phase for all deformation sequences. The ferrite data is in good agreement with the earlier measurements on these samples at POLDI (cf. Figure 57(a)). Only a small difference between the two measurements exist for two data points: The data point *Ax HT* at 1% plastic strain is slightly in tension in Figure **79**(a) with +30 με (POLDI -30 με) and the data point *Tr Creep* at 1% plastic strain is less

compressive in Figure 79(a) with -40 µε (POLDI -150 µε). The reason for this slight difference is unknown, but could in principle be due to small sample alignment errors so that the gauge volume is not fully immersed in the neutron beam, which might lead to slight shifts in the diffraction peak (so-called spurious strains, [11]).

Moreover, the two methods of unit cell refinement by Pawley and in addition by Rietveld, which both are implemented in the GSAS software package, do not alter the unit cell paramter within the experimental error for the unit cell parameter obtained for one method. The Rietveld refinement further suggests that the sample is not textured.
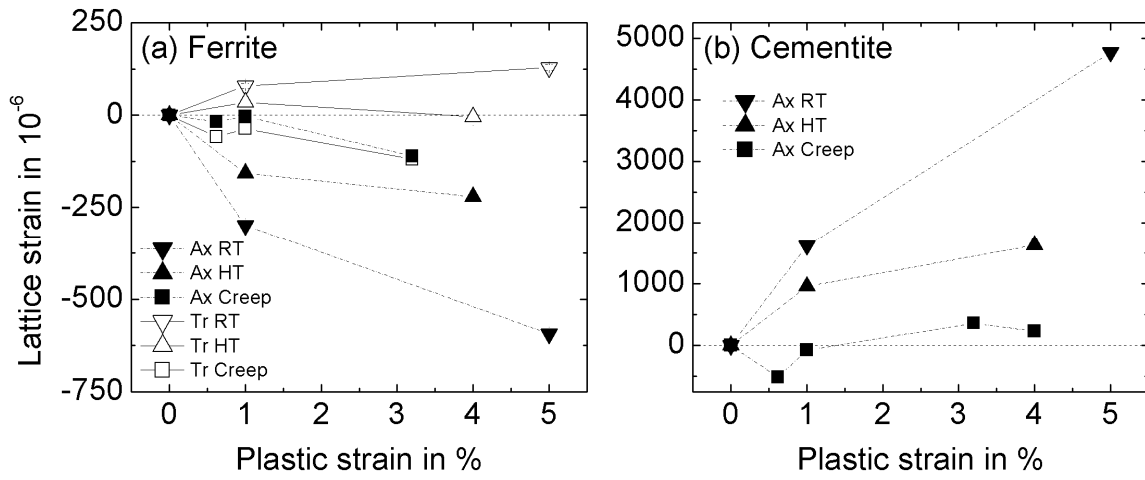

Figure 79 Residual lattice strain measurements of the pre-deformed sample with the legend shown in (a). (a) Ferrite phase strain and (b) axial cementite phase strain.

The axial cementite phase (Figure 79(b)) is in tension for both the RT and HT tensile sequences. Only beyond 1% plastic strain it is significantly larger at RT and at large plastic strains. At RT, cementite phase strain is strongly increasing in between 1% and 5% plastic strain, at HT, it is less strong increasing in between 1% and 4% plastic strain. In the crept sequences, the changes are within the uncertainty (200 µε) provided by the fitting routine.

3.5.1.3   Ferrite peak broadening

The evolution of the peak width may give a hint towards the dominant deformation mechanisms (cf. §1.2.4.1) and is therefore shown here. At ENGIN-X, the standard single peak fitting routine uses a peak profile consisting of a convolution of a truncated exponential with a Voigt function [117]. The width (w_v) of the Voigt function is the recommended parameter to describe the peak width [144]. The peak broadening is calculated from the relative change in the peak width: $(w_v - w^0_v)/w^0_v$, where w^0_v is the corresponding width from the undeformed sample (*HT134*). The peak broadening of the three ferrite diffraction peaks with the highest intensity and for all deformation sequences is shown in Figure 80 (a) and (b) for the axial and the transverse direction, respectively.
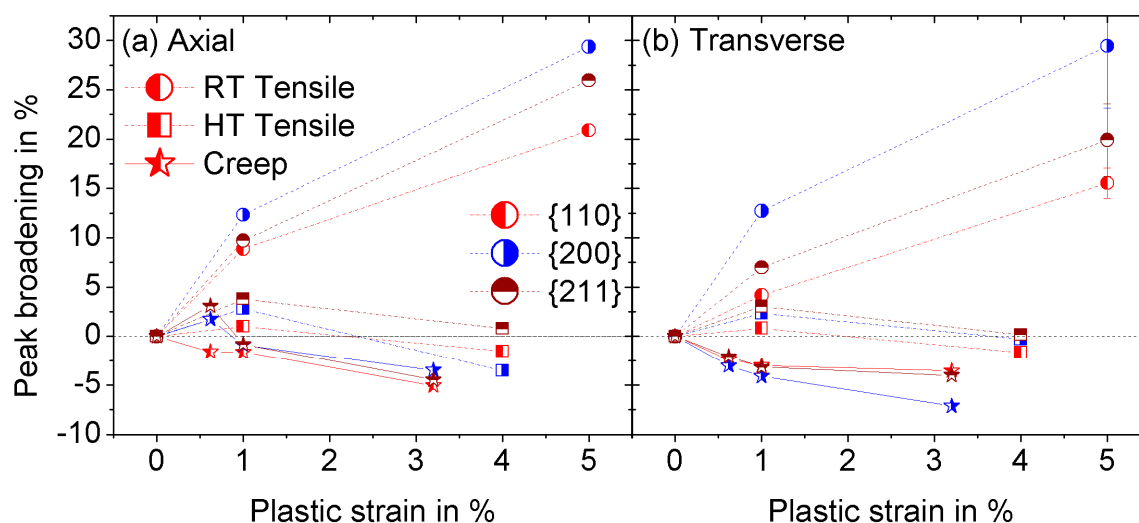
Figure 80 Diffraction peak broadening of ferrite in the (a) axial and (b) transverse direction. Error bars from the fitting uncertainly exemplarily shown in (b) at 5% plastic strain RT only: ±1.5% for the {110}, ±6.3% for the {200} and ±3.7% for the {211}. For all other reflections, the error on the peak broadening is larger than 10% and their contribution is therefore not shown.

For RT deformation, a significant broadening of about 30% after 5% plastic strain is observed. For HT deformation (tensile and creep) the broadening is almost within the error bars. The error is calculated from the uncertainty of the peak width, given by the fitting routine and subsequent error propagation and is exemplarily shown in (b) for the RT data points at 5% plastic strain. The thermally aged sample (*HT101*), however, does not alter the peak width at all and precisely lies on the dashed zero-line. Its contribution is not shown here for clarity. Neglecting the large error bars, then a trend can be observed for the HT deformed samples: That is, the HT tensile sample is slightly increased at 1% plastic strain, but then decreased at 4% plastic strain. The broadening of the crept samples already decrease from the very beginning, however with the difference that the contribution from the {200} and the {211} ferrite peaks are positive in the axial but negative in the transverse direction.

3.5.2 In situ HT tensile deformation

One sample (*EngX1*) has been tensile deformed at HT with a strain rate of 10^{-5} s^{-1} with several load/unload cycles. Figure 81(a) reminds the HT stress-strain curve and shows the unloading characteristics. In each unloaded state, one diffraction pattern has been acquired at the reduced d-spacing range (in between and with the {110} and {200} ferrite peak). Before loading and after the test, diffraction patterns have also been acquired at the full d-spacing range. During neutron acquisition in the unloaded state (ca. 2h), the (engineering) strain is decreasing slightly, as shown for the last unloaded state in the inset. The diffraction pattern therefore contains the information over this period of decreasing (engineering) strain, which has, however, no significant influence on

magnitude of the residual lattice strain, as investigated with the sample *EngX2* and shown later in this section (cf. Figure 83).
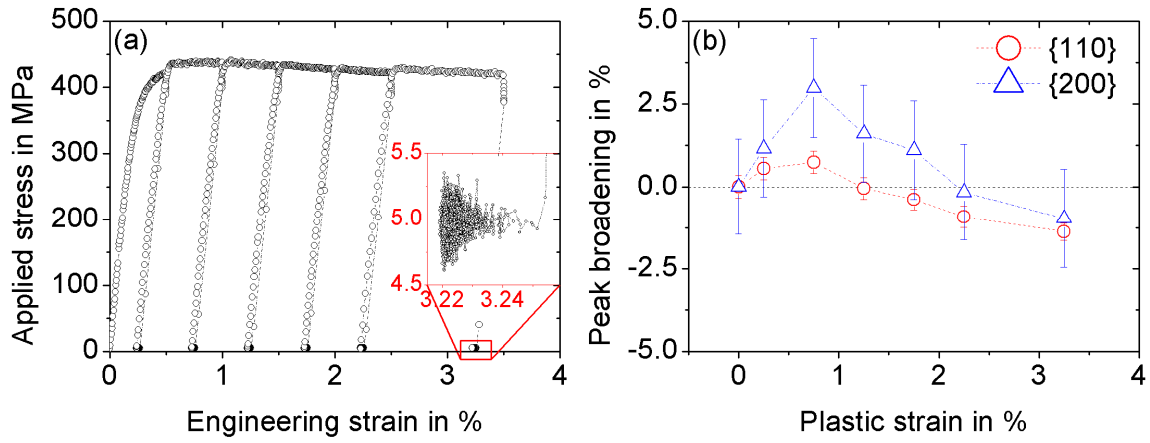

Figure 81: (a) Stress-strain curve with multiple load/unload cycles (sample *EngX1*). One diffraction pattern has been acquired in each unloaded state. (b) Ferrite peak broadening of the {110} and the {200} ferrite peak in the axial direction. The broadening in the transverse direction is similar and therefore omitted.

Peak broadening: The relative change in peak width for the {110} and the {200} ferrite peak in the axial direction is shown in Figure 81(b). The peak width is initially increasing and then decreasing, even below its initial value. This agrees well the findings in the ex situ HT tensile deformed samples (cf. Figure 80(a)). The larger amount of data points in Figure 81(b) allows confining this transition from increasing to decreasing peak width to happen in between 0.25% (second data point) and 1.25% (fourth data point) plastic strain. The evolution of peak width with plastic strain, as just described for the axial direction, is equally valid for the transverse direction (not shown here), which agrees with the results of the ex situ deformed samples in Figure 80(b).

Lattice strain: The evolution of the residual lattice strain of the {110} and the {200} grain family is shown in Figure 82 in (a) the axial and (b) the transverse direction:

Axial direction: The {110} is compressive and its magnitude increases but appears to run into saturation towards large plastic strains (>3.3%, last data point). The {200} ferrite is tensile, its magnitude initially increases in between 0% (first data point) and 0.75% (third data point) plastic strain and then decreases. Since the decrease in the {200} is more pronounced, which can also be seen from the lattice strain evolution during deformation in Figure 65, the difference between the {110} and the {200} constantly decreases from at around 0.75% (third data point) plastic strain towards higher plastic strains. The maximum and minimum difference of 680 µε and 560 µε, respectively, agrees well with the values obtained from the ex situ deformed samples at comparable plastic strains (cf. Figure 57(c)), 690 µε and 550 µε. The value of 560 µε for the seventh data point is preserved after cooling to RT (not shown). This intergranular load-transfer as a function of the deformation condition is discussed in §4.3. At the end of the deformation the ferrite phase strain has

been determined, at HT and then after cooling at RT, and found to be slightly reduced (cf. §1.1.4; different thermal expansion coefficients ferrite and cementite) by about 70 µε.

Transverse direction: The {110} ferrite is compressive and enters early (0.5% plastic strain) in saturation. The {200} ferrite is tensile and its magnitude increases with a decreasing rate towards large plastic strains. As a consequence, the difference between the {110} and the {200} constantly increases, which agrees with the observation from the pre-deformed samples in Figure 57(c). The ferrite phase strain reduces after cooling from HT to RT by about the same value (65 µε) as for the axial direction.
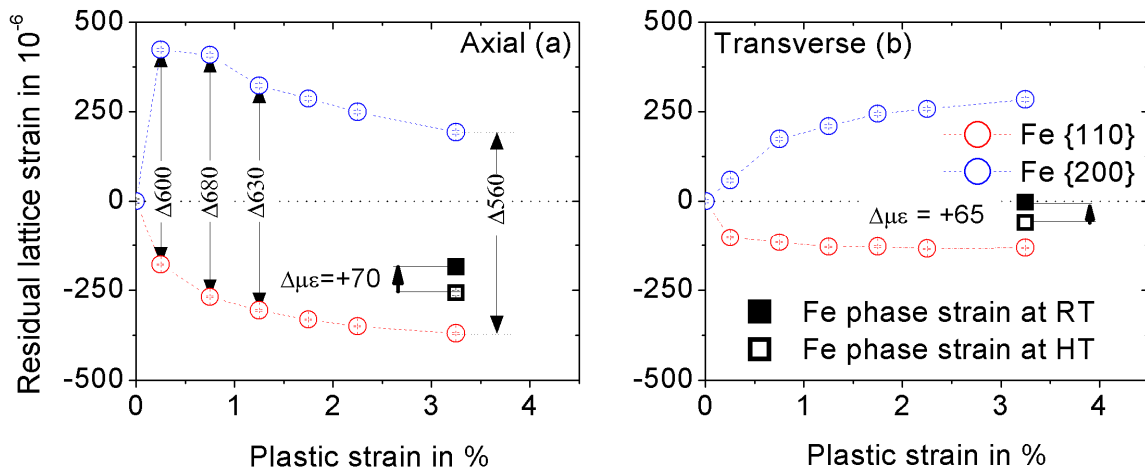

Figure 82 Residual lattice strain evolution in (a) the axial and (b) transverse transverse direction after HT tensile deformation with a strain rate of 10^{-5} s^{-1} (sample *EngX1*). The legend in (b) is valid for both plots (a) and (b).

Cementite: To pick up the cementite behaviour at HT is really difficult, since the corresponding peaks are far more *diffuse* than at RT due to the enhanced thermal vibration of the atoms around their lattice positions (Debye-Waller factor in the structure factor equation, not introduced in this dissertation, cf. [107]). This has already been seen with synchrotron X-rays in Figure 64, but with the smaller counting statistics of neutrons the uncertainties and the scatter for subsequent data points becomes too high. Also, the lattice strain at 3.3% plastic strain with a value of 1100 µε is much below the value of 1500 µε measured at RT (Sample *HT766*, Figure 79(b)). Note that the cementite will experience compressive strains when being cooled down and constrained by the ferrite matrix, reducing the value of 1100 µε. The information of the cementite obtained at HT is therefore of not much use and omitted in all subsequent plots showing HT data in §3.5.2 and §3.5.4.

A second sample (*EngX2*) was deformed at a strain rate of $5 \cdot 10^{-4}$ s^{-1}, which is 50 times that of the previous sample *EngX1*. This was done to see the influence of a higher strain rate on the accumulation of residual strain. Both stress-strain curves appear to be rather similar. One has to note that the curve for *EngX2* is described by only very little data points: The loading path (0 to 400 MPa), for instance, is described by only six data points. This is due to the limited frequency

with which the data could be written to the file. The lattice strain measurements have been performed in *almost* the same way as for sample *EngX1*: In addition the reduction of (engineering) strain in the unloaded state (cf. inset of Figure 81(a)) was investigated and correlated with the lattice strain evolution. Therefore, three diffraction patterns have been acquired in the unloaded state, as illustrated in Figure 83(a) for the first unload state:
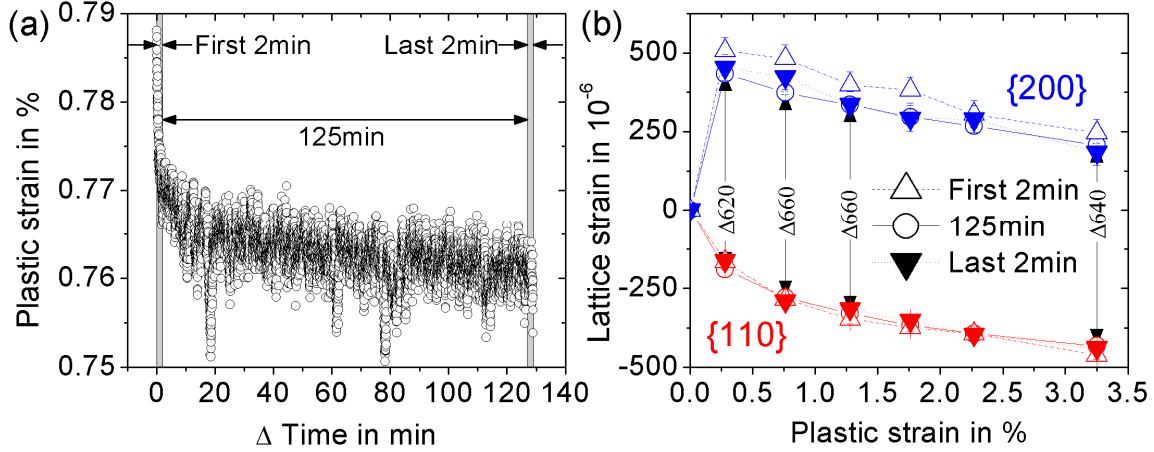

Figure 83 Sample *EngX2*, tensile deformed with a strain rate of $5 \cdot 10^{-4}$ s^{-1}: (a) Shows the (engineering) strain characteristics during the first unloaded state with a reduction of 0.025% in plastic strain. The grey rectangles indicate the two short acquisition periods of 2min (first and last), separated by a long acquisition period of 125min. The stress is constant at 5.0 ± 0.5 MPa. (b) Shows the residual lattice strain of the {110} and the {200} ferrite grain family in the axial direction for the three acquisitions periods and as a function of plastic strain. The arrows connect the data points with the long acquisition time 125min.

The first pattern was taken directly after unloading and for 2 min; the second pattern starting directly after the first one and for 125 min; the third pattern starting directly after the second one and again for 2 min. The (engineering) strain reduction here is about 0.025% over the whole period (129 min) and this value is about the same for all subsequent unloads. Figure 83(b) shows the corresponding residual lattice strain in the axial direction. The error obtained from the fitting routine is small compared to the scatter of the data points. Within this scatter, the lattice strain of the {110} for all three acquisition periods is the same. For the {200}, there seems to be a slight reduction after the first period. Within the scatter of the data points, the lattice strain of the last two periods is the same. In the transverse direction and within the scatter of the data points, there is no difference between the three acquisition periods for the {110} and {200} and the graph is therefore not shown here. A comparison of the peak width for the three acquisition periods is not possible since the error on the peak width for the short acquisition times (2 min) is too large.

Consider now the effect of an enhanced strain rate on the accumulation of residual strain. The measurements in both samples *EngX1* and *EngX2* are done at the same plastic strain values for direct comparison. In the axial direction, the evolution of the {110} and the {200} behave similarly

(cf. Figure 82(a) and Figure 83b): The difference between the {110} and {200} at small plastic strains is rather the same. This difference, however, does not decrease much for sample *EngX2* towards the last measurement point at 3.3% plastic strain and remains, with a value of 650 με, certainly larger as the one of the sample *EngX1* (560 με). This is mainly because the {110} in *EngX2* seems not to saturate at large plastic strains.

3.5.3 Stiffness of the {110} and {200} ferrite grain families at RT and HT

The ratio between the stiffness of the axial {110} and the axial {200} ferrite grain families appears to be larger at HT than at RT. This was observed during X-ray diffraction reported in §3.4.1.1 on the 1%CrMoV steel and in §3.4.3.2 on the spheroidized high-carbon steel and may play a role in the enhanced load-redistribution between both grain families during HT tensile deformation, discussed in section §4.3. ToF neutron diffraction with its good sampling statistics (cf. §3.2.2) was used to determine the stiffness of the {110} and the {200} ferrite grain families from one sample (*EngX3*, 1%CrMoV steel) and taking diffraction patterns first at RT and at five stress levels in between 0 to 350 MPa and then at HT and at five stress levels in between 0 **to** 200 MPa, with 5 min acquisition time at each stress level. The mechanical data is shown in **Figure 84**(a) and the diffraction data in **Figure 84**(b). The values of the linear regression are shown in Table 13. The stiffness of the {110} grain family decreases from 227 GPa at RT to 186 GPa at HT. The stiffness of the {200} grain family decreases from 176 GPa at RT to 122 GPa at HT. In summary, the ratio in stiffness ({110}/{200}) is larger at HT (1.52) than at RT (1.29), in agreement with the aforementioned XRD measurements.
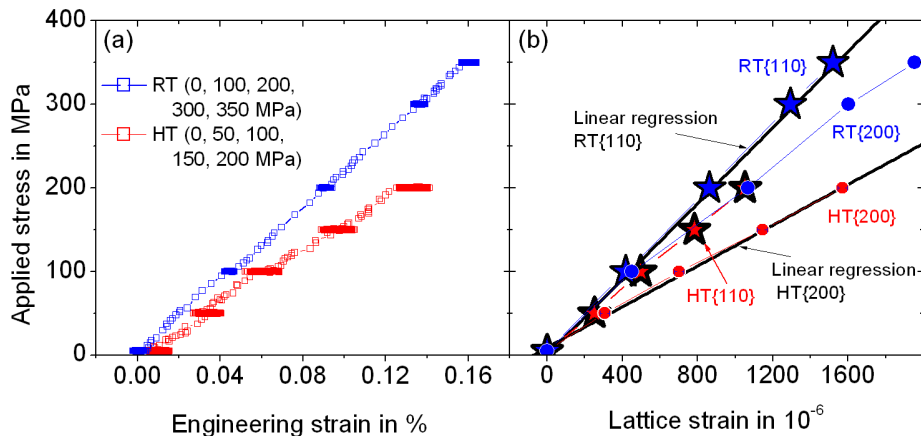
Figure 84 Measurements of the diffraction elastic constants of the 1%CrMoV steel at RT and HT. (a) Shows the mechanical data with dwells at the corresponding stress levels, where diffraction patterns have been acquired during 5min. (b) Shows the corresponding lattice strain data of the {110} and {200} ferrite grain families in the axial direction at RT and HT. The linear regression for the RT{110} and the HT{200} are shown as black line. The result of a linear regression for all four data sets is summarized in Table 13.

Table 13 Stiffness of the {110} and the {200} ferrite reflection during RT and HT loading (cf. Figure 84(a)) and determined by linear regression of the data in Figure 84(b).

Test	Axial {110}	Axial {200}	Ratio{110}/{200}
RT tensile	227±1GPa	176±1GPa	≈1.29
HT tensile	186±2GPa	122±3GPa	≈1.52

3.5.4 In situ HT creep deformation

In situ creep experiments have been performed at 565°C at two different stresses. One sample (*EngX3*) was creep deformed at 290 MPa for about 19 h and one sample (*EngX4*) was creep deformed at 330 MPa for about 11 h. During deformation, the diffraction pattern was recorded with the reduced d range (chopper at 50 Hz) and for about 12 min to capture fast changes in the {110} and the {200} grain families. These patterns can be summed to obtain larger counting statistics for the cementite, but also here, the peaks are very *diffuse* at HT (cf. §3.5.2) and of not much use and therefore not further considered. Figure 85 shows the results with the mechanical data and the lattice strain evolution in the axial and the transverse direction. The first row (a)-(c) shows the results for the stress 290 MPa and the second row (d)-(f) the results for the stress 330 MPa. The creep curves have been fitted with a function:

$$\varepsilon(t) = \varepsilon_0 + A \cdot t^{1/3} + B \cdot t + C \cdot t^3 \qquad \qquad \text{Eq. 35}$$

where ε_0 is the instantaneous strain on loading, t is the time at the corresponding stress. The terms with the coefficients A, B and C describe the primary, secondary and tertiary creep regime [145]. The coefficient C has been fixed to zero, since the creep curves did not enter the tertiary creep regime. The strain rate $d\varepsilon/dt$ has been derived and is plotted in (a) and (d) as a function of the (engineering) strain. The strain rate of both curves is decreasing (primary regime) within the investigated period and did not reach a steady-state (secondary regime) by the end of the test.

Consider first the lattice strain in the axial direction. At the onset of creep, the {200} is increasing and the {110} is decreasing. This can be seen from the values that are written along the data. The lattice strain of the {110} and the {200} then come towards saturation and the solid lines serve as a guide to the eye After unloading, the {110} is in compression and the {200} in tension. The difference between the {110} and the {200} amounts to about the same value of 580 µε for both creep tests and is preserved after cooling (not shown). A value of 580 µε is similar that what is measured in the pre-deformed samples (sample *HT133*, cf. Figure 54(d)) and after HT tensile deformation (sample *HT766*, cf. Figure 54(c)). The phase strain is compressive and its magnitude decreases after cooling down to RT by about 70 µε.

Consider now the lattice strain in the transverse direction. At the onset of creep, the magnitude of the {110} and the {200} is increasing. The difference between the {110} and {200} is increasing

during creep at 290 MPa (from $\Delta_1 = 250$ to $\Delta_2 = 300$) but remains constant during creep at 330 MPa ($\Delta_1 = 370$ and $\Delta_2 = 370$). At 290 MPa, the {200} increases with a higher rate as the {110} and both do not come into saturation before unloading. In the unloaded state both have about the same value. At 330 MPa, the {110} and the {200} reach saturation before unloading. In the unloaded state, the {110} is more compressive. Note that in the pre-deformed samples (cf. Figure 54(d)), which where creep deformed at 270 MPa, the {200} is the most compressive. The ferrite phase strain is compressive (as for the axial direction), in agreement with the results of the pre-deformed samples and its magnitude decreases after cooling down to RT by about 70 µε.
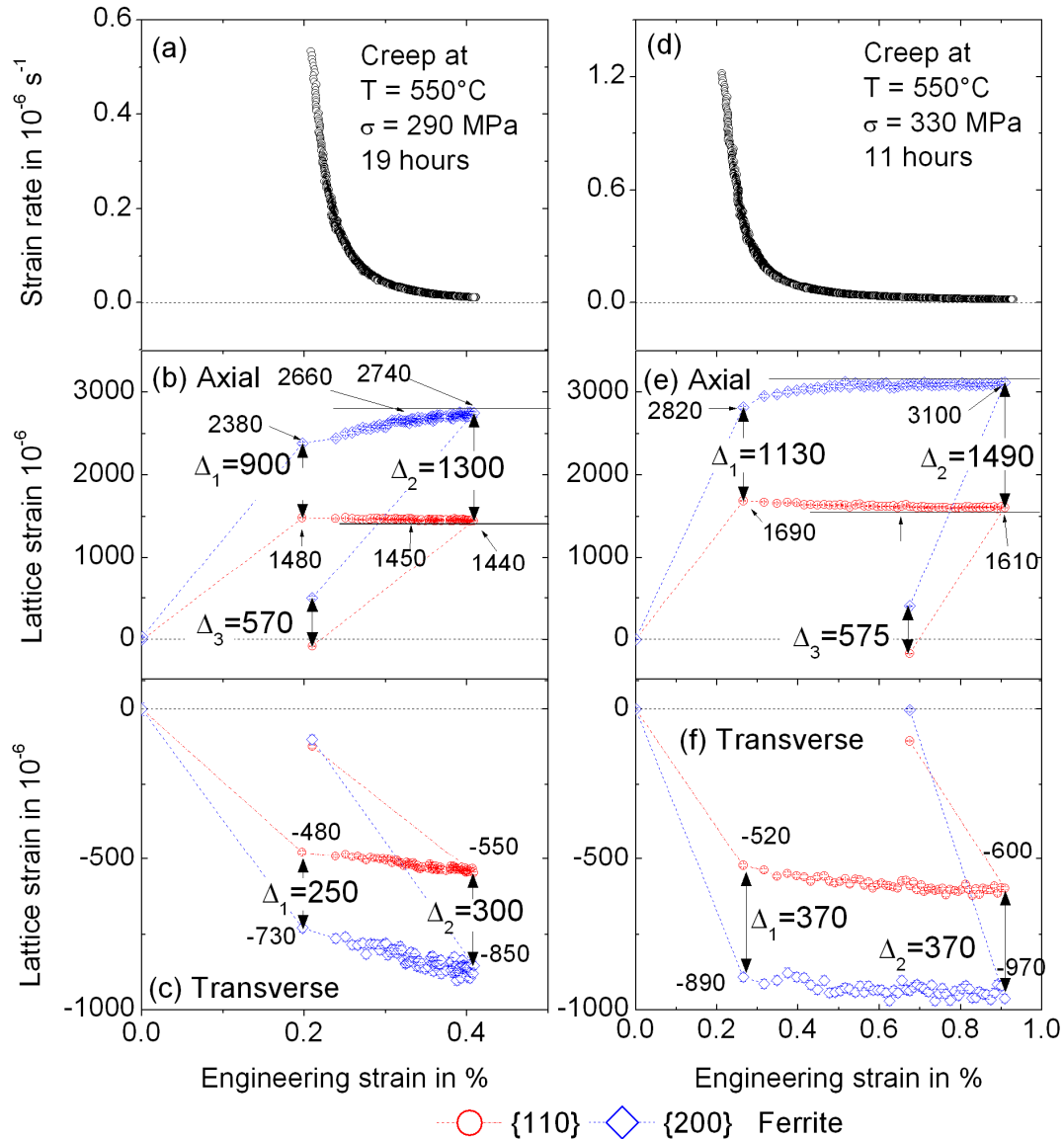

Figure 85 In situ creep test at 565°C and 290MPa (a)-(c) and 330MPa (d)-(f). The top row shows the strain rate as a function of the engineering strain, determined from the creep curves with Eq. 35.The lattice strain for the {110} and {200} ferrite grain families are then shown in the second row for the axial and in the third row for the transverse direction.

Main findings from §3.5:

Pre-deformed samples:

- *Ferrite lattice strain in good agreement with the POLDI measurements.*

- *Significant ferrite peak broadening for the RT tensile sequence; slight peak broadening at small plastic strains and decreasing peak width at large plastic strains for high tensile deformation; decreasing peak width in the crept samples.*

- *Peaks from additional phase evolve in the samples subjected to 565°C.*

HT tensile deformation:

- *Peak width initially increasing until about 1% plastic strain, and then decreasing.*

- *Difference in the {110} and {200} intergranular strain increases until about 1% plastic strain and then decreases.*

- *During cooling after plastic deformation the ferrite phase strain is slightly reduced by about 70 $\mu\varepsilon$ in both the axial and transverse direction.*

Creep deformation:

- *In the beginning, the axial lattice strain of the {110} decreases and the {200} increases. Both saturate towards the end of the primary creep regime. After unloading, the difference between the {110} and {200} amounts to about the same value (580 $\mu\varepsilon$) for both creep tests at 290 MPa and 330 MPa.*

3.6 Carbides in the pre-deformed 1%CrMoV samples

The pre-deformed samples from all deformation sequences (tensile and creep) and the sample *EngX1* were cut. The nomenclature of the samples tested and reported in this section is given in Table 14. The ferrite matrix was electrolytically dissolved (cf. §2.1.1.3) and the remaining powder (i.e. the carbides which are inert to this process) was characterized by its weight fraction and measured at the dedicated powder diffraction beamline at the Swiss Light Source, PSI.

Table 14 The table reminds the nomenclature of the samples reported in this section. For more details cf. §2.3.5.7

Sample name	Material	Deformation History
HT134	1%CrMoV (Batch A)	As-received
HT102	1%CrMoV (Batch A)	Ex situ: 1% ps. at RT
HT108	1%CrMoV (Batch A)	Ex situ: 5% ps. at RT
HT765	1%CrMoV (Batch B)	Ex situ: 1% ps. at HT
HT766	1%CrMoV (Batch B)	Ex situ: 4% ps. at HT
HT133	1%CrMoV (Batch A)	Ex situ: 0.6% ps. Creep/270MPa
HT135	1%CrMoV (Batch A)	Ex situ: 1.0% ps. Creep/270MPa
HT92	1%CrMoV (Batch A)	Ex situ: 3.2% ps. Creep/270MPa
HT101	1%CrMoV (Batch A)	Ex situ: 0.0% ps. Thermally aged
EngX1	1%CrMoV (Batch C)	In situ: Tensile at HT $\dot{\varepsilon} = 1 \cdot 10^{-5}\, s^{-1}$

3.6.1 Carbide weight fraction of 1%CrMoV steel

All results concerning the carbide weight fraction are shown in Figure 86.

First, an estimation of the uncertainty for the method of determining the weight fraction is given:

(i) A **large quantity** of about **15 g** from a block of material (ca. 2.5 x 2.5 x 2.5 cm^3) has been dissolved and the weight fraction of the remaining carbides determined. The remaining block has then been ground and the procedure has been repeated. In total, 5 tests have been performed, obtaining a carbide weight fraction 2.9 ± 0.1 wt%.

(ii) A **small quantity** of about **3 g** from the same block of material has been dissolved. The amount of 3 g is comparable to the amount of material, which has been dissolved from the gauge section of the deformed samples (cf. §Figure 22(b)). The weight fraction has been determined to 2.4 ± 4 wt%, which is slightly less than for case (i). In fact, some carbide powder always sticks to the glass beaker during the procedure. The relative loss of carbides hence decreases with an increasing amount of dissolved material, which seems natural.

Second, it was tested whether tempering causes additional formation of carbides. Therefore, a block of material has been tempered at 680°C for 12h, resulting in a weight fraction of 3%, which agrees well with that of the as-received material within the experimental error. Note that the carbides may still transform into other types of carbide without altering the total weight fraction, within the experimental error.

All these estimations were done on material from batch *C* (cf. §2.3.5.7) and in summary, a value of 3 wt% can be taken as an upper threshold. A further measurement on the material of batch *A* also gave the same weight fraction of carbides, within the experimental error.

The quantity of material that is dissolved with the gauge section of the deformed samples amounts to about 2g. The carbide weight fraction for the reference sample (*HT134*), for the RT tensile samples (*HT102, HT108*) and for the crept samples (*HT133, HT135, HT92, thermally aged HT101*) are all similar and below the 3 wt% threshold. For the HT tensile samples, the carbide weight fraction amounts to about 3.6% for the sample (*HT765*) deformed until 1% plastic strain and to about 4.8% for the sample (*HT766*) deformed until 4% plastic strain. Repeating these measurements on the remaining part of the gauge section provides similar values. This is a surprising result and there might be two reasons for that: Either the carbide weight fraction is intrinsically higher in theses samples (in fact, these samples are from batch *B*) or there is a kind of deformation induced or assisted precipitation. The carbide weight fraction in the corresponding grip sections is the same for both samples and below the threshold of 3% and is therefore considerably lower than that of the corresponding gauge section. The grip section has a larger diameter compared to the gauge section and is supposed not to have been plastically deformed. To cross-check these

results, the grip and the gauge section of a further sample tensile deformed at HT have been dissolved. That sample (*ENGX1*) is made from batch *C* and has been deformed in situ with several load/unload cycles up to 3.3% plastic strain at ENGIN-X. The carbide weight fraction here is similar for both the grip and the gauge section and is below 3 wt%. Furthermore, there is no direct evidence in the literature for deformation-assisted change in the matrix composition, by precipitation of carbides or transformation into other types, for comparable loading schemes. A deformation-assisted increase in the carbide content is therefore not confirmed. The only explanation remains that the (initial) carbide content in the two gauge sections is accidently higher. The enhanced carbide volume fraction has no significant effect on the accumulation of residual strain in the ferrite matrix during tensile deformation at HT, when compared to the in situ deformed sample. Also, a diffraction pattern from the (undeformed) grip section provides, within the experimental error, the same lattice parameter a^0 as the reference sample *HT134*.
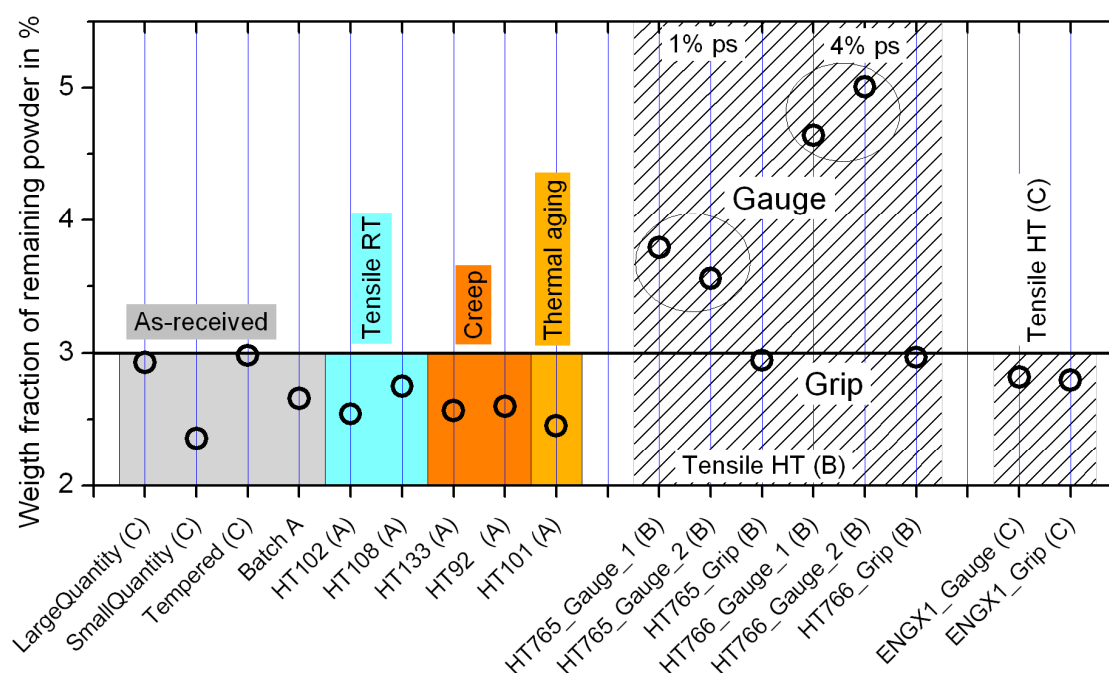
Figure 86 Weight fraction of the extracted carbides (data points are represented by the black circle) of the as-received material, the pre-deformed samples and the HT tensile deformed sample *ENGX1*, corresponding to the sample nomenclature Table 14. The letters A, B, C refer to the different batches of the material, defined in §2.3.5.7.

3.6.2 Information from diffraction pattern of the extracted carbides

The diffraction pattern of the powder of the as-received material was shown in Figure 53. No potential residua of the dissolution product were found in the pattern:

❖ No iron chloride $FeCl_2$ (PDF: 00-001-1106) Rhombohedral, R-3m(166) a=3.604 Å, c=17.591Å

❖ No iron chloride $FeCl_3$ (PDF: 01-077-0997) Rhombohedral, R-3 (148) a=6.056 Å, c=17.407 Å

Predominantly, only cementite and vanadium carbide are present. The presence of $M_{23}C_6$, M_6C, M_7V_3; M_2C is not very likely. The sensitivity of this dissolution procedure for these types of carbide was verified with the diffraction pattern of the carbides extracted from a similar type of steel (2CrMoNiWV), which is documented in the thesis of Mayer [146]. The diffraction pattern of the powder extracted from the deformed samples of all deformation sequences is the same.

In §3.5.1.1, some peaks in the range in between the {200} and the {110} have been observed in the neutron ToF pattern with the samples that have been exposed at 565°C for more than 550h. No corresponding peaks are however observed in XRD pattern from the carbide powder of these samples. To be sure, that this potential phase, for instance, did not dissolve during the carbide extraction, a part of the gauge section of sample *HT101* and *HT92*, i.e. the one with the highest intensity of those peaks, has been cut and this steel sample was then investigated at the MS beamline: Also there, there are no peaks at the locations where they appeared in the neutron diffraction pattern.

Peak shape: The peak shape of the powder extracted from the pre-deformed samples was investigated to address the extensive peak broadening of the cementite during deformation (cf. Figure 68). A detailed line profile analysis was not performed. The cementite diffraction peaks for all deformed sequences have about the same peak shape. This is shown for example for the (122) peak in Figure 87 (a) and (b) with the RT and HT deformed sequences. In addition, a powder has been severely smashed in a mortar to see the influence of such a large deformation on the peak shape, shown in Figure 87(c).
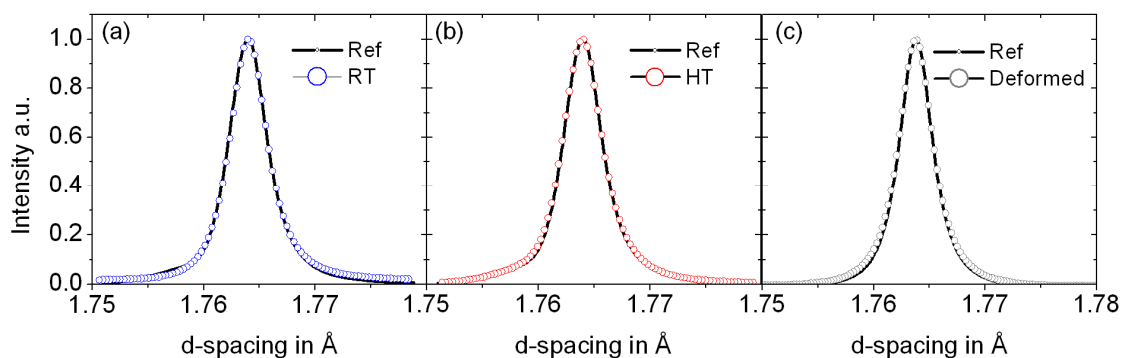
Figure 87 Peak shape of the axial (122) cementite orientation. The peak shape of the undeformed reference sample (*HT134*) is shown as black line and the peak shape of the deformed sample with symbols in the front. (a) Tensile deformed at RT to 5% plastic strain (sample *HT108*); (b) Tensile deformed at HT to 4% plastic strain (sample *HT766*); (c) Carbide powder from the reference sample severely smashed in a mortar. This latter result is from another beamtime, therefore both peaks are narrower than in (a) and (b). The intrinsic resolution is much smaller, justified from the diffraction pattern of the NAC reference powder.

Main findings from §3.6:

- *Upper limit of the carbide weight fraction 3%.*

- *Only cementite and vanadium carbide are the dominant second phases in all pre-deformed samples. The additional peaks observed in the ToF neutron diffraction pattern for the crept and thermally aged samples cannot be seen.*

- *Peak width of the cementite from all deformation sequences is similar, also when the powder is severely smashed in a mortar.*

4 Discussion

4.1 Complementary use of ToF neutron and synchrotron X-ray diffraction

Residual intergranular and interphase strain evolution as a function of plastic strain was investigated in a 1%CrMoV steel subjected to different loading conditions: Tensile deformation at ambient temperatures and tensile and creep deformation at 565°C and Although this might appear to be a straightforward task, the difficulty in characterization lies in both the low volume fraction of the carbides (< 3 wt%) and the inhomogeneous microstructure (cf. Figure 20) in terms of grain size, grain morphology and carbide segregation. A complementary use of (i) ToF neutron and (ii) synchrotron X-ray powder diffraction were needed:

Ad (i): ToF neutron diffraction provides a broad wavelength spectrum (1.1 to 5 Å) and a large illuminated gauge volume in addition to a large detector acceptance range of about ±15° with respect to the principle stress axes. This technique reproduces the axial lattice strain evolution during RT tensile deformation for the ferritic matrix throughout the elasto-plastic regime for several samples tested. This was reported in §3.2.2 and is summarized here in Figure 88(a). The residual strain from the in situ tests also follows nicely the trend of the evolution of residual strain with plastic strain measured from the pre-deformed samples in both the axial and the transverse direction. This was reported in §3.2.1 and is summarized here in Figure 88(b). These results suggest that ToF neutron diffraction probes a sufficiently large volume of material and number of ferrite grains, providing bulk representative information for both the interphase and intergranular strains. This technique therefore allows comparing quantitatively the residual lattice strain for samples subjected to different loading conditions.

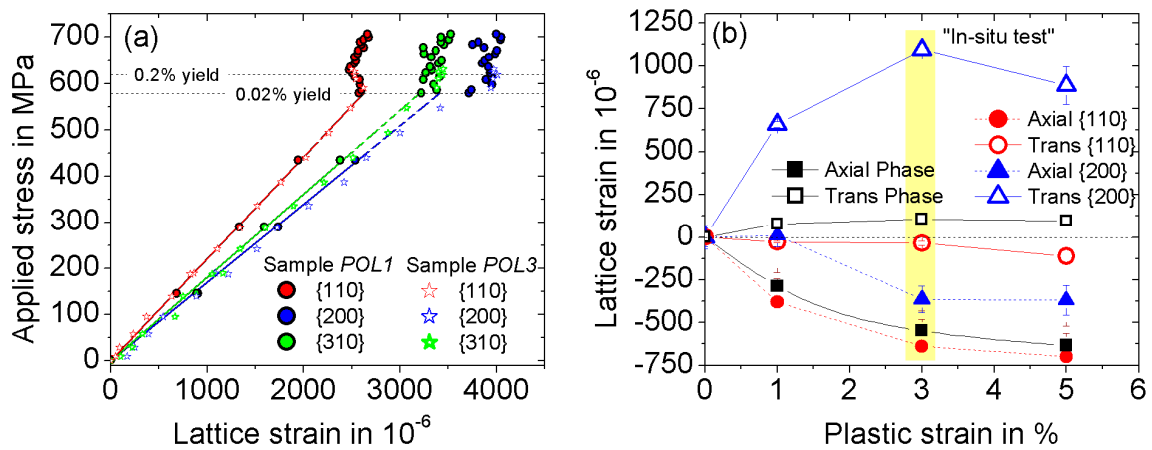Figure 88 Summary plots showing the lattice strain data obtained by ToF neutron diffraction (POLDI) from the 1%CrMoV steel: (a) In situ RT tensile deformation with two samples *POL1* and *POL2* (cf. Figure 57(a), §3.2.2), axial direction. (b) Residual lattice strain of the in situ test (from (a)) and from the pre-deformed samples (cf. Figure 57 (a) and (b), §3.2.1); for both the axial and transverse direction.

Ad (ii): X-rays from synchrotron sources provide enough counting statistics so that the behaviour of the diffraction peaks can be followed during *continuous* deformation. This is particularly important at HT where holding periods, in order to improve counting statistics, otherwise cause stress relaxation or creep. The powder diffraction technique used in this dissertation, however, does not probe a representative quantity of material causing sample-to-sample variations in the lattice strain behaviour (cf. Figure 61, §3.3.2.1) and a discrepancy between the residual strain measured and compared with the neutron data (cf. Figure 66, §3.4.1.1). The qualitative behaviour of the ferrite during RT loading however complies with the data of the neutron measurements. These are compared in Figure 89 (a) and (b). Most important is that information can be obtained from the small volume fraction second phase particles. At the onset of macroscopic yield, the plastifying ferrite matrix is shedding part of its load to the cementite and the lattice strain of the cementite is drastically increasing. This is shown in Figure 89(c). As a consequence, the ferrite is left in axial compression and the cementite in axial tension after unloading (not shown). This load transfer from the plastifying ferrite to the cementite during RT tensile deformation is just the typical behaviour that has frequently been reported ([15, 33, 48, 65], §1.3.1).
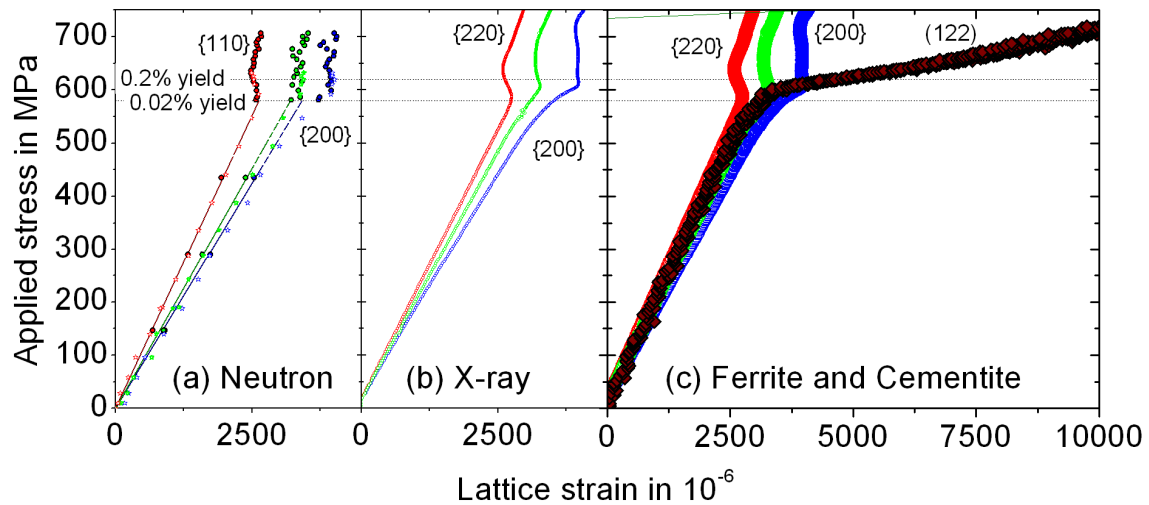
Figure 89 Summary plot showing the lattice strain data during RT tensile deformation. (a) and (b) compare the results of the ferrite {110}/{220}, {200} and {310} grain families determined with neutrons (cf. Figure 57(a), §3.2.2) and X-rays (cf. Figure 64(e), §3.4.1.1). (c) shows the ferrite grain families and the cementite (122) grain orientation (cf. Figure 64(e), §3.4.1.1).

4.2   Comparison of residual lattice strain from RT tensile deformation

The cementite volume fraction in the 1%CrMoV steel is considerably lower compared to the X-ray and neutron based internal and residual stress studies reported in literature (all at RT) and reviewed in §1.3.1. The range of carbon content of these steels is represented by the shaded area in Figure 90,

with a correspondingly minimum and maximum cementite volume fraction of 8% [53] and 34% [65], respectively. The carbide volume fraction (3%) of the 1%CrMoV steel is indicated by the blue dashed line. This 3% represents both cementite and vanadium carbide (cf. §3.1). Following the behaviour of the cementite by diffraction remains quite a challenge. The contribution of the vanadium carbide particles to the build-up of residual strain could not be elucidated (cf. Figure 59 and §3.4.2). The green dot-dashed line at 1.15wt % C in Figure 90 represents the high-carbon steel investigated in this dissertation with a cementite volume fraction of 20% and was used for comparison with the 1%CrMoV steel.
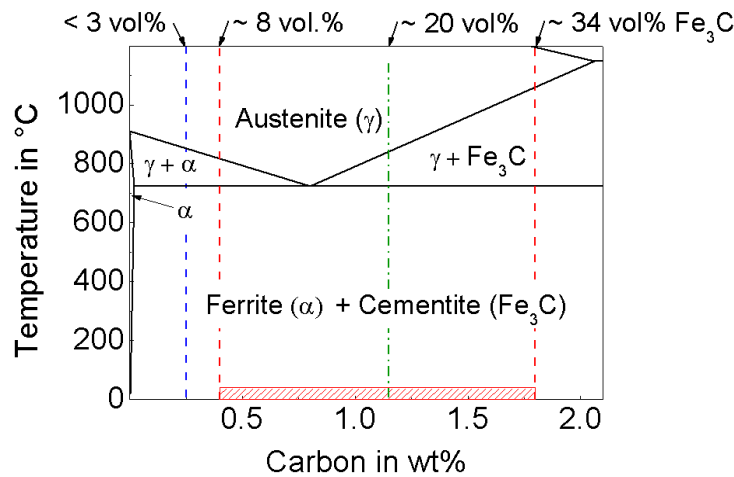

Figure 90 Iron-carbide phase diagram of a plain carbon steel. Alloying elements may alter the characteristics of the diagram, this is neglected here. The shaded area indicates the carbon content for the RT residual and internal stress studies that have yet been published (cf. literature review, §1.3.1). The blue dashed line indicates the carbon content for the 1%CrMoV steel and the green dot-dashed line indicates the carbon content for the high-carbon steel used in this dissertation.

Despite the low volume fraction of cementite in the 1%CrMoV steel, significant interphase strain is created after RT tensile deformation: The ferrite phase strain saturates towards 5% plastic strain and amounts *-650 $\mu\varepsilon$* and *+100 $\mu\varepsilon$* in the axial and transverse direction, respectively (cf. Figure 57(a), §3.2.1). First, with a simple conversion of strain to stress (Eq. 37, §4.3), a compressive stress of *150 MPa* in the axial direction is obtained. To put that value into context; this stress equals about 25% of the yield stress at RT. Second, the residual strain or stress is of comparable magnitude to those obtained by deformation of high-carbon steels with a correspondingly high volume fraction of cementite. In those steels, cementite is considered as a strengthening phase [15, 65]. Consider as reference the work of Oliver *et al.* [15] with spheroidized cementite particles. The average axial and transverse residual ferrite strain saturates at values of approximately *-900 $\mu\varepsilon$* and *+450 $\mu\varepsilon$*, respectively and an axial compressive stress of *150 MPa* was estimated. The absolute numbers of the residual lattice strain in the axial direction of the 1%CrMoV and Oliver's high-carbon steel are surprisingly not too dissimilar, considering the difference in cementite volume fraction of < 3% and

20%, respectively. The effects of the microstructure, morphology and volume fraction of cementite on the amount of accumulated residual ferrite phase strain, although attempts are made [62, 63], have not yet been convincingly elucidated. The information from the high-carbon steel, initially meant for addressing the cementite elastic anisotropy, may help and is discussed in the following. In Figure 91, the axial lattice strain of the {211} ferrite grain family is shown during RT tensile deformation of the pearlitic, the tempered pearlitic and the spheroidized microstructure.
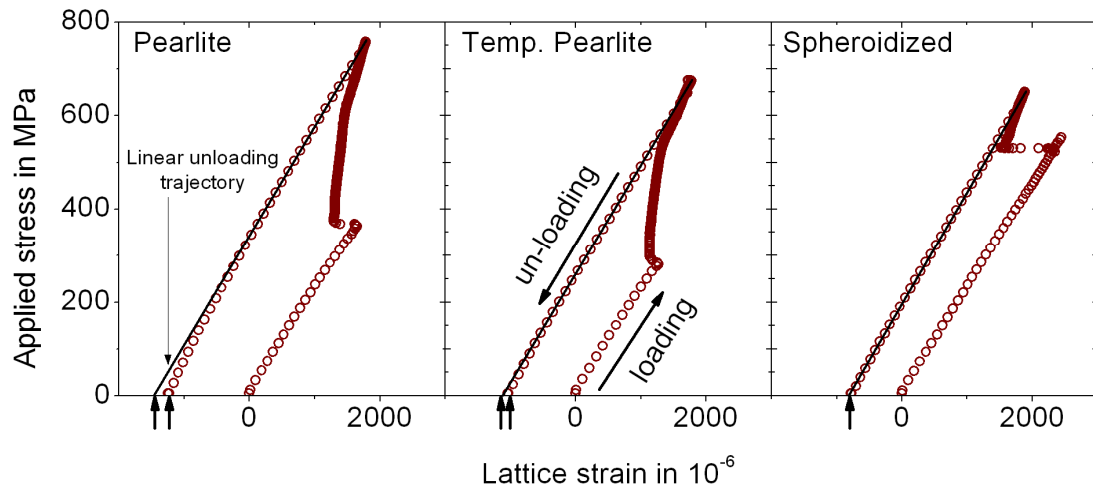

Figure 91 Evolution of the axial {211} ferrite lattice strain in the pearlitic (sample *HC1*), the tempered pearlitic (sample *HC2*) and the spheroidized (sample *HC3_1*) microstructure. All samples are tensile deformed at RT to about 4.5% plastic strain, The corresponding stress-strain curves are shown in Figure 71, §3.4.3.1. The arrows on the horizontal axis represent the lattice strain value of the actual data point and when a linear unloading trajectory (back line) is considered. These arrows are at different positions due to the relaxation of the lattice strain in the pearlitic and the tempered pearlitic microstructure during unloading.

All microstructures have about the same volume fraction of cementite (20%) and all three samples have been deformed to about the same amount (4.5%) of plastic strain (cf. Figure 71, §3.4.3.1). Due to the extensive strain hardening, the pearlitic and the tempered pearlitic microstructure experience a higher stress than the spheroidized microstructure. The {211} grain family is considered to be least affected by intergranular strains and is taken as reference for strain measurements when only one diffraction peak is considered [93, 94, 147]. The residual strain after unloading is plotted in Figure 92. The smallest and the largest magnitude of residual strain are obtained by the spheroidized (-780 µε) and the pearlitic (-1280 µε) microstructure, respectively. There are two major possibilities for the evolution of the residual lattice strain with plastic strain: Either the data point lies in a regime where the residual phase strain is already saturated, or, the data point lies in a regime where the residual phase strain is still increasing with further plastic strain. This is schematically shown for the data point of the spheroidized microstructure. Unfortunately, no load/unload cycles have been performed to follow the evolution of residual strain as a function of plastic strain. Some authors obtain the evolution of residual strain with plastic strain from a

continuous in situ tensile test by subtracting the extrapolated linear elastic response from the non-linear plastic response under load [65]. Because of the relaxation of the lattice strain during unloading, indicated in Figure 92 with the linear unloading trajectory, this procedure is not used. For instance, the residual lattice strain in the pearlitic microstructure shows a discrepancy of 210 με between the residual strain from the linear unloading trajectory (-1490 με) and the measured data point (-1280 με).

The steel investigated by Oliver *et al.* [15] is very similar to the high-carbon steel with the spheroidized microstructure and is used for a direct comparison: The ferrite phase strain saturates shortly after the end of Lüders band deformation [15], which amounts to about 1.5% plastic strain for the spheroidized steel and is indicated in Figure 92. Therefore, the measured data point (at 4.5% plastic strain) presumably lies in a saturated regime and is of a smaller magnitude as the data point of the pearlitic and the tempered pearlitic microstructure.
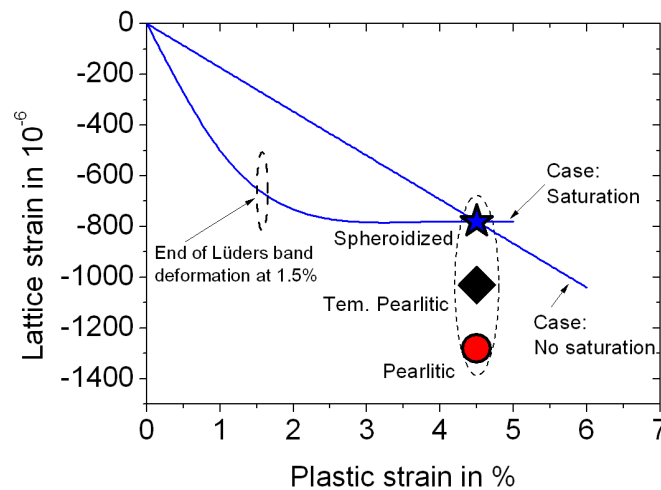

Figure 92 The three data points represent the residual axial strain of the {211} ferrite grain family from the pearlitic, the tempered pearlitic and the spheroidized microstructure after RT tensile deformation to 4.5% plastic strain. The lines schematically show the two cases where the data point may lies in a regime where the residual phase strain saturated or where the residual phase strain still increases in magnitude. The end of the Lüders band deformation for the spheroidized microstructure is around 1.5% plastic strain. In a similar steel, the residual ferrite lattice strain was found to be close to saturation [15].

These results suggest that the cementite volume fraction solely does not determine the amount of residual phase strain after plastic deformation. Other factors such as microstructure and morphology of cementite might be equally important and the residual phase strain may be smaller in a more homogeneous microstructure with spherical cementite particles than in a microstructure with a more complex morphology and arrangement of the cementite particles. This hypothesis then implies that the residual phase strain can be of a similar magnitude in both the 1%CrMoV and the high-carbon steels with sperical cementite particles, although the cementite volume fraction is considerably different.

4.3   Evolution of Type II microstrains for different loading conditions

Having shown that ToF neutron diffraction provides representative information for both Type II microstrains, i.e. the ferrite {*hkl*} lattice strain and ferrite phase strain, the residual strain accumulated after RT tensile deformation is compared with the residual strain accumulated after tensile and creep deformation at 565°C. In situ X-ray diffraction elucidates the role of the cementite.

Comment on the reference value:

The residual lattice strain in the ferrite matrix has been obtained from pre-deformed samples, using an undeformed sample as reference. An important aspect for the calculation of residual lattice strain is an appropriate choice for the stress-free parameters a^0 and d^0_{hkl}. This is of particular importance when comparing sequences deformed at ambient and high temperatures [148].

   First, compositional changes due to thermal assisted precipitation or element segregation can alter the lattice parameter. For instance, a 0.1 wt% change of carbon in solution can change the lattice parameter of ferrite by about 5000 $\mu\varepsilon$ [149]. To put that value into context: The maximum observed difference in residual ferrite phase strain amounts to 600 $\mu\varepsilon$, for the RT tensile deformed and creep deformed sequence shown Figure 57(a), §3.2.1. The stress-free parameters have therefore been determined after thermal aging at 565°C for 3000 h and compared to those from the reference sample. Within the experimental error no changes in both a^0 and d^0_{hkl} could be found (cf. Figure **57**(d)), which excludes any purely thermal induced change in composition. In fact, this is an expected result, as the material has been tempered at 700°C at the final stage of production. Furthermore, a potential deformation-assisted change in the matrix composition, by precipitation of carbides or transformation into other types of carbide, is unlikely. This was discussed in §3.6.

   Second, it is important to realize that thermoelastic stresses may actually alter the residual stress state during cooling, which may distort the comparison between the RT and HT results. Indeed, cementite has thermal expansion coefficients, which below its Curie temperature of about 230°C are significantly smaller than that of the ferrite. Alloying elements dissolved in the cementite may alter this temperature slightly. Furthermore, the thermal expansion of cementite is very anisotropic [150]. As a consequence, thermoelastic tensile and compressive stresses have been observed in the ferrite and the cementite, respectively [151]. Those stresses may easily exceed the matrix yield stress, causing stress relaxation in the constituents. From the in situ measurements, a slight increase of the ferrite phase strain upon cooling from HT to RT after tensile and creep deformation was observed to be of the order of 70 $\mu\varepsilon$, in both the axial and transverse direction.

Residual lattice strain in the ferrite matrix:

Figure 93 summarizes the results from the residual strain measurement of the pre-deformed samples in the axial direction showing in (a) the ferrite phase strain and in (b) the intergranular strains for the {110} and the {200} ferrite grain family. All measurements are done at RT and the shaded area represents the offset to HT (cf. *Comment on the reference value*).

The smallest amount of phase strain is obtained when the samples are only creep deformed. RT and HT tensile deformation gives about the same amount of phase strain for small deformations (data point at 1% plastic strain). At large deformations, the phase strain at RT increases considerably and saturates towards a value that is more than two times larger than that obtained during HT tensile deformation.
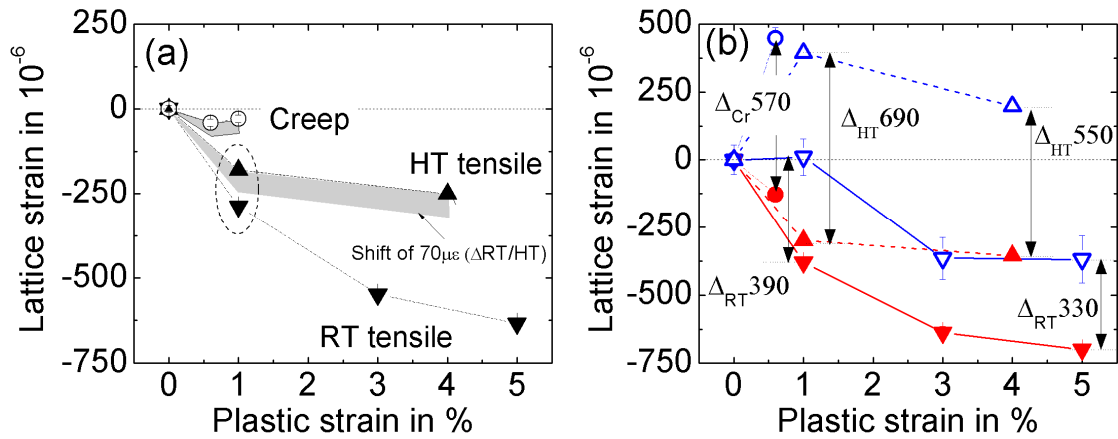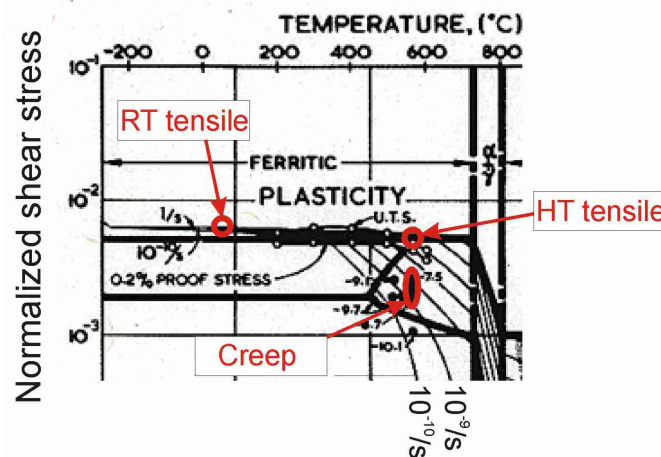

Figure 93 Summary plots showing the lattice strain evolution with plastic strain for the three deformation sequences RT tensile, HT tensile and creep measured with ToF neutron diffraction from the 1%CrMoV steel. (a) Axial ferrite phase strain, from Figure 57(a), §3.2.1. The shaded area underneath The HT tensile and creep data illustrates the difference 70με cooling. (b) Axial lattice strain for the {110} (filled symbols, red) and {200} (open symbols, blue) ferrite grain families, from Figure 57 (b)-(d), §3.2.1.

Large {*hkl*} lattice strains are introduced in all three deformation sequences, with the {110} and {200} marking the extremes in each sequence (b). Consider the difference between the {110} and the {200}. The largest difference (690 με) was observed during HT tensile deformation at small plastic strains. This difference is smaller (550 με) at large plastic strains and its value corresponds with that after creep deformation (570 με). The smallest difference has been observed for the RT tensile sequence with 390 με at small and 330 με at large plastic deformation.

In summary, the magnitude and the evolution of phase strain (but also the intergranular strain) with plastic strain is different for the three different loading sequences. The active and dominant deformation mechanisms for the three different loading sequneces are considered in the following section.

Possible dominating deformation mechanisms:

Consider the deformation mechanism diagram of a 1%CrMoV steel as introduced in §1.2.4.1. A reduced section is shown in Figure 94. The three markers should approximately represent the locations for the three deformation sequences. The RT tensile test was performed with a strain rate of 10^{-5} s^{-1} and the material strain-hardens in the plastic regime. In Figure 94, this domain is dominated by low temperature plasticity. The creep tests show a strain rate of the order of 10^{-8} to 10^{-9} s^{-1} in the steady-state regime (pre-deformed and in situ). In Figure 94, this domain is dominated by dislocation creep. The HT tensile test was performed with a strain rate of 10^{-5} s^{-1} (and $5 \cdot 10^{-4}$ s^{-1} for the second in situ test). The stress-strain curve reaches soon after the 0.2% yield its maximum stress and enters a steady-state like regime, which is characteristic for a dominating deformation mechanism that involves creep processes to maintain a microstructural balance.

Figure 94 Part of the deformation mechanisms map of the 1%CrMoV steel from [30] and already described in §1.2.4.1. The marks indicate the approximate location for the three deformation sequences.

Consider further the change in ferrite diffraction peak width of the deformed samples. The change in peak width (or peak broadening) represents the evolution of the materials' microstructure and therefore may give a hint towards the active and dominating deformation mechanisms. In general, the peak can broaden by a reduction in the coherent scattering length, such as the grain size, or, by an increase in inhomogeneous strain (variations in lattice spacings, Type II and III strains), such as for instance an increase in dislocation density. Diffraction line profile analysis is a powerful tool to extract microstructural parameters [152]. This has recently been performed to study the dislocation density and sub-grain size evolution during low cyclic fatigue loading in a similar type of steel (2CrMoNiWV) [153]. We did not indend to go into that detail but just to compare the evolution of the peak width for the different deformation sequences. Figure 95(a) compares samples tensile deformed at RT and creep deformed to the steady-state regime.

For RT tensile deformation a significant increase of the peak width of about 25% after 5% plastic strain is observed, which points towards a classical increase of the dislocation density with plastic deformation. The sample in the secondary creep regime has a slightly smaller peak width compared to the starting condition. Consider now the peak width of the samples tensile deformed at HT, shown in Figure 95(b). The peak width is first increasing and then decreasing and seems to reach saturation at large plastic strains and this final value corresponds with that in the secondary creep regime, shown in (a). Note that the instrumental contribution to the peak width is smaller than the measured peak width of the ferrite grain families.
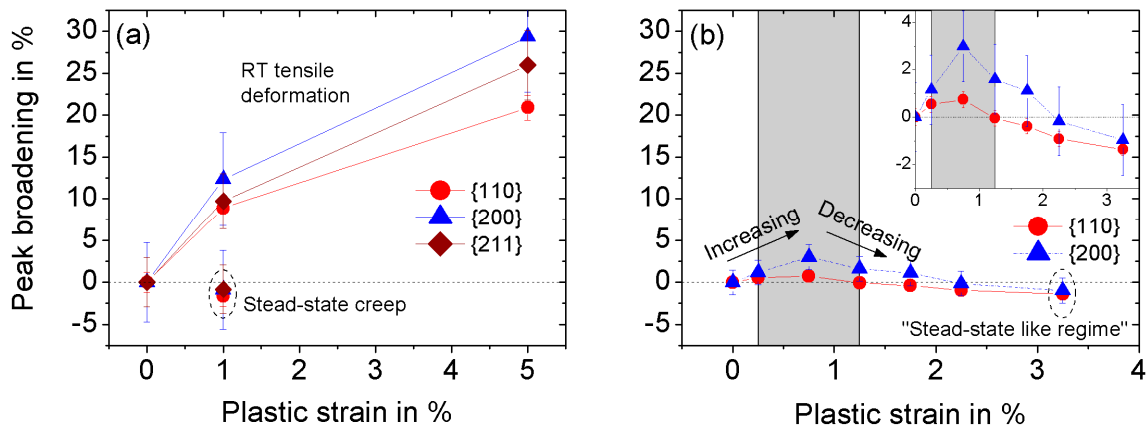

Figure 95 Summary plots showing the peak broadening as a function of the plastic strain for the three different deformation sequences: (a) RT tensile and creep from the pre-deformed samples (cf. Figure 80(a), §3.5.1.3). (b) HT tensile from the in situ test (Figure 81(b), §3.5.2). The data-set of the in situ test (rather than the pre-deformed samples) has been taken since there are more data points to describe the evolution of peak width with plastic strain.

The transition of increasing and decreasing peak width lies in between the 2nd and the 4th data point (0.25 to 1.25% plastic strain). That is also when the stress-strain curve reaches its maximum stress (about 0.5% plastic strain). This may in the following allow to comment on the behaviour of the interphase and intergranular strain during HT tensile deformation in these two regimes.

Combined ferrite and cementite residual lattice strain data:

Figure 96 shows the combined data of ferrite and cementite for the residual strain evolution with plastic strain during tensile deformation at RT and at HT. Note that the scale for the cementite and the ferrite is different for clarity. The cementite in (c) is measured at HT, the ferrite in (d) is measured at RT and the shaded area represents the offset. There are two types of shaded rectangles that allow the comparison between the RT and HT behaviour of the lattice strain in the early plastic regime until 1% plastic strain. In this regime, both the ferrite and cementite behave rather similarly and that is also where the increase in peak width has been observed during HT tensile deformation. Beyond this regime the lattice strain behaviour is considerably different at RT and HT. At RT the

ferrite phase strain keeps increasing and only seems to turn into saturation at high plastic strains. In literature, saturation is indeed observed during RT tensile deformation after a plastic strain of 5% and more [15, 44, 65], indicating that the shape misfit, between the plastically deforming ferrite matrix and the stiff cementite particles, does not continue to grow at the same rate with plastic strain but relaxation events happen. Local plastic flow at the ferrite-cementite interface is often anticipated to reduce this misfit [15, 65]. On the other hand, the HT data seems to turn very soon in a saturation regime. Assuming that this regime is dominated by creep deformation mechanisms, a parallel can be drawn with the creep test. There, the residual strain measurements suggest, that the ferrite phase strain at the end of the primary and in the secondary regime, does not change, which is in agreement with the in situ results for the {110} and {200} grain families (cf. Figure 85(e), §3.5.4). A parallel can be drawn to literature. Based on work on SiC reinforced aluminium composites, Winand *et al.* [72] concluded that stress relaxation mechanisms must be operating during creep. Otherwise, the matrix creep would continuously increase the misfit between the phases, violating the definition of the steady-state creep of a dynamic equilibrium between dislocation generation and annihilation [154]. Accordingly, the misfit between matrix and reinforcement, measured by neutron diffraction, was found to remain essentially constant during primary and secondary creep.
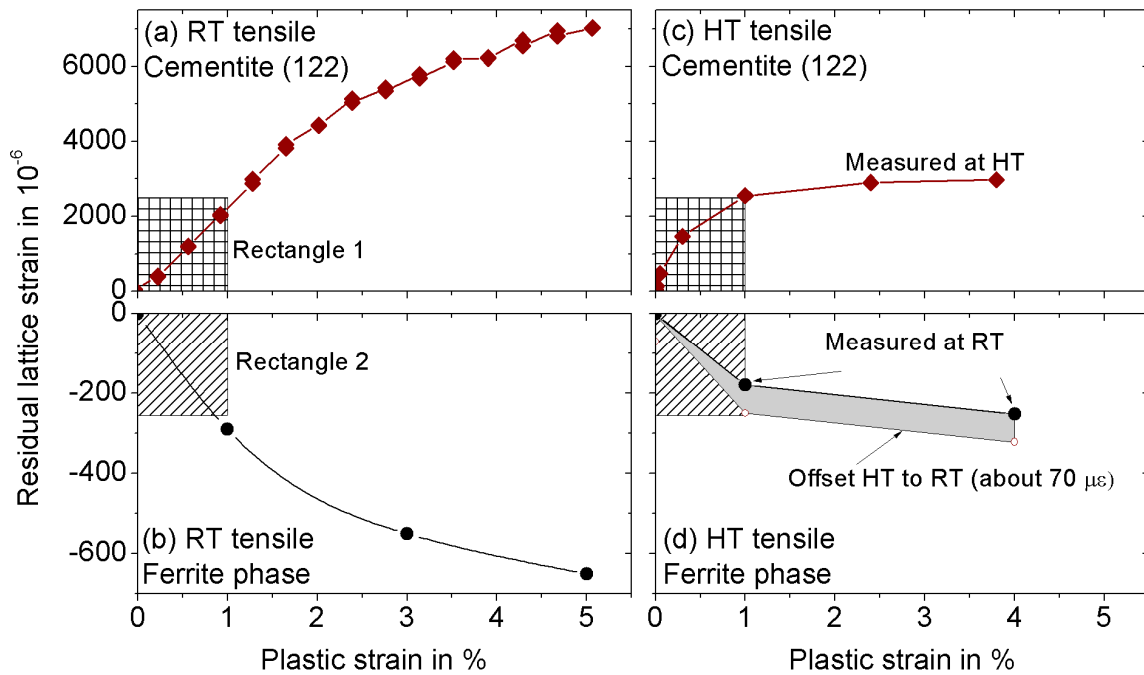

Figure 96 Summary plots showing the evolution of residual strain of the ferrite and the cementite with plastic strain during RT ((a) and (b)) and HT ((c) and (d)) tensile deformation. The corresponding data points are taken from: (a) Figure 67(a), §3.4.1.1; (b) Figure 57(a), §3.2.1; (c) Figure 67(b), §3.4.1.1 and (d) Figure 57(a), §3.2.1. The shaded area in (d) considers that the data points would be more compressive at HT. The two types of shaded rectangles (1 and 2) allow a direct comparison of the cementite and the ferrite, respectively, in the early plastic regime of the RT and the HT data. Each rectangle type has the same width and length.

This in summary suggests that the plastifying ferrite is shedding part of its load to the cementite in the very beginning of the HT tensile test. When the creep mechanisms become dominating, there is no further load transfer to the cementite. However, the phase strain that has been accumulated so far is maintained.

Axial and transverse response:

Only the axial response has yet been considered. Figure 97 shows a summary plot of the axial and transverse ferrite phase strain of the pre-deformed samples. The RT tensile deformed sequence is shown in (a), the creep deformed sample and the HT tensile sequence in (b). During RT tensile deformation, the ferrite phase strain in the axial and transverse direction is compressive and tensile, respectively, due the load-redistribution to the cementite. Consider now the ratio of axial and transverse residual strains. This ratio was discussed in detail by Oliver *et al.* [15]. Assuming a homogeneous and isotropic elasticity, with a microstructure containing cementite inclusions considered as randomly distributed and only elastically deforming spheres, the following relations should hold between the axial and the transverse residual strains, independent on the amount of plastic strain:

$$\varepsilon_{Tr}^{Fe} = -\frac{1}{2}\varepsilon_{Ax}^{Fe}$$

Eq. 36

For comparison, the data points of Oliver's RT tensile test on a steel with spheroidized cementite particles are added in (a) and marked with *Oliver*. The absolute number in lattice strain is somehow larger due to the higher volume fraction of cementite (20%).
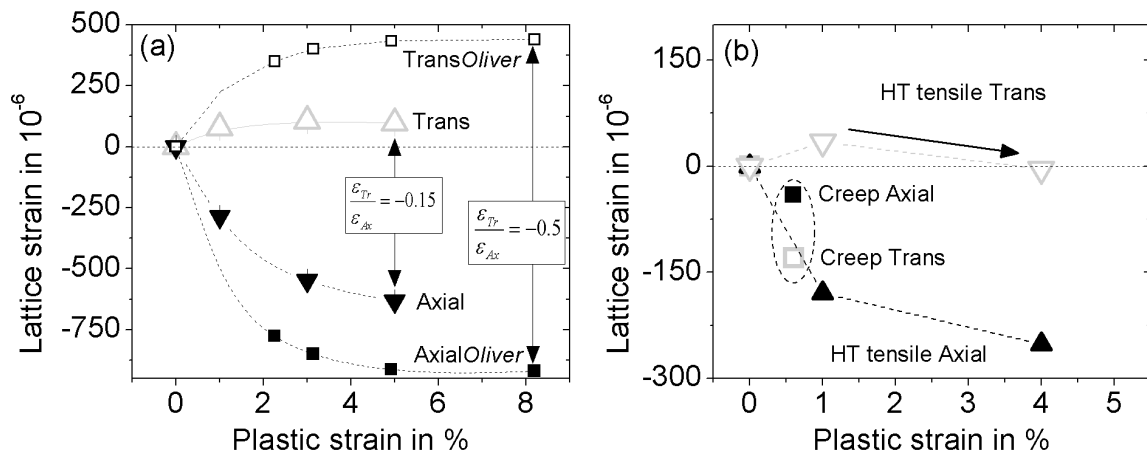

Figure 97 Summary plots showing the residual ferrite phase strain from the pre-deformed samples in both the axial and transverse direction, from Figure 57(a), §3.2.1. In (a) the RT tensile data is shown and compared to the results form a high-carbon steel with 20vol.% spheroidized cementite particles from Oliver *et al.* [15]. The ratio between the axial and the transverse direction is indicated. In (b) the HT tensile and creep data is shown. From Figure 79(a), §3.5.1.2.

A ratio of -0.5 for the transverse and axial direction was indeed observed by Oliver, as illustrated in Figure 97(a). It was explicitly mentioned that this may only be valid for a homogeneous microstructure with spheroidized particles and Eq. 36 is indeed not valid for the microstructure of the 1%CrMoV steel where the ratio between the axial and the transverse residual strain is more towards a value of -0.15 at large plastic strains.

Consider now the residual transverse and the residual axial lattice strain during creep deformation shown in Figure 97(b). Both data points are compressive. Surprisingly, the transverse data point is even more compressive than the axial one. In terms of load-redistribution this would suggest that the cementite is shedding load to the ferrite in the transverse direction, which seems to conflict with the behaviour in the axial direction. Figure 98 shows the evolution of the cementite lattice strain with time during an in situ creep test. Indeed, the axial and the transverse cementite grain orientations behave rather different: In the axial direction, the cementite residual lattice strain value is preserved, while in the transverse direction, the cementite residual lattice strain is decreasing in magnitude. Although the orgin for this behaviour is not clear, it might explain why, once creep mechanisms dominate, the transverse direction of the ferrite becomes (strongly) compressive. This is also observed during HT tensile deformation, shown in Figure 97(b), where the transverse residual ferrite strain becomes more compressive at large plastic strains, as indicated by the arrow.
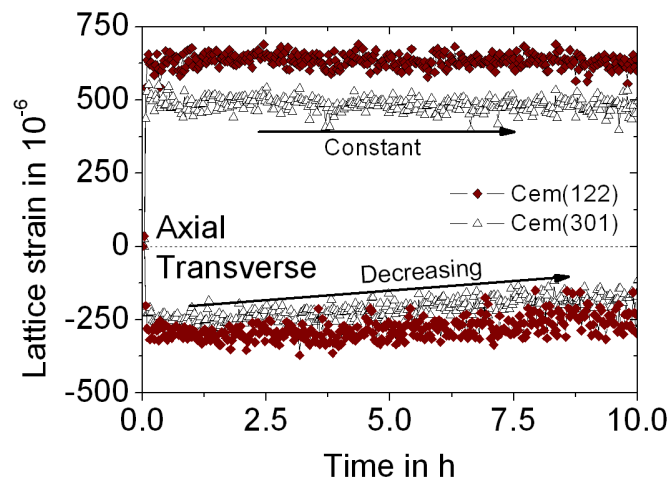

Figure 98 Summary plot showing the cementite lattice strain evolution of the (122) and the (301) grain orientation during in situ creep of the 1%CrMoV steel at a stress level of 130MPa at 565°C, i.e. below the onset of the transient regime at 200MPa. From Figure 69, §3.4.1.2. The transverse cementite strain is decreasing with time.

Intergranular strains during HT tensile deformation:

Two major differences in the evolution of the Type II strain during RT and HT tensile deformation have been observed in the early plastic regime: Larger residual intergranular strains and an early redistribution of load during HT tensile loading. Consider the latter observation first. The HT stress-stain curve is characterized by a transient regime followed by a steady-state like regime without work hardening. The yield stress (0.2%) and the residual lattice strain during HT tensile deformation (at least in the early plastic regime) are not significantly altered by the strain rate in the range of $5 \cdot 10^{-4}$ to 10^{-5} s^{-1}. This allows comparing the results of the experiments performed at the ToF neutron dffractometer and at the synchrotron X-ray beamline ID15B, since the in situ tensile tests with the loading-rig at ID15B can only be performed with a constant displacement rate and the actual strain rate, also due to the localized deformation (cf. §2.3.5.2), may be larger than 10^{-5} s^{-1}. Figure 99 shows the transient regime during HT tensile loading and combines: In (a) the mechanical data of the pre-deformed samples with a high reliability of the stress-strain behaviour and in (b) the diffraction data of the ferrite {220} and {200} and the cementite (122), where the mechanical data (strain) is not reliably measured.
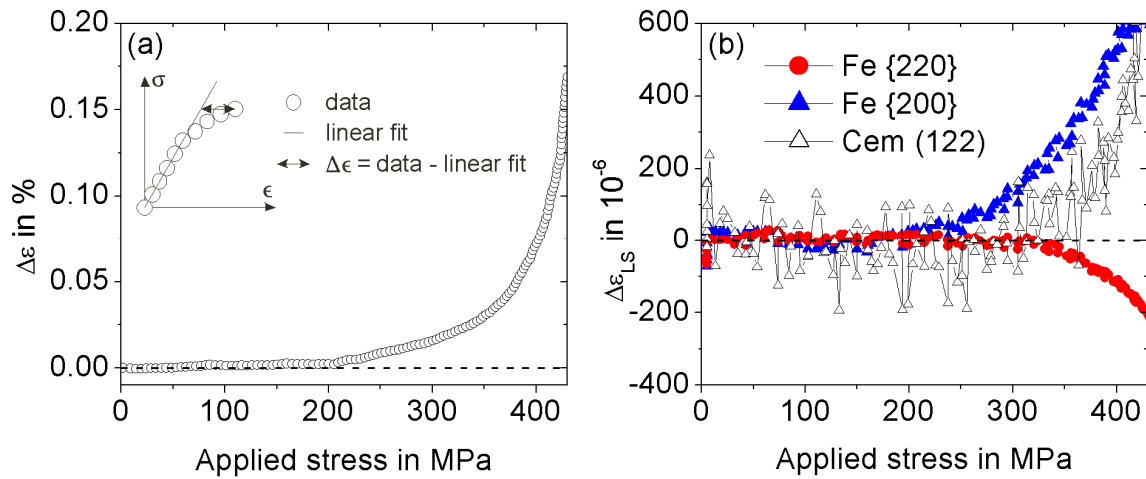

Figure 99: (a) Mechanical data from the pre-deformed sample, tensile deformed at HT until 1% plastic strain (sample *HT765*), Figure 55, §3.2.1. The 0.2% yield stress is around 435MPa. The inset reminds the definition of $\Delta\varepsilon$. (b) Diffraction data form the in situ HT tensile test (sample *ID2*) with synchrotron XRD at beamline ID15B, §3.4.1.1. The $\Delta\varepsilon_{LS}$ is calculated in the same way as shown in the inset of (a), being the difference of a linear fit of the data points in the range 0 to 150MPa and the data.

At a stress of about 200 MPa, the stress-strain curve deviates from its linear behaviour and one can observe a redistribution of load between the phases and between the ferrite grain families. The {110} type (here {220}) appears as the soft direction and sheds load to the (122) cementite and the {200} ferrite.

In addition to this early redistribution of load, a large difference between the {110} and {200} lattice strains were observed. These values are summarized in Table 15 for both in situ tensile tests. This difference amounts to 390 µε for RT tensile and to 570 µε for creep deformation.

Table 15 Summarizing the difference in the {110} and the {200} lattice strains for the two in situ HT tensile tests as a function of plastic strain. From §3.5.2.

Test	0.25%	0.75%	1.25%	1.75%	2.25%	3.25%
Strain rate 10^{-5} s^{-1}	600 µε	680 µε	630 µε	620 µε	600 µε	560 µε
Strain rate $5 \cdot 10^{-4}$ s^{-1}	620 µε	660 µε	660 µε	660 µε	660 µε	640 µε

Load transfer between the {110} and the {200} ferrite grain families has been investigated by Oliver *et al.* [15]. They compared the experimental results of a RT tensile test on a single-phase ferritic steel with the results of EPSC modelling. For the modelling, plastic deformation of the bcc crystal has been assumed by slip in <111> directions on {110}, {112}, {123} planes. The results are schematically summarized in Figure 100. In (a), an elastically anisotropic polycrystal has been assumed, i.e. the <110> is stiffer as the <200> direction (cf. Figure 6(b), §1.1.2.1.1). The residual strains after tensile deformation are compressive for the {110} and tensile for the {200}. In (b), an elastically isotropic polycrystal is assumed. The residual strains are now reversed compared to (a) with the {200} being compressive and the {110} being tensile. This first proves that the {200} grains are oriented most favourably and the {110} grains are oriented the least favourably for slip. Second, the difference in stiffness can be predominant over the plastic anisotropy: The stiffer grain families bear a larger portion of the load and therefore reach yield at lower applied stresses.
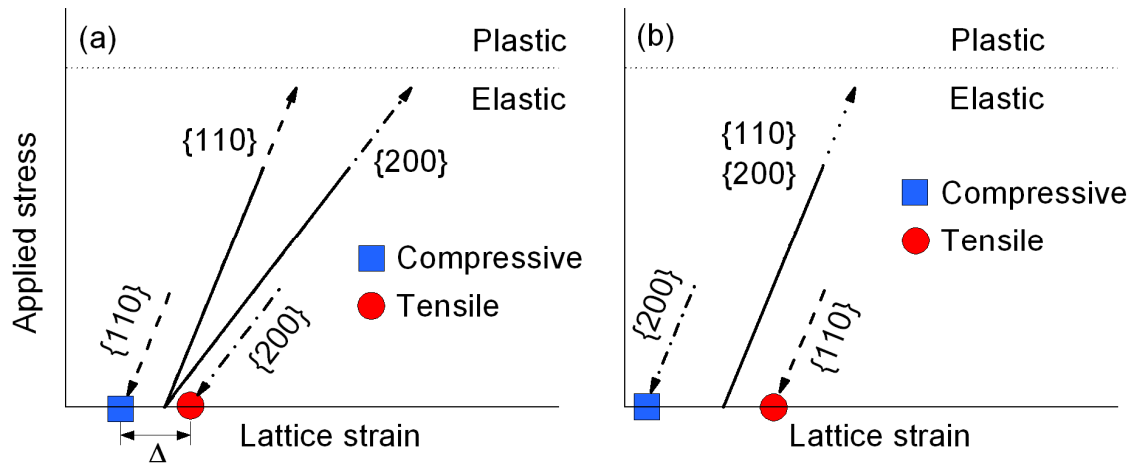

Figure 100 Schematic illustrating the influence of elastic anisotropy on the accumulation of residual lattice strain of the {110} and {200} grain families in a single-phase bcc steel, summarizing the results from EPSC modelling of Oliver *et al.* [15]. In (a), the {110} and {200} are considered as elastically anisotropic and in (b) as elastically isotropic. Δ is the difference in residual lattice strain between the {110} and {200}.

Consider now the axial stiffness for the {110} and the {200} grain family during tensile deformation at RT and HT. Table 16 summarized the results for the two steels investigated in this dissertation, the 1%CrMoV and the high-carbon steel with the spheroidized microstructure.

Table 16 Summarizing the stiffness of the {110} and the {200} ferrite reflection during RT and HT tensile loading: 1%CrMoV(XRD) §3.4.1.1, 1%CrMoV(neutron) §3.5.3, High-carbon steel with spheroidized microstructure §3.4.3.2,

Test	Axial {110} in GPa	Axial {200} in GPa	Ratio{ 110} / {200}
1%CrMoV (XRD)	RT 215±8: HT 175±7	RT 185±6: HT 130±9	RT ≈1.23: HT ≈1.42
1%CrMoV (neutron)	RT 227±1: HT 186±2	RT 176±1: HT 122±3	RT ≈1.29: HT ≈1.52
HighCarbonSteel(XRD)	RT 224±11: HT 183±9	RT 174±13: HT 98±17	RT ≈1.29: HT ≈1.87

In all cases, the stiffness ratio of the {110} and the {200} is larger at HT than at RT, pointing towards an increased elastic anisotropy at elevated temperatures. An increasing elastic anisotropy with increasing temperature is indeed predicted in literature by Razumovskiy *et al.* [155], who studied the elastic properties of pure (bcc) iron in the temperature interval $0\,K < T < T_c$ by first principles calculations. The Curie temperature T_c that marks the ferromagnetic to paramagnetic transition is about 770°C for pure iron. The calculations suggest that it is the change of magnetic order with temperature, which produces a decisive effect on the elastic anisotropy of pure (bcc) iron.

Given the assumption of Figure 100, a larger elastic anisotropy at HT may cause the stiffer grain families to bear a larger amount of load and start to yield earlier than the more compliant grain families, compared to at RT. This may be *a* possible explanation for the larger difference in the {110} and the {200} axial residual lattice strains and also might somehow contribute to the early load-redistribution between the {110} and {200} grain families, schematically summarized in Figure 101.
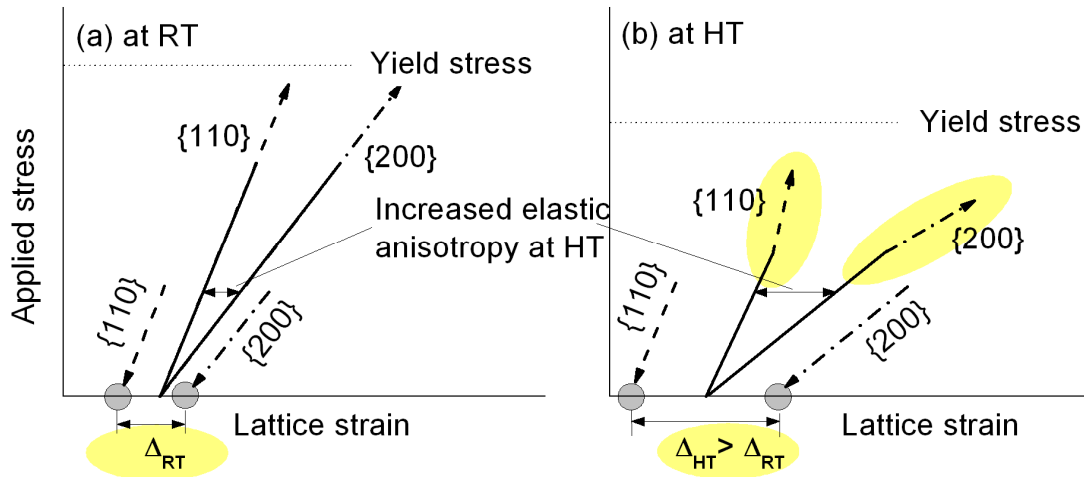

Figure 101 Schematic based on the assumption that a larger elastic anisotropy at HT causes an enhanced load transfer from the {110} to the {200}, which then could contribute to the early separation in the transient regime and a larger difference in the residual {*hkl*} lattice strains.

Note that at large plastic strains, the difference in strain between the {110} and {200} decreases (cf. Table 15): For the in situ tensile test with a strain rate of $10^{-5}\,s^{-1}$, this difference reaches at 3.3%

plastic strain the value that is obtained after creep deformation. For the in situ tensile test at the higher strain rate of $5 \cdot 10^{-4} \, s^{-1}$, the maximum value only seems to decreases at the end of the investigated plastic deformation at 3.3%.

The intergranular strains can be significantly influenced by the interphase strains as reported by Oliver et al. [15]. Figure 102 summarizes this observation and compares with the results obtain in this work. In (a) the residual intergranular strain after RT tensile deformation in a single-phase ferritic steel (labelled LC) and in a high-carbon steel ferritic steel with 20 vol% of spheroidized cementite particles (labelled HC) is shown, from Oliver et al. [15]. In the high-carbon steel, the ferrite phase strain is subtracted from the intergranular strain for a direct comparison. In the axial direction, the trend for the intergranular strains in the LC and the HC steel seem to be swapped, i.e. the {200} is most compressive in the HC steel. Oliver suggested that the interphase strains in the HC steel dominate over the intergranular effects: Since the {200} is the most compliant axial grain family and the ferrite is in a state of axial compression, the interphase strains then also produce the largest compressive residual strain in the {200}. In the transverse direction the interphase strain merely accentuates the trend due to intergranular misfit.
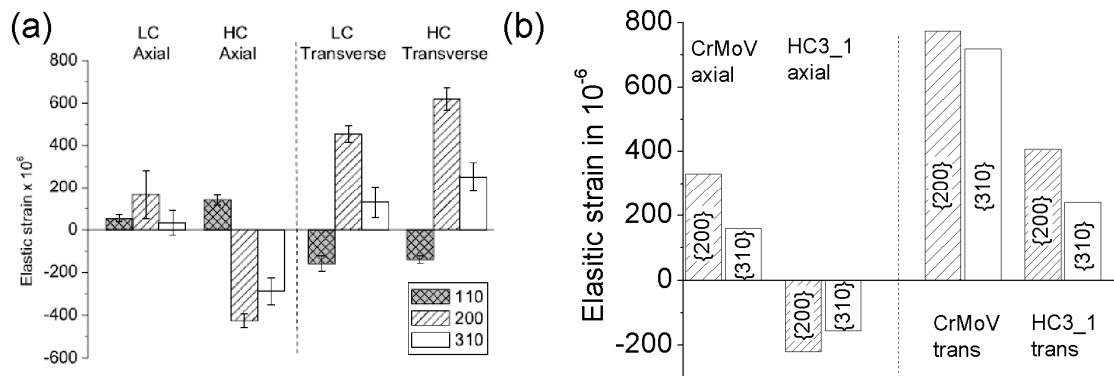

Figure 102 (a) Ferrite grain family intergranular residual strains, after subtraction of the phase-averaged residual strain, for the LC and the HC steels, at plastic strains of approximately 5% [15]. (b) Ferrite residual strain in the ferrite {200} and {301}, being consistent with the legend in (a). The residual strain of the {110} ferrite has been subtracted, since the phase strain in the spheroidized steel (HC3_1) is not available.

Figure 102(b) shows the lattice strains of the two materials investigated in this dissertation, the 1%CrMoV (< 3 vol% cementite) and the high-carbon steel with the spheroidized microstructure and 20 vol% cementite. Since the ferrite phase strain was not determined for the spheroidized microstructure, the lattice strain of the {110} is subtracted from the {200} and the {310}. Doing so it appears that the relative difference of the (residual) lattice strain between the three grain families in these two steels behave equivalent to the steel without (LC) and the steel with cementite particles (HC) of Figure 102(a). Given the aforementioned explanation of Oliver, it is rather surprising that the axial lattice strain of the 1%CrMoV behaves similar to the single ferrite phase LC, since a

significant amount of phase strain, similar to the HC steel, respectively, has been found (cf. §4.2). The origin for this observation is not yet elucidated.

Impact of ferrite phase strain on measurement of macrostrain:

Macro- and microstresses can be accumulated during manufacturing, which for instance includes hot forging for the 1%CrMoV steel, or during service due to temperature and applied stress gradients through the component thickness. Residual macrostresses can be detrimental when they reduce the tolerance of the material to an externally applied force and need therefore to be considered in engineering. In large (industrial) components, the residual macrostrains are typically measured by neutron diffraction due to the benefits of a high penetration depth (attenuation length 8 mm in steel) in combination with the well-defined rectangular gauge volume and sophisticated methods for sample manipulation [117, 156]. For such measurements, only a limited time per measuring point is allowed, since beamtime is limited and expensive. Limited counting statistics on other hand do not give access on the interphase stresses when the diffraction peaks of the second phase cannot be observed due to its low volume fraction. Since diffraction measures a superposition of micro- and macrostresses, it comes back to the well-known problem of obtaining a stress-free reference value a^0 and d^0_{hkl} [147, 148]. The following calculation should illustrate the approximate error one can obtain without considering the microstresses, the magnitude and sign (tensile or compressive) of which depends on the active deformation mechanisms. Consider a simple estimation of the residual phase strain in the axial and transverse direction as principal directions ε_{11} and ε_{22}, ε_{33}, respectively and an isotropic behaviour, the strain to stress conversion reads [157]:

$$\sigma_{ij} = \frac{E}{1+v}\left[\varepsilon_{ij} + \left(\frac{v}{1-2v}\right)(\varepsilon_{11} + \varepsilon_{22} + \varepsilon_{33})\right] \qquad \text{Eq. 37}$$

The axial and transverse residual ferrite phase strains from the three different deformation sequences at a (almost) saturated state and the corresponding stress values are listed in Table 17. A Young's modulus $E = 210$ GPa and Poisson's ratio $v = 0.28$ for steel has been assumed.

Table 17 Residual ferrite phase strain in the axial and transverse direction for about the saturation value in each loading sequence, taken from the pre-deformed samples measured at POLDI, Figure 57(a) §3.2.1. The stress is calculated using Eq. 37 assuming the strain as principal directions and the Young's modulus E = 210GPa and Poisson's ratio v = 0.28.

History	Strain axial	Strain trans	Stress axial	Stress trans
RT Tensile	-650 με	+100 με	-150 MPa	-14 MPa
HT Tensile	-250 με	-25 με	-130 MPa	-50 MPa
Creep	-50 με	-160 με	-60 MPa	-70 MPa

4.4   Characteristics of cementite

During the first in situ tensile tests with the 1%CrMoV steel at the MS beamline the following has been observed: In the elastic regime, the stiffness of some cementite grain orientations is larger than for others. This was reported in §3.3.2.3 and is summarized in Figure 103(a) for the axial direction of the (122) and (301) cementite grain orientation. In the plastic regime, the cementite peaks broaden extensively and become highly asymmetric. This was reported in §3.3.2.2 and is summarized in Figure 103(b) for the axial direction of the (122) cementite grain orientation. These characteristics have been followed in some more detail by investigating a high-carbon steel with a larger amount of cementite.
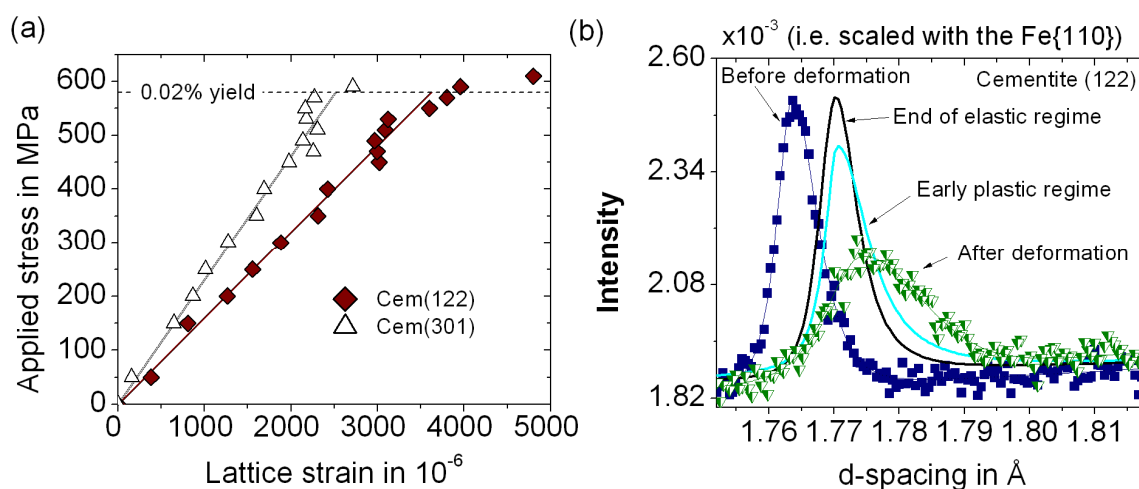

Figure 103 Summary plot showing the characteristics of cementite during RT tensile deformation. (a) The (122) and the (301) orientation in the elastic regime (axial direction), from Figure 63(a), §3.3.2.3. (b) The (122) diffraction peak before, during and after the tensile test (axial direction), from Figure 62(d), §3.3.2.2.

4.4.1   Elastic anisotropy of cementite

Both single peak and full pattern fitting have been applied in literature to study the evolution of lattice strain of the ferrite and cementite phase in various carbon steels. Full pattern fitting is used to determine the average phase strain in order to make comparisons between the phases and/or to obtain acceptable statistical uncertainties when diffraction from a low volume fraction second phase is too weak for single peak fitting. On the other hand, fitting the peaks individually provides the specific behaviour of these grain orientations. Single peak fitting can therefore resolve anisotropic behaviours for different (*hkl*) grain orientations during elasto-plastic deformation. For ferrite grain families, both elastic and plastic anisotropic behaviour are well known at RT [15, 65, 158], this being also accounted for by various modelling approaches aiming to understand the intergranular strain evolution [15]. This anisotropy may cause (*hkl*)-dependent shifts of the diffraction peaks and the use of full pattern Rietveld refinements, which assumes an undistorted crystal structure, may be

problematic. Therefore, a modified Rietveld refinement was proposed that accounts for this anisotropy in cubic crystal systems [97]. On the other hand, diffraction from cementite with laboratory X-rays and neutrons was often too weak to allow single peak fitting within reasonable uncertainties [15, 46, 49, 53] and isotropy was assumed for full pattern fitting. An elastic anisotropic behaviour of cementite has not yet been reported during in situ mechanical testing of carbon steel. One synchrotron X-ray diffraction study (Young *et al.* [65]) on an ultra high-carbon steel with 34% cementite, having good counting statistics to well resolve the individual peaks, reported on three cementite grain orientations – (202), (121), (200) – during RT tensile deformation. Two of these reflections, i.e. (202) and (121), might easily overlap with others (cf. Figure 59), depending on the resolution of the instrument and which is not further described. The interpretation of these results is therefore questionable. Neither is mentioned, why no other non-overlapping cementite reflections have been used. Note, that in Young's notation, the unit cell parameters are swapped and the indexation is here converted according to the convention in this dissertation: $(h,k,l)_{\text{Young}} \rightarrow (k,l,h)$. Young did not observe an anisotropic behaviour in the elastic regime, but reported that some cementite orientations carry more load than others in the plastic regime. The latter observation is discussed in §4.4.3.

During tensile loading at RT of the 1%CrMoV steel, the stiffness of some cementite grain orientations in the elastic regime are quite different from each other, pointing towards a significant elastic anisotropy for cementite. The (122) and (301) can be followed well due to their high intensity compared to other cementite peaks. The stiffness in the axial direction for the (122) and the (301) grain orientation is summarized in Table 18. In the following, the stiffness of a (*hkl*) grain orientation is written as E(*hkl*). The stiffnesses are E(122) = 160 GPa and E(301) = 230 GPa. To put that into context: The stiffness of the {110} and the {200} ferrite grain family are about E{110} = 225 GPa and E{200} = 180 GPa. The tempered bainitic cementite might still possess some particular crystallographic relationship with the ferrite, which might affect the lattice strain evolution of some cementite orientations. These details are not further considered here. Rather, a high-carbon steel has been tested and found that the (122) orientation is indeed significantly stiffer than the (301) orientation and this for different microstructures, i.e. pearlitic, tempered pearlitic and spheroidized. The difference is also preserved at elevated temperatures, as investigated for the spheroidized microstructure. For the 1%CrMoV steel the scatter on the data points is too large due to the volume fraction. The stiffness values for the (122) and (301) for the different microstructures are rather similar and also between RT and HT. Since the stiffness of the ferrite grain families is drastically lower at HT, e.g. $E^{RT}\{110\}$ = 225 GPa and $E^{HT}\{110\}$ = 185 GPa, the cementite may play a strengthening role in the elastic regime at HT.

Table 18 Axial stiffness of the (122) and the (301) cementite orientations during tensile loading at RT: 1%CrMoV (cf. §3.3.2.3), high-carbon steel pearlite, temp. pearlite and spheroidized microstructure (cf. §3.4.3.1) and during tensile loading at 500°C of the spheroidized microstructure.

	1%CrMoV	Pearlite	Temp. Pearlite	Spher. RT	Spher. 500°C
E(122) axial	160 GPa	180 GPa	170 GPa	180 GPa	180 GPa
E(301) axial	230 GPa	230 GPa	220 GPa	230 GPa	230 GPa

Only recently Nikolussi and co-workers have calculated by first principles studies the full set single crystal elastic constants C_{mn} of cementite [40]: They found an extreme elastic anisotropy of cementite and confirmed experimentally by synchrotron X-ray diffraction $sin^2\psi$ stress measurements on polycrystalline bulk Fe$_3$C, grown on α-Fe substrate. The extreme elastic anisotropy is caused by a very low value c_{44}, being only about 1/10 of c_{55} and c_{66}. The results comply with the calculations from another group [37]. Figure 104 shows a representation of the elastic modulus with crystallographic direction, reconstructed from the elastic constants given by Nikolussi [40] and using Eq.12 in §1.1.2.1.1. Geometry and colour code represent the magnitude of the elastic modulus E(hkl) for a given crystallographic direction [hkl]. The choice of axes is consistent with the indexation of the cementite diffraction peaks used in this dissertation. Superimposed are lines drawn with the [301] and [122] directions, which are found to be very close to the extreme upper and lower limits, respectively. It is clearly evident that a large difference exists in the absolute values between the result from first principles studies E(301) = 280 GPa and E(122) = 60 GPa, and the measured stiffness in the 1%CrMoV of E(301) = 230 GPa and E(122) = 160 GPa. Elastic grain interactions may influence the absolute values and bring them closer to the single crystal ferrite values with their extremes of 280 GPa and 130 GPa for the {222} and the {200} grain family (cf. Figure 6(b), §1.1.2.1.1).
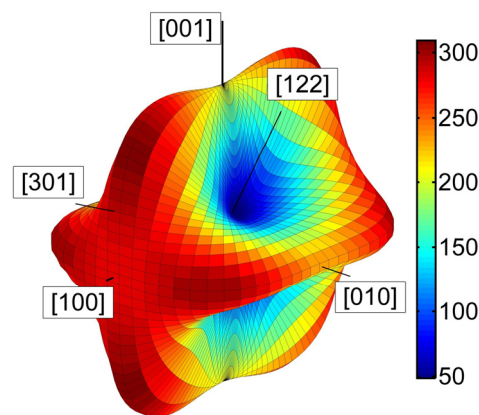

Figure 104 Surface of the modulus of elasticity reconstructed using the single crystal elastic constants C$_{mn}$ (in GPa) c$_{11}$=385, c$_{22}$=341, c$_{33}$=316, c$_{44}$=13, c$_{55}$=131, c$_{66}$=131, c$_{12}$=157, c$_{13}$=162, c$_{23}$=167 [40]. The magnitude is also represented by the colour code (unit GPa). The crystallographic directions [100], [010], [001] refer to a choice of axes with a = 5.0920, b = 6.741, c = 4.5170 Å [12], respectively.

The experimental results for the (301) and the (122) orientations are consistent for the different microstructures and agree well with the calculations, these being a rather stiff and compliant crystallographic direction, respectively. In spite of the large scatter (cf. Figure 63(b)) due to the low peak intensity in the 1%CrMoV steel, the axial stiffness in some further orientations decreases in the order: $(201) \rightarrow (211) \rightarrow (002) \rightarrow (102) / (221) \rightarrow (112)$. The corresponding single crystal values are: $285_{(201)} \rightarrow 197_{(211)} \rightarrow 190_{(002)} \rightarrow 226_{(102)} / 145_{(221)} \rightarrow 88_{(112)}$. This order is in good agreement with the observation in the 1%CrMoV steel and only the (102) falls out of the sequence. In fact, the (102) is embedded in between the {110} ferrite and the broad {200} vanadium carbide peaks (cf. Figure 59), lies in the moving direction of the {110} peak – with the scattering vector parallel to the loading direction – and is rather difficult to discern from the {110} tail, all of which might be a source of error.

Given the elastic anisotropy as shown in Figure 104, it is therefore not surprising that Young and co-workers did not observe a significant anisotropic effect with the axial slopes of the (200) and the (202) (in Young's notation (020) and (220)) orientations. For the (121) (Young (112)), however, a significantly lower value is expected, but again, this reflection might overlap with the (210), which indeed has a stiffness close to that of the (200) and the (202). The corresponding values calculated from single crystal elastic constants C_{mn} amount to: E(200) = 269 GPa, E(202) = 273 GPa, E(121) = 83 GPa and E(121) = 299 GPa.

The presence of an elastic anisotropy in cementite was confirmed and might have some direct consequences: (i) The assumption of an isotropic elastic behaviour, for instance, in the stress calculation from elastic strains using the diffraction elastic constants of some extreme orientations or the modelling of ferrite and cementite interaction [15, 65] is hence not really justified; (ii) The cementite stiffness was often assumed to be similar to that of ferrite, suggesting that the cementite does not act as a reinforcement in the elastic regime. This might need to be reconsidered, in particular at elevated temperatures; (iii) Elastic anisotropy between the different grain orientations might also affect the amount of load that cementite grain orientations carry once the ferrite matrix plastically deforms. Before considering this anisotropic behaviour in the steel's plastic regime (§4.4.3), the origin of the cementite peak asymmetry has to be addressed, since this questions the choice of the correct peak position, which is used for the lattice strain determination.

4.4.2 Origin of diffraction peak broadening

It is known that the cementite peaks broaden during plastic deformation, e.g. [15, 33]. The origin of this peak broadening is still under debate and the possible reasons are (i) an inhomogeneous strain field in the scattering volume (e.g. increasing dislocation density in grains during deformation), (ii) a reduction of the coherent scattering size (e.g. shrinking of the particle, twinning, breaking) and/or (iii) different strains from different particles [158].

In the 1%CrMoV steel and at the onset of ferrite plasticity, the cementite peaks start broadening and become asymmetric with the shallower tail towards larger lattice strains (i.e. the towards higher d-spacings in the axial and lower d-spacings in the transverser direction). This is summarized in Figure 103(b) in the beginning of this section §4.4 for the axial (122) peak. In spite of the broadening and asymmetry, the entire peak continues moving towards larger lattice strains and therefore takes load from the plastifying ferrite matrix. The shallower tail towards larger lattice strains would indicate that a small fraction of cementite particles are strained more than the majority of the particles. Figure 105(a) shows a schematic of the complex arrangement of the cementite particles within the ferritic matrix in the 1%CrMoV steel: There are elongated particles, spherical particles, particles at the grain boundaries and within the grains, small particles and large particles. Figure 105(b) schematically shows that, if these particles experience different stress states and would give rise to separate contributions, then this would convolute the actual broadened and asymmetric diffraction peak, as observed. This hypothesis, that the broadening of the cementite diffraction peak, at least in the early stage of plastic deformation, could originate from the range of local stress states experienced by the diffracting phase, i.e. "different strains from different particles" has been proposed in Ref [158].
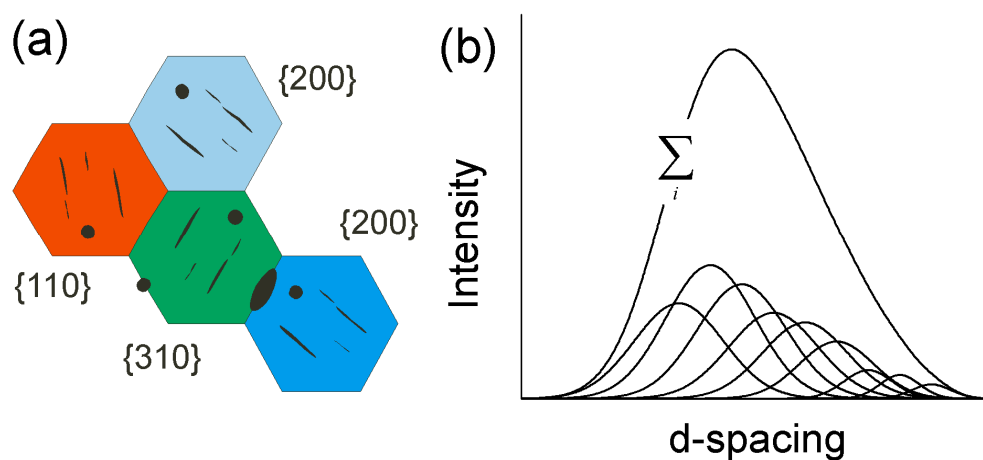

Figure 105 (a) Schematic of the cementite precipitates with different morphologies and locations embedded in the ferrite matrix. For simplicity, the ferrite grains, all of the same size, have been drawn with a honeycomb structure, which does not reflect the much more complex microstructure in the 1%CrMoV steel. (b) Schematic of the origin of the cementite peak broadening: "Different strain from different particles", where the resulting peak shape is a sum of the individual contributions i.

This hypothesis is supported by the observation of Wilson and Konnan [33] who reported on stress relaxation of the cementite particles when the constraining matrix is partially etched away; before the matrix was removed, the residual lattice strain of the cementite particle was about 0.3%. However, lattice strains of more than 1% are observed in the 1%CrMoV steel after RT tensile deformation to 4% plastic strain, which would correspond to stresses of several GPa using a simple

approximation (Eq. 37). These stresses are rather high and plastic deformation or fracture of the cementite particles can therefore not be excluded. Both events have been reported in literature, [67, 68] and [159], respectively. Their corresponding contribution to peak broadening can then originate from inhomogeneous strain fields around the lattice defects and a reduction of the coherent scattering size. When the latter occurs by particle fracture, this may cause (if a large fraction of particles do that) an instantaneous stress relaxation and corresponding shifts in the lattice strain, which was not observed. The question remains, how sensitive the peak broadening actually is to such events. To further address the origin of the peak broadening, the carbide powder of the 1%CrMoV steel has been extracted by dissolving the ferrite matrix. Figure 106 shows a summary plot with the peak shape of the axial (122) cementite orientation being embedded in the ferrite matrix and after extraction from the ferrite matrix. Results from RT and HT tensile test are shown. The peak broadening and increasing peak asymmetry with increasing plastic strain observed during RT tensile deformation is not observed in the extracted carbide powder, i.e. when the constraining ferritic matrix is removed, even in the samples deformed to large plastic strain of 5%. This confirms that the large peak broadening and asymmetry is due to "different strains from different particles". Note that severe deformation of the carbide powder, after extraction from the ferrite matrix, does not significantly increase the (122) peak shape apart from the slightly widened tails (cf. Figure 87). For comparison with the RT data, the peak evolution during HT tensile deformation is shown in Figure 106. The peak does not show a large broadening and extensive peak asymmetry. The reason could be due to enhanced relaxation effects during deformation at HT (e.g. creep), which limits the maximum stress that the cementite particles may experience.
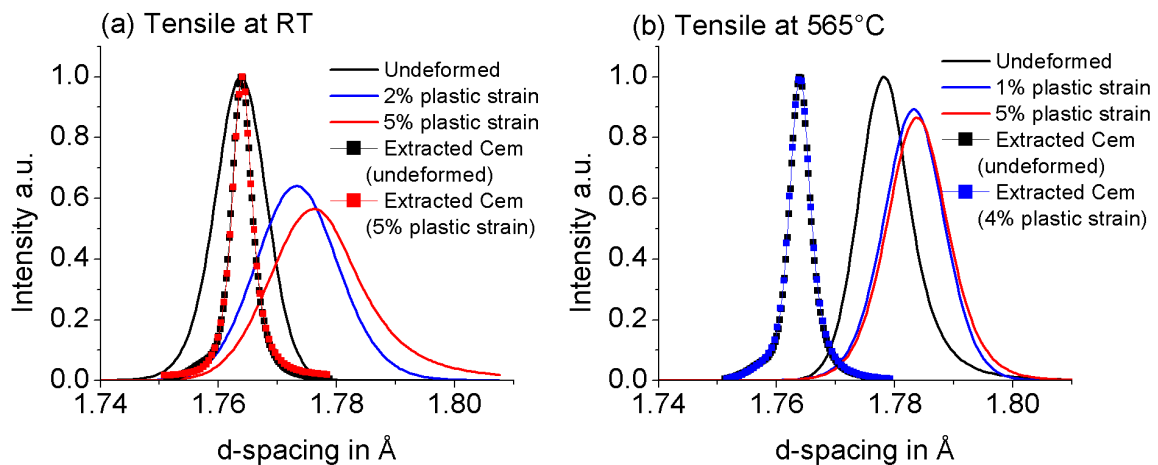

Figure 106 Peak shape of the cementite (122) reflection parallel to the loading axis (axial direction) of the 1%CrMoV samples tensile deformed at ambient temperature (a) and at 565°C (b). The pure lines represent the condition with the cementite embedded in the constraining ferrite matrix (cf. Figure 68, §3.4.1.1). The symbols represent the measurement on the extracted carbide powder (without the constraining ferrite matrix, cf. Figure 87, §3.6.2). Note that the instrumental broadening for the powder measurements (symbols) is smaller than the actual peak width, as confirmed with a standard powder (NAC) with much smaller intrinsic peak width.

Since the cementite particles are embedded in the ferrite matrix, the magnitude of the broadening and asymmetry must depend on the heterogeneity of the microstructure in terms of cementite particle size, size distribution, morphology and orientational characteristics with, and the location (e.g. within the grain or at the boundaries) within the ferrite matrix. Comparing two extreme microstructures, e.g. the pearlitic microstructure and the spheroidized microstructure with spherical cementite particles, should clearly indicate a difference in the peak shape after deformation. Figure **107** shows a part of the diffraction pattern of the high-carbon steel before and after RT tensile deformation, with the spheroidized and the pearlitic microstructure. The (301) and the (212) diffraction peaks of the spheroidized microstructure only show a moderate peak broadening and no significant asymmetry after deformation. On the other hand, the (301) peak shape in the pearlitic microstructure shows a significant second contribution to the actual peak shape towards larger lattice strains. The Δ indicates the large separation of about 1% lattice strain. One could argue that the neighbouring (231) peak contributes somehow to the (301) peak shape. In fact, the (231) stiffness according to Figure 104 is 133 GPa and therefore significantly lower than that of the (301) with 280 GPa. This difference in the stiffness might then also be reflected after deformation in the residual strain state (cf. §4.4.3). However, the intensity of the (231) is at least one order of magnitude lower than that of the (301), which also justifies the use of the (301) for single peak fitting. Furthermore, the (212) peak also shows this feature towards larger lattice strain and is certainly not affected by another peak. The origin for these two contributions to the peak shape in the pearlitic microstructure is not clear and should be investigated in more detail, also towards a potential plastic deformation of cementite.
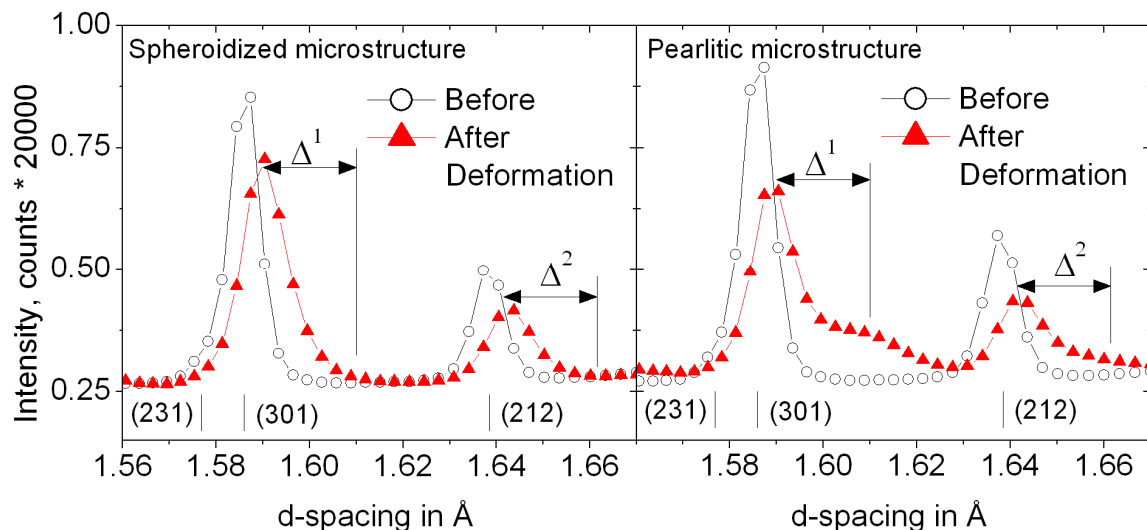

Figure 107 Part of the diffraction pattern of the spheroidized steel (*HC3_1*) and the pearlitic steel (*HC1*) from the axial direction, before and after deformation (to about 4.5% plastic strain). Δ^1 and Δ^2 equivalent to about 1% lattice strain.

4.4.3 Anisotropic behaviour of cementite in the plastic regime

It has been reported that some cementite grain orientations carry more load than others once the stress-strain curve enters the plastic regime [50, 65]. Assuming that cementite deforms only elastically, Young and co-workers [65] suggested that this load-carrying anisotropy can be due to a crystallographic relationship between the ferrite and the cementite phase.

Figure 108 shows the lattice strain evolution of the (122) and the (301) in the spheroidized microstructure during RT tensile deformation. These spherical cementite particles have a rather homogeneous strain state during deformation. This was seen from the diffraction peak in Figure 107. Due to the elastic anisotropy, the (301) is stiffer than the (122) in the elastic regime. Also in the plastic regime the slope of the (301) is stiffer than that of the (122). After unloading, the (122) accumulates far more residual strain than the (301).

Assuming that cementite does not deform plastically, which implies that there is also no plastic anisotropy in the sense of §1.1.2.1.2 with plastically soft and strong directions. Then one might draw the hypothesis that the cementite grain orientations, which are more compliant, also accumulate more residual strain after (plastic) tensile deformation. Local plastic flow around the cementite particles could for instance preserve the shape misfit after unloading.
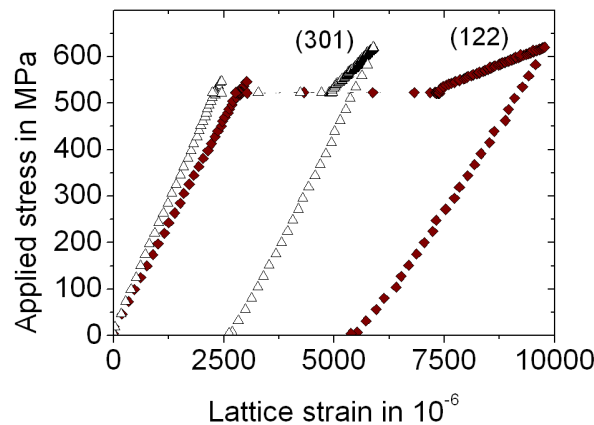

Figure 108 Summary plot showing the axial cementite (301) and (122) orientations during RT tensile deformation of the high-carbon steel with the spheroidized microstructure, from Figure 71(f), §3.4.3.1.

5 Summary and Outlook

This thesis reports on the evolution of residual lattice strain in a creep-resistant 1%CrMoV steel subjected to three different deformation conditions: Room temperature and high temperature (565°C, service conditions) tensile deformation and high temperature creep. This material exhibits a rather complex and inhomogeneous microstructure combined with a low volume fraction of second phase particles. Therefore, a complementary approach of in situ and ex situ ToF neutron and synchrotron X-ray diffraction has been followed. Furthermore the measurements are complemented with results obtained from high-carbon steels with various microstructures and high volume fraction of cementite.

The thesis focuses on the interplay between the ferrite matrix and embedded cementite particles. The contribution of second phase vanadium carbide on the accumulation of residual strain could not be elucidated; this may be a task for further studies.

The evolution of both the interphase and intergranular strain in the ferrite differs considerably depending on the deformation mode. The interphase strains result from a load-redistribution of the ferrite to the cementite. For small plastic strains until about 1% the (axial) interphase strains are of about the same magnitude after tensile deformation at RT and HT for the investigated strain rate of 10^{-5} s^{-1}. On the other hand, at the end of the primary creep regime nearly no interphase strains are present. When creep processes dominate the deformation, no further load-redistribution is observed in the steady-state regime. At larger plastic strains, the largest amount of interphase strain is therefore obtained by RT tensile deformation.

Intergranular strains are introduced after deformation for all deformation modes. The largest (axial) intergranular strains develop after HT tensile deformation and decrease towards large plastic strains to a value that is similar to that obtained in the steady-state regime of the creep deformed samples. The smallest intergranular strains are obtained after RT tensile deformation. A possible explanation is that the enhanced elastic anisotropy of the ferrite at HT, observed during tensile loading for the 1%CrMoV and confirmed for a high-carbon steel with a spheroidized microstructure, causes the enhanced load transfer between the stiff and the compliant grain families. This should, however, be investigated in more detail with a focus on the deformation mechanisms. The mechanical response during HT tensile deformation exhibits a marked elasto-plastic transient regime before entering a steady-state regime. The onset of this transient regime corresponds well with the onset of load-redistribution from the {110} to the {200} ferrite grain family and to the cementite.

The diffraction data clearly point towards an elastic anisotropy for cementite embedded in a ferrite matrix. This was found for the 1%CrMoV steel and all high-carbon steels and is also in agreement with first principal studies reported in literature. During RT tensile deformation the

cementite diffraction peaks exhibit significant asymmetric broadening. Diffraction experiments performed on carbide powder extracted from deformed and undeformed samples suggest that this is mainly caused by a broad distribution of local stress states that the various cementite particles experience within the ferrite matrix. In agreement, the cementite peak shape was found to be less broadened and more symmetric in the spheroidized microstructure compared with a more complex pearlitic microstructure. This topic is, however, not exhaustively investigated. For instance, dedicated diffraction line profile analysis could be performed on cementite powder extracted from spheroidized ferritic steel before and after deformation at RT and HT. This may shed further light on the question whether cementite may for instance plastically deform or fracture.

In order to make further progress in this field advanced modelling efforts are needed. In this work it is shown that many features present for the 1%CrMoV steel also exist in high-carbon steel with spheroidized microstructure. This more idealized microstructure may be an excellent starting point for such modelling efforts.

6 References

[1] T. Mayer, *Q Factor Variation in Cylindrical Testpieces Undergoing Mechanical and Thermal Loading*, Semester Project, Institute of Mechanical Systems, ETH Zurich, 2007.

[2] H.-D. Tietz, Grundlagen der Eigenspannungen, Distributed by Springer-Verlag, 1982.

[3] I. C. Noyan, J. B. Cohen, *Residual stress*, Springer-Verlag, New York, 1987.

[4] E. Heyn, *Eine Therorie der "Verfestigung" von metallischen Stoffen infolge Kaltreckens.* Festschrift der Kaiser-Wilhelm-Ges., Springer Verlag, Berlin, 1921, p. 121-131.

[5] G. Masing, Z. Techn. Phys. 6 (1925) 569-573.

[6] E. Macherauch, H. Wohlfahrt, U. Wolfstieg, Härterei-Tech. Mitt. 28 (1973) 201-211.

[7] P. J. Withers, Rep. Prog. Phys. 70 (2007) 2211-2264.

[8] B. Clausen, *Characterisation of Polycrystal Deformation by Numerical Modelling and Neutron Diffraction Measurements*, Ph.D. Thesis, Risø National Laboratory, 1997.

[9] Nye, *Physical properties of crystals*, Oxford University Press, 1985.

[10] G. E. Dieter, *Mechanical Metallurgy*, McGraw-Hill Book, London, 1988.

[11] M. T. Hutchings, P. J. Withers, T. M. Holden, T. Lorentzen, *Introduction to the charcaterization of residual stress by neutron diffraction*, Taylor&Francis, 2005.

[12] D. Fruchart, P. Chaudouet, R. Fruchart, A. Rouault, J. P. Senateur, J. Solid State Chem. 51 (1984) 246-252.

[13] G. I. Taylor, C. F. Elam, Proceedings of the Royal Society of London Series a-Containing Papers of a Mathematical and Physical Character 112 (1926) 337-361.

[14] A. J. Opinsky, R. Smoluchowski, Journal of Applied Physics 22 (1951) 1488-1492.

[15] E. C. Oliver, M. R. Daymond, P. J. Withers, Acta Mater. 52 (2004) 1937-1951.

[16] W. Voigt, Lehrbuch der Kristallphysik, Teubner Verlag, Berlin, 1910.

[17] A. Reuss, Zeitschrift Fur Angewandte Mathematik Und Mechanik 10 (1930) 266-274.

[18] G. I. Taylor, Journal of the Institute of Metals 62 (1938) 307-324.

[19] G. Sachs, Zeitschrift Des Vereines Deutscher Ingenieure 72 (1928) 734-736.

[20] E. C. Oliver, *The generation of internal stresses in single and two phase materials*, Ph.D. Thesis, University of Manchester, 2002.

[21] S. Hartmann, H. Ruppersberg, Mater. Sci. Eng., A 325 (2002) 414-423.

[22] I. G. Wood, L. Vocadlo, K. S. Knight, D. P. Dobson, W. G. Marshall, G. D. Price, J. Brodholt, J. Appl. Crystallogr. 37 (2004) 82-90.

[23] H. K. D. H. Bhadeshia, R. W. K. Honeycomb, *Steels: Microstructure and Properties*, Elsevier Ltd., Oxford, UK, 2006.

[24] H. K. D. H. Bhadeshia, *Bainite in Steels*, IOM Communications Ltd, 2001.

[25] B. A. Senior, Mater. Sci. Eng., A 103 (1988) 263-271.

[26] L. Binda, S. R. Holdsworth, E. Mazza, Int. J. Pres. Ves. Pip. 87 (2010) 319-325.

[27] P. G. Stone, J. D. Murray, J. Iron Steel Inst. 203 (1965) 1094-1107.

[28] J. F. Norton, A. Strang, J. Iron Steel Inst. 207 (1969) 193-&.

[29] M. F. Ashby, Acta Metall. 20 (1972) 887-897.

[30] H. Frost, M. Ashby, *Deformation-mechanism maps*, Pergamon Press, Oxford, 1982.

[31] S. R. Holdsworth, (*Private Communication*, 2011).

[32] N. Shinya, J. Kyono, H. Kushima, ISIJ Inter. 46 (2006) 1516-1522.

[33] D. V. Wilson, Y. A. Konnan, Acta Metallurgica 12 (1964) 617-628.

[34] H. Ledbetter, Mater. Sci. Eng., A 527 (2010) 2657-2661.

[35] J. Alkorta, J. G. Sevillano, J. Mater. Res. 27 (2012) 45-52.

[36] T. W. Clyne, P. J. Withers, *An introduction to metal matrix composites*, Cambridge University Press, Cambridge, 1993.

[37] C. Jiang, S. G. Srinivasan, A. Caro, S. A. Maloy, J. Appl. Phys. 103 (2008).

[38] Z. Q. Lv, F. C. Zhang, S. H. Sun, *e. al.*, Comput. Mater. Sci. 44 (2008) 690-694.

[39] K. O. E. Henriksson, N. Sandberg, J. Wallenius, Appl. Phys. Lett. 93 (2008).

[40] M. Nikolussi, S. L. Shang, T. Gressmann, A. Leineweber, E. Mittemeijer, Y. Wang, Z. K. Liu, Scripta Mater. 59 (2008) 814-817.

146

[41] V. Hauk, Zeitschrift Fur Metallkunde 46 (1955) 33-38.

[42] T. Hanabusa, J. Fukura, H. Fujiwara, Bull. of J.M.S.E (1969).

[43] L. Che, M. Gotoh, Y. Horimoto, Y. Hirose, J. Iron Steel Res. Inter. 14 (2007) 31-38.

[44] D. V. Wilson, P. S. Bate, Acta Metall. 34 (1986) 1107-1120.

[45] R. A. Winholtz, J. B. Cohen, Mater. Sci. Eng., A 154 (1992) 155-163.

[46] R. A. Winholtz, J. B. Cohen, Metall. Mater. Trans. A 23 (1992) 341-354.

[47] J. D. Almer, J. B. Cohen, R. A. Winholtz, Metall. Mater. Trans. A 29 (1998) 2127-2136.

[48] N. Bonner, G. Modlen, P. Webster, J. Root, T. Holden, Proceedings of ICRS-5, Linköping, Sweden (1997).

[49] Y. Tomota, P. Lukas, D. Neov, S. Harjo, Y. R. Abe, Acta Mater. 51 (2003) 805-817.

[50] A. Kanie, Y. Tomota, S. Torii, T. Kamiyama, ISIJ Inter. 44 (2004) 1952-1956.

[51] J. W. L. Pang, T. M. Holden, T. E. Mason, J. Strain Anal. Eng. Des. 33 (1998) 373-383.

[52] Y. Tomota, P. Lukas, S. Harjo, J. H. Park, N. Tsuchida, D. Neov, Acta Mater. 51 (2003) 819-830.

[53] M. R. Daymond, H. G. Priesmeyer, Acta Mater. 50 (2002) 1613-1626.

[54] K. VanAcker, J. Root, P. VanHoutte, E. Aernoudt, Acta Materialia 44 (1996) 4039-4049.

[55] M. Kriska, J. Tacq, K. Van Acker, M. Seefeldt, S. Van Petegem, Proceedings of 5th ECNS 340 (2012).

[56] Y. Tomota, T. Suzuki, A. Kanie, Y. Shiota, M. Uno, A. Moriai, N. Minakawa, Y. Morii, Acta Mater. 53 (2005) 463-467.

[57] M. L. Martinez-Perez, F. J. Mompean, J. Ruiz-Hervias, C. R. Borlado, J. M. Atienza, M. Garcia-Hernandez, M. Elices, J. Gil-Sevillano, R. L. Peng, T. Buslaps, Acta Mater. 52 (2004) 5303-5313.

[58] M. L. Martinez-Perez, C. R. Borlado, F. J. Mompean, M. Garcia-Hernandez, J. Gil-Sevillano, J. Ruiz-Hervias, J. M. Atienza, M. Elices, R. L. Peng, M. R. Daymond, Acta Mater. 53 (2005) 4415-4425.

[59] J. M. Atienza, M. L. Martinez-Perez, J. Ruiz-Hervias, F. Mompean, M. Garcia-Hernandez, M. Elices, Scripta Mater. 52 (2005) 305-309.

[60] J. M. Atienza, J. Ruiz-Hervias, M. L. Martinez-Perez, F. J. Mompean, M. Garcia-Hernandez, M. Elices, Scripta Mater. 52 (2005) 1223-1228.

[61] M. Seefeldt, A. Walentek, P. Van Houtte, M. Vrana, P. Lukas, Proceedings of 7th ECRS 524-525 (2006) 375-380.

[62] S. Morooka, Y. Tomota, T. Kamiyama, ISIJ Inter. 48 (2008) 525-530.

[63] Y. Tomota, O. Watanabe, A. Kanie, A. Moriai, N. Minakawa, Y. Moriai, Materials Science and Technology 19 (2003) 1715-1720.

[64] J. Q. da Fonseca, E. C. Oliver, P. S. Bate, P. J. Withers, Mater. Sci. Eng., A 437 (2006) 26-32.

[65] M. L. Young, J. D. Almer, M. R. Daymond, D. R. Haeffner, D. C. Dunand, Acta Mater. 55 (2007) 1999-2011.

[66] M. Umemoto, K. Tsuchiya, ISIJ Inter. 88 (2002) 11-22.

[67] A. Inoue, T. Ogura, T. Masumoto, Transactions of the Japan Institute of Metals 17 (1976) 149-157.

[68] J. G. Sevillano, Mater. Sci. Eng. 21 (1975) 221-225.

[69] V. G. Gavriljuk, Mater. Sci. Eng. A 345 (2003) 81-89.

[70] M. Umemoto, Y. Todaka, K. Tsuchiya, Thermec'2003, Pts 1-5 426-4 (2003) 859-864.

[71] A. Inoue, T. Ogura, T. Masumoto, Metall. Trans. A 8 (1977) 1689-1695.

[72] H. M. A. Winand, A. F. Whitehouse, P. J. Withers, Mater. Sci. Eng., A 284 (2000) 103-113.

[73] T. Mori, Y. Nakasone, M. Taya, K. Wakashima, Phil. Mag. Lett. 75 (1997) 359-365.

[74] T. Mori, K. Tanaka, Y. Nakasone, J. Huang, M. Taya, Cmmc 96 - Proceedings of the First International Conference on Ceramic and Metal Matrix Composites, Pts 1 and 2 127- (1997) 1145-1152.

[75] D. C. Stouffer, L. T. Dame, *Inelastic deformation of metals*, John Wiley & Sons, Inc., 1996.

[76] A. F. Whitehouse, T. W. Clyne, Acta Metall. Mater. 43 (1995) 2107-2114.

[77] S. Y. Huang, D. W. Brown, B. Clausen, Z. K. Teng, Y. F. Gao, P. K. Liaw, Metall. Mater. Trans. A 43A (2012) 1497-1508.

[78] H. Choo, D. Seo, J. Beddoes, M. A. M. Bourke, D. W. Brown, Appl. Phys. Lett. 85 (2004) 4654-4656.

[79] P. B. Prangnell, S. J. Barnes, S. M. Roberts, P. J. Withers, Mater. Sci. Eng., A 220 (1996) 41-56.

[80] M. Belassel, J. L. Lebrun, S. Deis, Proceedings of 4th ICRS4 (1994) 392-401.

[81] M. Belassel, V. Ji, J. L. Lebrun, e. al., J. Phys. IV 4 (1994) 261-264.

[82] L. Che, M. Gotoh, Y. Horimoto, Y. Hirose, L. Yang, J. Mater. Eng. Perform. 17 (2008) 445-453.

[83] M. E. Fitzpatrick, POLDI Beamtime Proposal (2011).

[84] A. Rao, P. J. Bouchard, M. E. Fitzpatrick, Anelasticity in Austenitic Steels, in: K. Fox, E. Hoffman, N. Manjooran, G. Pickrell (Eds.), Advances in Materials Science for Environmental and Nuclear Technology, vol 222, John Wiley & Sons, 2010, pp. 133-143.

[85] W. Blum, Mater. Sci. Eng., A 319 (2001) 8-15.

[86] W. Blum, P. Eisenlohr, F. Breutinger, Metall. Mater. Trans. A 33 (2002) 291-303.

[87] P. B. Prangnell, T. Downes, P. J. Withers, T. Lorentzen, Mater. Sci. Eng., A 197 (1995) 215-221.

[88] T. Lorentzen, M. R. Daymond, B. Clausen, C. N. Tome, Acta Mater. 50 (2002) 1627-1638.

[89] J. Bauschinger, Mitt. Mech.-Tech. München (1881).

[90] D. V. Wilson, Acta Metall. 13 (1965) 807-&.

[91] C. W. Sinclair, G. Saada, J. D. Embury, Phil. Mag. 86 (2006) 4081-4098.

[92] L. Thilly, S. Van Petegem, P. O. Renault, F. Lecouturier, V. Vidal, B. Schmitt, H. Van Swygenhoven, Acta Mater. 57 (2009) 3157-3169.

[93] G. A. E. Webster, *Polycrystalline materials - Determination of residual stresses by neutron diffraction*, ISO, Case postale 56, CH-1211 Geneva 20, Switzerland, 2001.

[94] M. E. Fitzpatrick, A. T. Fry, P. Holdway, F. A. Kandil, J. Shackleton, L. Suominen, NPL Publications 52 (2005).

[95] M. R. Daymond, P. J. Bouchard, Metall. Mater. Trans. A 37A (2006) 1863-1873.

[96] J. R. Bunn, D. Penumadu, C. R. Hubbard, Appl. Phys. A 99 (2010) 571-578.

[97] M. R. Daymond, M. A. M. Bourke, R. B. VonDreele, B. Clausen, T. Lorentzen, J. Appl. Phys. 82 (1997) 1554-1562.

[98] J. Repper, *Einfluss mikroskopischer Eigenspannungen auf die makroskopische Eigenspannungsanalyse mittels Neutronenbeugung*, Ph.D. Thesis, Technische Universität München, 2010.

[99] S. R. Holdsworth, (*Private Communication*, 2010).

[100] L. Binda, *Advanced creep damage and deformation assessment of materials subjected to steady and cyclic loading conditions at high temperatures*, Ph.D.Thesis, ETH Zurich, 2010.

[101] T. V. Rajan, C. P. Sharma, A. Sharma, *Heat Treatment*, Asoke K. Ghosh, Prentice-Hall of India Private Limited, New Delhi, 2006.

[102] A. Baltusnikas, R. Levinskas, Materials Science 12 (2006) 192-198.

[103] G. S. Pawley, J. Appl. Crystallogr. 14 (1981) 357-361.

[104] H. M. Rietveld, J. Appl. Crystallogr. 2 (1969) 65-71.

[105] M. R. Daymond, J. Appl. Phys. 96 (2004) 4263-4272.

[106] G. E. Bacon, *Neutron Diffraction*, Oxford University Press, Oxford, UK, 1975.

[107] B. D. Cullity, S. R. Stock, *Elements of X-ray Diffraction*, Prentice Hall, New Jersey, USA, 2001.

[108] http://www.psi.ch/niag/neutron-physics, (Access date: Feb. 1, 2013).

[109] NIST, http://physics.nist.gov/PhysRefData/XrayMassCoef/tab3.html, (Access data: Feb. 1, 2013).

[110] A. M. Korsunsky, S. Y. Zhang, D. Dini, W. J. J. Vorster, J. Liu, Residual Stresses Vii 524-525 (2006) 743-748.

148

[111] A. C. Thompson (Ed.), *X-ray data booklet*, Lawrence Berkeley National Laboratory, University of California, 2009.

[112] J. Falta, T. Möller, *Forschung mit Synchrotronstrahlung*, Vieweg+Teubner, Wiesbaden, 2010.

[113] http://www.ill.eu/, (Access date: Feb. 1, 2013).

[114] A. Dianoux, G. E. Lander, *Neutron Data Booklet*, ILL, Grenoble, France, 2003.

[115] U. Stuhr, H. Spitzer, J. Egger, A. Hofer, P. Rasmussen, D. Graf, A. Bollhalder, M. Schild, G. Bauer, W. Wagner, Nucl. Instrum. Methods Phys. Res., Sect. A 545 (2005) 330-338.

[116] J. R. Santisteban, *Stress Analysis by Energy-Dispersive Neutron Diffraction*, in: W. Reimers, A. R. Pyzalla, A. Schreyer, H. Clemens (Eds.), *Neutrons and Synhrotron Radiation in Engineering Materials Science*, WILEY-VCH, Weinheim, 2008.

[117] J. R. Santisteban, M. R. Daymond, J. A. James, L. Edwards, J. Appl. Crystallogr. 39 (2006) 812-825.

[118] U. Stuhr, Nucl. Instrum. Methods Phys. Res., Sect. A 545 (2005) 319-329.

[119] J. R. Taylor, *An introduction to error analysis*, University Science Books, Sausalito, CA 94965, USA, 1997.

[120] M. Beckert, H. Klemm, *Handbuch der metallographischen Ätzverfahren*, Deutscher Verlag für Grundstoffindustrie, Leipzig, 1962.

[121] A. H. Committee, *Metals Handbook: Metallography, Structures and Phase Diagrams*, American Society for Metals, Materials Park, Ohio, 1973.

[122] http://www.psi.ch/sls/ms/, (Access date: Feb. 1, 2013).

[123] http://mss.web.psi.ch/, (Access date: Feb. 1, 2013).

[124] H. Van Swygenhoven, B. Schmitt, P. M. Derlet, S. Van Petegem, *et al.*, Rev. Sci. Instrum. 77 (2006) 10.

[125] F. Gozzo, *SLS/MS/PD station Handbook*: from http://www.psi.ch/sls/ms/ (Access data: Feb. 1, 2013), 2007.

[126] A. Bergamaschi, A. Cervellino, R. Dinapoli, F. Gozzo, *e. al.*, J Synchrotron Radiat. 17 (2010) 653-668.

[127] S. Brandstetter, *Deformation mechanisms of nanocrystalline nickel studied by in situ X-ray diffraction*, Ph.D. Thesis, Ecole Polytechnique Fédérale de Lausanne (EPFL), 2008.

[128] Z. Budrovic, *Footprints of deformation mechanisms during in situ X-ray diffraction: nanocrystalline and ultrafine grained materials*, Ph.D. Thesis, Ecole Polytechnique Fédérale de Lausanne (EPFL), 2006.

[129] A. C. Larson, R. B. Von Dreele, Los Alamos National Laboratory Report LAUR 86-748 (2000).

[130] http://www.nist.gov, (Access data: Nov. 12, 2012).

[131] G. Courbion, G. Ferey, J. Solid State. Chem. 76 (1988) 426-431.

[132] http://www.esrf.eu/UsersAndScience/Experiments/StructMaterials/ID15, (Access date: Feb. 1, 2013).

[133] C. Eberl, D. S. Gianola, R. J. Thompson, *Digital Image Correlation and Tracking*, http://www.mathworks.com/matlabcentral/fileexchange/12413 (Access date, Feb. 1, 2013).

[134] S. R. Kalidindi, A. Abusafieh, E. ElDanaf, Exp. Mech. 37 (1997) 210-215.

[135] J. E. Daniels, M. Drakopoulos, J. Synchrotron Radiat. 16 (2009) 463-468.

[136] A. P. Hammersley, ESRF Internal Report, ESRF97HA02T (1997).

[137] A. P. Hammersley, S. O. Svensson, M. Hanfland, A. N. Fitch, D. Hausermann, High Pressure Res. 14 (1996) 235-248.

[138] http://sourceforge.net/apps/trac/fable/wiki/imaged11%20-%20fit2dcake, Python script to batch process radial integration with Fit2D, (Access data: Nov. 16, 2012).

[139] http://poldi.web.psi.ch, (Access date: Feb. 1, 2013).

[140] http://www.isis.stfc.ac.uk/instruments/engin-x/, (Access date: Feb 1, 2013).

[141] R. Haynes, A. M. Paradowska, M. A. H. Chowdhury, C. M. Goodway, *et al.*, Meas. Sci. Technol. 23 (2012).

[142] M. A. Weisser, http://ftp.esrf.eu/pub/UserReports/43992_A.pdf, Experimental Report (MA994) 2010, (Access data: Feb. 1, 2013).

[143] R. I. Kailasam, Effect of strain rate on the mechanical properties of Cr-Mo-V steel at elevated temperatures, in: Weapons Laboratory at Rock Island, 1972.

[144] S. Y. Zhang, Instrument Scientist ENGIN-X, Private Communication, in: 2012.

[145] V. M. Radhakrishnan, Mater. Sci. Tech. 7 (1991) 541-543.

[146] T. Mayer, *Characterisation and Modelling of the Microstructural and Mechanical Evolution of a Steam Turbine Rotor Steel*, Ph.D. Thesis, ETH Zurich, 2012.

[147] D. Dye, H. J. Stone, R. C. Reed, Curr. Opin. Solid State Mater. Sci. 5 (2001) 31-37.

[148] P. J. Withers, M. Preuss, A. Steuwer, J. W. L. Pang, J. Appl. Crystallogr. 40 (2007) 891-904.

[149] H. K. D. H. Bhadeshia, S. A. David, J. M. Vitek, R. W. Reed, J. Mater. Sci. Technol. 7 (1991) 686-698.

[150] A. Leineweber, J. Appl. Crystallogr. 45 (2012) 944-949.

[151] S. Hartmann, H. Ruppersberg, Mater. Sci. Eng., A 190 (1995) 231-239.

[152] E. J. Mittemeijer, P. Scardi, *Diffraction analysis of the microstructure of materials*, Springer, Berlin, 2004.

[153] T. Mayer, L. Balogh, C. Solenthaler, E. Müller Gubler, S. R. Holdsworth, Acta Mater. 60 (2012) 2485-2496.

[154] A. Madgwick, T. Mori, P. J. Withers, Mater. Sci. Eng., A 285 (2000) 408-411.

[155] V. I. Razumovskiy, A. V. Ruban, P. A. Korzhavyi, Phys. Rev. Lett. 107 (2011).

[156] S. Pierret, A. Evans, A. M. Paradowska, A. Kaestner, J. James, T. Etter, H. Van Swygenhoven, NDT&E Int. 45 (2012) 39-45.

[157] M. T. Hutchings, P. J. Withers, T. M. Holden, T. Lorentzen, *Introduction to the charcaterization of residual stress by neutron diffraction*, Taylor&Francis, 2005, p. 204.

[158] M. A. Weisser, A. D. Evans, S. Van Petegem, S. R. Holdsworth, H. Van Swygenhoven, Acta Mater. 59 (2011) 4448-4457.

[159] J. Gurland, Acta Metall. 20 (1972) 735-&.

Acknowledgements

Curriculum vitae

Michael Andreas Weisser

Born April 2, 1983 in DE-91710 Gunzenhausen

Nationality German

One child

2008 – present: PhD Student
Doctoral school at Ecole Polytechnique Fédérale de Lausanne (EPFL) and works in the Group Materials Science and Simulation, Paul-Scherrer Institute; Switzerland

Supervisor thesis: Prof. Dr. Helena Van Swygenhoven

2002 – 2008: Diploma in Materials Science and Engineering
Institute of General Materials Properties (Prof. Dr. M. Göken), University Erlangen-Nuremberg, Germany and Université Paris-Sud XI, Orsay, France.

Supervisor Diplomarbeit (*Dehngradienten unter Nanoindentierungen in Einkristallen – Experiment und Simulation, 2008*): Dr. Karsten Durst

Supervisor Studienarbeit (*Diffusion cationique dans l'oxyde de cuivre – Justification de la théorie de Wagner pour le système Cu / Cu₂O, 2005*): Dr. Bernard Lesage

Publications:

Schloth P, **Weisser MA**, Van Swygenhoven H, Van Petegem S, Susila P, Subramanya Sarma V, Murty BS, Lauterbach S, Heilmaier M, *Two strain-hardening mechanisms in nanocrystalline austenitic steel: An in situ synchrotron X-ray diffraction study*, Scripta Mater. 66, 690-693, (2012)

Weisser MA, Evans AD, Van Petegem S, Holdsworth SR, Van Swygenhoven H, *In situ room temperature tensile deformation of a 1%CrMoV bainitic steel using synchrotron and neutron diffraction*, Acta Mater. 59, 4448-4457, (2011)

Invited talk:

Weisser MA, Van Swygenhoven H, Schloth P, Van Petegem S, Subramanya Sarma V, Heilmaier M, *Two strain hardening mechanisms in nanocrystalline austenitic Fe-Cr-Ni-W steel*, TMS 2012, Orlando, FL, USA

Contributed talks:

Weisser MA, Van Petegem S, Holdsworth SR, Van Swygenhoven H, *Effect of different loading conditions on the accumulation of internal strain in a creep resistant bainitic steel*, TMS 2012, Orlando, FL, USA

Weisser MA, Evans AD, Van Petegem S, Holdsworth SR, Van Swygenhoven H, *Deformation studies of a creep resistant bainitic steel using synchrotron and neutron diffraction*, EUROMAT 2011, Montpellier, France

Weisser MA, Evans AD, Van Petegem S, Holdsworth SR, Van Swygenhoven H, *Deformation studies of a creep resistant bainitic steel using synchrotron and neutron diffraction*, MECA SENS VI, Hamburg, Germany

Weisser MA, Evans AD, Van Petegem S, Holdsworth SR, Van Swygenhoven H, *Deformation studies of a creep resistant bainitic steel using synchrotron and neutron diffraction*, TMS 2011, San Diego, CA, USA

Weisser MA, Evans AD, Van Petegem S, Holdsworth SR, Van Swygenhoven H, *In situ mechanical testing of creep resistant bainitic steel using synchrotron and neutron diffraction*, Materials Science and Engineering 2010, Darmstadt, Germany